Taming Optical Parametric Amplification:
Stable few cycle pulses at 210 to 10000 nm from
Ti:Sapphire and Yb-based lasers

Emanuel Wittmann

SIGILL: UNIVERSITAT: LUDOVIC: MAXIM:

Dissertation

München 2018

Taming Optical Parametric Amplification:
Stable few cycle pulses at 210 to 10000 nm from Ti:Sapphire and Yb-based lasers

Emanuel Wittmann

Dissertation
an der Fakultät für Physik
der Ludwig-Maximilians-Universität
München

vorgelegt von
Emanuel Wittmann
aus München

München, 17. Dezember 2018

Erstgutachter: Prof. Dr. Eberhard Riedle
Zweitgutachter: Prof. Dr. Jörg Schreiber

Tag der mündlichen Prüfung: 25. Februar 2019

Kurzfassung

Technisch relevante Femtosekunden-Lasersysteme sind aufgrund einer begrenzten Anzahl bekannter Lasermedien auf wenige Wellenlängen beschränkt. Die Abstimmbarkeit dieser Quellen wird durch den Prozess der optisch parametrischen Verstärkung (OPA) ermöglicht. Ein kleiner Teil der Laserleistung wird zur Erzeugung eines Seedpulses verwendet. Um die Abstimmbarkeit über einen großen Spektralbereich zu ermöglichen, wird ein Festkörper-Kontinuum verwendet. Mit einem starken Pumppuls kann ein ausgewählter Spektralanteil in einem geeigneten nichtlinearen Medium verstärkt werden. Um stabile und ultrakurze Pulse auf der 10 fs Skala zu erhalten, ist ein tiefes Verständnis jedes einzelnen Prozessschrittes erforderlich. In dieser Arbeit werden Ti:Saphir und Yb-basierte Lasersysteme zum Pumpen von OPAs eingesetzt. In der verwendeten Anordnung ist es möglich, Wiederholraten von 1 kHz bis 1 MHz und Eingangsenergien von 10 bis 300 µJ ohne größere Änderungen im Design zu nutzen. Wir erhalten ultrakurze Pulse vom UV bis zum MIR.

Neue Aspekte der Kontinuumserzeugung werden vorgestellt. Für die Erzeugung mit 1030 nm Licht werden verschiedene Kristalle hinsichtlich der sichtbaren und nahinfraroten Kontinuumsseite verglichen. Der bisher kaum berücksichtigte GSO erweist sich als vorteilhaft. Selbstkompression ohne externe Kompression wird gezeigt. Sie basiert auf einer 1 mm Saphir- oder YAG-Platte und einem astigmatismusfreien, achromatischen Teleskop - einem Schiefspiegler.

Das selbstkomprimierte, ungechirpte Kontinuum wird verwendet, um ein ultra-breitbandigen NOPA (nichtkollinearer OPA) zu seeden. Hier werden Quanteneffizienzen von bis zu 45% und 18 µJ Ausgangsenergie demonstriert und eine Kompression auf 6.7 fs gezeigt.

Das transmittierte Seedlicht und das verstärkte Signal nach der parametrischen Verstärkung können sich in deutlich unterschiedliche Richtungen ausbreiten. Dies wird als Folge einer Kerr-Linse bei den verwendeten Intensitäten erklärt. Eine pumpinduzierte Kerr-Linse wirkt auf den Signal-/Seedpuls. Bei nicht einwandfreier Einkopplung führt dies zu einer Ablenkung. Steht der Verstärkerkristall hinter der Fokalebene des Pumps, wird der Kerr-Linsen-Effekt durch Ausgleich der Strahldivergenz verringert. Dies ermöglicht auch, die Pumpintensität einfach zu reduzieren, indem man den Kristall weiter aus der Fokusebene heraus bewegt.

Bei MHz-Wiederholraten treten aufgrund der hohen Leistungen, die für die nichtlinearen Prozesse benötigt werden, thermische Probleme in einem NOPA auf. Für die Erzeugung der dritten Harmonischen (THG) eines Yb-Faserlasers wird die Erzeugung der zweiten Harmonischen (SHG) mit anschließender Summenfrequenz-Mischung verwendet. Die Zwei-Photonen-Absorption des UV Lichts führt zu messbarer Erwärmung im THG-Kristall. Daher ändert sich die Phasenanpassung und die UV-Leistung nimmt mit der Zeit ab. Mit einer Kompensationsplatte (αBBO) zwischen SHG- und THG-Kristall kann dieser Effekt minimiert werden. Durch die zeitliche Vorkompensation der Fundamentalen in Bezug auf die zweite Harmonische wird der Erzeugungsort der UV-Leistung an das Ende des THG Kristalls verschoben und das Volumen der Absorption minimiert. Dies ermöglicht langzeitstabilen, UV-gepumpten NOPA Betrieb auch bei 1 MHz Wiederholrate.

Ein OPA zur Erzeugung eines oktavbreiten Mittelinfrarotpulses um 8 µm wird gezeigt. Dafür wird ein 515 nm gepumpter NOPA vor einem kollinearen, 1030 nm gepumpten Verstärker auf LGS-Basis verwendet. Das Chirp-Management erfolgt hierbei ausschließlich durch ausgewählte Gläser und optische Filter. Das MIR-Feld wird zeitlich durch electro-optical sampling charakterisiert. Als Gate Puls wird die selbstkomprimierte Fundamentale in einem extrem einfachen Aufbau verwendet. Eine Kompression auf 1.4 Zyklen des MIR-Feldes und eine CEP-Stabilität kleiner als 94 mrad über eine Stunde werden gezeigt.

Short summary

Due to a limited number of known laser media technically relevant femtosecond laser systems are restricted to a few laser frequencies only. Tunability based on these sources is enabled by the process of optical parametric amplification (OPA). A small portion of the laser output is used to generate a seed pulse. To enable tunability over a large spectral range a bulk continuum is used. With a strong pump pulse a selected spectral part can be amplified in a suitable nonlinear medium. In order to obtain highly stable and ultrashort pulses on the 10 fs scale a deep understanding of each individual step in the process is necessary. In this work Ti:sapphire and Yb-based laser systems are used to pump OPAs. In the used topology it is possible to utilize repetition rates from 1 kHz to 1 MHz and input energies from 10 to 300 μJ without major changes of the design. We obtain ultrashort pulses from the UV to the MIR.

New aspects on bulk continuum generation are presented. For generation with 1030 nm light various crystals are compared regarding the visible and near infrared continuum side. The hitherto unconsidered GSO is found to be superior. Self-compression due to continuum generation is shown without the need for external compression. It bases on a 1 mm sapphire or YAG plate and an astigmatism-free, achromatic telescope – a Schiefspiegler.

The self-compressed, unchirped continuum is used to seed a NOPA (noncollinear OPA) for ultra-broadband pulse generation. With this system quantum efficiencies of up to 45% in the amplification process and 18 μJ output are demonstrated and compression down to 6.7 fs.

The transmitted seed light after optical parametric amplification and the amplified output can propagate in significantly different directions. This is explained as a consequence of Kerr lensing at the needed pump intensities. A pump induced Kerr lens is acting on the signal/seed pulse. This induces a deflection in the amplifier medium at imperfect input coupling. Locating the amplifier crystal behind the focal plane of the pump minimizes the self-lensing effect due to nonlinear balancing of the beam divergence. This also allows reducing the pump intensity simply by moving the crystal further away from the focal plane.

For MHz repetition rates serious thermal issues in a NOPA arise due to the high average power that is needed for the nonlinear processes. For third harmonic generation (THG) of an Yb-fiber laser, second harmonic generation (SHG) with subsequent sum-frequency mixing is demonstrated. Two-photon absorption of the UV leads to measureable heat in the THG crystal. The phase-matching conditions change and the UV power decreases over time. With a time delay compensation plate (αBBO) between the SHG and THG crystal this effect can be minimized. By temporally pre-compensating the fundamental with respect to the second harmonic, the generation locus of the main UV power is shifted to the end of the THG crystal and the volume for absorption is minimized. Stable UV pulses result. This enables a long term stable UV pumped NOPA output even at 1 MHz repetition rate.

An OPA for the generation of an octave spanning middle infrared pulse centered around 8 μm is presented. A 515 nm pumped NOPA with a subsequent collinear, 1030 nm pumped amplifier based on LGS is utilized. The chirp management is entirely by bulk material and selected optical filters. The MIR field is temporally characterized by electro-optical sampling. As gate pulse the self-compressed fundamental is used in an extremely simple setup. Electro-optical sampling reveals a compression down to 1.4 cycles of the MIR field and an intrinsically phase-locked CEP stability of better than 94 mrad over one hour.

Publications

The following publications have been produced in the scope of this thesis:

1. **Direct Generation of 7 fs Whitelight Pulses from Bulk Sapphire**
   E. Wittmann, M. Bradler, E. Riedle
   Ultrafast Phenomena XIX, Springer Proceedings in Physics **162**, 7258 (2015).
2. **Limitation of the SHG and THG Efficiency and Beam Break-up for Femtosecond Pulses by Kerr Lensing**
   E. Wittmann, S. Heimann, E. Riedle
   Conference on Lasers and Electro-Optics Europe, CLEO (2017).
3. **Dramatic Beam Steering by Kerr Lensing in Optical Parametric Amplifiers**
   E. Wittmann, H. Hecht, E. Riedle
   Conference on Lasers and Electro-Optics Europe, CLEO (2017).
4. **Phase-locked multi-terahertz electric fields exceeding 13 MV/cm at a 190 kHz repetition rate**
   M. Knorr, J. Raab, M. Tauer, P. Merkl, D. Peller, E. Wittmann, E. Riedle, C. Lange, R. Huber
   Opt. Lett. **42**, 4367 (2017).
5. **Time-Resolved Photoemission Electron Microscopy of a Plasmonic Slit Resonator using 1 MHz, 25 fs, UV-to-NIR-Tunable Pulses**
   B. Huber, M. Hensen, S. Pres, V. Lisinetskii, J. Lüttig, E. Wittmann, E. Krauss, D. Friedrich, B. Hecht, E. Riedle, T. Brixner
   In print for Book of Proceedings for Ultrafast Phenomena XXI (2018).
6. **Octave-spanning middle-infrared generation through optical parametric amplification in $LiGaS_2$**
   B.-H. Chen, E. Wittmann, Y. Morimoto, E. Riedle, P. Baum
   To be submitted.
7. **343 nm pumped noncollinear parametric amplifier with high long term stability at 1 MHz**
   E. Wittmann, B. Huber, S. Pres, V. Lisinetskii, T. Brixner, E.Riedle
   In preparation

8. **Impact of the Kerr Effect on efficient $\chi^{(2)}$ processes in the femtosecond range**
   E. Wittmann, E.Riedle
   In preparation

Table of Contents

1. Introduction 1

2. Basic concepts and theoretical aspects on nonlinear optics 7

3. Astigmatism free imaging with a spherical mirror folded telescope 31

4. Broadband noncollinear optical parametric amplification based on unchrirped white light seed 39

5. Dramatic beam steering by Kerr lensing in optical parametric amplifiers 49

6. Yb-fiber laser based, two-color noncollinear optical parametric amplifier optimized for long term stability at 1 MHz 69

7. Continuum generation at 1030 nm with various crystals 91

8. Few cycle pulse generation in the middle infrared (MIR) based on parametric amplification in LGS 99

9. Achromatic phase-matching based on Yb-fiber laser pumped NOPA system 137

10. Two photon absorption in bulk material: Convenient method to measure temporal pulse widths from the UV to the NIR 143

11. Summary, conclusion and future perspectives 159

12. References 167

Appendix

- Direct Generation of 7 fs Whitelight Pulses from Bulk Sapphire
- Phase-locked multi-terahertz electric fields exceeding 13 MV/cm at a 190 kHz repetition rate
- Calculations and estimations

Danksagung

Curriculum vitae

1. Introduction

The first femtosecond (*fs*) laser pulses have been demonstrated in the 1970s with dye lasers. However these systems suffered from the cumbersome handling of liquid or vaporous laser dyes and their limited achievable pulse energy. For the generation of ultrashort pulses mode-locked solid-state lasers have been developed a few years later. A major breakthrough for the generation of high output energies was the strategy of chirped pulse amplification (*CPA*) [Str85]. The concept was honored in 2018 with the Nobel Prize in physics for Gérard Mourou and Donna Strickland. *CPA* enables both, the generation of high peak intensities and high repetition rates for pulses in the femtosecond to picosecond regime. Temporally stretching the pulse before amplification reduces the intensity in the laser gain medium to circumvent crystal damage and ensure a low B-Integral for optimal performance. After amplification, the pulses are re-compressed to pulse durations between roughly 25 and 1300 fs. In particular Ti:sapphire based lasers or systems with Ytterbium or Erbium-doped fiber or solid-state gain media are nowadays widely in use. *CPA* allows a wide range of applications from laser physics and spectroscopy to medical applications like eye surgery and precise industrial techniques like metal cutting and welding.

For ultrafast transient spectroscopy shortest pulse durations are required for highest temporal resolution to unravel fastest chemical processes on the 20 to 50 fs timescale. Additionally the laser wavelength in the experiment has to match precisely to a certain absorption band for an excitation of the molecule under investigation. Consequently the need arises to tune the laser wavelength accordingly. In the past dye lasers were used for this purpose. However these systems were not precisely tunable to cover all requirements and consequently some trade-offs in the experiment had to be made. Nowadays optical parametric amplification (*OPA*) driven by a femtosecond laser source enables gap free tuning from the ultraviolet (*UV*) to the middle infrared (*MIR*). In *OPA* a strong pump pulse is used to nonlinearly amplify spectral components out of a weak chirped seed pulse in a nonlinear medium. Like in the honored *CPA* method the resulting amplified pulses can be compressed to shortest pulses after the amplification.

Because the spectral bandwidth of the tunable output is increased during the process, much shorter pulse durations, compared to the driving laser pulse, can be achieved - especially in a noncollinear geometry (*NOPA*). In most cases a supercontinuum generated in bulk material is used as a seed pulse [Ree95, Cer00, Rie00, Bra09].

Supercontinua are generated by irradiating optical materials like crystals, gases, glasses, liquids or fibers with laser pulses on the TW/cm^2 intensity level. Various cascaded nonlinear effects inside the medium spectrally broaden the fundamental beam to over an octave. The resulting spectra from bulk material are smooth and gap free. This makes bulk continua ideally suited for seeding an *OPA*. Spatially the resulting continuum pulse appears as a round and homogenous white spot featuring the polarization of the input beam – see Fig. 1.1. In the time domain, the continuum pulse is positively chirped, with a smooth phase.

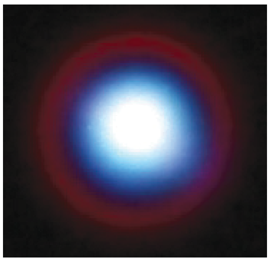

Fig. 1.1: Supercontinuum beam generated with a Ti:sapphire laser.

The pump pulse for amplification can be either the laser fundamental itself or a harmonic of it, depending on the phase-matching conditions for the spectral region to be amplified. By temporally delaying the pump pulse with respect to the chirped seed continuum, spectral tunability of the amplified signal is achieved in the visible and near-infrared. Subsequent processes after the amplification like second harmonic generation (*SHG*), sum frequency generation (*SFG*) or difference frequency generation (*DFG*) extend the tuning range of *OPA*. The outstanding flexibility of this concept makes *OPA* also interesting for research areas besides ultrafast transient spectroscopy. Especially for near-field imaging [Kra16], time-resolved photoemission electron microscopy [Aes11], CARS microscopy [Gre05] or optical electron pulse compression [Kea16].

Particularly for the above-mentioned fields, the demand for high laser repetition rates from hundreds of kHz to the MHz regime is rising. The measurement time of single experiments will be reduced where applicable and frequently low pulse energies in the experiments are desired. However, high repetition rates are accompanied with high average power of the laser system. Sufficient pulse energies are needed to drive the nonlinear frequency conversion processes efficiently. Assume for example continuum generation in bulk material. Here roughly 1 µJ pulse energy is needed: at 1 kHz this energy corresponds to 1 mW of average power, at 1 MHz 1 µJ this amounts to 1 W of power! These high average powers can result in serious problems for stable *OPA* operation. For instance, absorption induced heat in some optical materials cannot dissipate between two laser pulses. The accumulated temperature can lead to crystal damage or significantly distort performance relevant physical effects like phase-matching or parametric amplification. The heating of the crystals due to two-photon absorption of the UV light can even be seen with commercial heat cameras – see Fig. 1.2.

A thermal beam pointing drift of the pump laser can influence the overall performance significantly. Additionally high nonlinear phase-shifts can occur. This will drastically limit the frequency conversion efficiency or lead to a beam break-up and phase distortions. The acquisition of nonlinear phase and beam distortions will strongly show up in the next nonlinear interaction after the amplification. All these issues lead to hardly controllable optical parameters and consequently to hardly interpretable results in experimental measurements.

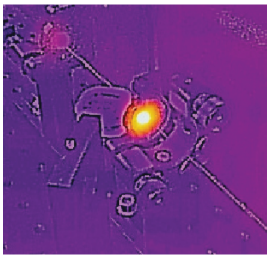

Fig. 1.2: TPA induced heat in a nonlinear crystal seen with a heat camera.

The aim of this thesis is to show that with a sound understanding of nonlinear optics simple and robust setups for nonlinear frequency conversion can be realized. With wisely chosen and flexible focusing geometries the intensities on nonlinear crystals are controllable and parasitic effects due to high average laser powers can be minimized. Based on the axiom "only no optic is a good optic" the presented setups are also drastically reduced in complexity compared to preliminary ones and developed for the daily use by experimentalists.

Optical parametric amplifiers pumped with Ti:sapphire lasers at 1 kHz or pumped by Yb-based laser sources between 50 kHz and 1 MHz are demonstrated. With input pulse energies of 10 µJ to 300 µJ long term stable operation is achieved and ultrashort pulses from the UV to the MIR are demonstrated and characterized.

The thesis is structured as followed. In the initial part, chapter 2, a brief introduction is given for the most relevant nonlinear optical phenomena. Basics and new insights on supercontinuum generation, optical parametric amplification and *type I* phase-matching conditions for *SHG* in BBO crystals are demonstrated. Parasitic nonlinear effects limiting the *SHG* and subsequent *THG* efficiency are shown. Conversion efficiency limits are given. Below theses limits undistorted harmonics in space, time and the frequency domain are obtained. Above these limits parasitic nonlinearities limit and hinder the overall performance. Additionally the bandwidth and angular acceptance of BBO crystals are described in detail to demonstrate how nonlinear crystals for frequency conversion should be chosen correctly. It will also be discussed why a focused beam geometry is excellently suited for frequency conversion or parametric amplification if the crystal is located behind the focal plane. In contrast to a collimated beam, a focused beam allows to simply move the crystal along the beam axis for an adjustment of the position dependent optimal intensity. Additionally, the divergence of the beam will be balanced by the nonlinear Kerr lens inside the crystal and perfect phase-matching results. The Kerr lensing and its consequences for parametric amplification will also be discussed in detail in chapter 5.

In chapter 3 a central issue in ultrafast optics is discussed - the need to collimate and focus ultrashort pulses with a very wide spectrum without diffractive elements. Diffractive lenses introduce an unacceptable chirp and also chromatic aberrations. Theoretically parabolic mirrors would be ideal for imaging. However, their optical quality is far inferior to spherical mirrors and the off-axis parabolas are only useful in the *IR*. A combination of a concave and a convex spherical mirror with suitable ratio of radii of curvature is presented here. It can focus and collimate beams without any detectable astigmatism. This is found at angles where a single spherical mirror already introduces a large aberration. It is demonstrated experimentally as well as theoretically with ray tracing. The presented Schiefspiegler telescope is used to image a nearly un-chirped white light seed in a noncollinear optical amplifier. This newly developed concept on ultrashort pulse generation is demonstrated in chapter 4. Compression down to the Fourier limit of the resulting pulses will be shown in the sub-10 fs range with output energies up to 18 µJ at 1 kHz repetition rate. It is explained how intrinsically un-chirped seed pulses will drastically reduce the effort for the generation of sub-10 fs pulses

Chapter 5 gives new insights on instabilities of parametric amplifiers arising from a thermal beam pointing drift of the pump laser. It will be shown that the transmitted seed light after optical parametric amplification and the amplified output can propagate in significantly different directions. This is explained experimentally and theoretically as a consequence of Kerr lensing inside the amplifier crystal at the needed pump intensities in combination with imperfect input coupling due to the beam pointing of the pump laser. It will also be demonstrated that during continuum generation the beam pointing angle is drastically increased, roughly by a factor of 10.

An Yb-fiber laser system pumped *NOPA* system that is optimized for long term stability is described in full details in chapter 6. The third harmonic wavelength (343 nm) is used as a pump pulse for amplification. For BBO crystals wavelengths below 360 nm will lead to two-photon absorption (*TPA*). At higher repetition rates like 200 kHz or higher this will lead to a temperature gradient in the crystal – see also Fig. 1.2. Consequently the phase-matching conditions change and the conversion efficiency decreases with time. This is already detectable on a few minutes timescale. To minimize the *TPA* in a third harmonic generation crystal a new strategy is introduced: A delay pre-compensation plate between the second harmonic and the fundamental wave is utilized to reduce the actual sum frequency mixing length to a minimum at the end of the subsequent *THG* crystal. Hence the two photon absorption induced heating is minimized and the efficiency of the *THG* is constant over time. This solves thermal issues and the *NOPA* output energy is long-time stable.

In chapter 7 a brief overview of bulk materials for continuum generation at 1030 nm is given. Various crystals are compared regarding spectral bandwidth on the short and the long wavelength side of the fundamental. The needed pulse energies for stable operation are compared. The knowledge is transferred to directly seed a single stage, 515 nm pumped *NOPA* system in the NIR region. In chapter 8 this *NOPA* system is used to seed a subsequent *LGS* based, collinear amplifier pumped at 1030 nm. With a seed wavelength of 1180 nm, the resulting idler pulse is centered around 8 µm. A gain factor of 2 is shown in MIR amplification with an octave spanning spectrum. The pulses are compressed close to single cycle simply by transmission through selected amounts of Germanium. The MIR pulses are characterized via electro-optical sampling (*EOS*) in Gallium Selenide. As ultra-short gate pulse the self-compressed laser fundamental is used in *EOS*. Self-compression due to continuum generation from roughly 300 fs to sub-10 fs in a thin crystal plate is shown at 1030 nm in an extremely simple setup. The electro-optical sampling reveals a compression down to 1.4 cycles of the MIR field and an intrinsically phase-locked *CEP* stability of better than 94 mrad over one hour.

For the first time the concept of achromatic second harmonic generation is shown for a *NOPA* pumped by an Yb-fiber laser system to obtain ultra-broad *UV* and deep blue spectra. This can be found in chapter 9. Spectra with sub-5 fs Fourier limits are demonstrated centered around 350 nm at a repetition rate of 200 kHz. This is a much broader spectral width compared to other attempts known from the literature leading to the shortest possible *UV* pulse durations in this wavelength region.

For the temporal characterization of ultrashort pulses a new and compact tool based on *TPA* is presented in chapter 10. Since in the *UV* region no phase-matching in nonlinear crystals can be achieved, common simple autocorrelation techniques like *SHG* intensity autocorrelation cannot be used. Therefore the newly developed *TPA* autocorrelator is presented for this wavelength region. Moreover it is demonstrated that *TPA* autocorrelation measurements can not only be performed in the *UV* but also in the *VIS* and *NIR* range with the identical setup. No optics change is needed over the whole spectral range from 190 to 1100 nm. Additionally, the potential to measure sub-10 fs pulses based on *TPA* is highlighted – see Fig. 1.3.

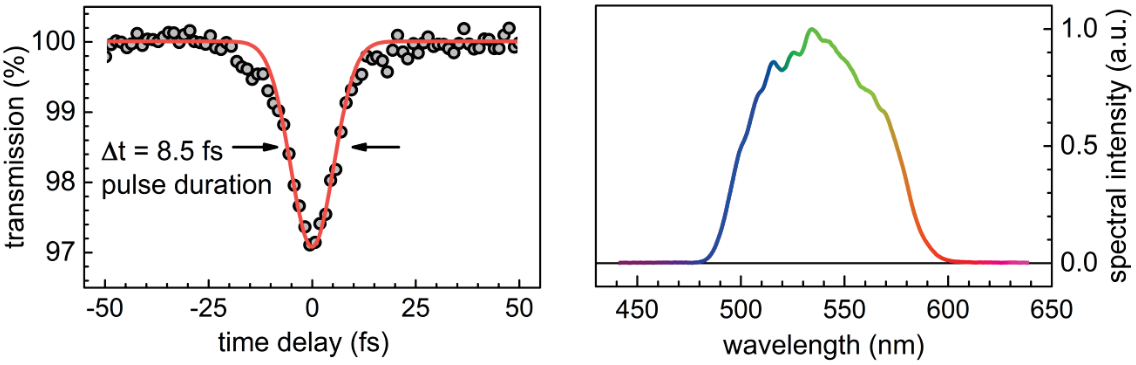

Fig. 1.3: TPA based sub-10 fs autocorrelation of a broadband NOPA pulse in a 200 µm substrate.

This is of major relevance since in *TPA* no phase-matching constraints are limiting the measurement. Contrary to the situation of a *SHG* intensity autocorrelation where extremely thin crystals have to be employed for characterizing sub-10 fs pulses due to the limited acceptance bandwidth for frequency doubling. These thin crystals are hardly available. Other methods like *SPIDER* or *FROG* are rather complex compared to the presented method. For temporal pulse characterization based on *TPA* a sample thickness of even 200 µm is shown to support the measurement of sub-10 fs pulses. Furthermore, it is shown that this concept works also for repetition rates up to (at least) 1 MHz.

2. Basic concepts and theoretical aspects on nonlinear optics

2.1 Supercontinuum generation

Supercontinuum generation (SCG) is a generally applicable method to broaden the spectrum of femtosecond laser pulses at various input wavelengths. It was first reported in 1970 by Alfano and Shapiro [Alf70a, Alf70b]. Nowadays, there is a wide field of applications for continuum pulses: continuum pulses as a seed in OPAs, NOPAs and OPCPAs [Cer03, Rie00, Sta14], continuum probe pulses in transient spectroscopy [Ern01, Meg09, Rie13], LIDAR [Mej03], coherence tomography [Har01] and weather control [Wol18]. In principle continuum generation is possible in every material transparent to the driving laser frequency. Usually continua are generated in optical fibers [Ran00, Dud06], liquids [Wit96, Bro99], crystals [Kan03, Dub17] and gases [Cor86, Ber07]. A quite new and efficient approach for continuum generation is the use of multiple plates [Lu14]. The generation in optical fibers allows generating continua spanning over a multi octave range. However, the generation is quite unhandy and the resulting spectra are most times highly structured. Continua from liquids suffer from shot to shot instabilities, for rather obvious reasons of the fluid physical state. Continuum generation in gases requires complex laboratory hardware. An advantage from this method is however the compressibility of the resulting pulses. Compression down to one optical cycle has been demonstrated [Cou06].

In this work the main focus is on bulk continuum generation. These continua are smooth, gap-free, reveal a very high shot-to-shot stability and preserve the polarization of the fundamental laser [Bra09].

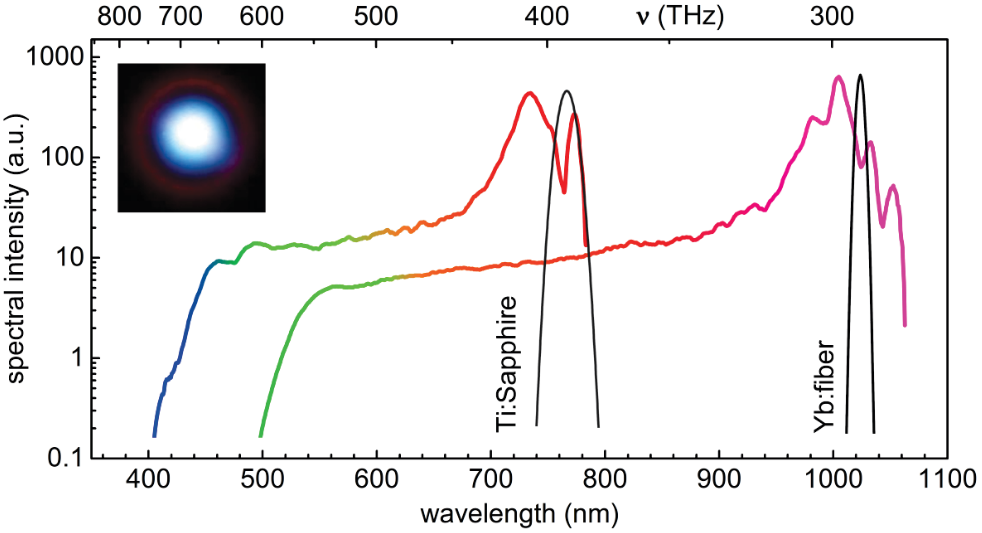

Fig. 2.1: Supercontinuum generation in 4 mm YAG crystal with a Ti:Sapphire laser and an Yb:fiber laser. The inset photograph shows a typical beam profile.

For seeding parametric amplifiers two crystals are commonly used: Sapphire [Ree94] and Yttrium Aluminum Granat (YAG) [Bra09]. YAG possesses a higher damage threshold and roughly a factor of 2 less energy for continuum generation is needed compared to sapphire. The Fourier limit of, e.g., an 800 nm or 1030 nm pumped continuum from sapphire or YAG amounts to less than 4 fs – compare Fig. 2.1. In this chapter, some of the theoretical aspects of continuum generation are described, to allow further understanding of this process.

Continuum generation is a highly nonlinear process; it is an interplay of various cascaded nonlinear effects. The most important one is the **Kerr effect** - it triggers all of the other processes. The refractive index of a medium gets modified when high intensities of radiation are present. It reads:

$$n = n_0 + n_2 \cdot I(z,t), \tag{2.1}$$

where n_0 is the linear refractive index and n_2 is the nonlinear refractive index of the medium. $I(z,t)$ is the spatial and temporal intensity distribution of the light field. One consequence of the effect is **self-focusing** [Kel65]. Self-focusing is necessary to increase the ~1 TW/cm^2 intensity level on the front surface of the crystal to a level on the order of 10 TW/cm^2 for continuum generation inside the medium. The intensity on the front surface is reached by focusing the fundamental beam with a lens. Typically a focal length of $f = 50$ mm is used.

Let $I(z,t)$ be a Gaussian intensity distribution of a laser pulse in time and in space. According to Eq. (2.1) this pulse sees a higher refractive index of the medium on the propagation axis, compared to the edges. This causes the wavefronts $R(z)$ to bend, because the pulse travels a longer optical path at the position of its intensity maximum (Fig 2.2).

A generalized equation and quantity for the nonlinearity of the interaction of the pulse with the medium is given by the **B-Integral**. It measures the nonlinear phase-shift $\Delta\phi_{NL}$.

$$B = \frac{2\pi}{\lambda} \cdot \int_0^d n_2 \cdot I(z,t)\, dz \tag{2.2}$$

B-Integrals greater than 3 indicate, that self-focusing is likely to occur. For continuum generation B-Integrals > 20 can be estimated, depending on the used parameters.

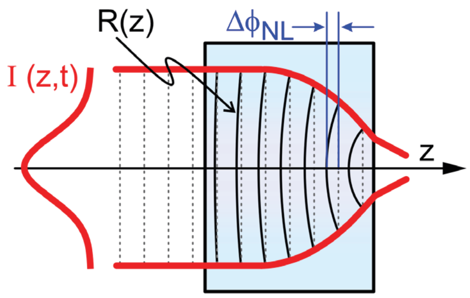

Fig. 2.2: Scheme for Kerr effect induced self-focusing of a Gaussian intensity distribution.

Another major effect leading to supercontinuum generation is **self-phase modulation** [Sto78, And83]. It describes a positive and negative shift in frequency around the center frequency due to nonlinear propagation. From Eq. (2.1) it follows that the refractive index of a medium gets modified in the presence of high intensity radiation. For light pulses this effect will be dependent on time. An optical laser pulse with a Gaussian intensity distribution in time $I(t) = I_0 \cdot exp(-4\,ln(2) \cdot t^2/\tau^2)$, where τ is the FWHM pulse duration, is assumed. The phase of the pulse reads:

$$\phi(t) = k \cdot z - \omega_0 \cdot t = \frac{2\pi}{\lambda} \cdot (n_0 + n_2 \cdot I(t)) \cdot z - \omega_0 \cdot t. \qquad (2.3)$$

This corresponds to an instantaneous frequency change $\Delta\omega(t)$ given by:

$$\Delta\omega(t) = -\frac{\partial \phi(t)}{\partial t} = -\frac{2\pi}{\lambda} \cdot z \cdot n_2 \cdot \frac{\partial I(t)}{\partial t}. \qquad (2.4)$$

For the Gaussian intensity distribution the frequency shift is given in Fig. 2.3 as a black line in the lower panel.

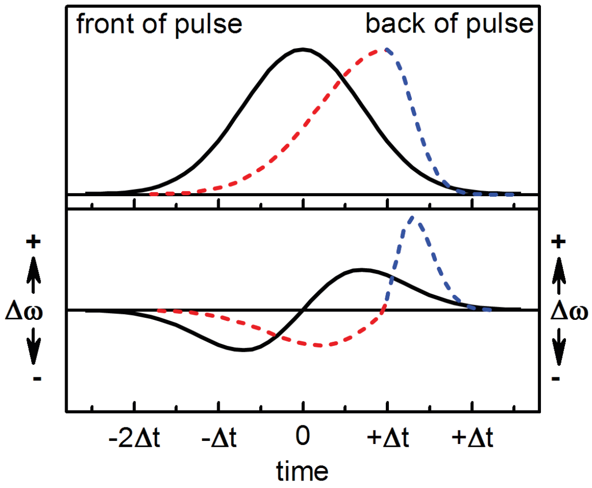

Fig. 2.3: Gaussian intensity distribution of a laser pulse in time (black line, upper panel) and instantaneous frequency $\Delta\omega(t)$ (black line, lower panel) due to self-phase modulation. Colored lines denote self-steepening and the resulting asymmetric instantaneous frequency. Figure adapted from [Bra14b].

From Eq. (2.4) and Fig. 2.3 it can be seen, that for the lower intensity regime, where no continuum generation occurs, self-phase modulation broadens the spectrum symmetrically around its center frequency. This phenomenon is also effectively used to moderately increase the spectral bandwidth and gain shorter pulse durations in Ref. [Kre13]. For the case of continuum generation, self-focusing leads to higher and higher intensities inside the medium. Consequently, the effect of **self-steepening** [And83, Chi05] has to be taken into account. Due to the Kerr-effect the maximum of the temporal intensity distribution has a longer optical path, compared to the edges of the distribution, since the nonlinear refractive index increases with intensity. This leads to a steepening in the temporal structure, as qualitatively shown in the upper panel of Fig. 2.3. Because the peak propagates slower, the back of the pulse steeps, while the front is becoming smoother in time. The instantaneous frequency of the self-steeped pulse – according to Eq. (2.4) – is shown in red and blue in the lower panel of Fig. 2.3. It demonstrates that self-steepening leads to an asymmetric broadening of the pulse. The steepened back of the driving pulse generates the higher frequencies with a higher overall frequency shift to the blue. The smoothed front of the pulse generates the lower frequencies. The overall frequency shift to the red region is lower compared to the blue, due to the asymmetric self-steepened intensity distribution.

Fig. 2.4 shows the near infrared part of a continuum generated in 10 mm YAG with 1030 nm[1] pulses. The blue shift shown in Fig. 2.1 measures roughly 300 THz, whereas the red shift on the near infrared side amounts to about 130 THz maximally, for the case of YAG with 10 mm medium length. To explain this discrepancy the laser plasma interaction in the material has also to be taken into account.

---

[1] A detailed description and an analysis of on the generation of the near infrared continua will be given in chapter 7. There are also various materials presented and compared.

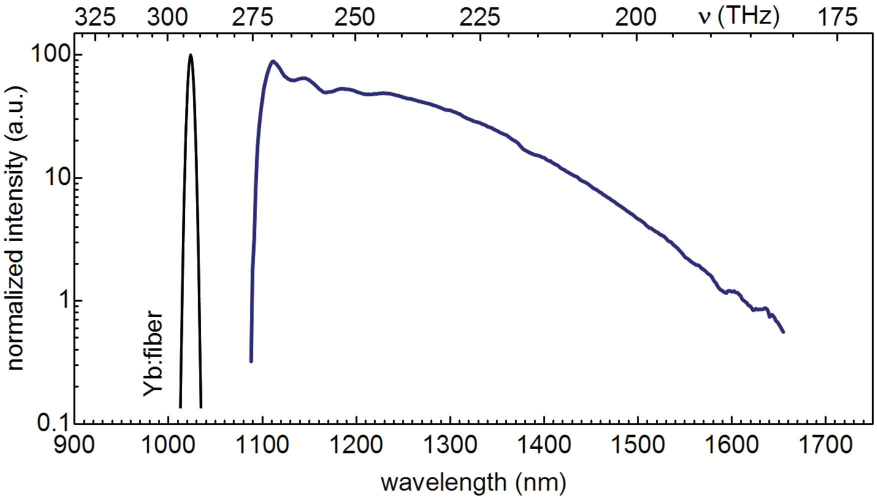

Fig. 2.4: Near infrared parts of continua from a YAG crystal generated with 1030 nm.

Because of the high intensities due to self-focusing, bound electrons are excited from the valence to the conduction band of the medium and form an **electron plasma**. This plasma channel is usually called a filament. The presence of free electrons inside the medium obviously has a contribution to the refractive index.

$$n = n_0 + n_2 \cdot I(z,t) + n_{plasma} \cdot I(z,t). \tag{2.5}$$

According to the Drude model [Raz66] n_{plasma} is given by:

$$n_{plasma} = -\frac{4\pi \cdot e^2 \cdot N_e(z,t)}{2 \cdot m_e \cdot \omega_0^2}. \tag{2.6}$$

$N_e(z,t)$ is the number of free electrons created at position z. e and m_e correspond to the charge and the mass of an electron in *cgs* units, respectively. ω_0 is the central laser frequency. The additional term in Eq. (2.6) due to interaction with the free electrons has two consequences. On the one hand, it influences self-focusing. With more electrons excited to the conduction band, $N_e(z,t)$ rises, up to a level where the absolute value of $n_{plasma} \cdot I(z,t)$ exceeds $n_2 \cdot I(z,t)$. At this level, self-focusing stops and the beam diverges. This prevents the beam from collapsing to a singularity [Gae00]. On the other hand, the contribution of the plasma term in the refractive index will modify the self-phase modulation.

Liu et al. approximated the number of free electrons $N_e(z,t)$, created at the nonlinear focus, by the relation [Liu02]:

$$N_e(z,t) \approx N_0 \cdot K(z) \cdot \int_{-\infty}^{t} I(z,t)^m \, dt, \tag{2.7}$$

where N_0 is the number of initially present neutral particles in the focal volume, *K(z)* is a proportionality constant and *m* is the minimum number of photons to be absorbed to overcome the energy gap between the valence and the conduction band of the material. Inserting Eq. (2.8) into Eq. (2.6) gives for the refractive index:

$$n = n_0 + n_2 \cdot I(z,t) - \frac{2\pi \cdot e^2 \cdot N_0 \cdot K(z)}{m_e \cdot \omega_0^2} \cdot \int_{-\infty}^{t} I^m(z,t)\,dt\,. \tag{2.8}$$

Considering the effect of self-phase modulation according to Eqs. (2.3) and (2.4) the instantaneous frequency including plasma effects reads:

$$\Delta\omega(t) = -\frac{\partial\phi(t)}{\partial t} \propto -\frac{\partial n}{\partial t} = \underbrace{n_2 \cdot \frac{\partial I(z,t)}{\partial t}}_{\text{SPM:blue and red shift}} + \underbrace{\frac{2\pi \cdot e^2 \cdot N_0}{m_e \cdot \omega_0^2} \cdot I(z,t)^m}_{\text{plasma: blue shift only}} \tag{2.9}$$

From Eq. (2.9) it can be seen that plasma generation only leads to a blue shift in continuum generation [Gae00], since it is dependent on the amplitude of the spatio-temporal intensity distribution of the laser pulse, only. Combined with the introduced asymmetric broadening due to self-steepening this explains semi-quantitatively the obtained continua.

The effects described here are only the most relevant for a principle understanding of continuum generation in bulk material. In fact, there are many others like pulse splitting [Ran96], intensity clamping [Bec01] avalanche ionization [Yab72] and the effect of group velocity dispersion [Dha14] that have to be taken into account for a correct description of the phenomenon of continuum generation.

Wavelength dependent propagation and self-compression of bulk continua

The visible part of bulk continua from single filaments show a flat temporal phase. Usually the generated continua are highly chirped [Cer99, Mac00, Zio04]. A full compression of the continuum pulse was not shown yet. In precise investigations of the continuum generation and propagation [Wit13, Bra14b, appendix A1] it is found that the inability to compress bulk continua stems from the highly wavelength dependent propagation and effective generation locus. Frequencies close to the fundamental wavelength follow the filament channel longer than shorter wavelengths due to the group velocity dispersion. Hence bluer frequencies start to diverge earlier inside the crystal, leading to a wavelength selective propagation. As a consequence the imaging of a continuum is wavelength dependent. Even with reflective imaging one can find the blue part of the continuum focuses earlier then the red. This is shown in Fig. 2.5a). Here the continuum is generated in a 3 mm Sapphire plate. The pump source is a small fraction of the output of a Ti:Sapphire amplifier (CPA 2001, Clark MXR, 778 nm, 170 fs) focused with a $f = 50$ mm plano-convex lens. For imaging of the continuum a Schiefspiegler telescope is utilized (see chapter 3 for detailed description) to prevent chromatic error and astigmatism. For simplicity the telescope is denoted as black arrow. The energy for continuum generation is varied from 800 nJ to 2 µJ. This corresponds to the energy range for single filament continuum generation. The propagation of selected frequencies is measured with interference filters ($\Delta\lambda = 10$ nm) and a commercial beam profiler (Photon Inc.). The focus position of each selected frequency is shown in dependence of the pump energy for continuum generation. With increasing pump energy the filament channel length increases [Bra14b].

The extended filament channel leads to an even greater wavelength dependency of the propagation, since the described dispersion effects are more relevant for longer propagation distances. However, even for minimal utilized pump energy, the blue part of the continuum focuses earlier then the red for the case of a 3 mm Sapphire plate.

The crystal should be terminated at a point where the dispersion effects are not yet relevant. Ideally, the continuum should be generated at the very end of the crystal. A short crystal on the order of 1 mm thickness is found to be suitable. A focal length of $f = 50$ mm is used to focus onto the 1 mm Sapphire plate. Here, more energy is needed for continuum generation, because stronger self-focusing is needed for the shorter crystal. It can be seen that with the 1 mm sapphire crystal no local separation occurs and all colors diverge simultaneously. This leads to identical focal positions of each wavelength – see Fig. 2.5b).

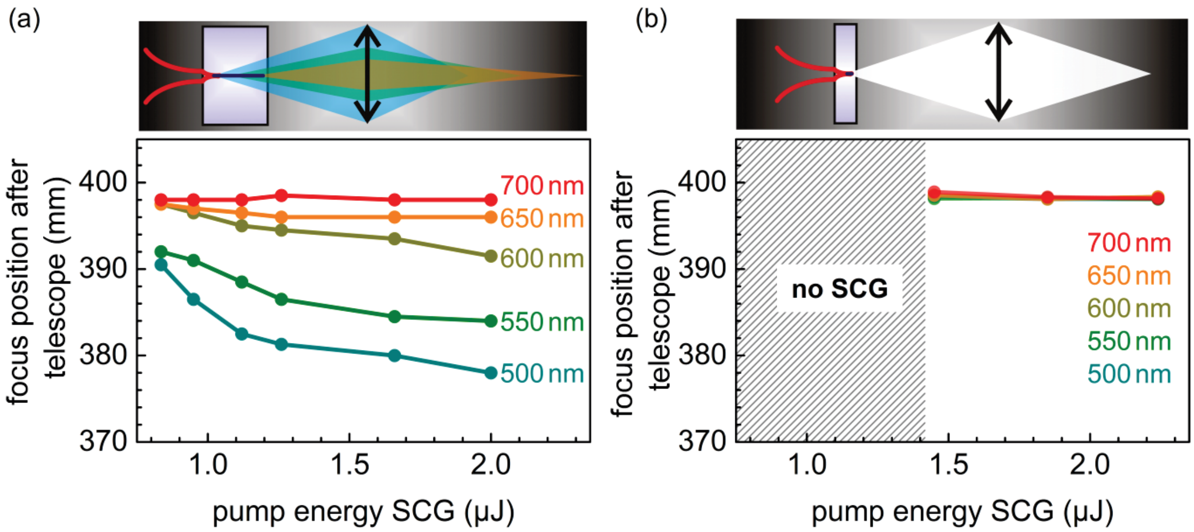

Fig. 2.5: continuum generation with *f* = 50 mm in a 3 mm Sapphire plate (a) and with *f* = 50 mm in a 1 mm Sapphire plate (b). Corresponding focal planes of selected wavelengths for different input energies are given. Black arrows denote the imaging telescope. Adapted from Ref. [Wit13].

By minimizing the pulse energy for continuum generation in the 1 mm Sapphire plate, the generation locus can be optimized close the output surface of the crystal. This leads to a chirp free continuum as the newly generated colors pass through nearly no extra material, and all colors have the same spatial properties.

For insight into the spectro-temporal distribution of the sapphire continuum of the 1 mm plate, the chirp is determined with our transient spectrometer [Meg09]. With a 200 nJ, 25 fs pump pulse centered around 470 nm and the sapphire continuum as probe, the cross correlation via two-photon absorption is measured in a GG400 substrate (130 µm, Schott AG). Two-photon absorption of pump and probe only occurs for temporal overlap and allows determining the group delay for every wavelength of the continuum probe. Since there are only reflective metallic optics in the probe beam path, the signal represents the intrinsic spectral chirp of the continuum after propagation through just a short length of air. Fig. 2.6 shows that all spectral components from 550 to 700 nm coincide in time. The chirp for the short wavelength range mainly originates from the propagation in air.

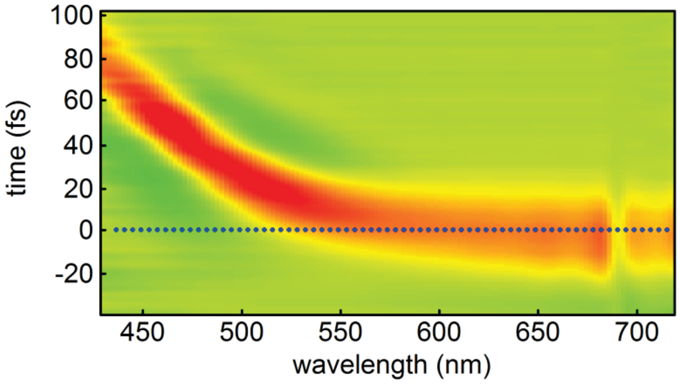

Fig. 2.6: Transient absorption measurement in 130 µm GG400 to determine the chirp of the continuum generated in a 1 mm sapphire plate. Adapted from Refs. [Wit13, Bra14b, appendix A1].

It was shown that it is possible to obtain intrinsically nearly un-chirped white light pulses directly from bulk filamentation. In the literature only a few examples for white light compression can be found. By studying the propagation properties of the continuum a straightforward way was found for the generation of intrinsically ultra-short continuum pulses. With the imaging by a Schiefspiegler telescope, also any chromatic aberrations as well as astigmatism can be avoided. Such pulses are highly interesting for broadband amplification – see chapter 4, ultrafast 2D spectroscopy [Ful15] and for the generation of ultrashort gate pulses for electro-optical sampling – see chapter 8.

The described wavelength selective propagation of continua makes it necessary to use a moveable lens for relay imaging in an OPA. Moving the lens along the beam axis allows optimizing the spot size of the seed spot to the spot size of the pump beam.

In chapter 8 it is shown that this presented concept of self-compression due to continuum generation in bulk material works also for an Yb-doped laser system with pulses centered around 1030 nm at 50 kHz. Instead of a 1 mm Sapphire plate, a 1 mm YAG plate is used because of the higher damage threshold and the lower needed energy for continuum generation. An autocorrelation trace of the resulting self-compressed pulse as short as 9 fs is shown.

In the scope of this work continua are mainly used to seed optical parametric amplifiers. Consequently, the subsequent section will give a brief introduction in the process of optical parametric amplification.

2.2 Optical parametric amplification

In the first part of this chapter, details on supercontinuum generation have been described. With a suitable pump pulse selected portions of a continuum seed can be amplified in a nonlinear medium. This principle enables both, tunability over a large spectral range and the generation of ultrashort pulses. The underlying process is called optical parametric amplification (OPA), which shall be briefly reviewed in this section. For a deeper understanding the interested reader is referred to the tutorial by Manzoni and Cerullo [Man16] or, for the case of noncollinear optical parametric amplifiers, to the review articles [Rie00, Cer03].

The process of optical parametric amplification describes the effect of amplifying weak seed photons (frequency ω_s) – e.g. of a continuum – with a strong pump pulse (frequency ω_p) in a nonlinear medium. As a consequence of energy conservation, a third pulse is generated – this pulse is called the idler pulse, its frequency is ω_i given by

$$\hbar \cdot \omega_p = \hbar \cdot \omega_s + \hbar \cdot \omega_i \ . \tag{2.11}$$

Since three waves are interacting in the medium, the OPA process is described with three coupled differential equations [Yar95]:

$$\begin{aligned} \frac{dA_s}{dz} &= -\frac{1}{2}\alpha_s \cdot A_s - \frac{j}{2}\kappa \cdot \tilde{A}_i \cdot A_p \cdot e^{-j\cdot\Delta k\cdot z} \\ \frac{d\tilde{A}_i}{dz} &= -\frac{1}{2}\alpha_i \cdot \tilde{A}_i + \frac{j}{2}\kappa \cdot A_s \cdot \tilde{A}_p \cdot e^{\,j\cdot\Delta k\cdot z} \\ \frac{dA_p}{dz} &= -\frac{1}{2}\alpha_p \cdot A_p - \frac{j}{2}\kappa \cdot A_s \cdot A_i \cdot e^{\,j\cdot\Delta k\cdot z} \end{aligned} \tag{2.12}$$

A_ℓ is a field variable introduced for convenience, according to

$$A_\ell = \sqrt{\frac{n_\ell}{\omega_\ell}} \cdot E_\ell \qquad \ell = s,\ i,\ p\,, \tag{2.13}$$

where *s, i, p* denotes signal, idler and pump, respectively and E_ℓ is the corresponding electric field strength, n_ℓ the refractive index and ω_ℓ the corresponding frequency. For the complex number here j is used, to not confuse with the abbreviation i for idler. The wave vector mismatch is given by

$$\Delta k = k_p - (k_s + k_i). \tag{2.14}$$

Ref. [Yar95] uses A_ℓ instead of the electric field strength E to use a single coupling parameter κ.

$$\kappa = d_{eff} \cdot \varepsilon_0 \cdot \sqrt{\left(\frac{\mu}{\varepsilon_0}\right) \cdot \frac{\omega_s \cdot \omega_i \cdot \omega_p}{n_s \cdot n_i \cdot n_p}} . \tag{2.15}$$

Note: Ref. [Yar95] uses in Eq. (2.15) not the common d_{eff} parameter, but a different nonlinear coefficient (in MKS units). Here d_{eff} is used – this corresponds to the value which is given by [SNLO] – multiplied by the vacuum permittivity ε_0 to get consistent with Yariv.

The first summand from all three differential equations of (2.12) vanishes, since the parameter α is given by:

$$\alpha = \sigma \cdot \sqrt{\frac{\mu}{\varepsilon}} \approx 0 , \tag{2.16}$$

where σ is the conductivity of the nonlinear medium, which is close to zero for an amplifier crystal like BBO.

For small scale amplification the pump depletion can be neglected. In this case the coupled differential equations of Eq. (2.12) can be simplified and a gain factor G can be extracted as an approximated solution [Yar95, Ree95, Bra11] :

$$G = \frac{1}{4} \cdot \exp\left(2 \cdot L \cdot \sqrt{\frac{8 \cdot \pi^2 \cdot d_{eff}^2 \cdot I_p}{n_s \cdot n_i \cdot n_p \cdot \lambda_s \cdot \lambda_i \cdot \varepsilon_0 \cdot c_0}} \right). \tag{2.17}$$

Here, L is the medium length and c_0 the vacuum speed of light. For *0.7 mm* effective crystal length, a seed wavelength of $\lambda_s = 550\ nm$, $d_{eff} = 2.06\ pm/V$ - for *400 nm pump* pulses BBO as amplifier medium, and a pump intensity of $150\ GW/cm^2$, the value of G relates to $G \approx 2 \cdot 10^4$. For a seed pulse energy of *0.5 nJ* this corresponds to *10 μJ* after amplification.

For higher pump intensities or longer effective crystal lengths, pump depletion has to be taken into account to calculate realistic output values of the parametric process. A software code for integrating the coupled differential equations of Eq. (2.12) in infinitesimal small steps is given in appendix A5. It will be used to calculate the amplification for a 2 mm BBO crystal in chapter 5.

There are two principles for optical parametric amplification: The collinear and the noncollinear geometry. The term refers to the relative propagation direction of the pump and the seed beam. The advantage of the noncollinear geometry is the amplification of broad bandwidths [Gal95, Cer99, Wil97, Rie00, Cer03, Hom08, Bra14a]. With a suitable angle between signal and idler, effective group velocity matching can be reached in the propagation direction of the signal wave. The noncollinear geometry of pump and seed (signal) beam – with angle ψ between the beams – results in an angle Ω between the signal and the idler beam, that is approximately given by the relation [Rie00]

$$\Omega \approx \psi \cdot \left(1 + \frac{\lambda_{\text{idler}}}{\lambda_{\text{signal}}}\right). \tag{2.18}$$

The idler group velocity is larger than the group velocity of the signal in the BBO crystal. Consequently a suitable angle Ω can be found where the projection of the idler group velocity onto the propagation direction will match the signal group velocity, i.e.

$$v_{\text{group,idler}} \cdot \cos(\Omega) = v_{\text{group,signal}} \cdot \tag{2.19}$$

This concept avoids pulse lengthening and consequently supports the generation of tunable pulses with sub-10 fs pulse durations [Cer99, Kob00, Bal02a, Bau06]. A software code provided by Arlee Smith [SNLO] allows calculating the phase-matching conditions easily. A new concept for the generation of sub-10 fs pulses based on an un-chirped seed continuum is presented in chapter 4 of this thesis.

In the collinear phase-matched geometry, the three group velocities are not generally matched over the length of the amplifier crystal. The differing speeds will lead to an unavoidable pulse lengthening. However, in this configuration, the resulting idler pulse is not spectrally dispersed, as it is the case for the noncollinear arrangement due to energy conservation. Therefore, in the collinear geometry the idler pulse is usable for further experiments and extends the tuning range provided by the seed spectrum. In chapter 8 a collinear phase-matched configuration is used for generating middle-infrared spectra close to single cycle duration.

2.3 Phase-matching properties of type I Second Harmonic Generation in *beta barium borate* (BBO)

Visible NOPA pulses can be converted to shortest UV pulses by Second Harmonic Generation (SHG) in nonlinear crystals. SHG is also important to characterize pulse lengths, e.g., in a SHG intensity autocorrelator [Koz04]. One crystal that is widespread nowadays for SHG is beta-barium borate (BBO) [Nik91, Zha00]. In this section a brief introduction to the most important phase-matching properties for SHG are reviewed. For a deeper understanding of this phenomenon the reader may refer to the literature [Yar88, Boy03, Smi15]. The most decisive parameters for any frequency conversion in a single crystal are the crystal thickness L and the cutting angle θ_{PM}. The crystal thickness determines the possible conversion bandwidth but also the conversion efficiency – reasonable tradeoffs have to be made. For shortest pulse durations very thin crystals on the order of 25 µm are needed. Although, some suppliers can be found offering these thin crystals even without substrate support, it is important to measure the thickness before use. During the time span of this work, many crystals were bought as 50 µm crystals, but in fact were thicker by 30 - 40%.

With a spectrophotometer the NIR transmission of the crystals can be measured. Etaloning will lead to equidistant fringes on the measured spectrum in the frequency domain. The frequency spacing is equal to the free spectral range and hence the thickness of the crystal can be calculated easily from the measurement. By introducing polarizers into the unpolarized light source of the spectrophotometer, the contrast of the fringes can be enhanced. Either the ordinary or the extraordinary light propagation is selected in the crystal and beating contributions to the measured signal are avoided. The thickness of the crystal defines both the acceptance angle and the acceptance bandwidth.

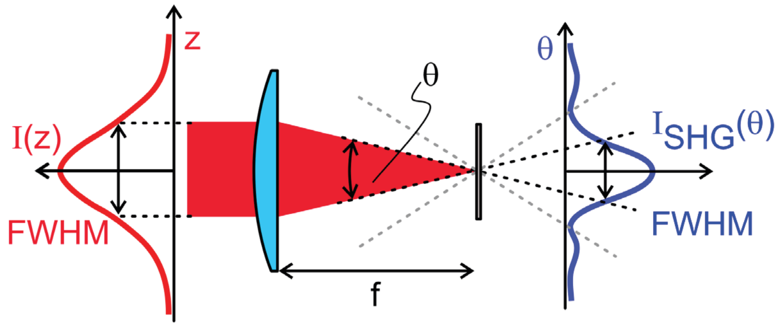

Fig. 2.7: Angle acceptance in second harmonic generation. For details see text.

Fig. 2.7 illustrates the angular acceptance for second harmonic generation. To enhance the efficiency of frequency doubling the input pulse usually is focused with a focusing element with focal length *f*. Depending on the initial size of the beam on the focusing element and its focal length, this will lead to a specific propagation angle θ of the input beam. The acceptance angle $\Delta\theta$ is defined as the value for which the intensity distribution of the second harmonic drops to half of its maximum – see Fig. 2.7.

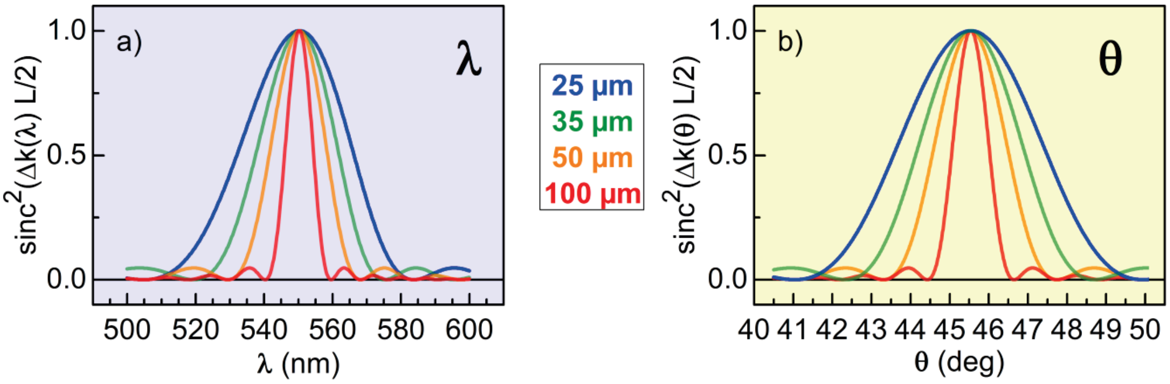

Fig. 2.8: a) Normalized spectral efficiency function (Eq. 2.20) for SHG of 550 nm for various BBO thicknesses, at a fixed angle of $\theta = 45.5°$

b) Normalized angular efficiency function (Eq. 2.20) for SHG of 550 nm for various BBO thicknesses, at a fixed wavelength of $\lambda = 550$ nm.

Fig. 2.8 shows typical phase-matching (normalized efficiency) functions for angle acceptance and acceptance bandwidth for different crystal thicknesses for the case of second harmonic generation of 550 nm. It is calculated by solving Eq. (2.20) for varying input wavelength (a) or input angle (b).

$$I_{SHG}(\lambda,\theta) \propto \mathrm{sinc}\left(\Delta k(\lambda,\theta)\cdot\frac{L}{2}\right)^2 \cdot I(\lambda)^2_{fundamental}, \tag{2.20}$$

where $\Delta k(\lambda,\theta)$ is given by

$$\Delta k(\lambda,\theta) = \frac{4\pi}{\lambda}\cdot\left(n_{BBO}\left(\frac{\lambda}{2},\theta\right) - n_{oBBO}(\lambda)\right). \tag{2.21}$$

Here $n_{BBO}(\lambda/2,\theta)$ refers to the effective refractive index of the second harmonic:

$$n_{BBO}\left(\frac{\lambda}{2},\theta\right) = \sqrt{\left(\frac{\cos(\theta)}{n_{oBBO}(\lambda)}\right)^2 + \left(\frac{\sin(\theta)}{n_{eBBO}(\lambda)}\right)^2}, \tag{2.22}$$

where n_o denotes the ordinary and n_e the extraordinary refractive index of the crystal, respectively. The dispersion coefficients used for the calculation can be found in [Zha00].

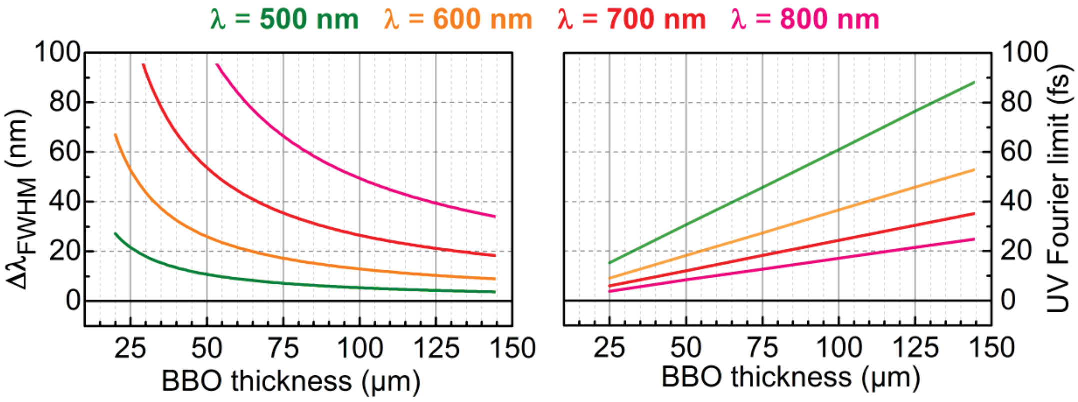

Fig. 2.9: FWHM of the acceptance bandwidth (left panel) and possible UV Fourier limit (right panel) in SHG for different crystal thicknesses and center wavelengths.

Fig. 2.9 shows how the values of the acceptance bandwidth (left panel) and corresponding UV-Fourier limit (right panel) change with center wavelengths and BBO crystal thickness. The resulting Fourier limits of the UV pulses amounts to roughly 90% of the pulse duration that is obtained by assuming a Gaussian distribution in the visible with a spectral width corresponding to the $\Delta\lambda_{FWHM}$ values of Fig. 2.9. The Fourier limits are calculated as follows. It is assumed that the pulse is significantly chirped for SHG, so the frequency is just doubled for all spectral components individually without cross-term contributions [Bau04b]. For example, a Gaussian pulse, centred at 600 nm is considerd. According to Fig. 2.9 the possible FWHM of the spectral distribution is 26 nm for a 50 μm BBO crystal thickness. In Fig. 2.10a) the visible spectrum of the pulse (black line) and the phase-matching function for the 50 μm crystal (orange line) is shown. It can be seen that the $sinc^2$ function falls off steeper at the blue edge of the spectrum. This leads to a slight narrowing of the obtained UV spectrum (Fig. 2.10b). The UV spectrum is obtained by multiplying the $sinc^2$ phase-matching function with the squared intensity distribution of the visible spectrum and shifting the wavelength scale accordingly by a factor of 1/2. The correpsonding pulse in the time domain is obtained by Fourier transformation of the corresponding field (not shown), assuming a flat phase, Fig. 2.10c). It follows that for using the $\Delta\lambda_{FWHM}$ values of Fig. 2.9 undistorted pulses in the time domain are obtained. Thinner crystals lead to slightly broader spectra and hence shorter possible pulse durations. However, for thinner crystals the conversion efficiency is lower – this will be discussed in the following. But for thicker crystals, the side-lobes of the $sinc^2$ functions will contribute to the second harmonic spectrum – see red line for 125 μm BBO thickness.

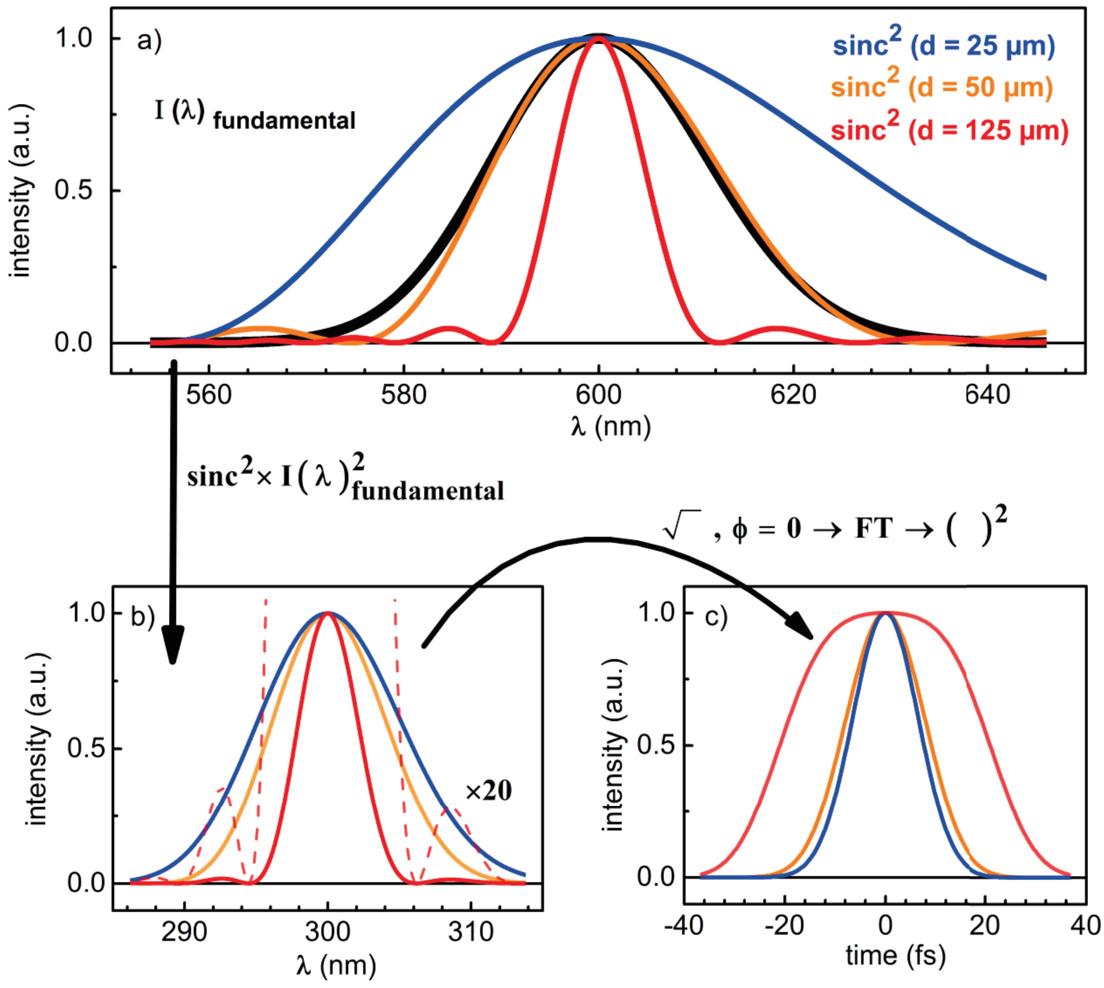

Fig. 2.10: a) Spectral distribution of a visible pulse around 600 nm with $\Delta\lambda_{FWHM} = 26$ nm (black line). *sinc*^{2} phase-matching functions for 25 µm (blue), 50 µm (orange) and 125 µm (red line) BBO thickness. b) calculated second harmonic spectrum for the three different crystal thicknesses. c) representation of the three UV spectra in the time domain.

Even if the contrast of the side lobes to the peak of the second harmonic spectrum is very high – it might not even be seen with a common spectrometer under real experimental conditions – they have a huge impact on the pulse structure in the time domain. The temporal distribution deviates strongly from a Gaussian shape and is more flat-top like, see red line in Fig. 2.10c). A serious problem with this flat-top like pulse shape is that an intensity autocorrelation of these pulses will look Gaussian again and consequently a wrong pulse duration is obtained.

For even thicker crystals, the side lobes of the *sinc*^{2}-function will be seen more pronounced in the second harmonic spectrum. Since these parts would be phase shifted by $\pm\pi$, the resulting UV pulse will not be compressible anymore.

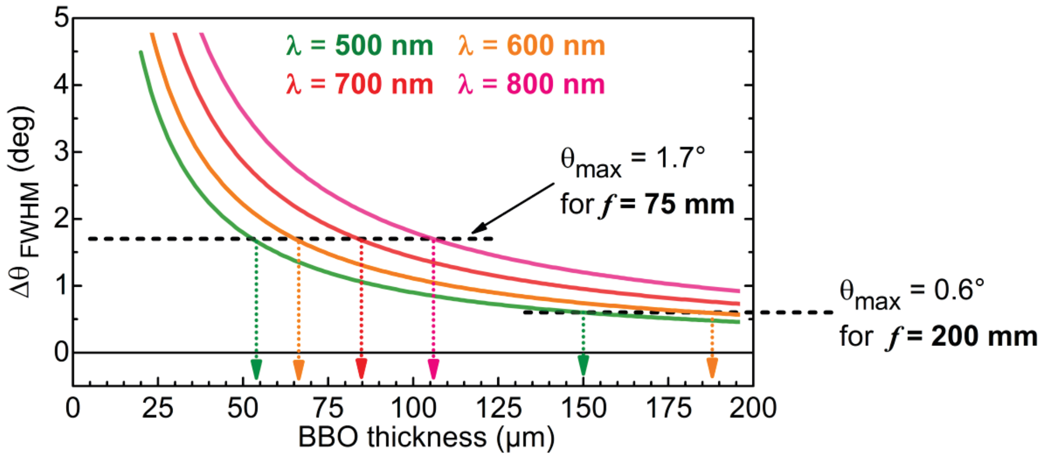

Fig. 2.11: Acceptance angle for second harmonic generation for various BBO thicknesses and fundamental wavelengths.

As mentioned, conversion efficiency of second harmonic generation with thin crystals can be rather low. Especially for NOPA systems operating at high repetition rates with low pulse energy this is a serious issue for frequency doubling. To enhance the conversion efficiency the incoming beam has to be focused towards the doubling crystal. Shorter focal lengths lead to a sharper focusing and consequently higher intensities. However, care has to be taken that the acceptance angle of the doubling crystal is not exceeded by the focusing geometry. Fig. 2.11 gives values for the angular acceptance in dependence of the BBO thickness for different wavelengths.

A typical FWHM beam spot size of the high repetition rate NOPA system presented in chapter 6 is 2.2 mm. Focusing the beam with a concave mirror with $f = 200$ mm leads to a divergence angle $\theta = 0.6°$. For f = 75 mm an angle of $\theta = 1.7°$ is obtained. These focal lengths set an upper and a lower limit for experimental implementation. Longer focal lengths than 200 mm seem to be not necessary and shorter than 75 mm will not be easily implemented due to astigmatism. Even 75 mm might be too short a focal length already and could require the fundamental beam to propagate through the doubling crystal before reflecting the focused beam back to the doubling crystal, in order to keep the angle of incidence as small as possible on the mirror to avoid astigmatism.

In table II.1 the maximum BBO thicknesses regarding angular acceptance are summarized for the two given focal lengths. A beam spot size of FWHM = 2.2 mm is assumed. The listed values correspond to the dotted arrows of Fig. 2.11.

TABLE II.1: Maximum BBO thickness for different wavelengths regarding the angular acceptance in second harmonic generation. A spot size of FWHM = 2.2 mm is considered for a long and short focal length.

λ	**max. BBO thickness for $f = 75$ mm**	**max. BBO thickness for $f = 200$ mm**
500 nm	54 µm	150 µm
600 nm	67 µm	188 µm
700 nm	85 µm	240 µm
800 nm	106 µm	305 µm

In table II.2 a few "real existing" crystals of our lab are listed. Their thickness is measured with a spectrophotometer as described above. Additionally the acceptance angle and the acceptance bandwidth are calculated for the centre wavelength (defined by the cutting angle θ_{PM}). The calculation is done easiest by plotting the *sinc*^{2} phase-matching function (like in Fig. 2.8) and reading off the FWHM value of the resulting distribution.

For example the crystal of the second row of table II.2 cut at 35° for frequency doubling close to 680 nm has a thickness of 50.9 µm. This limits the bandwidth of the fundamental pulse for frequency conversion to 42.1 nm. Assuming a beam spot size of FWHM = 2.2 mm this leads to minimum possible focal length of $f = 2.2$ mm / tan (2.5°) ≈ 60 mm with regard to the acceptance angle $\Delta\theta$. Since commonly only discrete focal lengths are available, the listed values are "rounded" to the next reasonable/available value. In the present case of the example from 60 mm to $f = 75$ mm.

TABLE II.2: Experimental needed parameters for SHG of some BBO crystals of our lab.

angle θ_{PM}	**centre wavelength**	**measured thickness**	**accept. bandwidth**	**accept. angle $\Delta\theta$**	**min. focal length**	**supplier**
30°	780 nm	**124.3 µm**	35.4 nm	1.4°	**~ 100 mm**	BlueBean
35°	680 nm	**50.9 µm**	42.1 nm	2.1°	**~ 75 mm**	Castech
45°	555 nm	**44.8 µm**	19.8 nm	2.2°	**~ 75 mm**	Castech
60°	460 nm	**50.6 µm**	7.2 nm	1.8°	**~ 75 mm**	Castech
62.9°	450 nm	**29.5 µm**	10.9 nm	3.1°	**~ 50 mm**	Castech

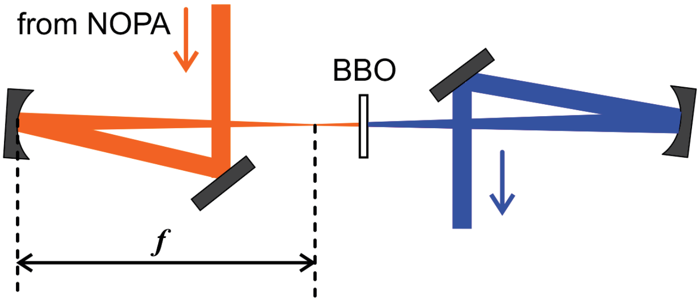

Fig. 2.12: Scheme for frequency doubling of NOPA pulses.

Fig. 2.12 shows the scheme for frequency doubling of NOPA pulses as used in our transient spectrometer according to Ref. [Meg09] for UV pump pulse generation. The NOPA output beam is collimated and compressed in the visible with a folded fused silica prism compressor. At the frequency doubling crystal the visible pulses are overcompensated to obtain compressed UV pulses without an additional compressor. To not add additional chirp to the pulses in the visible, the pulses are focused by a concave silver mirror under a small angle of incidence instead of a lens. After frequency doubling, the beam is collimated by a concave dielectric mirror. This mirror usually has a focal length of 250 mm and has a dielectric coating that depends on the used UV wavelength.

With the BBO with θ_{PM} = 35°, 50.9 µm a NOPA pulse centered around 670 nm with 38 nm bandwidth and a pulse energy of 2.5 µJ is frequency converted in this scheme. The bandwidth of the NOPA signal is narrowed close to the acceptance bandwidth of the crystal, to roughly 38 nm by increasing the white light chirp inside the NOPA. This is done by placing a 14.5 mm BK7 glass block in the seed beam path [Ste09].

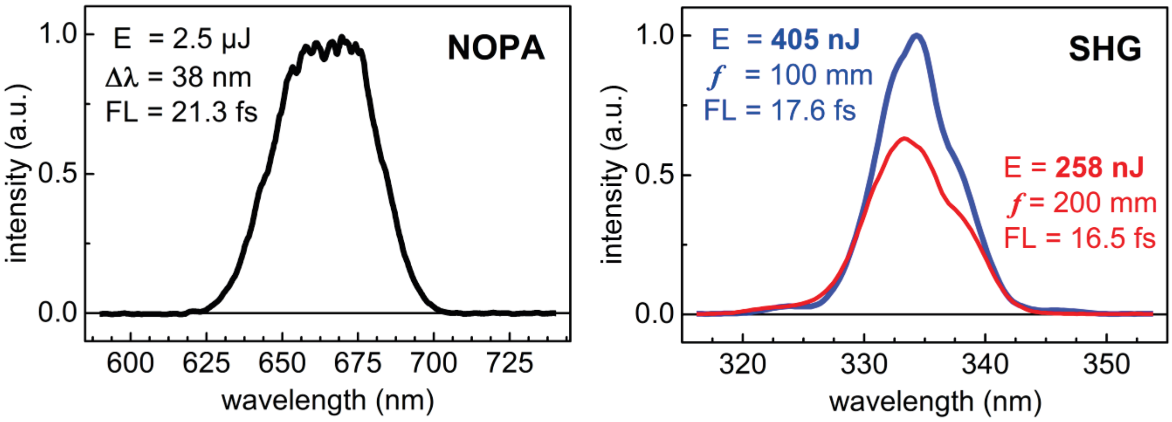

Fig. 2.13: Left: NOPA output signal narrowed to the acceptance bandwidth of the SHG crystal. Right: Second harmonic spectrum obtained with 50.9 µm BBO crystal for f = 100 mm (blue) and f = 200 mm (red) focal length.

By changing the focal length of the mirror, that focuses towards the BBO crystal, from $f = 200$ mm to $f = 100$ mm an increase of a factor 1.6 in obtained UV energy is measured. The UV energy increases from 258 to 405 nJ while the spectral shape in the UV is almost identical for both configurations. For the longer focal length this corresponds to a doubling efficiency of 10%, for the shorter one to an efficiency of 16%.

The precise knowledge of crystal thicknesses and the resultant bandwidth and angular acceptance is of major importance for frequency conversion, especially for high repetition rate NOPA systems with low pulse energy on the 200 – 500 nJ level. Thin crystals are required for the generation of ultra-short pulses. But for thin crystals efficiency is low. Therefore it is important to be flexible in the experimental setup, to be able to change focal lengths in order to achieve sufficient efficiency in frequency doubling.

Comment on bandwidths in SNLO: The value "*Mix accept bw*" (the acceptance bandwidth) given under "*QMIX*" in the SNLO code [SNLO], can be either for "*OPO*" acceptance or "*Mix*" acceptance. By choosing "*Mix*", one of the red waves tunes along with the blue wave. This means, there are two acceptance bands, one for tuning one red wave along with the blue wave, the second for tuning the second red wave along with the blue wave. The two bandwidths are listed separately. If both red waves have the same polarization and tune together, the acceptance band is half of the two listed equal values [Smi18]. The same applies to the value "*Mix accept ang*" (the acceptance angle). Consequently, for type I SHG the value for the acceptance angle is half of the two listed values in SNLO.

In Fig. 2.12 it can be seen that the frequency doubling crystal is located slightly behind the focal plane of the fundamental beam. In the next section it is demonstrated how this position enables perfect phase-matching due to balancing the natural divergence by Kerr-nonlinearities. It will also be shown that these nonlinearities can lead to distorted pulses when too high an efficiency is pushed.

2.4 Limitation of the SHG and THG Efficiency and Beam Break-up for Femtosecond Pulses by Kerr Lensing

For many applications the second and third harmonic of a laser system is required and quite often, of course, high pulse energies are desired. Therefore the efficiency of the SHG and THG processes must be high. In the literature high efficiencies can be found very frequently. Values up to 60 % and higher for SHG are reported for the femtosecond pulse regime and BBO as nonlinear medium [Ada08, Rot12a, Pup15a]. It is demonstrated that pushing to such high efficiency leads to distorted beam profiles and broadened, structured spectra of the harmonics due to the Kerr effect in the nonlinear medium. Calculations show that for a common focusing geometry of SHG, very high nonlinear phase shifts are acquired when the crystal gets close to the focal plane of the fundamental beam – see Fig. 2.14. It is simulated that a 100 μm BBO crystal is moved through the focal plane of a 30 fs pulse centred around 550 nm with 10 μJ pulse energy. For the beam size FWHM = 2 mm is assumed and the beam is focused with $f = 200$ mm towards the crystal. With the help of a Kerr-lens matrix [Sie86] the change of the convergence/divergence $\Delta\theta$ due to the Kerr effect is estimated according to the sketch in Fig. 2.14, with the nonlinear refractive index of BBO $n_2 = 5\cdot 10^{-20}\ \mathrm{m^2/W}$, taken from Ref. [Bac13].

$\Delta\theta$ is the value how the Kerr-nonlinearity changes the convergence (in front of the focal plane) or divergence (behind the focal plane) of the beam due to the nonlinear bending of the wave-front inside the doubling crystal – see sketch in Fig. 2.14. The nonlinear self-lensing leads also to smaller beam widths inside the crystal and hence higher intensities are present.

The nonlinear phase shift can lead to strong self-focusing even in such extremely thin crystals. B-Integrals higher than 10 are reached easily. Consequently, the convergence in the crystal is strongly changed and the phase matching angle in the crystal can readily be lost. In Fig. 2.14 this is shown as the grey area in the range of ±0.7 mm from the focal region. This is where the self-focusing is so strong that the angle increases to the level where the phase-matching function $sinc(\Delta kL/2)^2 = 0$. This is at $\Delta kL/2 = \pi$. The level is marked with a red, dashed line. At this point the B-Integral is highly above the critical value of 3. Thus, this leads to parts of the UV spectrum with a phase shift of $\pm\pi$ – compare the angular dependence of the phase-matching function in Fig. 2.8.

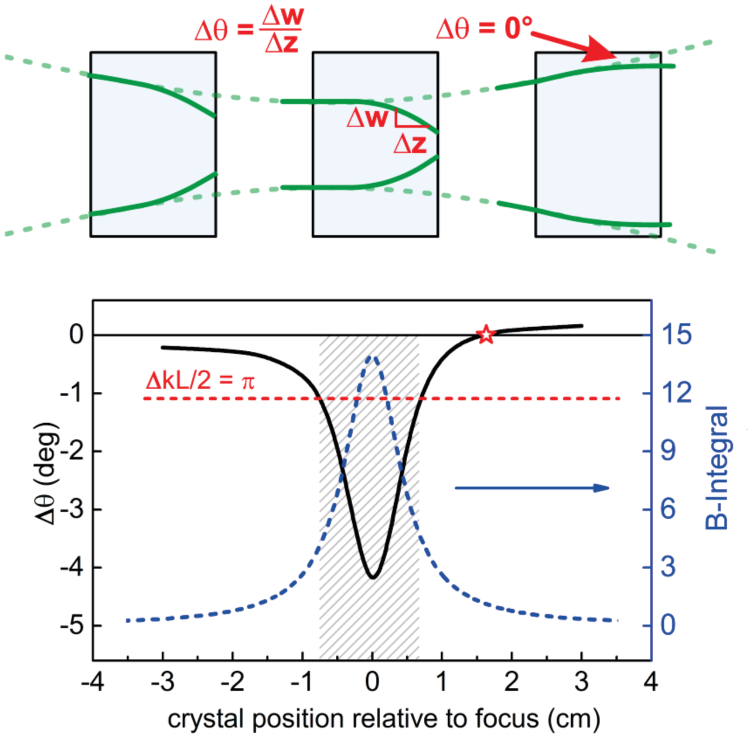

Fig. 2.14: Top panel: Sketch for the crystal position relative to the focused beam (dashed line, beam propagates from left to right). Induced self-lensing effects on the propagation are shown as solid line. Below: Kerr effect induced convergence change (black line) as a function of a 100 μm BBO crystal position relative to the focus position. Shown is also the position dependent B-Integral (blue line).

This limits the doubling efficiency and leads to strongly distorted beam profiles as well as spectra and incompressible pulses. Remarkably, at about +15 mm in the situation of Fig. 2.14 there is a point where the beam divergence is just matched by the Kerr induced focusing and a perfect phase matching condition for the transformed beam results. It is denoted as a red star. This is where the doubling crystal should be located optimally, to obtain the highest efficiency.

The nonlinear distortions show up also in a broadening of the resulting spectra due to self-phase modulation – see Fig. 2.15. Here a Ti:sapphire laser, centered around 775 nm with a nominal pulse duration of 150 fs and a pulse energy of 155 μJ, is frequency doubled in a 300 μm BBO. The Fourier limit of the fundamental pulse is about 90 fs. The beam is focused with an *f* = 250 mm lens towards the SHG crystal, located behind the focal region. The efficiency of frequency doubling is increased by moving the crystal closer to the focus. From an efficiency level of 35% on the blue spectrum gets modulated. The Fourier limit of

31 fs at 40% efficiency is almost half the value of 59.7 fs at a level of 24.5%. The experiment is repeated with an Yb:fiber laser system, operating at 1030 nm with roughly 320 fs pulse duration at 200 kHz with 20 µJ pulse energy. The Fourier limit of the fundamental amounts to 275 fs. The beam is focused with a 250 mm lens towards the BBO crystal (thickness 0.8 mm). Here an efficiency of 46% can be reached for the second harmonic, accompanied by a drastic spectral distortion and broadening. The Fourier limit reaches down to 73 fs for this case.

Once the pulse is distorted due to parasitic nonlinearities, also beam break-up can occur. In Fig. 2.16 beam profiles of the second and subsequent third harmonic of the Yb:fiber laser are compared for high and moderate doubling efficiency.

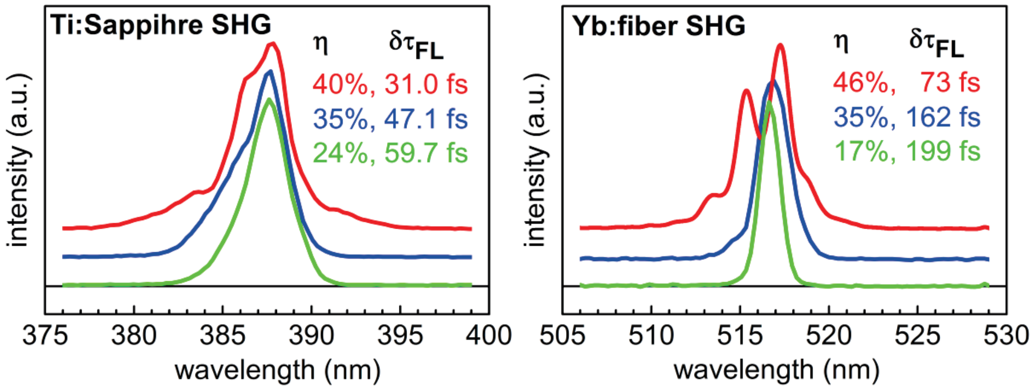

Fig. 2.15: Spectral broadening with varying efficiency (η) of frequency doubling by moving the crystal relative to the focal plane of the fundamental beam. $\delta\tau_{FL}$ corresponds to the Fourier limit of the converted spectrum. For a Ti:Sapphire laser (left) and an Yb:fiber laser (right).

Fig. 2.16 shows the second and third harmonic beam profiles for high efficiency conversion of 20 µJ, 1030 nm, 320 fs pulses. Clearly there is a beam break-up that is not tolerable. If the efficiencies are lowered to 31 and 10 %, respectively, the beam profile cleans up very well. At the same time the distortion of the spectrum is avoided – compare Fig. 2.15. For third harmonic generation a subsequent BBO crystal (type II, $\theta = 40°$) is used for sum-frequency mixing with an intermediate focus. For details on the THG process, compare chapter 6.

The reason for this dramatic beam break up for high efficiency frequency doubling is that – as it is shown in Fig. 2.14 – the high intensity of the fundamental leads to a Kerr induced self-focusing. This increases the divergence of the beam inside the crystal to values where the $sinc^2$ phase-matching function exhibit side lobes. After SHG these spectral side lobes are phase-shifted by $\pm\pi$. After sum frequency mixing with the fundamental to the third harmonic, this will show up as intensity modulation of the resulting beam. This effect can be seen on the beam profile of the third harmonic for 40% efficiency of the second harmonic in Fig. 2.16.

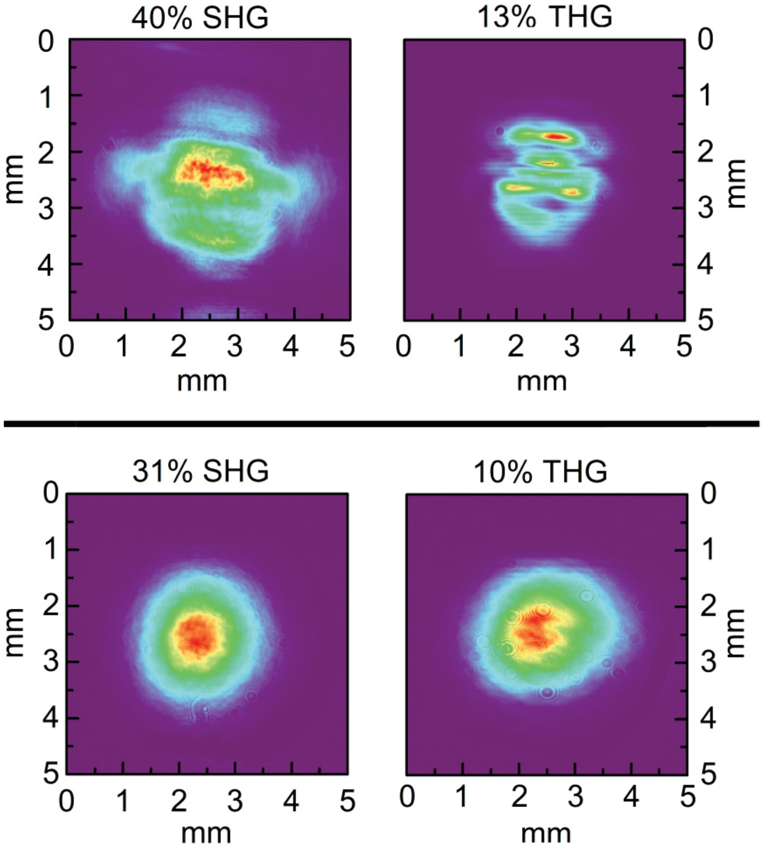

Fig. 2.16: Beam profiles of the second and third harmonic of 1030 nm for high (upper row) and moderate (lower up) SHG efficiency.

Optical parametric amplification, second harmonic generation and supercontinuum generation are effects of major relevance for all setups and experiments demonstrated in this work. Therefore, they have been described briefly in this section. These effects are the basis for the generation of ultra-short pulses. To prevent ultra-short pulses from temporal stretching, dispersive material in the beam path has to be avoided. In the next chapter a simple, folded mirror telescope is presented that allows to collimate or to image in a reflective way. In this way the use of lenses is avoided and pulses can be prevented from getting chirped.

3. Astigmatism free imaging with a spherical mirror folded telescope

A central issue in ultrafast optics is the need to focus and collimate pulses with a very wide spectrum, like a supercontinuum, without diffractive elements [Dob10, Meg09]. Diffractive lenses introduce an unacceptable chirp and also chromatic aberrations. Theoretically parabolic mirrors would be ideal. However, their optical quality is far inferior to spherical mirrors for short focal lengths and off-axis parabolics are only useful in the IR, because of their rather poor surface quality [Bur13] which results from the manufacturing process.

In this chapter a combination of a concave and a convex spherical mirror with suitable ratio of radii of curvature is presented. It is a *Schiefspiegler* type telescope [Kut53] and allows focusing and collimating beams without any detectable astigmatism. This is found at angles where a single spherical mirror already introduces a large aberration. The advantage compared to other reflective mirror telescopes, like the *Cassegrain*- or *Newton* telescope, is that due to the introduction of a tilt angle between the mirrors there is no obstruction in the light path due to the secondary mirror. It would be very inelegant in spectroscopy or laser physics, since parts of the laser mode would be blocked. A different approach is to minimize the astigmatism by two off-axis spherical mirrors for the sagittal and meridional plane [Ern01]. But this requires reflecting the beam out of the plane, which makes the setup unhandy. The system presented here, uses two spherical mirrors in plane under selected angles of incidence. A scheme of the Schiefspiegler telescope is given in Fig. 3.1.

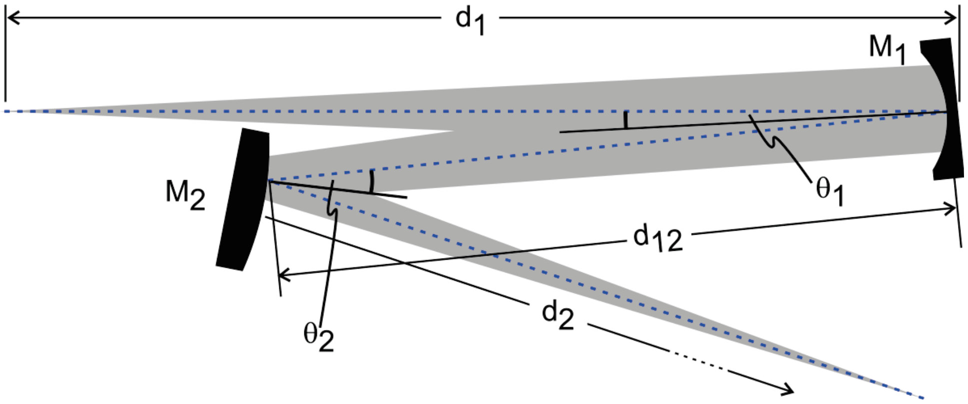

Fig. 3.1: Schiefspiegler telescope setup with parameters:

- concave spherical mirror M_1 with radius R_{M1} under an angle of incidence θ_1
- convex spherical mirror M_2 with radius R_{M2} under an angle of incidence θ_2
- distance d_{12} – distance between mirror M_1 and M_2
- distance of the light source to the first mirror d_1
- propagation distance d_2 from mirror M_2.

The focal lengths of the mirrors can be estimated and chosen according to a linear two lens based telescope with the overall focal length approximated

$$\frac{1}{f} \approx \frac{1}{f_1} + \frac{1}{f_2} - \frac{d_{12}}{f_1 f_2}, \tag{3.1}$$

with

$$f_i = \frac{R_{Mi}}{2}. \tag{3.2}$$

With the ABCD matrix formalism an angle θ_2 can be found numerically, depending on all parameters of the system, to correct for the astigmatism introduced by the primary mirror. This is done by calculating the sagittal (*s*, horizontal) and the meridional (*m*, vertical) plane of the in-falling beam separately, and solve for an angle θ_2 for which both focal planes are localized equally. The matrix systems for both the sagittal and meridional plane after the secondary mirror are given by formula (3.3).

$$\begin{aligned}
\begin{pmatrix} A & B \\ C & D \end{pmatrix}_s &= \begin{pmatrix} 1 & 0 \\ \frac{2}{R_{M2}} \cdot \cos(\theta_2) & 1 \end{pmatrix} \begin{pmatrix} 1 & d_{12} \\ 0 & 1 \end{pmatrix} \begin{pmatrix} 1 & 0 \\ \frac{2}{R_{M1}} \cdot \cos(\theta_1) & 1 \end{pmatrix} \begin{pmatrix} 1 & d_1 \\ 0 & 1 \end{pmatrix} \\
\begin{pmatrix} A & B \\ C & D \end{pmatrix}_m &= \begin{pmatrix} 1 & 0 \\ \frac{2}{R_{M2}} \cdot \frac{1}{\cos(\theta_2)} & 1 \end{pmatrix} \begin{pmatrix} 1 & d_{12} \\ 0 & 1 \end{pmatrix} \begin{pmatrix} 1 & 0 \\ \frac{2}{R_{M1}} \cdot \frac{1}{\cos(\theta_1)} & 1 \end{pmatrix} \begin{pmatrix} 1 & d_1 \\ 0 & 1 \end{pmatrix}
\end{aligned} \tag{3.3}$$

By calculating the complex beam parameter *q* for both planes after secondary mirror M_2 and solving for the beam width *w*, a two dimensional ray tracing can be performed to visualize the beam propagation before, in between and after the telescope.

$$\frac{1}{q(z)} = \frac{1}{R(z)} - \frac{i \cdot \lambda}{\pi \cdot w(z)} \quad , \quad q' = \frac{A \cdot q + B}{C \cdot q + D}. \tag{3.4}$$

Fig. 3.2 shows the calculation for the astigmatism compensation of the primary mirror M_1. The dashed, vertical arrows denote the first (focusing) and the second (defocusing) mirror, respectively. To represent the propagation more clearly, the calculated propagation is shown linearized and not tilted as in Fig. 3.1. The red and blue dashed lines show the astigmatic propagation of the primary mirror as it would propagate without correction by the second mirror. Despite of a slight ellipticity the corrected beam propagates without astigmatism – the meridional and sagittal focal planes are located exactly at the same distance, as the yellow magnification inset shows. The ratio between both planes is shown in the lower panel for the situation of a single focusing mirror (grey, dashed line) and the telescope case (black line), also indicating slight ellipticity but no astigmatism for the case with two mirrors.

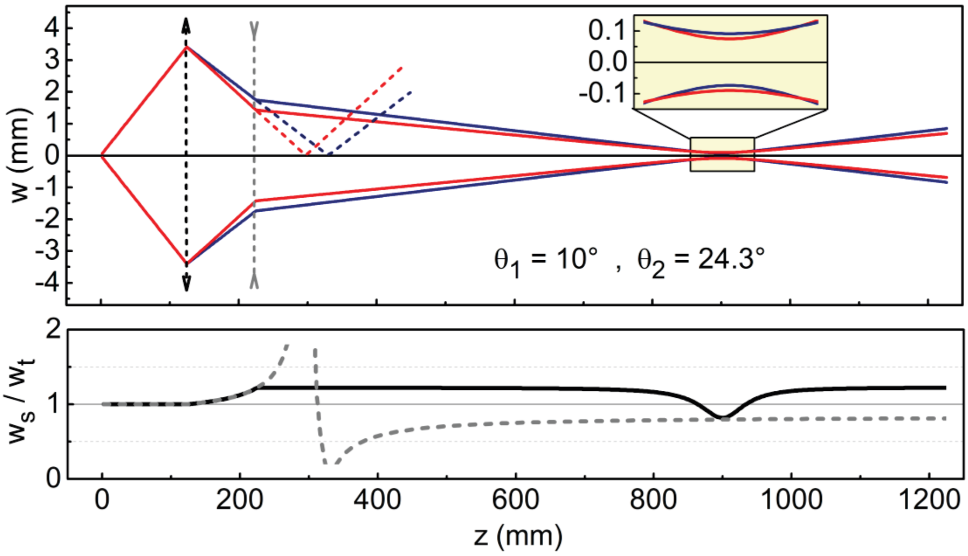

Fig. 3.2: Ray tracing through a Schiefspiegler telescope where a single mirror would already show large astigmatism (blue and red dotted line). Dashed, vertical arrows denote positions of the primary and secondary mirror.

Keeping the angle θ_l as small as possible under real experimental conditions improves the propagation regarding the ellipticity of the beam profile. As Fig. 3.3 shows, both planes (blue line and red, dashed line) are lying on top of each other. Even in the focus region (yellow, magnified inset) both planes of the beam are propagating identically. The ratio of the sagittal and the meridional plane (black line in the lower panel) is on a constant value of 1, corresponding to an astigmatism free, radially symmetric beam profile.

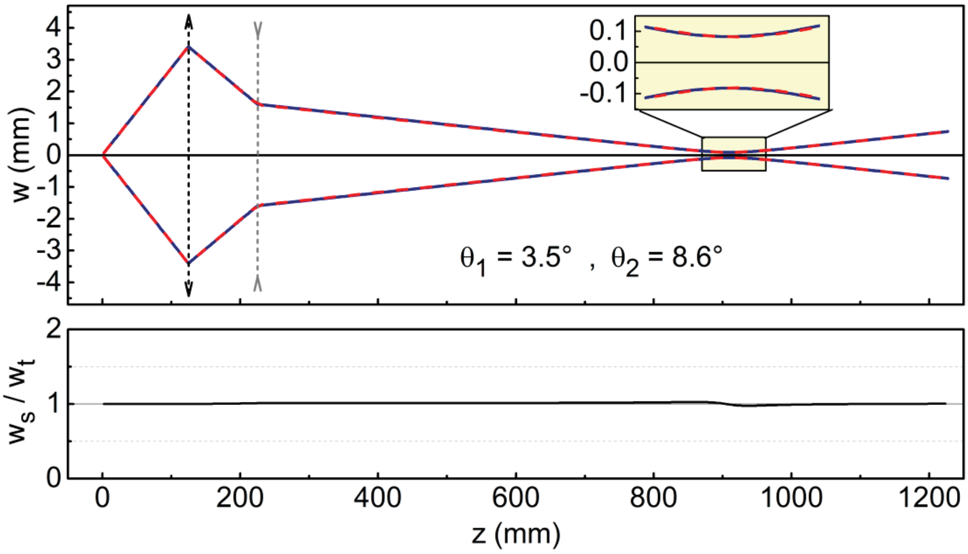

Fig. 3.3: Ray tracing through a Schiefspiegler telescope with a small angle of the primary mirror. Dashed, vertical arrows denote positions of primary and secondary mirror.

Gomez-Vieyra et al. published a formula for a two mirror astigmatism compensating telescope [Gom09, Gom11]. However, they proposed an arrangement, similar to that of Fig. 3.1, to also image out of the horizontal plane after the secondary mirror. By neglecting some higher order terms in their derivation and keeping a fixed propagation height in the horizontal plane, the angle θ_2 to correct for the aberration of the primary mirror, amounts to

$$\theta_2 \approx \theta_1 \cdot d_1 \cdot \frac{\sqrt{|R_{M1} R_{M2}|}}{(d_1 + d_{12}) \cdot |R_{M1}| - 2 \cdot d_1 \cdot d_{12}}. \tag{3.5}$$

Focusing collimated beams with the telescope (Fig. 3.4b) is equal to a great distance d_1 from the source to the primary mirror M_1. In this case, Eq. 3.5 simplifies to

$$\theta_2^{\text{collimated}} = \lim_{d_1 \to \infty} \theta_2 \approx \theta_1 \cdot \frac{\sqrt{|R_{M1} R_{M2}|}}{|R_{M1}| - 2 \cdot d_{12}}. \tag{3.6}$$

In Fig. 3.4 the approximation with Eq. 3.5 (balls) is compared to the numerical solution (lines) for the case of relay imaging (a) and focusing of a collimated beam (b). The angle θ_1 is kept at a constant value of 3.4° for both cases. A MathCad program for calculating all relevant parameters of the telescope is given in appendix A3.

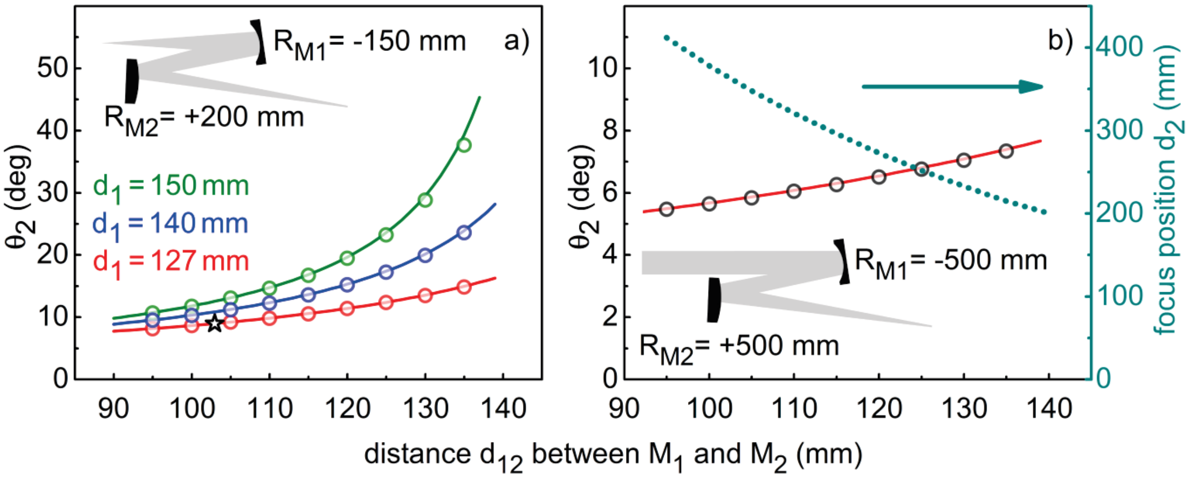

Fig. 3.4: Comparison of the approximation of the correction angle θ_2 calculated with the approximation of Eq. 3.5 (balls) and the numerical solution (straight line) for the relay imaging case (a) and the focusing of a collimated beam (b) depending on the mirror separation d_{12}. The focus position for the case of focusing (b) is given in turquois, dotted line.

For given focal lengths the correction angle of mirror M_2 increases with the mirror separation d_{12} and the distance to the focus decreases. It has to be noticed that the approximated and the numerical solutions are in very good agreement.

For a white light continuum, generated in a 1 mm sapphire plate with 778 nm, 1 kHz, a pulse duration of nominally 150 fs and with a pulse energy of 1.8 µJ the imaging quality of the telescope is shown in Fig. 3.5.

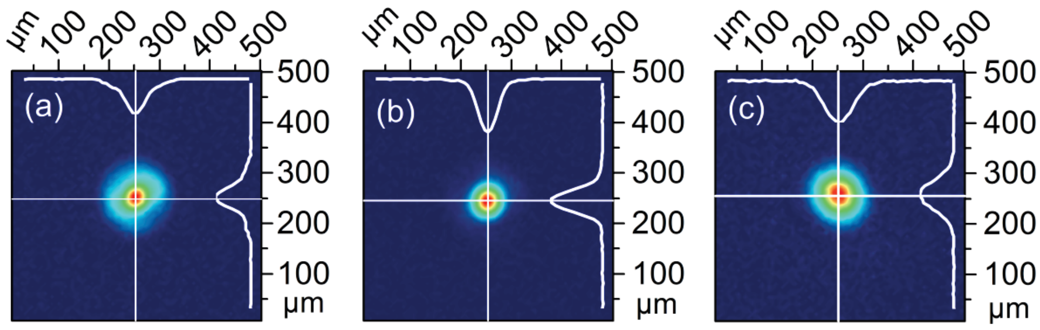

Fig. 3.5: Beam profiles of a white light continuum pulse (10 nm around 550 nm selected with an interference filter) imaged with the Schiefspiegler telescope at the beginning of the Rayleigh range (a), at the focus (b) and at the end of the Rayleigh range (c).

The profile data from Fig. 3.5 was taken with a commercial beam profiler (PhotonInc., USBeamPro). With an interference filter a part of the continuum, centered around 550 nm, was measured selectively. Fig. 3.5 (b) shows the focal spot, whereas (a) and (c) corresponds to the positions where the beam waist is bigger by a factor of $\sqrt{2}$, this corresponds to the Rayleigh length of the imaged continuum. The internal profile cross sections of the meridional and sagittal plane show that the beam profile stays radially symmetric within its Rayleigh range. In Fig. 3.5 (a), in front of the focus, the profile is slightly distorted. This behavior is attributed to the spherical aberration introduced by the mirrors as reported in [Bow08a].

In the next chapter, the Schiefspiegler telescope presented here will be used to image an unchirped continuum to seed an ultra-broadband amplifier. This is done for three different reasons. Firstly, a lens introduces chirp, whereas the telescope works in a reflective way. Secondly, the surface quality of spherical mirrors is superior to parabolic mirrors – this avoids phase distortions. Thirdly, a single spherical mirror introduces astigmatism, while the Schiefspiegler geometry compensates this. The astigmatism of the seed beam would be transferred to the NOPA signal. For compression to shortest pulse durations with a prism compressor this might cause serious problems.

Additionally, in chapter 8 the presented telescope will be used to image an unchirped continuum which serves as a gate pulse for electro-optical sampling of a middle infrared pulse for the identical three reasons.

Comment on the alignment of the telescope: Since the alignment and the focus position strongly depends on the mirror positions, it is recommended to mount them on precise mechanical translation stages. As shown, the angle of the first mirror should be kept as small as possible. Since it reflects back to the source, this angle might be the most erroneous value (due to the lack of space for adjustment). I always used a business card with a small hole, carefully punched with the tip of a pen. In a calculated distance from the hole I marked the position where the beam should hit when the angle is correct. By fixing the business card to a moveable mount, the card can be moved in a way that the central spot of the light source propagates through the hole. Then the reflection of M_1 is easily steered to the mark on the business card. For the second mirror I used simple trigonometry. It is best to calculate where the beam should hit, e.g., in 1 m distance. Locate an alignment tool at the calculated position and steer the beam to it. From there on, move a beam profiler up and down the beam line while monitoring the horizontal and vertical beam width. By slightly optimizing the horizontal angle of mirror M_2 there should be a position where the astigmatism vanishes. In the vertical direction the astigmatism manifests in a tilted meridional and sagittal focal line. This can be corrected with the two vertical adjustment screws of M_1 and M_2, just like for the alignment of a beam over tapped holes on the laser table.

4. Broadband noncollinear optical parametric amplification based on unchirped white light seed

In this chapter, an un-chirped continuum from a 1 mm sapphire plate (see chapter 2, or appendix A1 for details) will be used to seed an ultra-broadband NOPA, pumped by a Ti:Sapphire laser. By the use of thicker generation media of the typical thickness of 3 - 5 mm, the resulting continua are highly chirped [Mac00, Zio04, Bra14b]. Nevertheless, for most spectroscopic applications the resulting bandwidths, after amplification of chirped continua are sufficient, corresponding to well below 20 fs pulses. For getting pulse durations below 10 fs, different approaches have to be considered. Basically, there are two things that can be done. Either stretching the pump pulse to match a large amount of continuum frequencies during amplification [Bau06] or using less chirped seed light [Kob00, Bal02]. The method with stretched pump pulses was published in 2006 in the group.

In this work, an approach with an intrinsically nearly un-chirped seed continuum light for amplification is presented. It makes a seed pre-compressor unnecessary and therefore drastically reduces the complexity of the setup compared to, e.g., Ref. [Kob00]. To avoid additional chirping of the continuum the light is imaged with the use of a Schiefspiegler telescope [Kut53], which was presented and calculated in chapter 3. The use of a single spherical focusing mirror would introduce astigmatism. The spatial aberration would also show up after amplification and would cause serious problems in the next nonlinear interaction downstream the beam towards the experiment. Theoretically, parabolic mirrors would be ideal for the imaging of the continuum, but due to the available optical quality they are only suitable for infrared sources. The Schiefspiegler telescope ensures to have the imaging quality of a spherical lens but without dispersion.

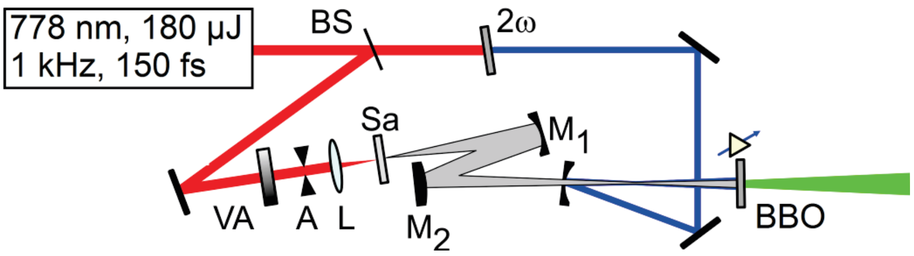

Fig. 4.1: Setup of a noncollinear optical parametric amplifier with unchirped seed light. *BS*: beam splitter (AR on backside), 2ω: SHG 700 μm BBO, *VA*: variable neutral density filter, *A*: aperture, L: $f = 50$ mm lens, M_1, M_2: Schiefspiegler telescope with spherical silver mirrors (for details, see text).

Single stage amplification

A schematic of the setup is shown in Fig. 4.1. A fraction of 180 µJ of a Ti:Sapphire chirped pulse amplifier (Clark MXR Inc., CPA 2001) is used to pump the system. The repetition rate of the laser system is at 1 kHz with a nominal pulse duration of 150 fs. The input is linearly polarized in the horizontal plane.

The incoming beam is split into two arms with a beam splitter comprised of a fused silica substrate with broadband antireflection coating on its backside and uncoated on the front surface, to avoid a reflection from this surface. For continuum generation roughly 4% of the input – corresponding to about 7 µJ – is split off. With a variable neutral density attenuator (*VA*) and an aperture (*A*) the energy is optimized to about 2 µJ for continuum generation in the 1 mm sapphire plate (*Sa*). With a combination of a concave, spherical silver mirror M_1 (R = - 150 mm) and a convex, spherical silver mirror M_2 (R = 200 mm) the continuum is imaged towards the amplification crystal, a 2 mm BBO cut at 32.5°. For details on the Schiefspiegler telescope geometry and calculation, see chapter 3. The distance between the sapphire plate and M_1 is 127 mm, M_1 and M_2 are separated by 103 mm and the angles of incidence for M_1 and M_2 are 3.4° and 8.9°, respectively. The focal plane of the continuum is roughly 740 mm behind the sapphire plate. The amplifier crystal is located roughly 1 cm behind the focal region, corresponding to a $1/e^2$ beam width of 200 µm.

The transmitted beam of the initial beam splitter is frequency doubled in a 700 µm BBO, cut at 30°, with a doubling efficiency of 30%, resulting in 51 µJ energy. Two high reflective mirrors for 389 nm separate the residual fundamental and the frequency doubled pump pulses. A concave focusing mirror with f = 250 mm is used to focus the pump beam in front of the amplifier crystal. The focusing mirror is placed under the beam path of the continuum, to allow for the tuning of the noncollinearity angle in vertical direction. The focal plane of both, the continuum and the pump beam is located in front of the amplifier crystal, due to two reasons: First, in front of the focus spherical aberration is present in the beam [Bow08b]. Secondly, the curvature of the wave-front from a diverging beam is helping to compensate Kerr lensing in the amplifier crystal – compare chapter 5.

The seed continuum spectrum, including the corresponding RMS stability, is shown in Fig. 4.2. The RMS fluctuation measurement was done by implementing a 1 mm sapphire continuum into our transient setup [Meg09] and analyze it with the spectrograph. The fluctuation is on the order of 1% RMS, which is an acceptable value to seed an amplifier. The Fourier limit of the continuum spectrum amounts to about 3.8 fs.

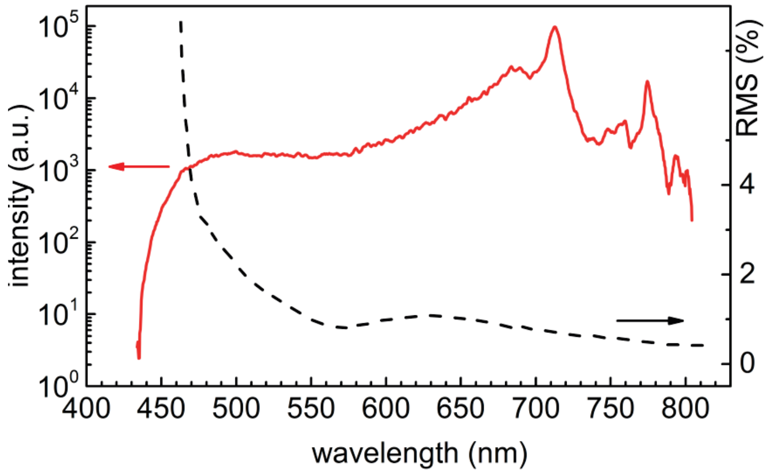

Fig. 4.2: Continuum generated with 778 nm in 1 mm sapphire crystal. RMS stability of the continuum on the right axis.

In Fig. 4.3 two amplified output spectra of the single stage NOPA are shown. The spectra were recorded with a fiber coupled spectrometer (Ocean Optics, HR4000) and intensity calibrated afterwards. The noncollinearity angle is set to 3.7°. The Fourier limit of the spectrum shown in red corresponds to 5.3 fs. By adjusting the phase-matching angle the spectral width could be enhanced to 4.5 fs Fourier limit. Since the seed pulse is very short compared to the pump pulse, the resulting amplified output energy of 3 μJ is relatively low. This corresponds to 10% quantum efficiency in the parametric process. But nearly the whole spectral width of the continuum pulse is amplified.

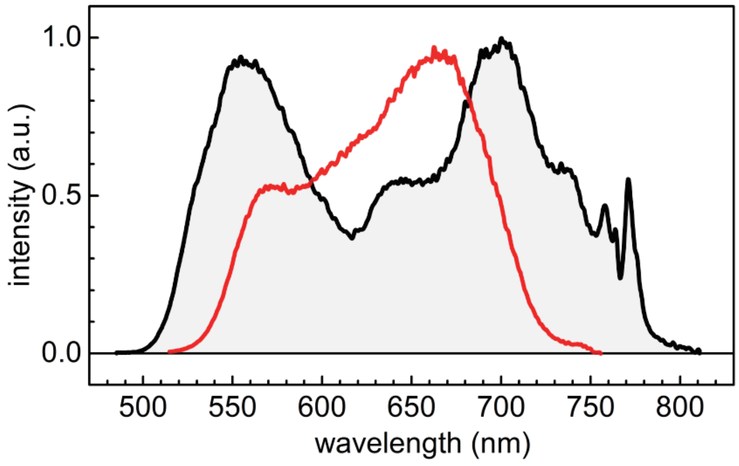

Fig. 4.3: Broadband NOPA output for different phase-matching conditions, with a pulse energy of $E = 3$ μJ.

The pulse width of the uncompressed NOPA output corresponds to 77.8 fs. This elongation is caused by the dispersion added in the 2 mm amplifier BBO. The beam after amplification is collimated by a spherical silver mirror (R_{cc} = -1000 mm) under a small angle and reflected by a metallic beam splitter, to attenuate the pulse to a proper energy without dispersion, towards the SHG intensity autocorrelator [Koz04]. The autocorrelation measurement (dots) and the corresponding Gaussian fit (red line) is shown in Fig. 4.4.

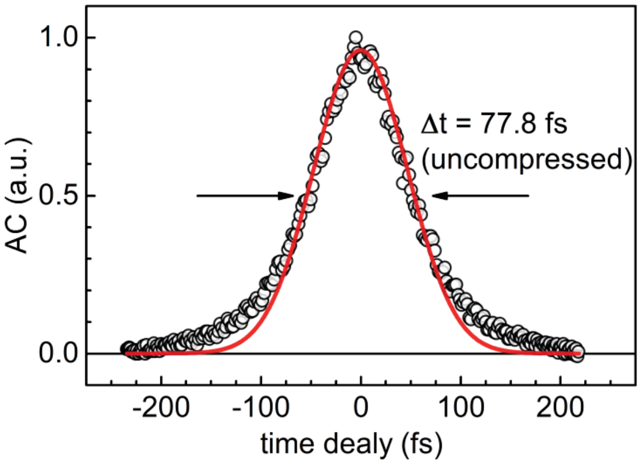

Fig. 4.4: Autocorrelation measurement of the uncompressed NOPA output with unchirped white light seed.

To cover the full spectral width of the pulse in temporal characterization, the thinnest available BBO crystal with 25 µm thickness and a cutting angle of θ = 40° was used for the SHG autocorrelation measurement. In Ref. [Koz03] the temporal widths of the uncompressed NOPA output pulses for chirped seed light was measured for various central wavelengths. It was demonstrated that independent from additional chirp in the seed light beam path the temporal width of the output is close to the value of the UV pump beam. As Fig. 4.4 demonstrates this is not the case for the use of unchirped seed light. In turn, this allows the use of a second amplification stage without the loss of spectral bandwidth but enhancing the amplification efficiency.

Operation with pre- and main amplification stage

Fig. 4.5 shows a schematic for a setup similar to Fig. 4.1, with a second UV pumped amplification stage added. To not introduce astigmatism in the subsequent stage and to avoid dispersive material, the pre-amplified signal of the first stage is also imaged with the help of a Schiefspiegler telescope towards the second amplifier crystal. For this purpose a fraction of 250 µJ of the CPA is used. The splitting for continuum generation and all parts of the generation is identical to the initial single stage setup. Roughly 2 µJ are used for continuum generation in a 1 mm sapphire plate. The energy is optimized with the help of the variable attenuator (*VA*) and the position of the lens L_1 (plano-convex, fused silica, $f = 50$ mm). For optimizing the stability of the continuum an aperture (*A*) gently narrows the beam diameter of the fundamental. Like in the previous single stage setup, the distance between the sapphire plate and M_1 is 127 mm, M_1 and M_2 are separated by 103 mm and the angles of incidence for M_1 and M_2 are 3.4° and 8.9°, respectively. The focal plane of the continuum is roughly 740 mm behind the sapphire plate. The amplifier crystal (1 mm BBO, 32.5°, type I) is located roughly 1 cm behind the focal region, corresponding to a $1/e^2$ beam width of 200 µm.

Behind the pre-amplifier crystal the first convex spherical silver mirror (M_3) of Schiefspiegler #2 ($R_{M3} = +1000$ mm) is located in 355 mm distance, with an angle of incidence of 6°. The second mirror of the telescope (M_4), a concave spherical silver mirror, with $R_{M4} = -500$ mm, is in 295 mm distance of the mirror M_3. The angle of incidence on this mirror amounts to 2°. This geometry enables anastigmatic imaging of the pre-amplified signal towards the second amplifier crystal, which is located 560 mm downstream from mirror M_4. The focal plane of the pre-amplified signal is roughly 4 cm in front of the amplifier crystal.

The overall efficiency of second harmonic generation for the pump pulse is 30%, corresponding to 71 µJ in total. With the help of a beam splitter 16 µJ are used to pump the pre-amplifier stage. The remaining 55 µJ are used to pump the second amplification stage (2 mm BBO, 32.5°, type I). The beam splitter for the separation of the pump branch is fixed on a mechanical translation stage for adjusting and optimizing the temporal overlap of the pre-amplifier stage. In the first stage the pump is focused with the help of a concave HR mirror ($R_{cc} = -300$ mm) in a distance of roughly 17 cm in front of the pre-amplifier crystal. For the second stage the pump beam is focused with a plano-convex, fused silica lens with $f = 750$ mm (L_2). By moving the lens along the *z*-axis, the pump beam waist on the amplifier crystal can be optimized to the amplification and beam profile. This is advantageous, since the spot-size of the white light at the crystal cannot be adjusted easily without losing the proper alignment of the Schiefspiegler telescope. The focal plane of the pump beam is located roughly 15 cm in front of the amplifier crystal. This corresponds to a $1/e^2$ beam width of roughly 250 µm and a pump intensity of about 260 GW/cm^2. In other setups designed in the group the use of lenses in the UV pump beam is avoided. In the present case it allows more flexibility in the focusing geometry without losing the temporal overlap. At the same time it adds some additional chirp for improved temporal overlap with the seed.

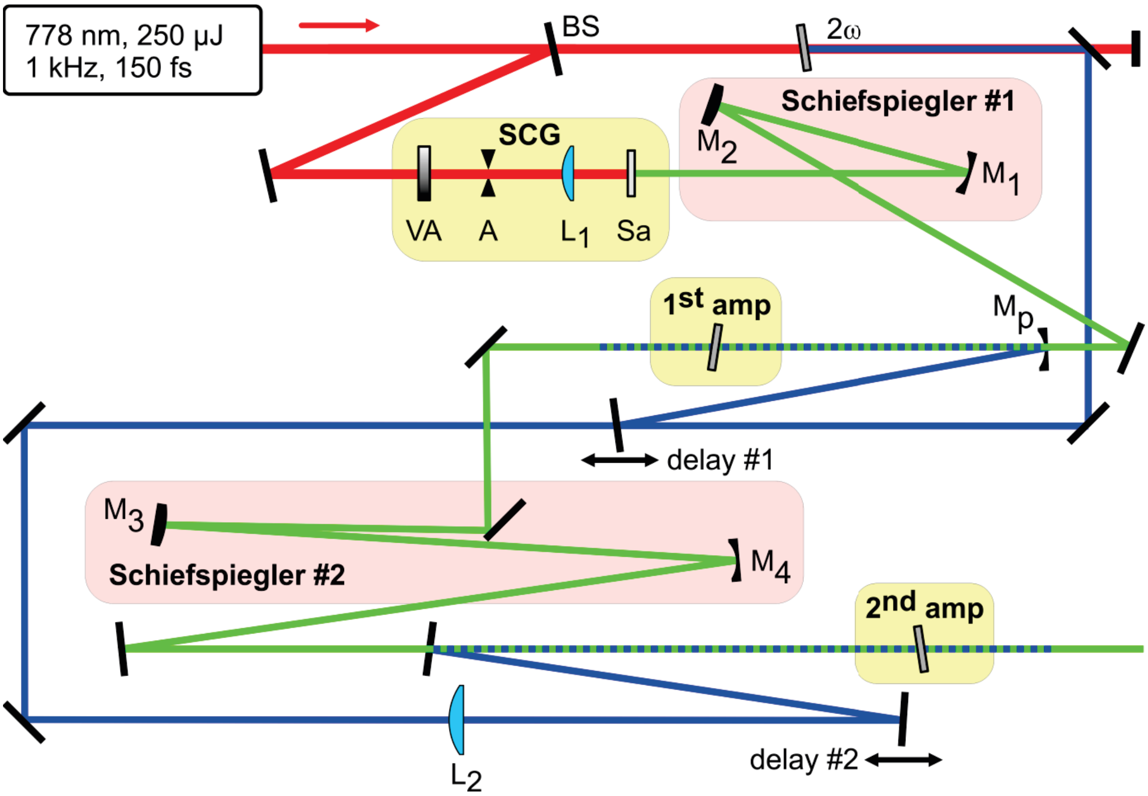

Fig. 4.5: Scheme for a two stage ultra-broadband noncollinear parametric amplifier.

- **BS**: beam splitter (AR on backside)
- **2ω**: 700 µm BBO, type I, $\theta = 30°$ for second harmonic generation
- **VA**: variable neutral density filter for optimizing SCG energy
- **A**: aperture, to slightly crop the fundamental beam before SCG
- **L$_1$**: $f = 50$ mm lens, AR coated for 800 nm
- **M$_1$, M$_2$**: Schiefspiegler telescope #1 with spherical silver mirrors ($R_{M1} = -150$ mm, $R_{M2} = +200$ mm)
- **M$_p$**: spherical focusing mirror for pump beam ($R_{cc} = -150$ mm)
- **delay#1**: beam splitter ($R = 15\%$ in s-polarization) on a mechanical translation stage, for splitting pump branches and optimization of temporal overlap in the pre-amplifier stage
- **1st amp**: pre-amplifier, 1 mm BBO, type I, $\theta = 32.5°$
- **M$_3$, M$_4$**: Schiefspiegler telescope #2 with spherical silver mirrors ($R_{M3} = +1000$ mm, $R_{M4} = -500$ mm)
- **delay #2**: HR mirror for pump beam on mechanical translation stage for optimization of temporal overlap in the main-amplifier stage
- **L$_2$**: plano-convex , fused silica lens, $f = 750$ mm lens
- **2nd amp**: main amplifier, 2 mm BBO, type I, $\theta = 32.5°$.

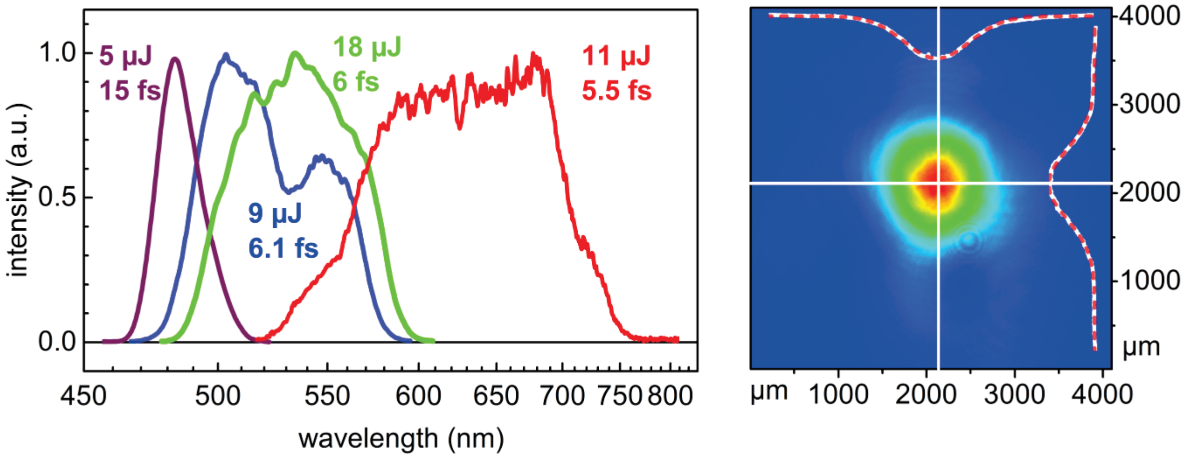

Fig. 4.6: Left: spectra of a two stage noncollinear optical parametric amplifier with un-chirped seed light with corresponding measured pulse energy and the calculated Fourier limit. Right: Typical beam profile of the two stage NOPA output. Cross sections are shown in white, the corresponding Gaussian fit in red, dotted lines.

Resulting spectra of the amplification for the given geometry with corresponding pulse energies and calculated Fourier limits are given in Fig. 4.6. It is shown that the spectral width of the single stage amplifier is maintained for the arrangement with pre-amplifier and main amplifier stage. Quantum efficiencies up to 45% are demonstrated with Fourier limits well below 10 fs. The slight chirp of the seed allows tunability of the system. So it is possible to amplify 480 nm pulses with a full width at half maximum of 20 nm, corresponding to 15 fs Fourier limit, quite easily. A beam profile of the output after the second amplifier stage is shown in the right panel of Fig. 4.6. The profile was measured with a commercial beam profiler (Photon Inc., USBeamPro). It is seen, that a proper alignment of the two Schiefspiegler telescopes renders a smooth and symmetric Gaussian beam profile after amplification. For comparison, a Gaussian fit is shown to the cross sections of the horizontal and vertical plane of the beam. After the second amplifier crystal, the amplified signal is collimated with a spherical silver mirror with radius of curvature of R_{cc} = -1000 mm under a small angle to avoid astigmatism – see Fig. 4.7. With a D-shaped mirror, the light is coupled into a Brewster-angled chirped mirror [Bau06] arrangement, to pre-compensate for third order dispersion. The number of reflections – and therefore the amount of third order dispersion compensation – is adjustable via the distance of the two mirrors. The quantity of mirror bounces is doubled by reflecting the light back into itself with an end mirror. After passing the chirped mirrors, the light is compressed with a fused silica prism compressor. The apex angle of the prisms is cut for Brewster angle transmission – 68.9°.

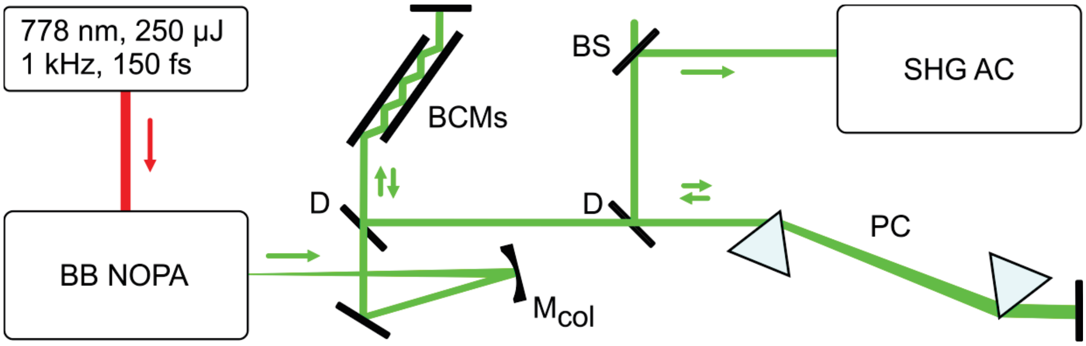

Fig. 4.7: Setup for compression of the broadband NOPA output with the combination of Brewster angled chirped mirrors (*BCMs*) and a fused silica prism compressor (*PC*), *D*: D-shaped mirror; M_{col}: spherical silver mirror, R_{cc} = -1000 mm; *BS*: beam splitter for attenuating the pulse energy without dispersion.

The pulse duration is characterized with the help of a second harmonic intensity autocorrelator [Koz04]. For a proper attenuation of the pulse energy a reflective beam splitter is used in front of the autocorrelator. The pulse energy used for autocorrelation is between 100 – 200 nJ. To offer sufficient phase-matching bandwidth, a 25 µm BBO, type I is used for second harmonic generation in the autocorrelator. The autocorrelation and the calculated Fourier limit of the pulse – shown in blue in Fig. 4.6 – is displayed in Fig. 4.8. The pulse duration is 6.7 fs with a Fourier limit of 6.1 fs. This corresponds to a time-bandwidth product of 0.46, assuming a Gaussian distribution. Here, 24 reflections on the chirped mirrors are used. The prism apex separation is 33 cm. The wings in the autocorrelation show up due to the spectral shape of the pulse and are also seen in the calculated curve. The amplitude of the wings is below 10% of the main peak.

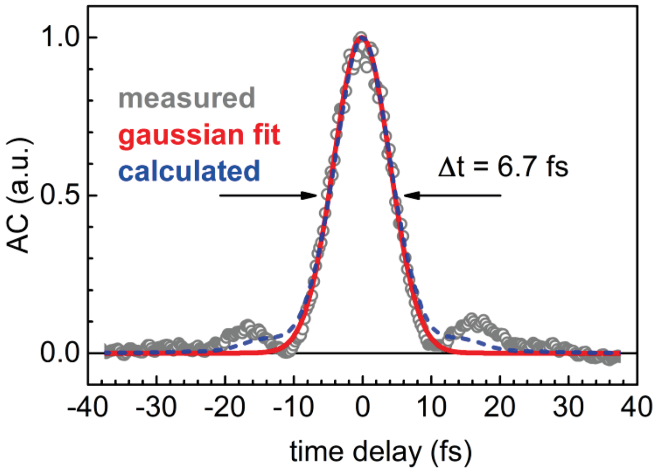

Fig. 4.8: SHG autocorrelation trace of a 6.7 fs pulse. The Gaussian fit is shown in red. The calculated Fourier limit is shown in blue.

In this chapter, a new method for amplification of sub-10 fs pulses was demonstrated. A nearly chirp free continuum is amplified with the second harmonic of a Ti:Sapphire laser at 1 kHz. In order to avoid additional chirp in the continuum, a Schiefspiegler telescope of two spherical mirrors is used for imaging.

Even with a second amplification stage the spectral width of the amplification is maintained. It is shown, that excellent beam profiles result after amplification due to the high imaging quality of the telescope. The compression of the pulses to below 10 fs, with the combination of Brewster angled chirped mirrors and a prism compressor, is demonstrated. The presented light source would be an interesting candidate for further experiments, like ultra-broadband sum-frequency mixing with NIR pulses to the range around 400 nm or achromatic phase-matching to the UV range.

Contrary to previous reports the presented setup provides higher pulse energies for pulses well below 10 fs. Unhandy pre-compensation of the seed pulse [Kob00, Bal02] is avoided.

Stretching the pump pulse for broadband amplification [Bal02, Bau06] leads to elongated output pulses and significantly increased higher order chirp in the prism compressor. With the presented method this behavior is avoided easily.

The subsequent chapter depicts how a thermal beam pointing of the pump laser system translates to a white light seeded noncollinear optical parametric amplifier. It is found that the Kerr lens inside the white light medium (also sapphire in this case) increases the input pointing by a factor of 10.

5. Dramatic Beam Steering by Kerr Lensing in Optical Parametric Amplifiers

Ti:sapphire or Ytterbium based femtosecond laser systems primarily generate pulses at 800 or 1030 nm. To generate fully tunable pulses over the full visible and NIR range, optical parametric amplifiers and in particular white light seeded noncollinear optical parametric amplifiers (NOPAs) are now widely used [Cer00, Rie00, Cer03, Kob00, Hom08, Lie14, Bra14]. For highest energy pulses this scheme is expanded to OPCPAs [Sta14]. Energy and beam pointing stability of parametric sources are very crucial regarding potential applications. Surprisingly, only few examples regarding pointing stability can be found in the literature [Kum15]. In this chapter it is investigated – to the best of my knowledge for the first time – how the beam pointing instability of a pump laser source translates to the output signal of a parametric amplifier. Since nowadays laser-companies specify the values for the beam pointing stability of state of the art laser systems only very loosely – values of just < 200 µrad are commonly given – the following experiment suggested itself.

A thermal beam pointing instability of a Ti:Sapphire amplifier (Clark MXR Inc., CPA2001) is simulated with a piezo driven mirror mount – PZM in Fig. 5.1 (Newport Corporation, AG-M100N). The steered beam is used to pump a noncollinear optical parametric amplifier. In this way it is possible to correlate the changes in the input angle $\Delta\theta_1$ and the resulting NOPA output signal angle $\Delta\theta_2$.

The angle change $\Delta\theta_1$ was monitored by introducing a plane parallel 160 µm FS window (BS 1) into the input beam and measuring the drift of the reflection on a commercial beam profiler (CCD) in a known distance. The transmitted beam with a pulse energy of roughly 200 µJ is used to pump the NOPA.

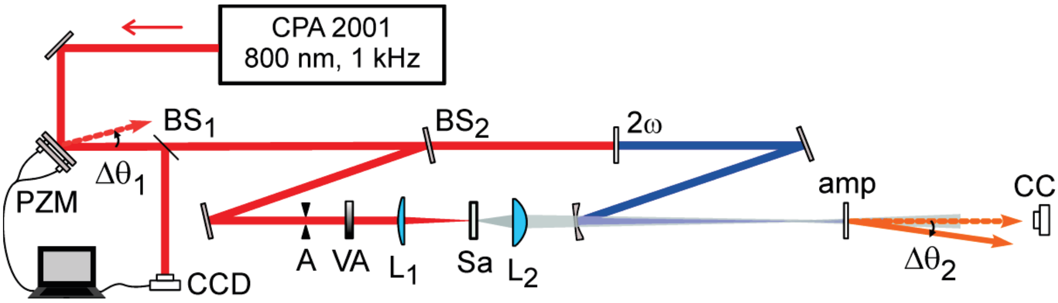

Fig. 5.1: Setup for measuring the correlation between deviations of the beam's input angle $\Delta\theta_1$ into a NOPA system and the resulting change of the amplified output signal $\Delta\theta_2$. For details, see text.

Initially the influence of the Kerr effect driven self-focusing and filamentation process inside the 3 mm sapphire plate (Sa) for seed pulse generation is determined. The angle change in the seed beam path is measured for the case of continuum generation in sapphire and referenced to the situation without the sapphire plate – Fig. 5.2. This is done by placing a beam profiler in two precisely determined distances after the re-focusing lens L_2 and reading off the relative drift on the camera array by software. To enlarge accuracy a bandpass filter with a FWHM of about 10 nm around 550 nm was placed in the white light beam path. For the measurement of the fundamental beam (without SCG) the energy was attenuated with a variable attenuator, which is usually used to optimize continuum generation, to not saturate the camera.

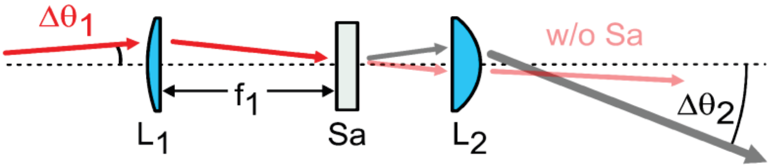

Fig. 5.2: Input beam angle variation $\Delta\theta_1$ with continuum generation (grey) and without sapphire plate (Sa) inserted (w/o Sa) and resulting angle $\Delta\theta_2$ in the seed beam path.

It can be seen from Fig. 5.3 that the filamentation process inside the sapphire plate boosts the angle change by a factor on the order of 10.

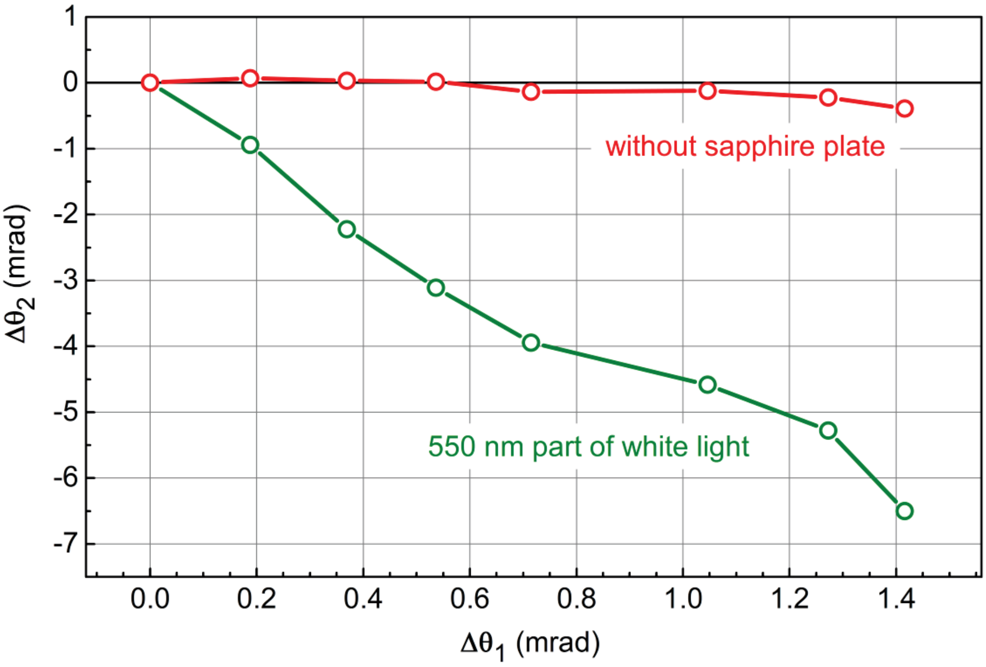

Fig. 5.3: Increase in output angle variation $\Delta\theta_2$ in seed beam path due to the influence of continuum generation.

Without sapphire plate the angle change is reduced by transmission through the telescope of L_1 and L_2. That means the angle after the telescope $\Delta\theta_2$ is smaller compared to the input angle $\Delta\theta_1$. Both cases will be verified with the help of ABCD matrix formalism. All used matrices follow the nomenclature of Ref. [Sie86].

For the case without sapphire plate the propagation through the telescope can be described with the well-known ABCD matrix M_f for a thin lens with focal length f and the propagation matrix M_d for a beam propagation of distance z.

$$\mathrm{M_d}(z) = \begin{pmatrix} 1 & z \\ 0 & 1 \end{pmatrix} \qquad \mathrm{M_f}(f) = \begin{pmatrix} 1 & 0 \\ -\frac{1}{f} & 1 \end{pmatrix}. \tag{5.1}$$

The total matrix M for the lens system is obtained by sequential multiplication of the matrices

$$\mathrm{M} = \mathrm{M_f}(f_2) \cdot \mathrm{M_d}(z) \cdot \mathrm{M_f}(f_1), \tag{5.2}$$

where the focal lengths of the two lenses are $f_1 = 80$ mm and $f_2 = 30$ mm. The distance z between the two lenses is roughly 113 mm. For the calculation of the resulting angle change a vector $\vec{r}$ is needed, it is given by

$$\vec{r} = \begin{pmatrix} \Delta x \\ \Delta\theta \end{pmatrix}, \tag{5.3}$$

where Δx is the spatial offset from the center on first the lens and $\Delta\theta$ is the angle of the incoming beam – see Fig. 5.2. By multiplying the vector with the initial values in front of the telescope to the total matrix given in Eq. (5.2), the resulting values of angle and offset for propagation after the telescope are obtained.

$$\begin{pmatrix} \Delta x_2 \\ \Delta\theta_2 \end{pmatrix} = \mathrm{M} \cdot \begin{pmatrix} \Delta x_1 \\ \Delta\theta_1 \end{pmatrix}. \tag{5.4}$$

The result of the input angle dependent calculation is shown in Fig. 5.5. It is compared to the situation with inserted sapphire plate. Therefore in the next section it is briefly described how this situation will be calculated including nonlinear effects in the white light crystal.

5.1 Simulation of the Kerr lens in the white light crystal

In order to simulate the effect of the Kerr-lens inside the SCG crystal on the beam propagation, only self-focusing inside the sapphire plate is taken into account. For simplicity other filamentation processes are neglected at this point. This allows the use of an ABCD matrix describing a Kerr lens. This matrix is called "duct" matrix and is suitable for materials with radially varying index of refraction – e.g. introduced by a Kerr lens [Sie86]. In the literature the matrix is quite common for resonator analysis and ray tracing including Kerr lensing [Pen96, Gra00, Ras13]. In this work the concept is applied to continuum generation and optical parametric amplifiers. The matrix reads:

$$M_{\mathrm{duct}} = \begin{pmatrix} \cos(\gamma \cdot d) & \frac{1}{n' \cdot \gamma} \cdot \sin(\gamma \cdot d) \\ -n' \cdot \gamma \cdot \sin(\gamma \cdot d) & \cos(\gamma \cdot d) \end{pmatrix}, \tag{5.5}$$

with the refractive index

$$n' = n_0 + n_2 \cdot \frac{2P}{\pi w^2}. \tag{5.6}$$

The factor γ is introduced for convenience and is given by the relation

$$\gamma = \frac{1}{w^2} \cdot \sqrt{\frac{8 \cdot n_2 \cdot P}{\pi \cdot n'}}, \tag{5.7}$$

where P is the radiation power, d the length of the nonlinear medium, w corresponds to the $1/e^2$ radius of the spatial beam profile; n_0 and n_2 are the linear and nonlinear refractive indices of the medium.

For a 3 mm sapphire crystal a self-focusing distance can be found numerically to be 0.7 mm, with a refractive index of $n = 1.76$ at 778 nm, a nonlinear refractive index of $2.8 \cdot 10^{-16}$ m^2/W and an intensity of about 1000 GW/cm^2, assuming a temporal pulse width of 150 fs, pulse energy of $E = 1$ µJ and a width of $w = 20$ µm on the entrance surface.

With the matrices M_d for propagation and M_f for a thin lens, a total matrix of the system M_{SCG} can be formulated.

$$M_{SCG} = M_f(f_2) \cdot M_d(z_2) \cdot M_{\mathrm{duct}}(d, P, w) \cdot M_d(z_1) \cdot M_f(f_1), \tag{5.8}$$

where z_1 ($\approx$ 780 mm) and z_2 ($\approx$ 31 mm) are the distances of lens 1 and 2 to the sapphire plate. The comparison between the measurement and the matrix simulations on the angle deviation is given in Fig. 5.5. The angle change is calculated according to Eq. (5.4).

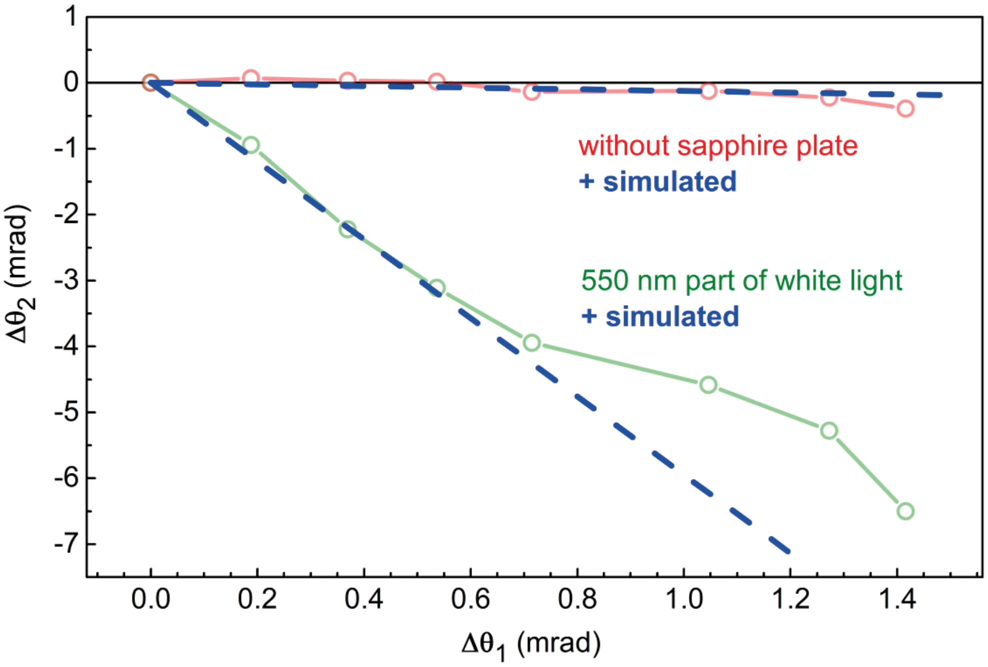

Fig. 5.5: Measurement of the beam deviation for the case of continuum generation (green) and without sapphire plate (red) and theoretical calculations for both cases (blue, dashed lines).

For the case without sapphire plate in the beam path, the calculation and the measurement match well over the entire range of input angle change $\Delta\theta_1$ up to 1.4 mrad – this is the value before continuum generation breaks down. The calculation for the case of continuum generation reproduces the measurements well up to a value of approximately $\Delta\theta_1 = 0.7$ mrad. It is assumed, that above this value the – highly sensitive – generation process of continuum generation is distorted too much for this simplified model. Nevertheless, the trend and the magnitude of the effect is clearly reproduced by applying the "duct" matrix to the system.

The matrix of Eq. (5.5) is highly dependent on the pulse energy. The dependence of the continuum generation energy on the simulation is shown in Fig. 5.6 compared to the measurement.

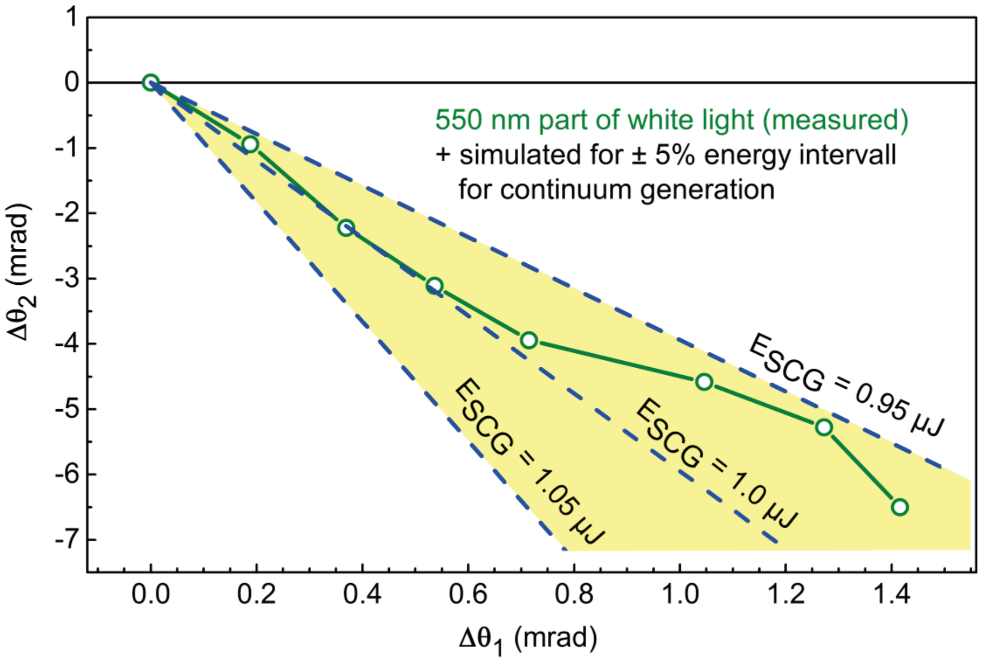

Fig. 5.6: Energy dependence in the simulation of the driving pulses for continuum generation.

An energy variation of ± 5% of the driving pulses is used for calculation. With decreasing energy *E* the magnitude of the resulting angle $\Delta\theta_2$ is reduced – see Fig. 5.6. This could be explained by the increasing filament length with higher energy of the driving pulses [Bra14b].

It has to be noted that the modeling is only of semi-quantitative nature, even if it describes the measurements very accurately. Here the filamentation process is neglected where high nonlinearities enter in combination to spectrally broaden the Ti:Sapphire pulse to a continuum.

5.2 Influence of pump laser beam pointing on the NOPA output energy

In the next part is discussed how the input angle change and the resulting Kerr lens driven boost of this angle in the seed beam will translate to the amplified NOPA signal. For observing the effect of input angle deviation on amplified NOPA output pulses, a single NOPA stage is used – see Fig. 5.1. The incoming light is frequency doubled in a 700 µm BBO to 389 nm with an efficiency of 30% to amplify the seed light in a 1 mm BBO crystal cut at 32.5°. The blue pump beam energy is roughly 20 µJ and is focused with a spherical concave mirror (R = -300 mm) in front of the amplifier crystal. The beam waist on the crystal is approximately 200 µm corresponding to a peak intensity of 200 GW/cm^2. The imaging of the continuum is optimized by moving the re-focusing lens L_2 in beam direction and monitoring the amplified output energy and the shape of the resulting beam profile. The focal plane of the continuum is also located in front of the amplifier crystal. Working with the focal planes of pump and seed in front of the amplifier crystal was empirically found to work best since the early years of NOPA development. In this chapter the physical reason for the empirical approach is described and is found to be reasonable for compensating the nonlinear bending of wave fronts due to Kerr lensing.

Initially, it is monitored how the output signal energy of the NOPA pulses decreases with an input angle change of the fundamental beam – see Fig. 5.7.

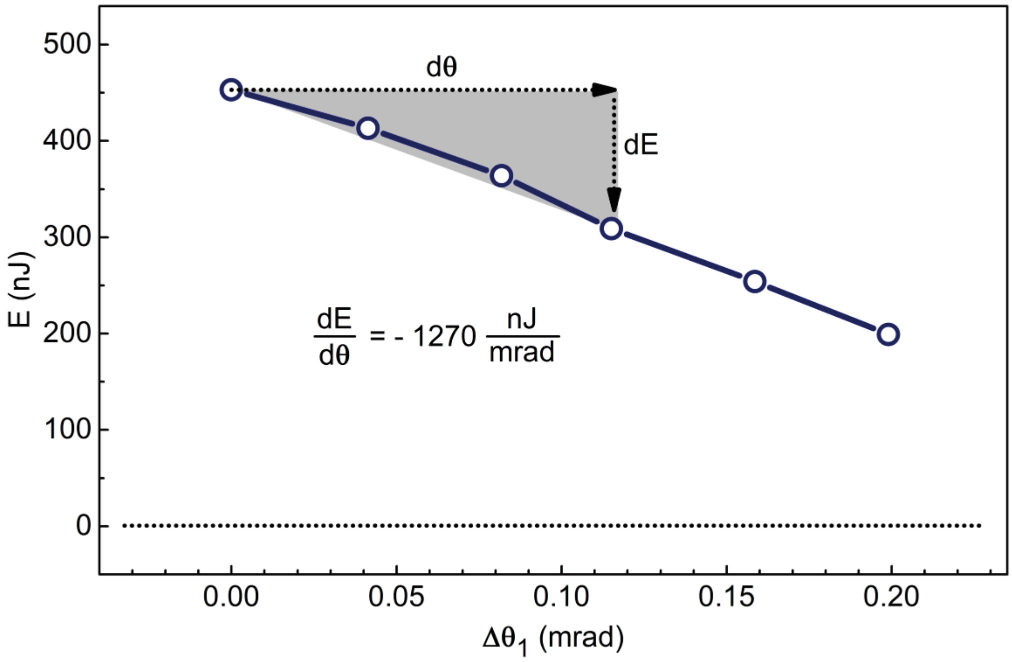

Fig. 5.7: NOPA input angle variation and resulting decrease in output energy of the amplified pulses. Values see text.

The NOPA signal was tuned to a center wavelength of 590 nm, with an initial energy of 450 nJ. The spectral width of the output corresponds to a Fourier limit of 11 fs. The fundamental input beam was steered by the piezo controlled mirror mount and the beam deviation was referenced by a beam profiler. The resulting output energy was monitored by a sensitive thermal power meter head (Coherent Inc., PS10Q) and averaged over approximately 5000 laser shots for each piezo step. The amplification of the NOPA breaks down for angle changes greater than 200 µrad, for smaller changes there is a linear decrease with

$$\frac{dE}{d\theta} = -1270 \frac{nJ}{mrad}. \tag{5.9}$$

This value allows estimating a pointing induced noise of an amplifier output. Assuming a quite realistic beam pointing stability of a laser system with $\Delta\theta = \pm 20$ µrad this can be directly translated into a noise level.

$$\Delta E = \frac{dE}{d\theta} \cdot \Delta\theta = 1270 \frac{nJ}{mrad} \cdot 20\,\mu rad = 25.4\,nJ. \tag{5.10}$$

For the single NOPA stage centered at 590 nm with an energy of E = 450 nJ this corresponds to a noise level of 5%.

$$\frac{\Delta E}{E} \approx 5\,\%. \tag{5.11}$$

With a beam pointing stability of $\Delta\theta = \pm 200$ µrad or even greater, the output of the amplification would fluctuate catastrophically between "on" and "off".

5.3 Kerr lensing in the amplifier crystal – change of the pointing direction

Subsequently, the effect of the introduced beam pointing of the output signal is demonstrated. At first glance, the spatial beam pointing conversion between input and output angle change might look quite surprising. The pointing direction of the seed beam changes after amplification – see Fig. 5.8. It is recommended to the reader to watch a short video clip of this phenomenon, by following this link: http://www.nopa-agriedle.info/KLD.html

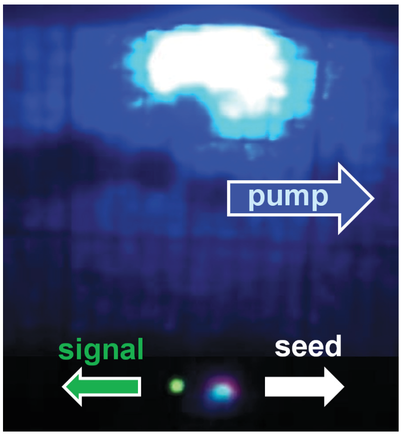

Fig. 5.8: Pump and Signal going to the same direction with input beam angle change, while amplified signal goes to the opposite direction.

As the input angle changes by $\Delta\theta_1$, the change of the pump beam at the locus of amplification at the amplifier crystal is changed also by $\Delta\theta_1$. But, as mentioned previously, the angle change for the seed beam is magnified, due to the Kerr effect inside the Sapphire plate, by roughly $10\cdot\Delta\theta_1$.

The amplified NOPA output changes direction and the magnitude of the angle increases by a factor of 3. This is shown in Fig. 5.9. It shows a quantitative measurement of the involved angle changes as well as the change of sign of the direction for the seed beam (black) and the amplified NOPA signal (orange).

The observed effect is understandable by considering the Kerr effect inside the amplifier crystal. In this case a "cross Kerr effect" must be responsible for the angle deviation of the amplified signal. In the well-known process of cross-phase modulation a strong pump beam modifies a weaker signal at temporal and spatial overlap. Less known is that the Kerr effect can also lead to a cross-lensing effect for a beam introduced by a second beam. The refractive index of the medium gets modified on the pump axis due to the Kerr effect. Thus the weak seed beam inside the NOPA can get influenced by the Kerr lens introduced by the pump. Generally all phase distortions of the pump beam are transferred to the signal and the idler [Wei08]. An easy experiment to prove this is to spatially narrow the pump beam with an aperture in a way that interference fringes are observable in the beam profile. After amplification these fringes will also be visible in the NOPA output signal.

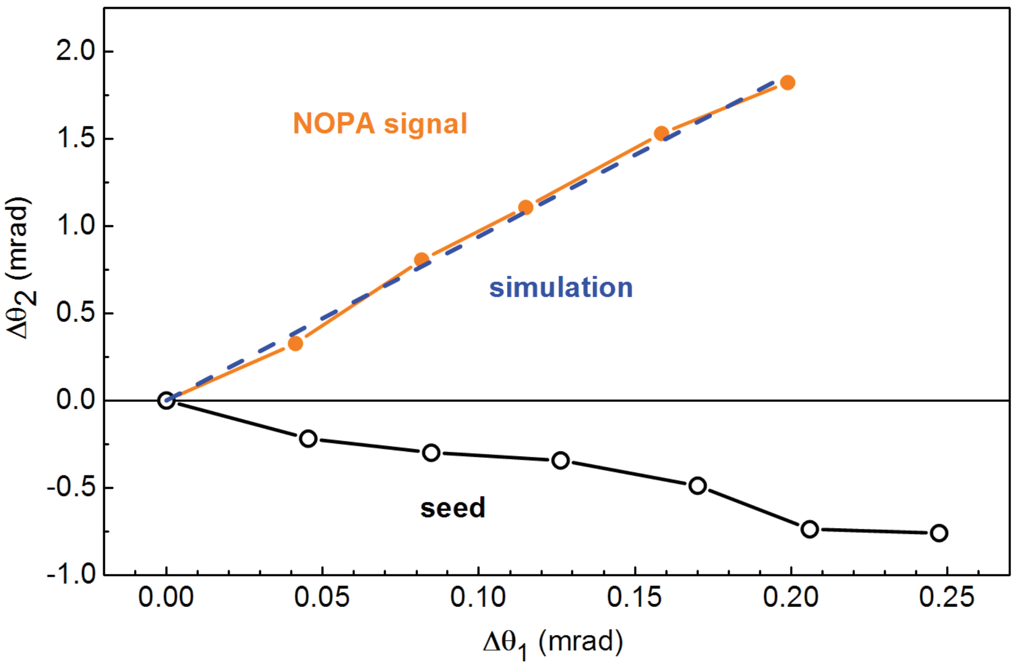

Fig. 5.9: Input beam angle change $\Delta\theta_1$ as well as angle change $\Delta\theta_2$ of the seed beam (black) and the amplified NOPA signal (orange) with different sign and magnitude. The blue dotted line is calculated via the "duct" matrix method.

The effect of cross Kerr lensing in the parametric amplifier is readily understood in a simplified picture by a mixture of nonlinear and geometric optics – see Fig. 5.10. As shown previously, the angle of the seed beam path drastically increases due to the Kerr lensing effect inside the sapphire plate. For the sake of convenience it is assumed for the moment that only the seed beam path angle is changed while the pump beam direction stays constant. If now the pump beam with a Gaussian intensity profile enters the amplifier medium it will experience a self-focusing effect due to Kerr lensing. In Fig. 5.10 a) the nonlinear effect is – very simplified – denoted as a focusing lens inside the medium. If the seed beam hits this "lens" centrally at temporal and spatial overlap, the signal gets amplified and its direction is not influenced by the refractive index change introduced by the pump. Signal and residual seed are propagating on top of each other. An angle change of the seed beam path with a constant position of the Kerr lens leads to the case that the "lens" will be hit off axis by the seed beam – see Fig. 5.10 b). Consequently the amplified signal gets redirected to the other side of the pump axis. It gets deflected to the opposite direction of the induced angle change $\Delta\theta_1$.

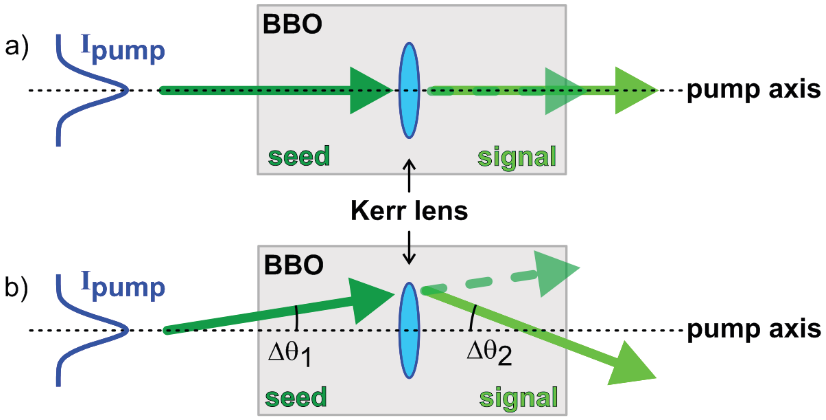

Fig. 5.10: Scheme to explain cross Kerr lens driven signal angle deviation. (a) Seed hits a pump induced Kerr lens centrally. (b) Seed hits pump induced Kerr lens off-axis and frequencies with temporal overlap get deflected (signal) while residual seed without temporal overlap propagates unaltered.

A second "duct" matrix is added to Eq. (5.8) to simulate a second Kerr lens in the amplifier. The matrix for the whole seed beam path inside the NOPA reads:

$$\begin{aligned} M_{seed} = \; & M_{duct\,BBO}(d,P,w) \cdot M_d(z_3) \cdot \\ & \cdot M_f(f_2) \cdot M_d(z_2) \cdot M_{duct\,SCG}(d,P,w) \cdot M_d(z_1) \cdot M_f(f_1) \end{aligned} \tag{5.12}$$

For the calculation of the Kerr lens matrix $M_{duct\ BBO}$ it has to be noted that the parameters of the pump are chosen because the effect is generated by the pump beam. A pump beam width $w = 157$ µm, an energy $E = 15$ µJ and a pulse duration of $\Delta t = 130$ fs is used for calculation. The distance from lens L_2 to the crystal is roughly $z_3 = 270$ mm. The resulting calculated angle deviation for the NOPA signal after a second Kerr lens inside the amplifier BBO is given for the matrix system of Eq. (5.12) in Fig. 5.9. It exactly reproduces the observed behavior.

According to the scheme of Fig. 5.10, only the wavelengths of the chirped white light that overlap temporal with the pump pulse are amplified and deflected. The residual, unamplified, white light is propagating disjunct from the amplified signal since there is no cross lensing effect without temporal overlap. Hence, for the disjunct case, the residual white light seed should not contain the amplified signal wavelengths after the amplifier BBO. This is proven for a 515 nm pumped NOPA system, where the disjunct propagation was adjusted consciously to observe the spectral distribution of the residual seed with a fiber-coupled spectrometer. In Fig. 5.11 it can be seen that the amplified wavelengths (red peak) are missing in the residual seed (black line) compared to the seed without the pump (grey line).

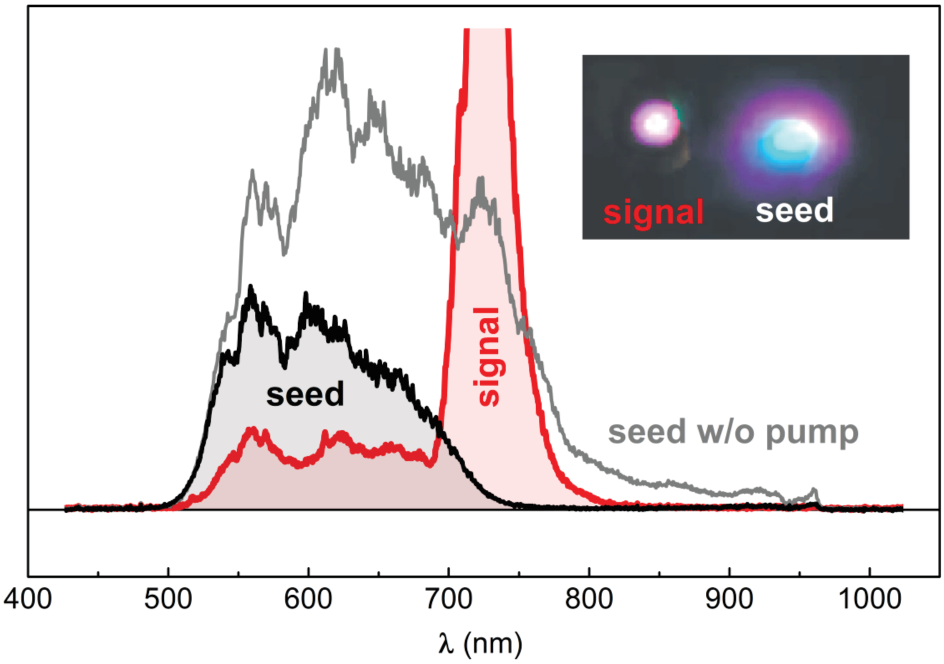

Fig. 5.11: Uncalibrated spectral distributions for the white light seed without the pump pulse (grey line), the residual white light seed (black line, right spot in inset picture) and the amplified signal (red line, left spot in inset picture)[1].

The resulting beam direction after tilting a steering mirror is always a combination of a parallel offset and an angle change, because mostly the mirror is not tilted around its center. Consequently, the influence of a parallel offset of the beam steered to the NOPA system was also measured. It was simulated by placing a plane parallel, 8 mm thick, fused silica plate perpendicular to the fundamental beam in front of the NOPA setup. By tilting the window along the horizontal axis, a **parallel offset** could be introduced. Like in the case of an angle deviation of the incoming light – Fig. 5.1 – the offset was monitored by a CCD in front of the setup. Interestingly, it turns out, that compared to the angle change, the parallel offset has nearly no impact on the performance. Below a value of 1.3 mm offset nothing drastic could be measured in the performance of the system. For higher offset levels continuum generation gets modified. At a level of 1.9 mm the white light becomes instable and ceases at a level of 2.3 mm. Since there is no angle change in the beam path, also the change in direction of seed and signal is not observable. Remarkably, the NOPA output energy also is quite stable up to the level of 1.9 mm parallel offset.

---

[1] Spectra measured by Dr. Victor Lisinetskii at the *University of Würzburg* with the setup presented in the subsequent chapter 6.

The effect of amplified signal and seed that are not propagating collinearly after amplification has been observed many times before in the group and even was found to be beneficial for background suppression in detection when seeding a NOPA with continuous laser light sources [Hom13]. In this thesis this phenomenon is now evaluated experimentally and is explained theoretically with the effect of cross Kerr lensing between pump and seed in the amplification process. Few examples can be found in the literature where this effect is also described. It is, however, used in a transient spectrometer for temporal characterization of broadband pulses or the measurement of time resolved third order nonlinear responses of molecular samples [Fer13, Li14, Rei14].

5.4 Direct visualization and quantification of the pump induced Kerr lens

The Kerr lens of the pump acting on the signal in the NOPA crystal can be directly visualized with the divergence of the amplified signal. Lower intensity leads to weaker self-lensing. Hence, a change in signal divergence is expected with respect to the pump energy. Therefore a λ/2 plate is placed in front of the second harmonic generation crystal in order to attenuate the second harmonic pump beam. At two different positions behind the amplifier crystal the beam profile width of the amplified signal is detected with a beam profiler, while the pump energy is monitored with a thermal power meter. The divergence of the signal results from the ratio of beam widths and the distances to the beam profiler. Fig. 5.12 shows how the signal divergence drops with increasing pump energy. This effect of changing signal divergence is also observable by bare eye – a change of the spot size of the signal can be seen on a white business card right after the amplifier crystal by simultaneously varying the pump energy.

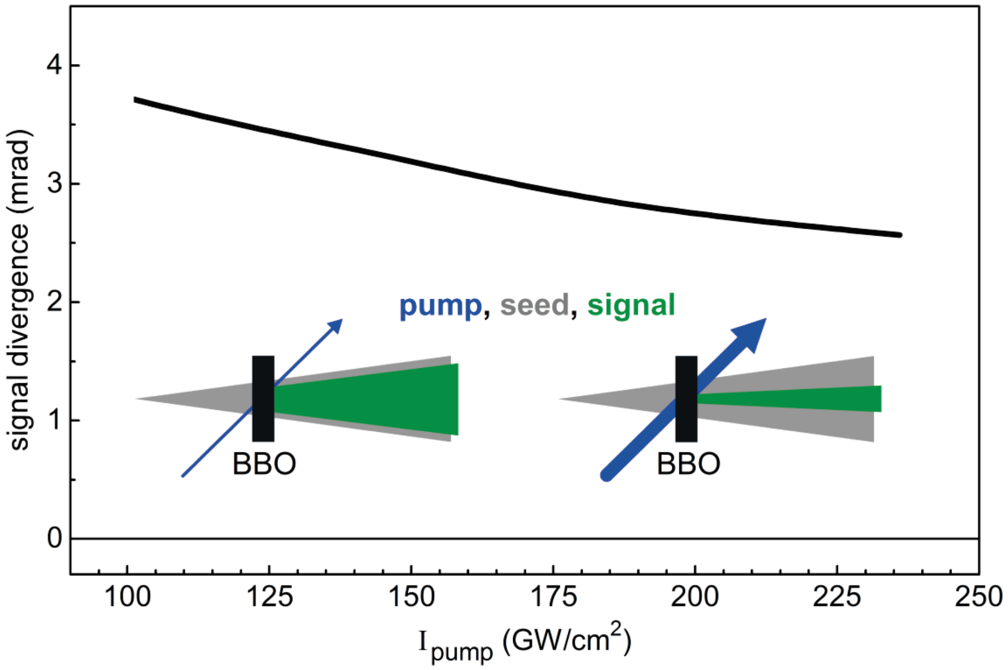

Fig. 5.12: Pump energy dependence on the measured divergence of the amplified signal after a 2 mm BBO amplifier crystal.

To quantify nonlinearities in transparent media, the B-Integral is frequently used.

$$B = \frac{2\pi}{\lambda} \cdot \int n_2 \cdot I(t,z)\, dz\,. \tag{5.13}$$

The B-Integral gives a value for the accumulated nonlinear phase shift of a beam on the optical axis due to the Kerr effect (compare chapter 2.1). Therefore, a high value for B corresponds to strong self-focusing. A value larger than 3 is attributed to the case where self-focusing is likely to occur [Wei09].

In the design of chirped-pulse amplifiers even a relatively low value of 1 or 2 is known to distort the performance and compressibility of the system [Chu93, Per94]. Here B-Integral values for a NOPA of our own design are estimated.

Intensities between 150 and 200 GW/cm² are common to pump a NOPA crystal [Cer03]. The intensity is needed to amplify the nJ level seed light to about 10 µJ output energy. The seed light energy level is estimated according to Ref. [Bra09] for a 4 mm YAG crystal by roughly 10 pJ/nm. Assuming, for simplicity, a spectral window of 50 nm of the chirped seed continuum overlapping in time with the pump pulse this gives 0.5 nJ seed pulse energy, approximately. To obtain the output energy after amplification the coupled differential equations (see chapter 2.2) are solved by summing over small slices over the crystal. The used calculation can be found in appendix A5.

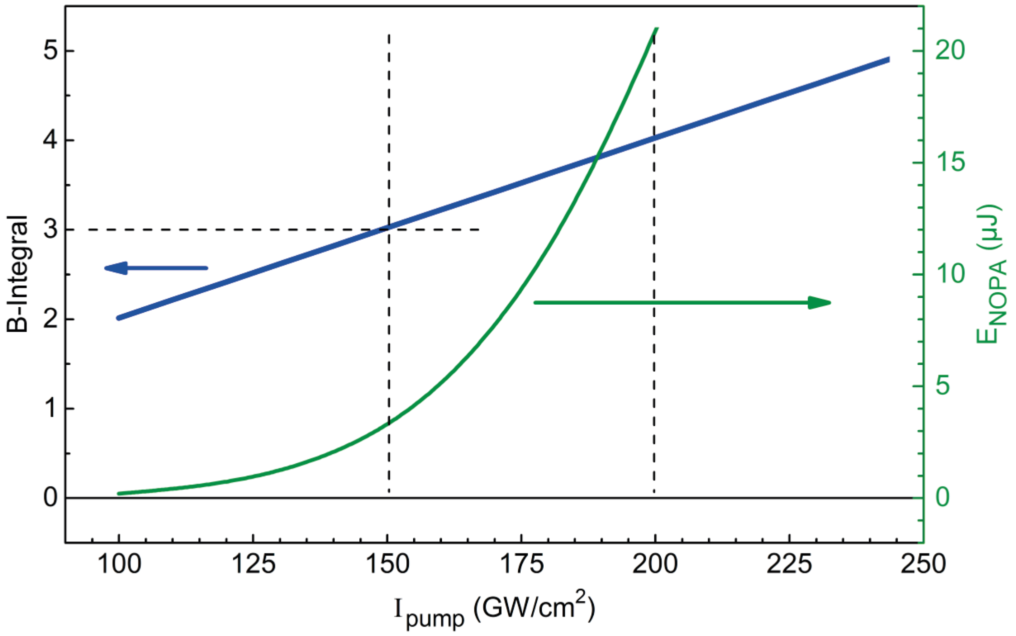

Fig. 5.13: B-Integral for a 2 mm amplifier BBO crystal pumped with 400 nm (blue line) versus pump intensity. Corresponding theoretical NOPA output energy calculated with the G-factor (green line).

From Fig. 5.13 it can be seen that in the pump intensity range of 150 – 200 GW/cm^2 (marked area) NOPA output energies of 4 – 20 µJ result theoretically. The calculation is done for a pump wavelength of 400 nm, a 2 mm amplifier BBO cut at 32.5° and a central wavelength of 550 nm. The corresponding B-Integral after the NOPA crystal in that range of pump intensities is intrinsically larger than 3.

Other crystals have very similar conditions. Basically, it would be ideal to use a crystal with a very large nonlinearity d_{eff} - less intensity would be needed for the same gain. Thus, it would be possible to amplify to the same output energy level with lower B-Integral, leading to smaller undesired nonlinearities like self-focusing. Unfortunately, such a crystal does not exist. TABLE V lists a few common crystals which fulfill the phase matching condition for the amplification of 550 nm light with a 400 nm pump pulse. These crystals are shown for comparison to BBO. They do not solve the problem, since either their nonlinearity d_{eff} is lower or the acceptance bandwidth is to narrow. The lower d_{eff} leads to higher needed pump intensities and therefore worsens the situation of self-focusing. A lower acceptance bandwidth leads to narrow output spectra - no ultrashort pulses can be obtained.

Bismuth triborate (BiBO) has a higher coefficient d_{eff} than BBO, but the acceptance bandwidth is much narrower compared to BBO. Potassium dihydrogen phosphate (KDP) has a much broader acceptance bandwidth compared to BBO, but its nonlinear coefficient is smaller by a factor of 7. Since the exponent of the gain G increases squared with d_{eff} in Eq. (2.17) of chapter 2.2, the intensity has to be increased roughly by a factor of 50 to get to the same value of G as for BBO. This will also lead to a factor of 50 higher B-Integral for amplification in KDP since the values for the nonlinear refractive index n_2 are quite similar.

Consequently, for amplifying in the visible range, with UV pump pulses, BBO is still the material of choice.

TABLE V: d_{eff} and acceptance bandwidth for various crystals for amplifying a 550 nm signal with 400 nm pump pulses.

	d_{eff} (pm/V) [SNLO]	OPO acceptance bandwidth (cm$^{-1}\cdot$ cm) [SNLO]	n_2 (10^{-16} cm^2/W)
BBO	2.06	21.26	6.5 [Bac13]
BiBO	2.6	9.19	7.4 [Mil08]
KDP	0.292	141.55	5.9 [Kur96]
LBO	0.805	38.34	2.6 [Li01]

5.5 Ray tracing of the amplified signal with pump induced Kerr lensing

Since the Kerr lens is introduced by the pump pulse, the full crystal length contributes to the B-Integral and the self-focusing effect of the pump. For a fixed crystal length of 2 mm and a signal wavelength around 700 nm, the signal will experience a much weaker self-focusing because the effective length of the pump induced Kerr lens is limited by the finite temporal overlap between pump and signal inside the crystal. The group velocity mismatch of the signal and the pump wavelength decreases the effective crystal length because the parametric interaction stops once the pulses are temporally separated. For 400 nm pump pulses the group velocity mismatch (GVM) is zero for pulses near 490 nm and increases to 150 fs/mm for 700 nm for a noncollinearity angle of 3.7° [Pie06].

In Fig. 5.14 this situation is demonstrated qualitatively for a 700 nm seed wavelength out of the continuum. The continuum is generated at position 0 mm and is relay imaged with a *f* = 30 mm lens towards the BBO crystal. The 400 nm pump is focused with *f* = 250 mm at a positon of 930 mm. In the upper panel the situation for a pump intensity of 250 GW/cm^2 is illustrated. It results in a sharp focus of the pump beam right behind the BBO crystal. The lower effective crystal length due to the GVM of pump and seed, 1 mm approximately, leads to a smooth and weaker self-focusing of the seed beam after amplification.

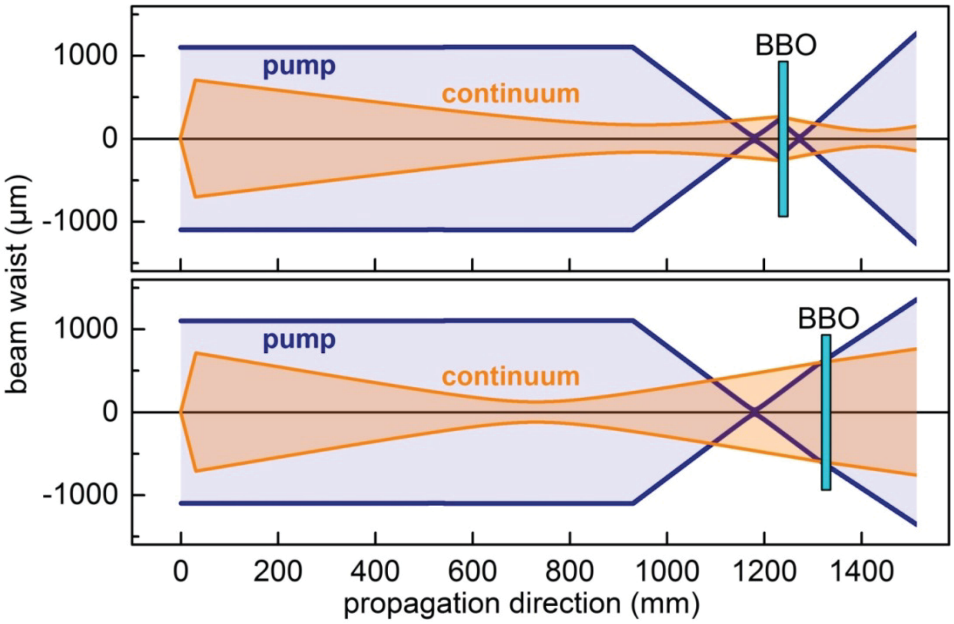

Fig. 5.14: Simulation of 400 nm pump and 700 nm seed propagation, for high (upper panel) and low (lower panel) pump intensity.

The pump intensity can be reduced by shifting the BBO further away from the focal plane of the beam. For the case of lower intensity (lower panel in Fig. 5.14) with 50 GW/cm^2 the effect of self-lensing ceases. Of course this drop in pump intensity will drastically reduce the gain. For the given intensities this relates to a diminution of the gain from roughly $1 \cdot 10^5$ to 150. In other words, the optimum lies in-between. This should motivate to not pump the amplifier too hard. If for an experiment low energy is needed only – let's assume 100 nJ at 1 kHz – it makes no sense to go for 15 µJ energy of the NOPA output. The nonlinearity inside the amplifier crystal strongly modulates the wave-front of the pump beam acting on the signal. This space time coupling will strongly show up as parasitic effect in the next non-linear interaction downstream in the experiment, like second harmonic generation. With lower intensities the undesired nonlinearities can be reduced - an improved spatial beam quality results.

This simulation also illustrates why it is reasonable to work behind the focal planes of both, the pump and the seed beam. Not only because in front of the focus spherical aberration is present [Bow08b], but also the orientation of curvature of the wave-front would reinforce the Kerr lensing. Behind the focal plane the curvature of the wave fronts helps to keep self-lensing effects smaller.

These new aspects regarding the Kerr-lens induced distortions are also a new motivation for the already well-established concept of Ref. [Rie00] for the use of a pre-amplifier, especially for 1 kHz, high energy NOPAs. The pre-amplifier should be operated such that only 1 – 5% of the desired final output energy is amplified. In the second amplification stage this pre-amplified signal can then be amplified to the final output energy with a lower intensity and hence a lower B-Integral compared to directly amplify the lower nJ level seed photons. A high amplification in both (or even more) stages will lead to different curvatures of the wave fronts, making the resulting pulses hard to compress.

In this chapter it was shown how beam pointing instabilities of a pump laser system translates to the output of a parametric amplifier. A thermal beam pointing drift was simulated with a piezo driven mirror mount on the order of 100 µrad. It was shown experimentally that the pointing of the pump laser is increased in the amplifier. The behavior is attributed to Kerr lensing inside the system. In the white light crystal the needed high intensity for filamentation is mainly achieved by self-focusing. Here, the Kerr lens inside the continuum generation crystal increases the pointing of the seed beam path dramatically. Afterwards, there is a subsequent Kerr-lens in the amplification medium introduced by the pump pulse. By comparing the Gain factor and the B-Integral at needed pump intensities for output energies on the order of 10 µJ, it was demonstrated that Kerr-lensing is intrinsic in the amplification process of the given parameters. Since the Kerr lens inside the continuum generation crystal increases the magnitude of the pointing instability drastically – roughly by a factor of 10, the angle changes differently for pump and seed beam path. Both beam paths have the same number of reflections on mirrors (compare Fig. 5.1), so the pointing at the amplifier crystal is symmetric – pump and seed deviate in the same direction but with different magnitudes of angle deviation. Consequently, the part of the seed beam, temporally overlapping with the pump pulse, hits the Kerr lens – introduced by the pump inside the amplifier crystal – off center. Hence this part gets amplified and deflected to the opposite direction, while the parts without temporal overlap do not interact with the pump Kerr lens and propagate unaffectedly (see Fig. 5.10). This explains the well-known observation of noncollinearly propagating seed and signal beams.

The Kerr lens – introduced by the pump, acting on the seed - inside the amplifier medium is also directly visualized by varying the pump intensity and measuring the change in signal divergence after amplification (Fig. 5.12).

By introducing the "duct" matrix (Eq. 5.5) a Kerr lens can be simulated and the above described observations are explained by ABCD matrix ray tracing with very high accuracy.

The Kerr focusing of both the pump and the signal may lead to strongly different radii of their wave fronts that will eventually lead to a beam breakup of the amplified signal for experimentally used beams. The acquisition of nonlinear phase and beam distortion will strongly show up in the next nonlinear interaction downstream, particularly in multi-stage OPCPA designs [Skr12].

Even though very moderate pulse energies are needed for many experiments (on the order of 100 nJ or even less for excitation pulses in spectroscopic experiments), users are frequently tending towards a NOPA alignment for high energy output pulses above 10 µJ. No doubt it might often be needed, but if not, intensities on the amplifier crystals should be reduced by just moving them further away from the pump focus. Accumulating less nonlinear phase shift during amplification will help for a better beam profile and compressibility of the pulses – two major parameters for any kind of experiment.

In addition, the experiments shown in this chapter demonstrate that for the operation of an optical parametric amplifier the pointing stability of the pump laser system is of major importance. It has been analyzed that an angle variation of the laser source is magnified by propagating through a Kerr lens. As mentioned previously, the seed and the pump beam path experience different magnitudes of angle variation, due to the Kerr lensing effect in continuum generation. It is obvious, that this also affects the spatial overlap in the amplification crystal and the output energy after amplification ceases. In Fig. 5.7 the angle variation of the pump laser is related to the decrease of signal energy. This gives an estimation value for the noise of the amplifier due to beam pointing. Which, in the case for the given geometry, is ±5% for an angle variation of ± 20 µrad. So a laser source with high pointing stability should be chosen for the best performance or a stabilization system could be implemented.

6. Yb-fiber laser based, two-color noncollinear optical parametric amplifier optimized for long term stability at 1 MHz

Spectroscopic pump probe experiments of ultrafast processes require shortest tunable laser pulses. The pump pulse is conveniently generated with a parametric amplifier to enable a large tunable frequency range. The probe pulse can be a supercontinuum [Meg09] or a second pulse of a tunable source [Sch08a]. In this chapter a NOPA source is presented that uses the second and the third harmonic of an Yb-fiber laser source to amplify a portion out of two continua generated by the fundamental and the second harmonic (see schematic in Fig. 6.1), respectively.

The arrangement gives two independently tunable output pulses. The UV pumped branch is tunable from 400 to 900 nm. The green pumped branch is tunable from 630 to 950 nm. A sub-10 fs pulse is demonstrated. Similar setups have already been shown [Sch08b, Hom08, Bra14, Lie14, Nil14]. Here, the main focus is on the issues that come along with high repetition rates, like two-photon induced heating of the BBO crystals by the third harmonic around 343 nm.

The used Yb-fiber laser system for optical parametric amplification is a 35 W *Tangerine* by *Amplitude Systems*. The central wavelength is roughly 1030 nm, with a spectral width of 6.7 nm, corresponding to 233 fs Fourier limit. The beam size is 1.7 mm (FWHM). The repetition rate of the system can be chosen via a PC program from single shot to 2 MHz. For most experiments in this chapter 200 kHz or 1 MHz are used. Independent of the repetition rate, 20 µJ pulse energy is used to pump the system. In principle, the PC interface allows modifying the output power, but it was found that by using the function called "efficiency" the fundamental spot size changes. Hence an external combination of a half-wave plate and a polarizer is used for adjustment of the pulse energy in front of the NOPA.

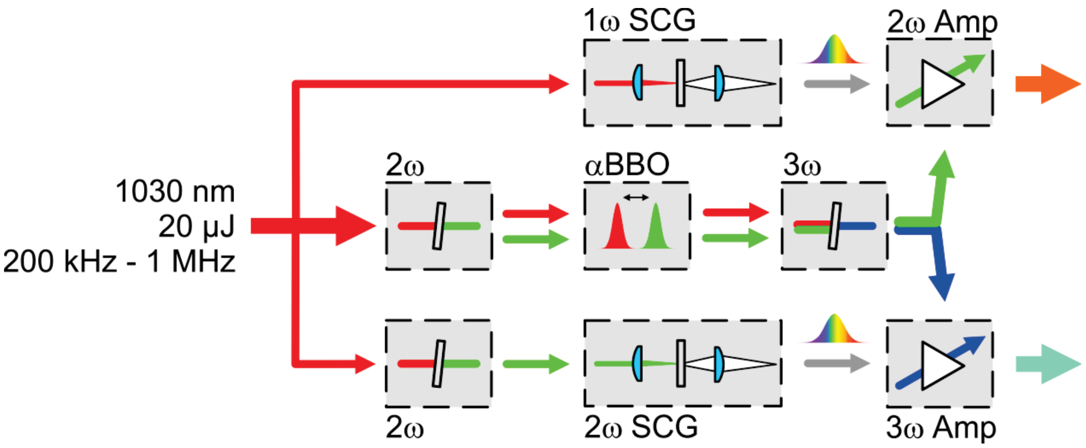

Fig. 6.1: Schematic view of the two color NOPA setup. For details see text.

6.1 Laser warm up pointing

Yb-fiber lasers are known to operate stable over long time periods. However, if the system was shut down, it will take as much as an hour until stable operation is obtained after start up – see Fig. 6.2. The main issue is not the output power that is typically monitored, but the beam pointing.

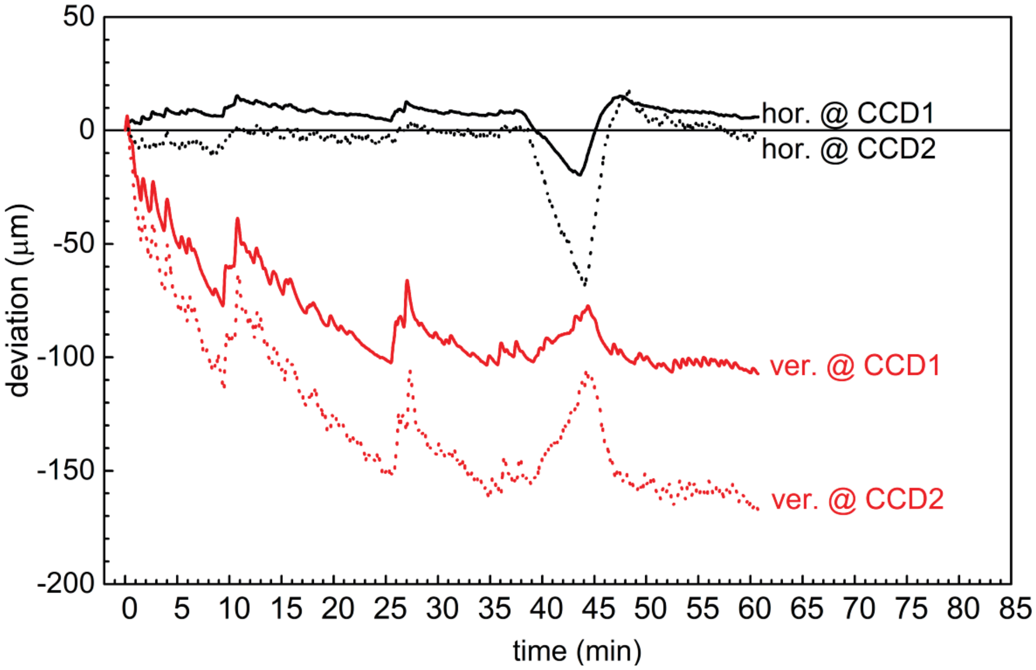

Fig. 6.2: Pointing of Tangerine during warm up phase. CCD 1 and 2 are located 29 and 211 cm after the laser head, respectively.

The beam pointing during the warm up phase has been monitored with two CCD cameras at 29 and 211 cm after the laser head. The laser was operating in full power at a repetition rate of 200 kHz. The beam was attenuated by multiple reflections on glass wedges in order to not saturate the cameras. The maximum drift is about 160 µm in 211 cm distance. This corresponds to a pointing of 76 µrad. For comparison: in the previous chapter it has been demonstrated, that for angle variations of 180 µrad the NOPA amplification breaks down. After roughly 50 minutes the beam position stabilizes. Also the pronounced spikes vanish. To conclude: it is highly recommended not to start aligning of the experiment after switching on the laser system. The warm up procedure takes roughly one hour. Before that time no alignment makes sense, since the beam is not yet stable regarding its position. This warm up behavior will repeat after closing and opening the internal laser shutter. Instead of using the shutter, it is recommended to block the beam externally, with a sandblasted beam dump.

6.2 Seed generation with 1ω and 2ω in 4 mm YAG

In this part a detailed look on the generation of the two independent seed pulses and the used optics is given. The incoming light is split into two arms with the help of an initial half wave plate and a Brewster angled thin film polarizer (*TFP 1*) – see Fig. 6.3. The vertically polarized reflection of *TFP 1* is used for pump pulse generation – see chapter 6.3. The horizontally polarized transmission is used to generate the seed pulses. From previous experiments it is known that the transmission of a thin film polarizer exhibits a much cleaner polarization. Therefore, this arm is better suited for continuum generation. A depolarization of the driving pulse would also show up in the continuum and hinder the subsequent amplification process from optimal performance. Especially with regard to the long term stability for high repetition rate systems, this configuration has proven beneficial. The polarization of the reflected arm, used for pump pulse generation cleans up anyhow after frequency conversion. Additionally, in this geometry the major part of the incoming laser power is reflected for pump pulse generation. This avoids the transmittance of the high power part through the *TFP* (3 mm thickness) to ensure a low B-Integral.

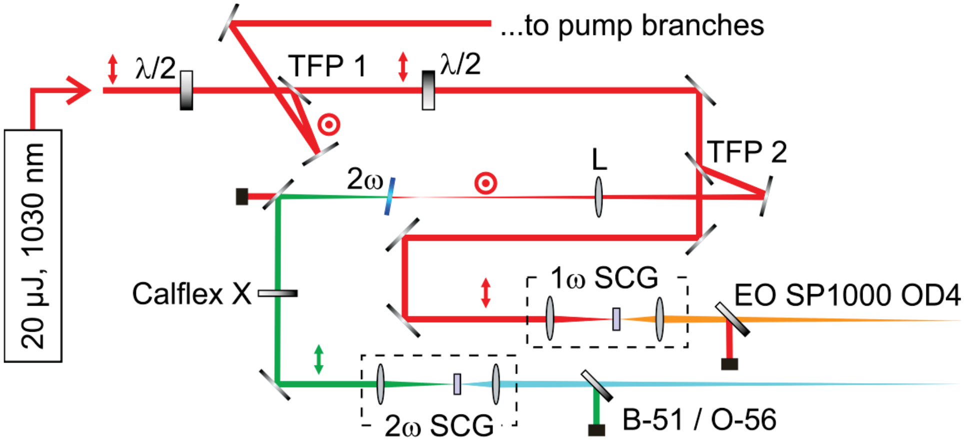

Fig. 6.3: Concept for decoupled generation of two continua seed pulses.

- **λ/2**: zero order half-wave plate for 1030 nm
- **TFP 1 & 2**: Brewster angled thin film polarizer
- **L:** *f* = 250 mm lens for SHG (AR 1030 nm)
- **2ω**: SHG in 0.8 mm, type I, 23.5° BBO
- **Calflex X**: dichroic shortpass filter to suppress 1030 nm and transmit 515 nm (*Optics Balzers*)
- **1ω SCG**: f = 50 mm (AR 1030 nm), 4 mm YAG and *f* = 30 mm for relay imaging
- **2ω SCG**: f = 50 mm (AR 515 nm), 4 mm YAG and *f* = 30 mm for relay imaging
- **EO SP1000 OD4**: *Edmund Optics* shortpass filter to suppress 1030 nm
- **B-51 / O-56**: *Optics Balzers* dichroic filter for the short and long wavelength side of the continuum, respectively.

A second combination of a half-wave plate and a Brewster angled thin film polarizer (*TFP 2*) is used to split the white light generation beam in two branches. The vertically polarized reflection is frequency doubled in 0.8 mm BBO. To enhance efficiency, the beam is focused down towards the crystal with an AR coated lens *L* (*f* = 250 mm). After frequency doubling the reflection of *TFP 2*, two dielectric mirrors transmit the residual 1030 nm and steer the horizontally polarized 515 nm beam to the 4 mm YAG (*2ωSCG*). To fully suppress the 1030 nm after frequency doubling a *Calflex X* (Balzers) filter is used additionally. It reflects 1030 nm and transmits 515 nm. A collimation lens is avoided, to not add chirp on the 515 nm pulses. This would lead to a higher energy needed for continuum generation. Instead, the beam is directly focused with an AR coated *f* = 50 mm lens (fused silica) onto the entrance surface of the YAG crystal. The lens is just set back by a few millimeters to compensate for the divergence of the 515 nm beam. The resulting supercontinuum is relay imaged towards the amplifier crystal with an uncoated, plano-convex fused silica lens (*f* = 30 mm). To suppress the 515 nm after continuum generation two different filters can be used. *B-51* (Optics Balzers) for transmitted wavelengths shorter than 515 nm. *O-56* (Optics Balzers) for transmitted wavelengths greater than 515 nm – see Fig. 6.4a). This prevents the residual fundamental to introduce distortions in the subsequent amplification process.

The horizontally polarized transmission of *TFP 2* is used to generate a supercontinuum in 4 mm YAG with 1030 nm. The beam is focused with an *f* = 50 mm plano-convex lens (BK7) onto the entrance surface. The continuum is relay imaged with an uncoated, plano-convex fused silica lens (*f* = 30 mm). After 1ω continuum generation a short pass filter (*Edmund Optics,* SP1000, OD4) is used to suppress the fundamental – see Fig. 6.4b). This prevents the residual fundamental to introduce distortions in the subsequent amplification process.

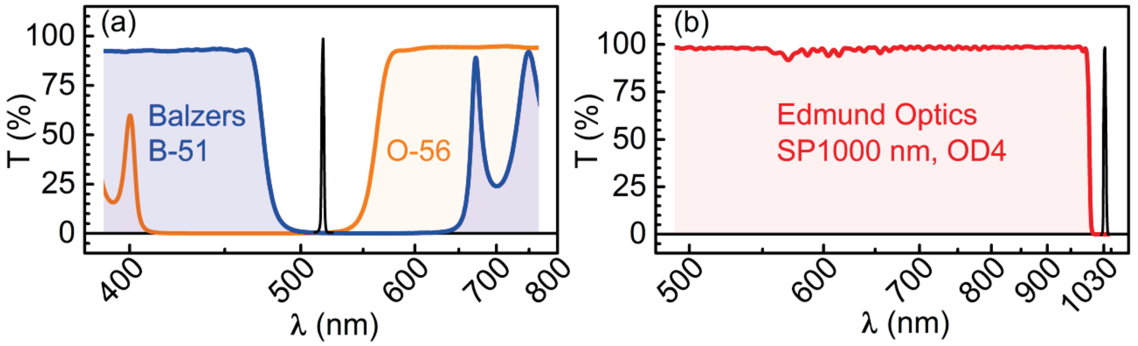

Fig. 6.4: Transmission curves of filters to block the driving pulses for continuum generation. (a) B-51 and O-56 filter (AOI = 0°, 10° respectively) to block 515 nm pulses (black); (b) *Edmund Optics* short pass 1000 nm (OD 4.0) to block 1030 nm pulses (black), AOI = 10°.

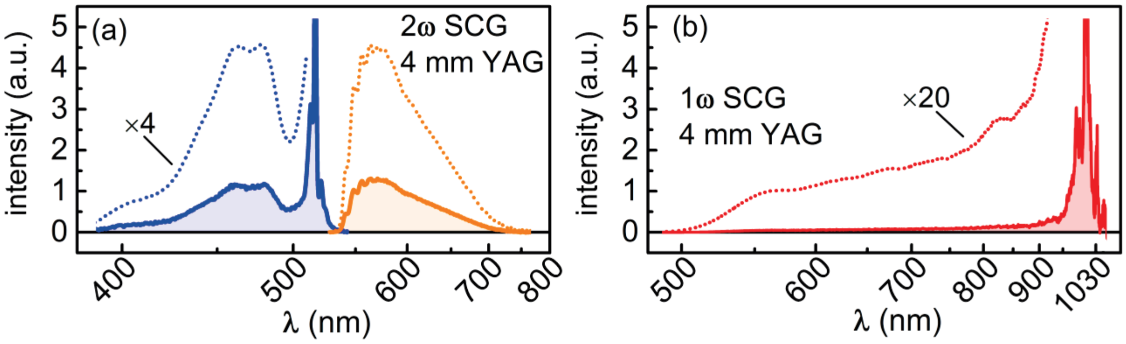

Fig. 6.5: Continua generated in 4 mm YAG plates. (a) blue and red wavelength side of the 515 nm pumped continuum (b) continuum pumped by 1030 nm.

In this geometry both continua are horizontally polarized. After amplification the horizontal seed polarization is maintained on the amplified output signal. For compression with a prism compressor the horizontal polarization is beneficial. It enables a Brewster angle configuration of the prisms to ensure highest throughput – for fused silica prisms a typical throughput is 85%.

To demonstrate the stability of the 1030 nm continuum, a long term measurement of optical power of selected, newly generated frequencies is shown – see Fig. 6.6. For the stability measurement a bandpass filter ($\Delta\lambda = 10$ nm at 550 nm, *Thorlabs,* FB550-10) was placed behind the short pass filter to monitor selected frequencies close to the cut-off wavelength. Here continua are known to be most instable. Consequently, this region is the best indicator for potential distortions. The transmission is monitored with an acquisition rate of 1 Hz by a sensitive photodiode based power meter sensor (*Thorlabs*, S120VC) over 2 hours at a repetition rate of 1 MHz.

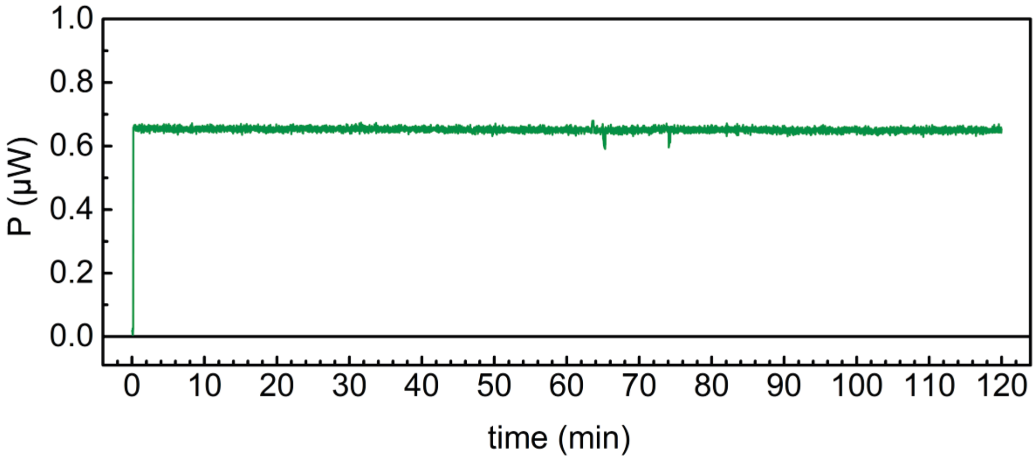

Fig. 6.6: Long term stability of selected continuum wavelengths centered around 550 nm, generated with 1.3 µJ of 1030 nm in a 4 mm YAG plate at 1 MHz.

6.3 Second and third harmonic generation with static delay compensation plate to reduce two-photon absorption induced phase-matching loss

For amplification of selected spectral portions out of the seed pulses, the second and the third harmonic of the fundamental is used. Therefore, the vertically polarized reflection of *TFP 1* is frequency doubled and subsequently sum-frequency mixed with the fundamental.

Up to now a type III configuration for third harmonic generation (THG) was frequently used for pump pulse generation in a NOPA [Hom08, Bra14]. After frequency doubling in a 0.8 mm type I BBO crystal cut at 23.5°, the subsequent sum-frequency mixing for THG (1030 nm (o) + 515 nm (e) --> 343 nm (e)) takes place in a type III BBO crystal cut at 62.9°. The advantage of this setup is that both generated pump wavelengths (515 and 343 nm) have extraordinary polarization after mixing. Therefore, no additional half-wave plate is needed after frequency conversion for subsequent type I amplification. The type III THG configuration seems to work fine for the use of an IMPULSE (CLARK-MXR, Inc.) pump laser at the University of Halle-Wittenberg in the group of Wolf Widdra [Hom08, Hoe11]. However, by the use of the Tangerine (Amplitude Systems) as a pump laser for a NOPA according to Ref. [Bra14] the type III configuration seems to fail. Especially for 1 MHz repetition rates the THG and the NOPA crystals are found to degrade rapidly in the laboratories of Isabelle Thomann at the Rice University. This issue is attributed to the two-photon absorption (TPA) induced heating of the BBO crystals under UV radiation.

A new concept in type II configuration for third harmonic generation with a delay compensation plate between the SHG and the THG crystal is described in this chapter. In this way the generated heat in the THG crystal can be reduced to a minimum. A heat camera photography (FLIRone, FLIR Systems, Inc.) of the THG crystal compares both configurations impressively – Fig. 6.7.

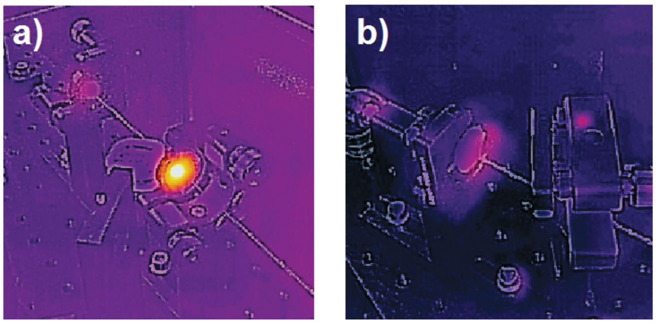

Fig. 6.7: Heat camera photography of the THG crystals. a) Type III phase-matching: clearly visible heat in the crystal due to TPA. b) New type II concept including a delay compensation plate: no "heat spot" is detected in the THG crystal.

In the type III configuration the heating of the crystal due to two-photon absorption of the third harmonic is clearly visible with the heat camera (Fig. 6.7a).

The two-photon absorption (TPA) coefficient of BBO varies in the range of 320 and 360 nm between 0.29 and 0.08 cm/GW [Hom11]. The third harmonic of 1030 nm corresponds to 343 nm and hence is in this range – here two-photon absorption is likely to happen, since the used pulses for THG have intensities up to 100 GW/cm^2. For 343 nm pulses this amounts to a transmission of 85% inside a 3 mm BBO [Bra14]. Two-photon induced absorption of the newly generated frequencies in the UV leads to a high thermal load inside the BBO crystal and will change the phase-matching conditions of the mixing process and leads to degradation of the UV power over time [Kum15]. According to [Rot14] the thermal change is on the order 50°C for a 1 mm BBO and the used parameters. A temperature change of 50°C changes the needed phase-matching angle by 0.2° [SNLO] – this is equal to nearly a full revolution (~310°) of an adjustment screw from a typical 1" mirror mount with 170 turns-per-inch precision thread. Obviously, this will heavily alter the optimum THG efficiency.

The THG efficiency for both configurations, shown in Fig. 6.7, was set to be roughly 15% or 2.55 µJ at 200 kHz. Both pictures were recorded roughly 5 minutes after opening the impinging laser light. The nonlinearity coefficient d_{eff} for THG is 0.41 pm/V for type III and 1.24 pm/V for type II. The third harmonic generation efficiency scales with $d_{eff} \cdot I^2$ [Boy03], where I is the intensity. This leads to a 9 times lower intensity needed for the type II configuration compared to type III. Obviously, a higher intensity leads to higher TPA. Concerning this, the type II configuration is intrinsically advantageous. Additionally, a αBBO plate ($\theta = 70.0°$, $d = 1.1$ mm) for delay compensation is introduced between the SHG and THG crystal in the presented configuration – see Fig. 6.8. This compensation plate does not only compensate for the group velocity mismatch (between fundamental and SHG) introduced by the second harmonic crystal, but also overcompensates the relative pulse delays for the thickness of the third harmonic generation crystal.

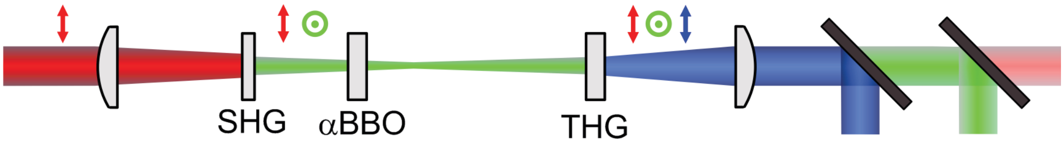

Fig. 6.8: THG scheme with delay compensation: SHG: in a 0.8 mm, type I BBO cut at 23.5°; αBBO: delay compensator, 1.1 mm thick αBBO cut at 70.0°, THG: in a 1.0 mm, type II BBO cut at 40.0°.

The second harmonic is generated in a 0.8 mm, type I BBO crystal cut at 23.5°. The generated second harmonic falls behind the fundamental by 45 fs due to group velocity mismatch in the SHG crystal (left panel, Fig. 6.8). With 515 nm polarized extraordinary and 1030 nm polarized ordinary a time delay of –267 fs can be introduced by the αBBO plate (center panel of Fig. 6.9). This overcompensation shifts the temporal overlap of the pulses to the end of the THG crystal (right panel).

For sum frequency mixing to the third harmonic a 1.0 mm, type II BBO cut at 40.0° is employed. The group velocity mismatch inside the THG crystal is 345 fs/mm between the fundamental and the second harmonic, 470 fs/mm for the fundamental and the third harmonic and 125 fs/mm for the second and third harmonic. Consequently, the pulses fully overlap at the end of the THG crystal. This reduces the two-photon absorption volume for 343 nm light in the BBO. Due to the centrosymmetric crystal structure of the αBBO, no undesired second order processes take place inside this medium. It has a large birefringence and a ten times higher damage threshold than calcite. The use of a calcite plate for similar purposes has been shown in Ref. [Nil14], but in the publication no over-compensation was taken into account. Additionally, the high UV transparency of αBBO reduces the possibility of two or three photon absorption. The parameters of the αBBO plate were exclusively calculated and designed for this setup and manufactured by *Newlight Photonics, Inc*.

The propagation of the pulses during third harmonic generation with the αBBO delay compensator plate can be simulated with the *"2-dimensional short-pulse mixing"* package of SNLO [SNLO]. Fig. 6.9 shows the results of the simulation. All relevant parameters for the described THG generation are summarized in TABLE VI.

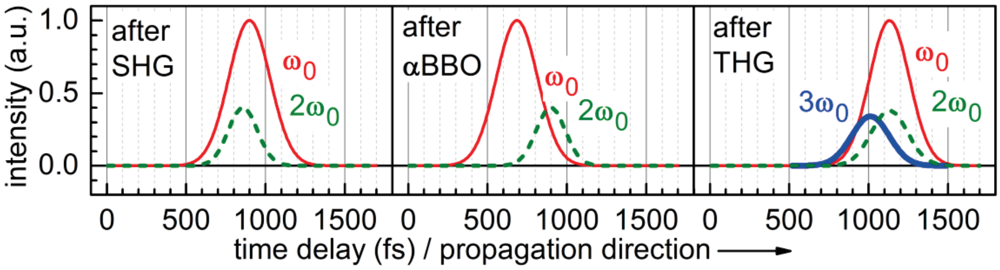

Fig. 6.9: Simulation of temporal propagation of the pulses for third harmonic generation with delay over-compensation between ω_0 und $2\omega_0$. Pulses are propagating from left to right.

TABLE VI: Summarized parameters for the used third harmonic generation scheme.

	interaction	**θ**	**d** (mm)	***d*_eff** (pm/V)	***ρ*** (μm)	**ω ↔ 2ω** (fs / mm)	**ω ↔ 3ω** (fs / mm)	**2ω ↔ 3ω** (fs / mm)
SHG	type I *(oo → e)*	23.5°	0.8	2.01	45.5	45		
αBBO	*no nonlinearity*	70.0°	1.1	-	-51.3	-267		
THG	type II *(eo → o)*	40.0°	1.0	1.24	55.1	345	470	125

Although the second harmonic and fundamental fields start slowly building up the UV field in the first "slices" of the crystal, the maximal UV intensity is generated at the end of the crystal, where the maxima of the fundamental and second harmonic field overlap. In Fig. 6.9 this evolution of the UV pulse is shown for three "slices" inside the THG crystal, after entering the crystal with the temporal pre-delay between fundamental and second harmonic introduced by the αBBO plate. By shifting the generation locus of the main UV power to the end of the crystal, two-photon absorption inside the THG crystal is reduced to a minimum, since the optical path for the maximal evolved UV field is minimized. Moreover, the αBBO compensation plate corrects for the walk-off ρ introduced by second harmonic generation (TABLE VI) – this is also advantageous for the efficiency of third harmonic generation and allows to move the crystal further from the focal plane.

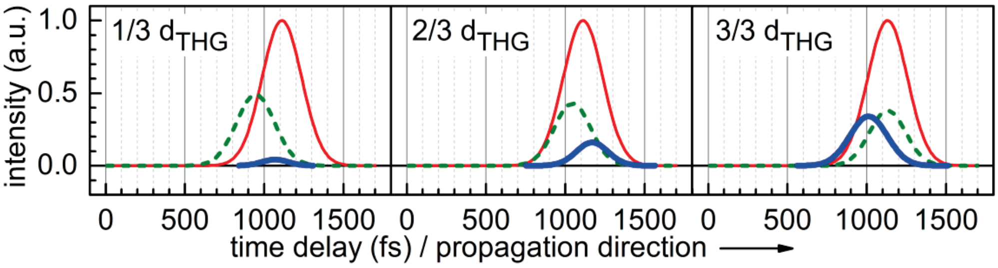

Fig. 6.10: Evolution of the third harmonic inside the mixing crystal after propagating through 1/3 (left panel), 2/3 (panel in the middle) and of the full thickness (right panel) of the THG crystal. Pulses are propagating from left to right.

Due to the concept of delay pre-compensation with an αBBO plate, the thermal load is drastically reduced and no significant "heat spot" is detected inside or on the THG crystal.

For the presented type II configuration including the delay compensation plate a long term power monitoring measurement is shown in Fig. 6.11. As a consequence of generating the main UV power close to the exit surface of the THG crystal, no two-photon absorption induced change of phase matching conditions takes place inside the crystal and long term stable UV pulse generation is maintained.

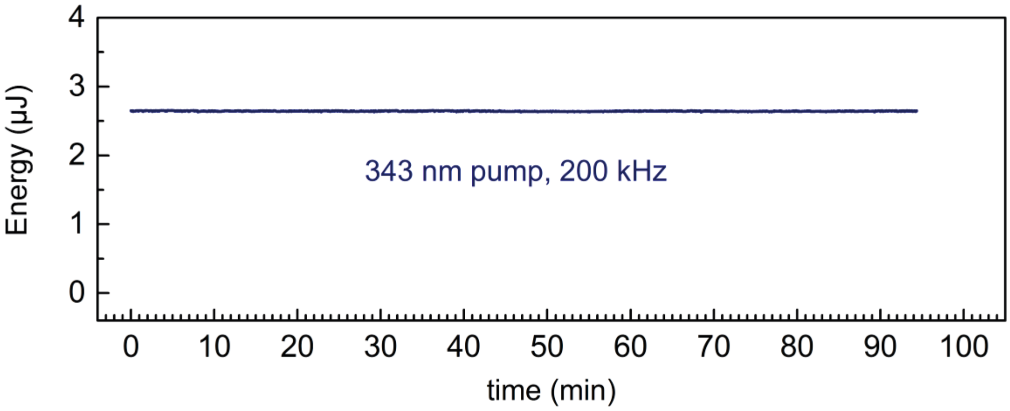

Fig. 6.11: Long term monitoring of the third harmonic generation (343 nm) in type II configuration with delay compensation plate. $E = 2.55$ µJ at 200 kHz.

6.4 Detailed NOPA setup at a glance

In this section the whole two-color pumped / two-color seeded NOPA setup is described. The description for each numbered optical element is found on the next page.

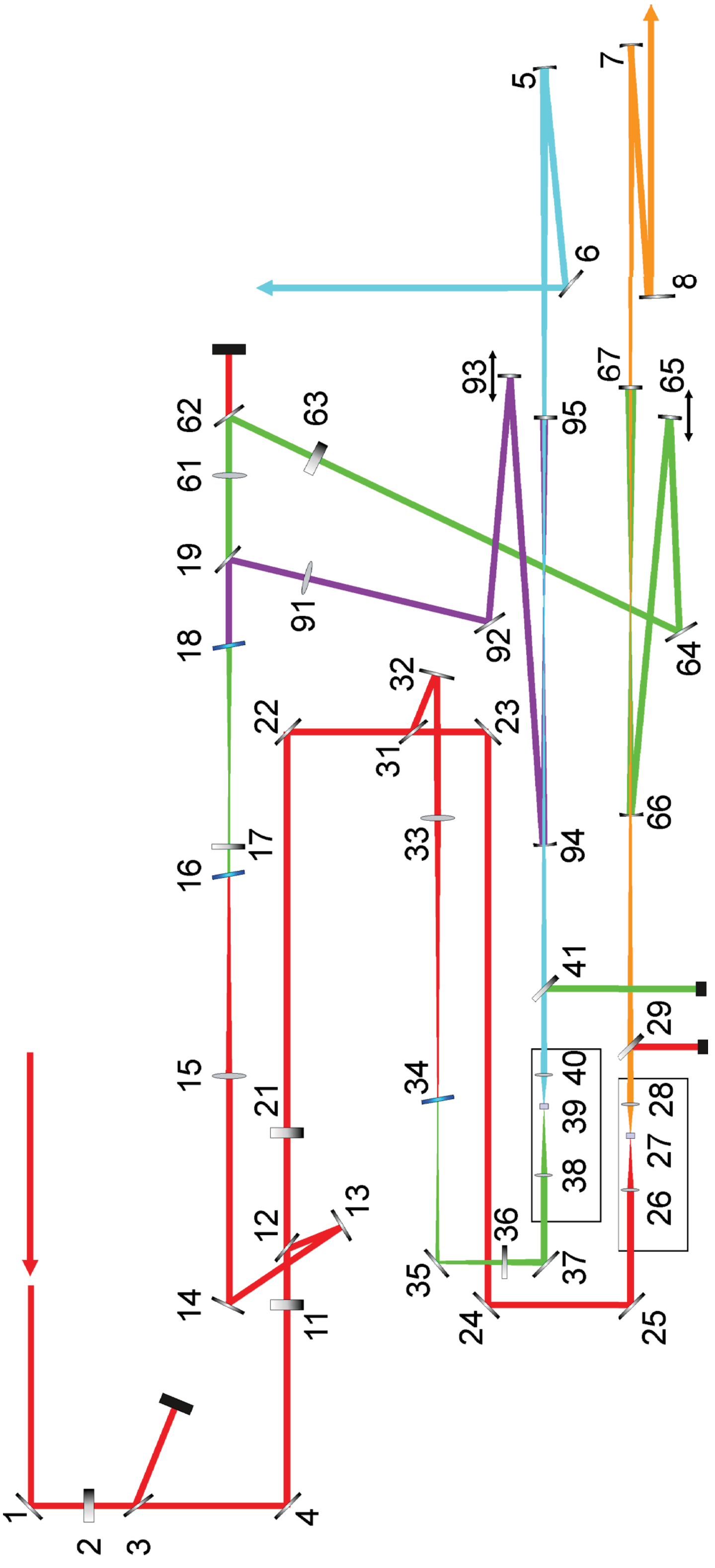

Fig. 6.12: Setup of the NOPA system. For descriptions to each element, see next page.

1, 4	dielectric beam steering mirrors from Tangerine to NOPA
2	zero order $\lambda/2$-plate for 1030 nm
3	Brewster angle thin film polarizer
5,7	collimation mirrors (Ag, R = -1000 mm)
6,8	flat Ag beam steering mirrors for NOPA output beams

11	zero order $\lambda/2$-plate for 1030 nm
12	thin film polarizer to split off light for continuum generation
13,14	dielectric beam steering mirrors for fundamental light
15	plano-convex, focusing lens for pump SHG and THG (f = 250 mm)
16	pump SHG BBO crystal (type I, d = 0.8 mm, θ = 23.5°)
17	αBBO time delay compensator (d = 1.1 mm, θ = 70.0°)
18	pump THG BBO crystal (type II, d = 1.0 mm, θ = 40.0°)
19	dichroic mirror to separate UV and green pump light

21	zero order $\lambda/2$-plate for 1030 nm
22,23,24,25	dielectric beam steering mirrors for fundamental light
26	plano-convex BK7 lens for 1ω continuum generation (f = 50 mm, AR1030)
27	1ω continuum generation crystal, 4 mm YAG
28	relay imaging lens, FS (f = 30 mm, uncoated)
29	*Edmund Optics* short pass filter to block 1030 nm after continuum generation

31	thin film polarizer to split off light for green pumped continuum generation
32	dielectric beam steering mirror for fundamental light
33	plano-convex focusing lens for SHG (f = 250 mm, AR1030)
34	BBO crystal (type I, d = 0.8 mm, θ = 23.5°)
35	dielectric beam steering mirror for 515 nm
36	*Calflex X* filter to block light residual 1030 nm light after SHG
37	dielectric beam steering mirror for green light
38	plano-convex FS lens for 2ω continuum generation (f = 50 mm, AR515)
39	2ω continuum generation crystal, 4 mm YAG
40	relay imaging lens, FS (f = 30 mm, uncoated)
41	filter to block 515 nm after continuum generation (*O-56* or *B-51*)

61	plano-convex collimating lens for green pump light (f = 250 mm, AR515)
62,64	dielectric beam steering mirrors for green pump light
63	zero order $\lambda/2$-plate for 515 nm
65	flat dielectric mirror, delay for green pumped stage
66	dielectric focusing mirror for green pumped stage (f = 250 mm)
67	NOPA BBO crystal for green pumped stage (type I, d = 3 mm, θ = 24°)

91	collimating lens for UV pump light (f = 250 mm, AR343)
92	dielectric beam steering mirror for UV pump light
93	flat dielectric mirror, delay for UV pumped stage
94	dielectric focusing mirror for UV pumped stage (f = 250 mm)
95	NOPA BBO crystal for UV pumped stage (type I, d = 5 mm, θ = 37°)

6.5 Performance of the UV pumped NOPA stage and balancing TPA in the amplifier BBO

Section 6.3 of this chapter demonstrated and described the problem of two-photon absorption induced heating of a BBO crystal used for third harmonic generation. The temperature gradient alters the phase-matching. Obviously, this is also an issue inside the amplifier BBO for a UV pump beam. At least this effect also occurs for high repetition rates when there is no time for thermal cooling of the crystal between the impinging pulses. For a Ti:sapphire second harmonic (~400 nm) pumped NOPA system with 1 kHz repetition rate this is not an issue - no heating can be seen in the amplifier BBO with the FLIR camera. For higher repetition rates this problem can be handled by reducing the UV pump intensity on the amplifier crystal. With the use of a thicker crystal the output energy can be maintained.

Fig. 6.13 quantifies the problem of too high an UV pump intensity on the amplification crystal. In the left panel the energy of the UV pump pulse is shown in front (black) and behind the 2 mm BBO amplification crystal (type I, cut at 37.0°). In front of the BBO the energy of the pump pulse is $E = 2.65\ \mu J$ at 200 kHz. With a distance of 28 cm from the focusing mirror (#94 in Fig. 6.12) to the BBO, the UV intensity is roughly 50 GW/cm², yielding a transmission of approximately 75%. Over 90 minutes this decreases further to 68% transmission. Carefully steering the UV pump to a "new" spot on the crystal surface immediately resets the transmission to the initial value of 75%. Monitoring the amplified output of the NOPA at 460 nm at 200 kHz, an initial output energy of 320 nJ is measured – see the right panel in Fig. 6.13. After 13 minutes the energy decreased to 254 nJ. This equals a loss of 20% in output energy on a 10 minute timescale.

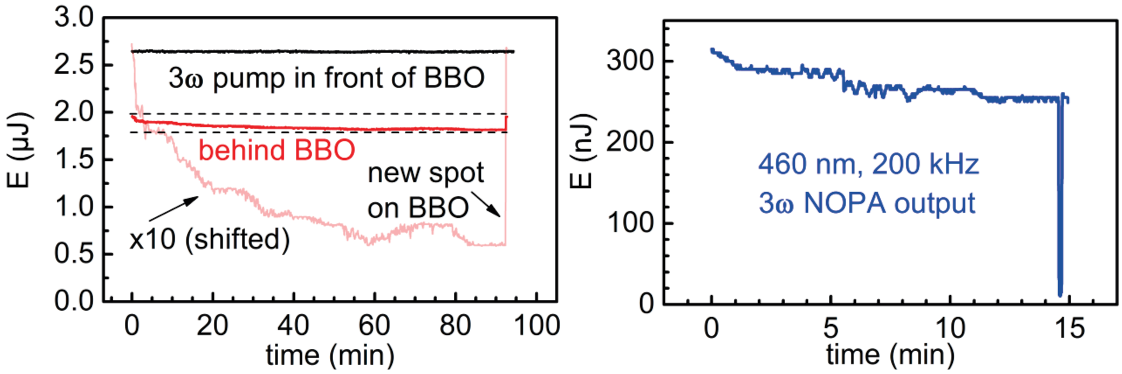

Fig. 6.13: Left panel: measurement of 3ω pump energy in front (black line) and behind (red) of 2 mm amplifier BBO. Right panel: corresponding NOPA output energy at 460 nm.

To minimize this two-photon induced effect, the UV pump intensity has to be reduced. To maintain the output energy, a thicker amplifier crystal can be implemented.

The gain factor for amplification in the BBO reads:

$$G = \frac{1}{4}\exp\left(2 \cdot d_{BBO} \cdot \sqrt{\frac{8\pi^2 d_{eff}^2 I_{pump}}{n_p \cdot n_s \cdot n_i \cdot \lambda_i \cdot \lambda_s \cdot \varepsilon_0 \cdot c}}\right), \tag{6.1}$$

where n_p,n_s,n_i are the refractive indices for pump, signal and idler, respectively. λ_s, λ_i are the signal and idler wavelengths. d_{eff} is the nonlinear coefficient, ε_0 is the vacuum permittivity and c the speed of light. Changing the crystal thickness from 2 mm to 5 mm will lead to a constant gain by reducing the intensity roughly by a factor of 5. Since only the crystal thickness and the intensity changes in Eq. (6.1) while all other parameters stay constant, the condition for constant G reads:

$$d_{BBO} \cdot \sqrt{I_{pump}} = 2\,\text{mm} \cdot \sqrt{50\ \text{GW / cm}^2} \approx 5\,\text{mm} \cdot \sqrt{10\ \text{GW / cm}^2}\,. \tag{6.2}$$

Reducing the intensity is done by setting the thicker crystal further away from the beam waist of the UV pump beam. From initially 28 cm distance to the focusing mirror (#94) for the 2 mm BBO, to 32 cm distance for the 5 mm BBO.

Not only the integral effect of two photon absorption is reduced by a factor of 2.5 [Bra14] with the combination of lower intensity with a longer interaction volume, but also the B-Integral drops from the approximate value of 2 to 0.6. If there is no need for "high" output pulse energies in the experiment, it is therefore reasonable to keep the intensity on the crystals low - especially for the case of pump wavelengths in a range where two-photon absorption is likely to happen. In return, undistorted pulses with long term stability are obtained. Fig. 14 shows the stability for the 3ω pumped NOPA at a center wavelength of 460 nm. For 200 kHz there is a constant output energy of 270 nJ over the measurement time of 1 hour. To preserve the amplifier BBO, the pump intensity was reduced by slightly moving the crystal further out of the focus before switching the pump laser to a repetition rate of 1 MHz. But even with the 5 times higher average power, at 1 MHz repetition rate, the thermalization can be equilibrated for low pump intensity. No deterioration was measured – with 190 nJ the pulses centered around 460 nm are long term stable over the whole duration of the measurement of nearly two hours. The RMS value is about 1.3 % for a repetition rate of 200 kHz and 2.2 % for a repetition rate of 1 MHz for the UV pumped branch.

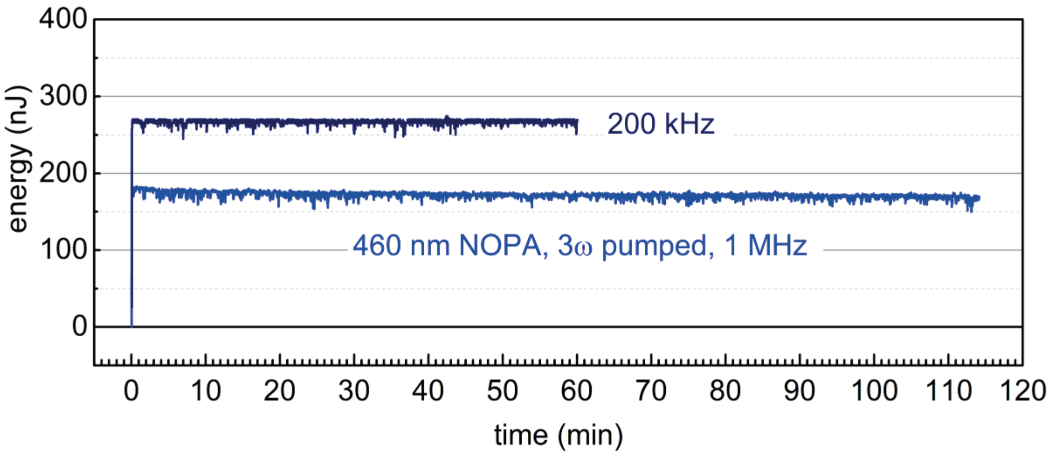

Fig. 6.14: Long term stability of the UV pumped NOPA output with 200 kHz and 1 MHz repetition rate at 460 nm for a 5 mm amplification BBO.

For future stability improvements, the power instabilities of the outputs seen in Fig. 6.14 are highlighted in Fig. 6.15. By averaging the data to one effective measurement per minute, it can be seen that the system is long term stable on a "slow" time scale. Without averaging, there are dips in the output energy on the order of 5% in amplitude on a 1 s timescale.

These instabilities are attributed to the beam pointing of the pump laser source. In the UV pumped branch there are numerous frequency conversions: second harmonic generation and subsequent sum-frequency mixing for the pump beam and second harmonic generation with subsequent continuum generation for the seed beam path. How nonlinearities can magnify the beam pointing due to a Kerr lens and hence increase instabilities in the performance can be found in chapter 5 of this thesis. To improve signal stability, a pump laser with very high pointing stability should be chosen. If this is not possible, a beam stabilization system should be implemented.

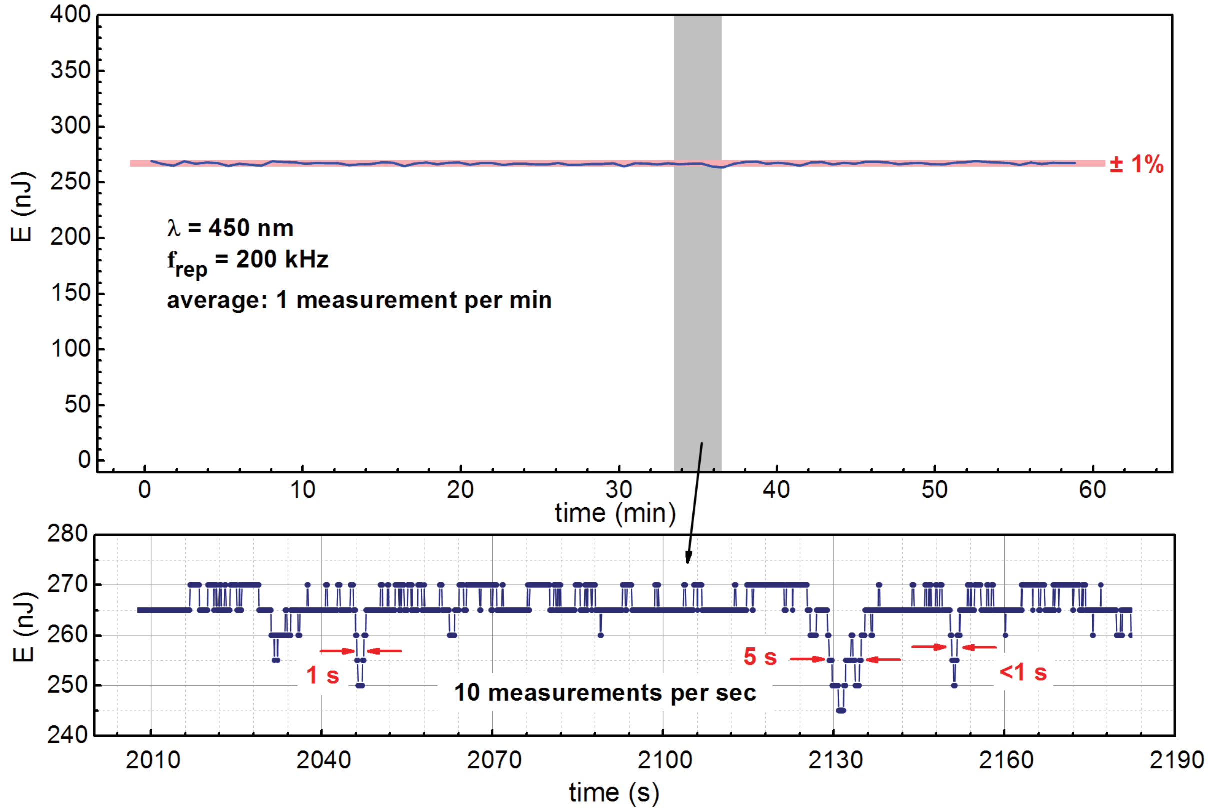

Fig. 6.15: Stability measurement of UV pumped NOPA stage at a repetition rate of 200 kHz. RMS value is 1.3%. Averaged data for long term stability measurement (upper panel) and visualization of fast drops in output energy (lower panel) corresponds to the timescale of the grey area in panel above.

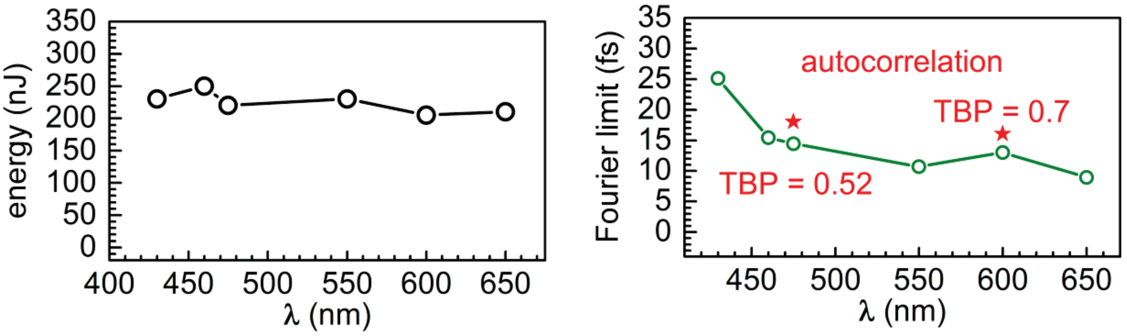

Fig. 6.16: Energy levels of third harmonic pumped NOPA output (black), Fourier limits (green) and deconvoluted autocorrelation widths (red stars).

Fig. 6.16 and Fig. 6.17 demonstrate the tuning range of the system for the 343 nm pumped branch, seeded with the 2ω white light. To show the compressibility of the system, the NOPA output was compressed with a sequence of two Brewster angle fused silica prisms [Wil97, Rie00]. The pulse duration was measured with a second harmonic intensity autocorrelator [Koz04].

The measured pulse durations are close to the Fourier limit and time-bandwidth products of 0.5 are achieved routinely. If shorter pulses are needed, Brewster-angled chirped mirrors [Bau06] can be applied in combination with a prism compressor to minimize third and higher order dispersion.

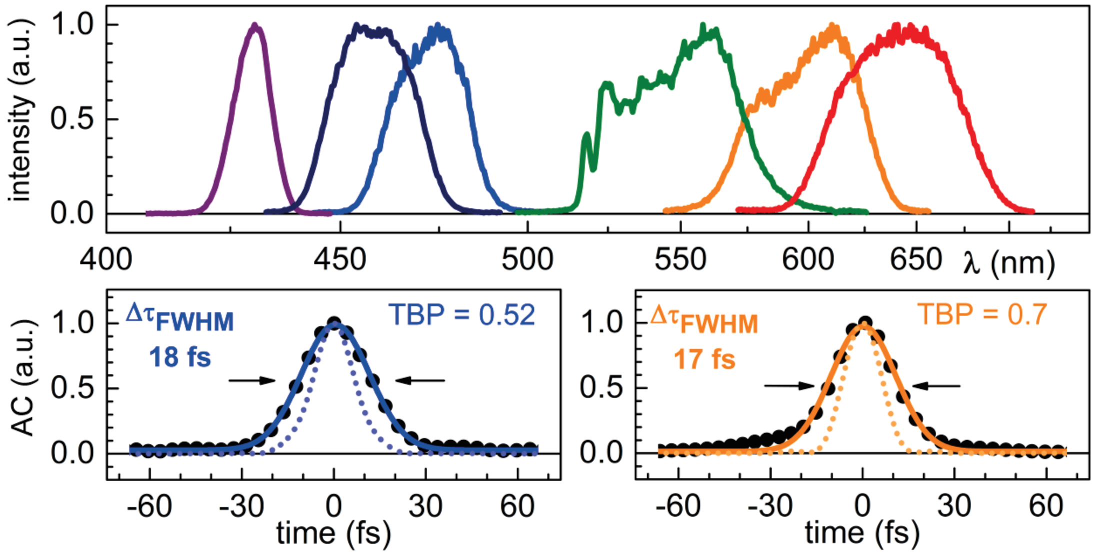

Fig. 6.17: Spectra of third harmonic pumped NOPA seeded with 2ω white light upper panel, and autocorrelation traces for 470 nm and 600 nm pulses (dotted lines show calculated Fourier limits).

6.6 Performance of the second harmonic pumped NOPA branch

For the generation of pulses from the red to the NIR, the second harmonic pump beam is used together with the seed continuum generated by 1030 nm pulses. The reuse of the second harmonic after third harmonic generation leads to slightly temporal stretched second harmonic pulses. Since the initial temporal pulse duration of the fundamental pulse is rather long already (~300 fs) and dispersion is small in this (red to NIR) wavelength region, the resulting NOPA pulses are spectrally very broad and flat-top like. If short pulses in the red or the NIR are needed, this is a straightforward method to generate them. Care has to be taken, that the efficiency of SHG and THG stays at moderate values. Otherwise, strong spatio-temporal distortions of the pump pulses are obtained – compare chapter 2. Here the efficiency for SHG is kept at a level of 35% and for THG at 13%. The available green pump pulse energy corresponds to 5 µJ for amplification in a type I, 3 mm, $\theta = 24°$ BBO crystal. The advantage of using the residual second harmonic in one single setup in combination with the third harmonic is the resulting flexibility. For example, wavelengths below 630 nm cannot be amplified with the 515 nm pump due to idler absorption in the BBO crystal. For even shorter wavelengths phase-matching cannot be achieved anymore. However, in this setup only minor modifications in the beam path have to be made to use the 1ω continuum as a seed for the third harmonic pumped amplifier. This enables the amplification of wavelengths close to the second harmonic. With a proper dichroic it is also possible to seed both amplifiers with the same seed light generator.

Relevant output spectra and pulse energies for the second harmonic pumped branch are shown in Fig. 6.18. Fourier limits below 10 fs can be achieved quite easily. The pulses can also be compressed intriguingly close to the Fourier limit with a standalone fused silica prism compressor, since higher order dispersion effects of the prism material is negligibly small in this wavelength region.

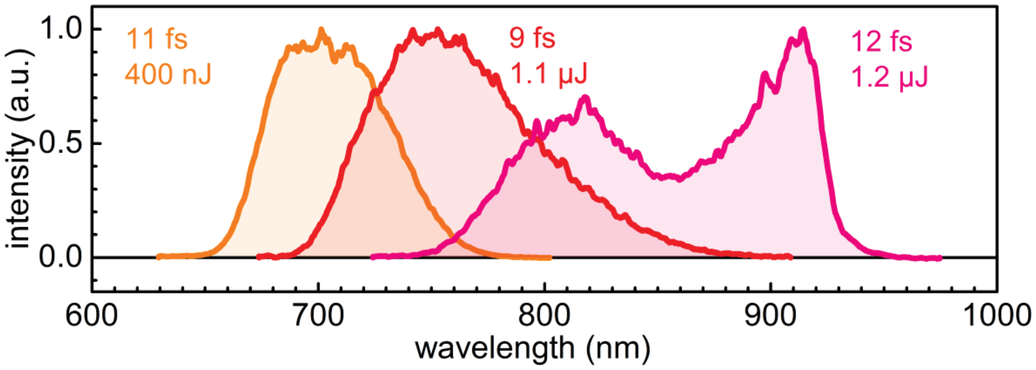

Fig. 6.18: Spectra of the 515 nm pumped NOPA, seeded with 1ω white light at 200 kHz. Corresponding pulse energies and Fourier limits are given.

An 8.1 fs pulse is measured with a Fourier limit of 7.6 fs. Assuming a sech^2 pulse shape, this corresponds to a time bandwidth product of 0.36! The pulse is measured with a second harmonic intensity autocorrelator. Care was taken that the BBO thickness for autocorrelation supports the full bandwidth of the incident pulse. A thickness of 35 µm was employed. The spectrum is demonstrated in Fig. 6.19a), the autocorrelation data (grey dots), the $sech^2$ fit and the calculated Fourier limit (blue) is shown in Fig. 6.19b).

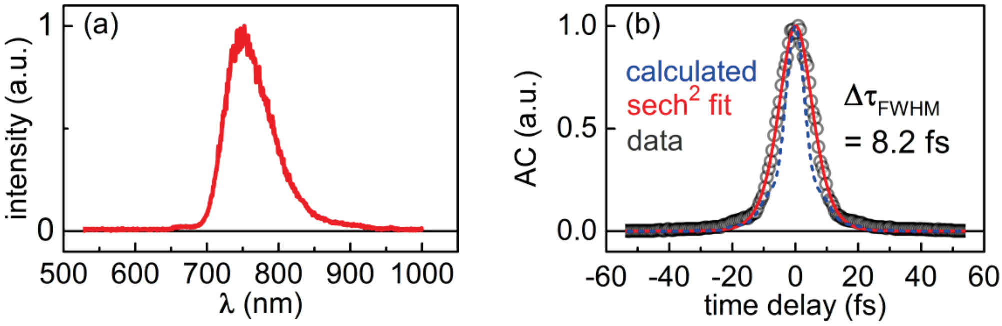

Fig. 6.19: Demonstration of a sub-10 fs pulse with the 2ω pumped NOPA branch at 750 nm with 400 nJ at a repetition rate of 200 kHz.

The long-term stability of the green pumped NOPA branch is illustrated in Fig. 6.20. The NOPA was centered around 750 nm, at a repetition rate of 1 MHz, with a pulse energy of roughly 410 nJ. On the time scale of 60 min the output pulse energy shows no significant drop. Also there are no measurable oscillations present, as it is seen in the UV pumped branch. This might be due to less nonlinear interactions (compared to the UV pumped branch) before the amplification.

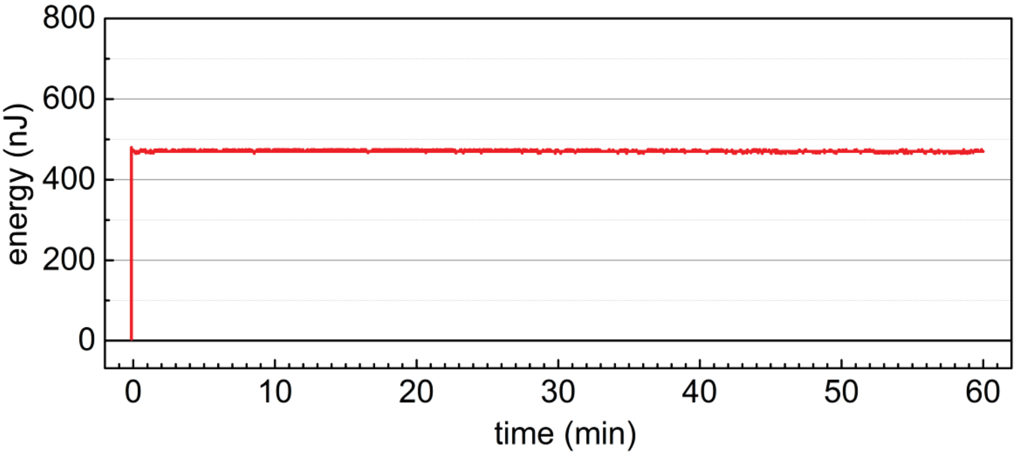

Fig. 6.20: Long term stability of second harmonic pumped NOPA. Pulses centered around 750 nm at 1 MHz repetition rate.

In chapter 10 output pulses of this NOPA source will be frequency doubled to the blue / UV region. With the prism compressor located in the visible the resulting UV pulses are compressed to pulse durations as short as 13 fs. The proof will be made that a compact UV autocorrelator of our own design [Hom11] can measure these pulses up to 1 MHz repetition rate.

In this chapter it was shown, how to correctly generate and use UV pulses at high repetition rates regarding long term stability of NOPA pulses. Two-photon absorption can lead to temperature gradients in BBO crystals. Consequently, this leads to a change of the phase-matching condition. As a result, the pulse energy decreases with time. With a αBBO plate between the SHG and subsequent THG crystal, the effective generation locus of the third harmonic can be shifted to the very end of the THG crystal. This drastically decreases the volume of two-photon absorption inside the medium. No significant heat is dissipated in the THG crystal and stable UV pump pulses result. On the amplifier crystal this issue was solved by reducing the pump intensity in combination with a larger amplifier crystal thickness.

In contrast to Ref. [Lie14], the setup presented here shows better over-all efficiency, even at higher repetition rates. Additionally, our concept to enhance the tuning range with two pump pulses and seed continua seems to be superior to the concept of enhancing the tuning range via optical parametric amplification with subsequent continuum generation. In this work with the presented setup smoother spectra and pulses with better peak/satellite contrast in the time domain are obtained.

The setup of Ref. [Nil14] also uses the concept of a time-delay compensation plate between SHG and THG. Contrary to our concept the used plate only compensates for the GVM introduced by the SHG crystal. This surely enhances the efficiency of THG. However, in terms of long-time stability the strategy to temporally overcompensate the pulses for the thickness of the THG crystal is more reasonable, because the temperature gradient inside the THG crystal is reduced as shown. Additionally, αBBO has of higher damage threshold than the calcite used in ref. [Nil14]. Especially for the MHz regime with high average powers this seems to be relevant.

The presented setup is used at the University of Würzburg in the laboratories of Tobias Brixner for time-resolved photoemission electron microscopy. For details on the experimental application see our forthcoming publication: B. Huber et al. "*Time-resolved photoemission electron microscopy of a plasmonic slit resonator using 1 MHz, 25 fs, UV-to-NIR-tunable pulses,*" Ultrafast Phenomena 2018 Proceedings.

During the experimental development of the light source presented in this chapter, it was also shown that the system works with lower repetition rate and high input energy (180 µJ at 22 kHz). The resulting output energy is on the order of 5 µJ energy per pulse. This has paved the way for the experiment of chapter 5. Here a 50 kHz, 515 nm pumped NOPA with 150 µJ input energy is used to generate a NIR seed for MIR amplification.

In the subsequent chapter also an Yb-based laser source will be used to compare various crystals for supercontinuum generation with 1030 nm light regarding the needed energy, the bandwidth and especially the broadening to the near infrared side of the fundamental.

7. Continuum generation at 1030 nm with various crystals

It has been demonstrated that the concept of bulk continuum seeded optical parametric amplification is applicable from the lower repetition rate regimes, e.g., 1 kHz [Wil97, Rie00, Cer03], to higher repetition rates like 1 MHz [Ste06, Emo10, Bra14] or even 2 MHz [Sch08b, Nil14]. Generally, a higher repetition rate implies lower output energy of a system. At the same time, the energy needed for continuum generation stays fairly constant independent from the laser repetition rate. This is due to the fact that the process of continuum generation exhibits a lower bound of necessary power - the critical power P_{crit}:

$$P_{crit} = \frac{3.77 \cdot \lambda_0^2}{8\pi \cdot n_0 \cdot n_2} \tag{7.1}$$

where λ_0 represents the laser fundamental. n_0 and n_2 are the linear and nonlinear refractive index, respectively. Taking YAG continuum generation as a numerical example, with $\lambda_0 = 1030$ nm, $n_2 = 6.9 \cdot 10^{-16} \mathrm{cm}^2/\mathrm{W}$ [Koe06], and $n_0 = 1.82$ gives $P_{crit} = 1.3$ MW. For laser pulses with a pulse duration of $\Delta t = 300$ fs, this corresponds to a theoretical pulse energy higher than $E = 0.4$ µJ, estimated by

$$E = P_{crit} \cdot \Delta t = 1.3\,\mathrm{MW} \cdot 300\,\mathrm{fs} \approx 0.4\ \mu\mathrm{J}. \tag{7.2}$$

Yb-based laser sources are nowadays widely in use. These sources have a center wavelength around 1030 nm and are in most cases able to operate with a selectable repetition rate. Single stage, 515 nm pumped, noncollinear optical parametric amplifiers (NOPAs) are working very well for these systems [Sch08b, Lie14]. Typically for frequency doubling and amplification in these systems BBO crystals are in use. Since they are transparent down to 190 nm, two-photon absorption will not lead to thermal distortions for higher repetition rates – like in the case for third harmonic pumping where changing the input to high repetition rate is doable, but has to be done with great care – compare chapter 6.

For the MHz regime the output energy of the green pumped NOPAs are on the order of 400 nJ for 20 µJ input energy. The needed energy for continuum generation with 1030 nm in a 4 mm YAG crystal is experimentally found to be about 1.3 µJ for pulses around 200 fs and around 2 µJ for 300 fs pulses. So the needed energy for seed generation is roughly 3 – 7 times larger compared to the output energy. In this chapter crystals with lower critical power for 1030 nm pulses are presented. This might enhance the overall efficiency in terms of energy needed for seed generation compared to the NOPA output energy. Additionally, the near infrared side, the wavelength regime longer than 1030 nm, is investigated for these crystals. Namely, Scandium Aluminium Oxide (Sc_2O_3), Gadolinium Orthosilicate (GSO), Yttrium Orthovanadate (YVO_4) and Gadolinium Vanadate ($GdVO_4$) are investigated and compared to YAG. A detailed description of these crystals (except for GSO) is found in [Bra09, Bra14b] for continuum generation with Ti:Sapphire pulses. GSO is a scintillator material. It is yet quite unknown for supercontinuum generation. Only Ref. [Ryb14] investigated GSO for continuum generation for excitation wavelengths between 800 - 1600 nm. However, they did not observe the near infrared wavelength side of the continuum for this crystal – this is done in this chapter.

Fig. 7.1 shows the visible wavelength range of continua generated in various crystals with 1030 nm, 300 fs at 50 kHz. The spectra are recorded with a fiber-coupled spectrometer (Ocean Optics, HR4000) and the intensity is calibrated for the detector sensitivity afterwards with a black body radiation lamp (Ocean Optics, HL-3-plus-cal-ext). The residual fundamental after continuum generation is blocked with a shortpass filter (Edmund Optics, high precision shortpass 1000 nm). All spectra are recorded with identical integration time of the spectrometer and the identical fiber. To determine the spectral energy distributions of the continua an interference filter around 800 nm with a full width at half maximum of 10 nm (Thorlabs, FB800-10) is placed in the continuum beam path and its transmission is measured with a sensitive photodiode power sensor (Thorlabs, S120VC).

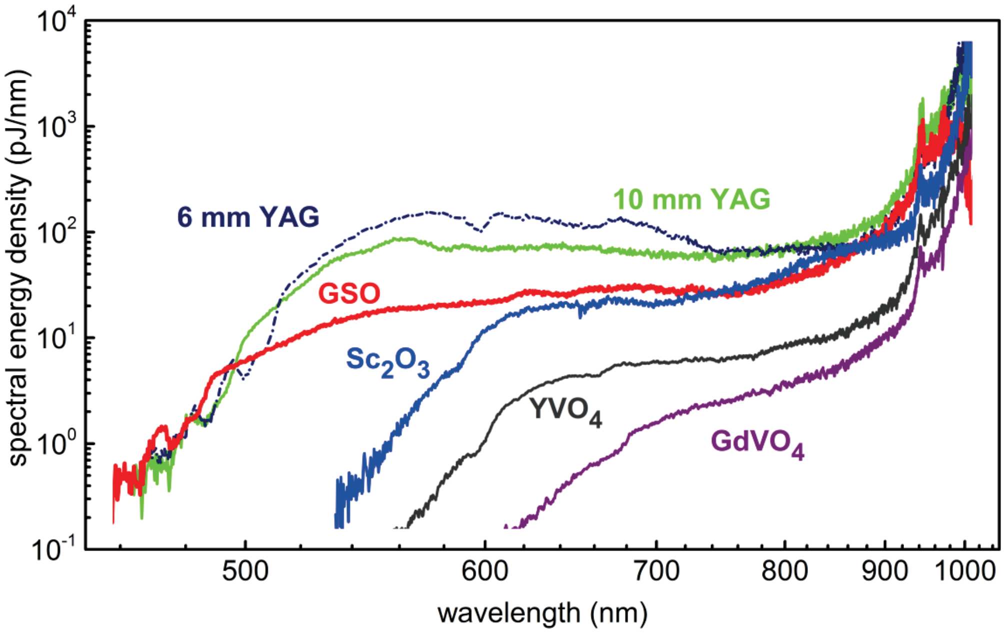

Fig. 7.1: Comparison of spectral energy densities and bandwidths of continua generated with 1030 nm for different crystals.

Close to the fundamental, above 800 nm, the 10 mm YAG crystal generates more photons compared to the other crystals in use. Remarkably, below 800 nm, the 6 mm YAG crystal has a higher spectral energy density, but its spectral width is slightly narrower compared to the 10 mm YAG. The broadest spectrum is generated in GSO, but on the visible side the spectral energy distribution is smaller by one order of magnitude compared to YAG.

Scandium Aluminum Oxide has a similar spectral energy distribution as GSO, but the spectral width is narrower. The cut-off wavelength is at 530 nm, whereas the GSO continuum spreads to 480 nm. The spectral energy distributions of YVO_4 and $GdVO_4$ are smaller by a factor of roughly 1.5 compared to YAG. At the same time, the needed energy for continuum generation is remarkably smaller for these crystals, compared to YAG. The needed minimum energy for continuum generation and for stable operation as well as the refractive indices, band gap, thickness of the used crystals and cut-off wavelengths are summarized in TABLE VII. In appendix A6 a formula for estimation of n_2 is given.

TABLE VII: minimum energy for continuum generation in various crystals E_{min}. Energy E_{stable} for stable continuum operation. Energies refer to 1030 nm, 260 fs, 50 kHz pulses. Also shown are the refractive index n_0, the nonlinear refractive index n_2 and the medium band gap E_g

	thickness (mm)	**E_{min} (µJ)**	**E_{stable} (µJ)**	**n_0**	**n_2 (10^{-16} cm^2/W)**	**E_g (eV)**	**blue cut-off (nm)**
YAG	6	1.8	2.10	1.82	6.9	6.5	490
	10	1.5	1.90				490
$ScAl_{12}O_{19}$	4	0.8	1.58	1.83	3.5	6.0	560
GSO	5	0.6	1.66	1.87	9.1	5.3	480
YVO_4	4	0.4	0.63	1.96	15	3.6	600
$GdVO_4$	4	0.5	0.60	2.01	15	3.6	650

For 515 nm pumped NOPA systems, the spectral width of the continua from Fig. 7.1 is not that limiting at all. By comparing the $GdVO_4$ and YVO_4 spectra with the optimum internal noncollinearity angle for broadband phase matching in a BBO crystal (see Fig. 7.2) it is clear that the spectral width is sufficient for the possible tuning range. Moreover, signal wavelengths lower than 660 nm (corresponding to an idler of 2340 nm) will lead to absorption of the idler in the BBO crystal.

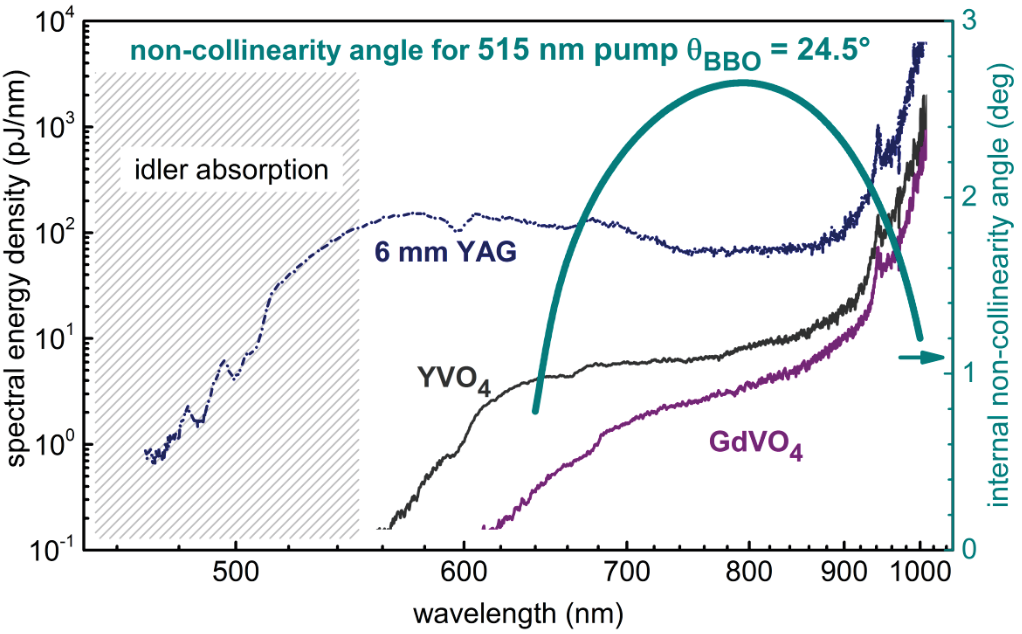

Fig. 7.2: optimum internal noncollinearity angle for a type I BBO crystal (cut at 24.5°) for 515 nm pump (green line), $GdVO_4$, YVO_4 and 6 mm YAG continua for comparison

Especially for 1030 nm laser systems with low output power (or if only a small fraction of the laser power is available to pump a NOPA system), these findings on continuum generation will improve the overall efficiency of future systems. Before saturation effects occur the output energy of the amplifier scales linearly with the seed pulse energy. However, the gain *G* of the amplification is proportional to the pump intensity:

$$G \propto \exp(\sqrt{I_{pump}}) \tag{7.3}$$

Here is a numerical example. Assume a 1 MHz, 10 W laser system with 1030 nm and 300 fs pulse duration. This corresponds to 10 µJ pulse energy. Commonly a 6 mm YAG crystal is used for seed pulse generation. According to TABLE VII, 1.8 µJ are split off for continuum generation. The remaining pulse energy is 8.2 µJ. With 30% efficiency for second harmonic generation this gives roughly 2.5 µJ energy for 515 nm pump pulses. According to the Manley-Rowe equation, this gives, with an efficiency of the OPA process of $\eta = 25\%$

$$E_{signal} = E_{pump} \cdot \frac{\lambda_{pump}}{\lambda_{signal}} \approx 400 \text{ nJ}, \tag{7.4}$$

where a signal wavelength of $\lambda_{signal} = 800$ nm is assumed. Assume now that the 6 mm YAG is replaced with a 4 mm of YVO_4. Hence, the needed energy for continuum generation is reduced to 0.5 µJ per pulse. The remaining pulse energy is 9.5 µJ. With 30 % for second harmonic generation, this refers to a pump pulse energy of 2.8 µJ for 515 nm. Applying equation (7.3) for these values, this gives a signal energy of 450 nJ, corresponding to 12% more output energy.

For various applications it is advantageous to directly seed the amplifier at wavelengths longer than the seed generating fundamental, in the NIR (see following chapter 8 on MIR generation). In general this is done in collinear amplifier geometry for this wavelength region. Experimentally it is often advantageous to introduce a slight noncollinearity between pump and seed – this avoids dichroic optics to separate pump, signal and idler after amplification [Pie00]. Besides from seeding optical parametric amplifiers, the results on continuum generation with 1030 nm are relevant for spectroscopy. In a potential transient spectrometer based on a 1030 nm pump laser system, these pulses can be used as broadband probe light in the near infrared region.

Fig. 7.3 shows the near infrared parts of the continua generated with the crystals of TABLE VII.

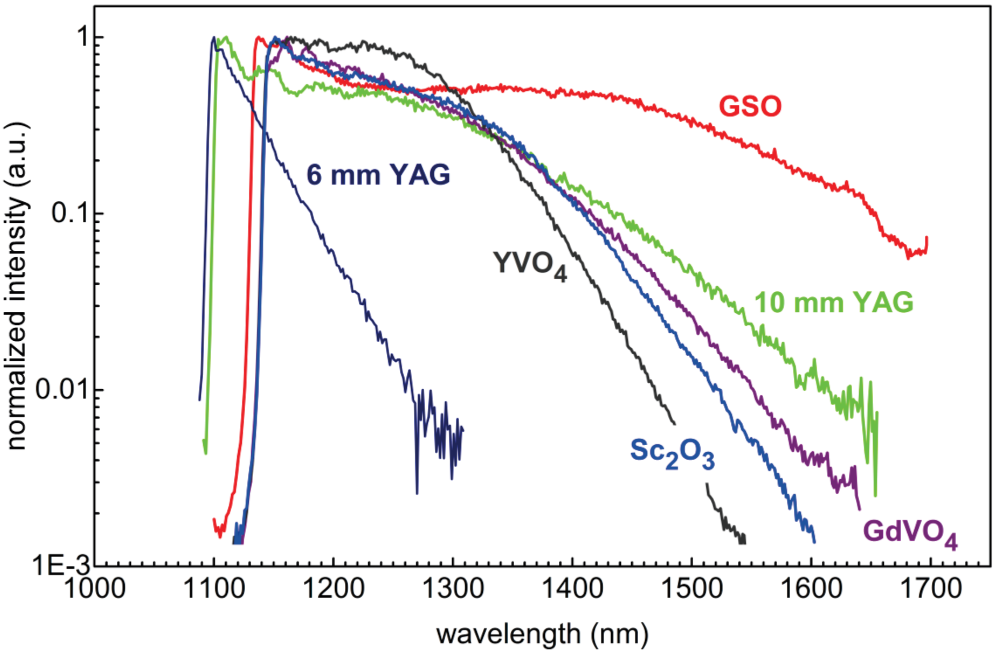

Fig. 7.3: Near infrared side of continua generated with 1030 nm, 300 fs, 50 kHz for various crystals.

The residual fundamental pulses after continuum generation are blocked with a longpass filter (Edmund Optics, high precision longpass 1100 nm). The filter is designed for an angle of incidence of 0° and was tilted to optimize the contrast of the continua. The spectra are measured with a fiber coupled near infrared spectrometer (Ibsen Photonics, ROCK NIR 900-1700 nm) with a low OH-content fiber. The spectra are intensity calibrated to the detector sensitivity afterwards to a black body radiation lamp (Ocean Optics, HL-3-plus-cal-ext).

The very first fact to be mentioned is that, compared to 800 nm excitation, a 6 mm YAG crystal does not offer a strong, plateau-like NIR shift, as reported in Ref. [Bra09]. For a 10 mm YAG plate the cut-off wavelength shifts from 1300 nm to 1600 nm – this is comparable to the case for Ti:Sapphire excitation. These findings are in good agreement with a theoretical and experimental study for continuum generation in YAG crystals by Dubietis and co-workers [Gal15].

The long wavelength cut-off for YVO_4, Sc_2O_3 and $GdVO_4$ is 1468 nm, 1522 nm and 1550 nm, respectively. Nevertheless it has to be mentioned that it is possible to optimize the continua for these crystals on the NIR side, but the spatial mode gets somewhat distorted. If enough energy is available, a 10 mm YAG plate or a GSO crystal is preferable, at least for the use of the NIR side. The measurable width of the continuum generated in GSO is only limited by the detection range of the used spectrometer.

With a bandpass filter for 1300 nm with a FWHM of 48 nm (Edmund Optics, 1300 nm hard coated broadband bandpass, OD > 4.0), the continua of the 10 mm YAG plate and the 5 mm GSO are compared regarding their spectral energy density. Since there was no sensitive power meter available for this wavelength, a NIR photodiode (EOT Inc., ET-3000) is used instead in combination with an oscilloscope. The newly generated frequencies are focused to the active area of the diode with an $f = 30$ mm lens and optimized to the highest signal. The measured amplitude for 10 mm YAG is 240 mV and for GSO 570 mV. Corresponding to a 2.4 times higher spectral energy density for GSO compared to YAG.

These two crystals enable us to directly seed a 515 nm pumped NOPA in the range of 1200 nm – 1600 nm. Fig. 7.4 demonstrates the tuning range for both crystals. The overall slightly higher amplification for GSO seeding is also an indication for the higher energy density of the continuum compared to the YAG continuum.

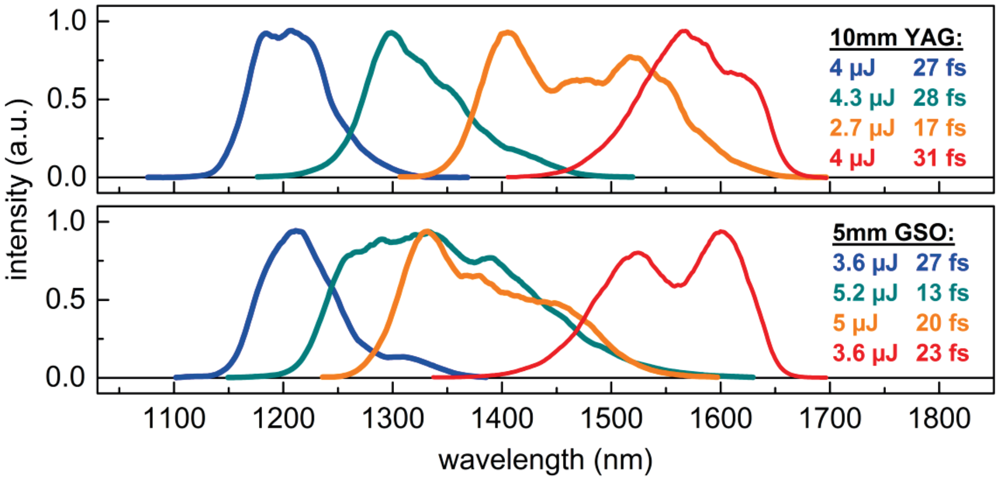

Fig. 7.4: NIR seeded tuning range of a 515 nm pumped NOPA for seed generation in a 10 mm YAG crystal (upper level) and a 5 mm GSO crystal (lower level) at 50 kHz with roughly 50 µJ for the 515 nm pump pulse.

The repetition rate of the laser system is 50 kHz. The pump energy of the 515 nm pulses are roughly 50 µJ. A 5 µJ output pulse at 1300 nm therefore corresponds to a quantum efficiency of 27%.

In this chapter new aspects for bulk continuum generation with 1030 nm pulses were reviewed. In terms of overall efficiency for an optical parametric amplifier, it might be reasonable to use "non-standard" crystals aside from the well-established ones, like YAG and sapphire. For seed pulse generation in the visible region, especially at high repetition rates for Yb-based sources GdVO4 or YVO4 seem to be a good choice.

Furthermore, it was shown that in contrast to continuum generation with Ti:Sapphire systems, a 4 or 6 mm YAG plate is not suitable for broad NIR continuum generation. Thicker plates have be implemented for Yb-based laser systems (here 10 mm YAG are used). A NIR continuum generated with 1030 nm based on a GSO crystal is demonstrated for the first time. Its spectral width on both, the visible and the NIR side is even superior to that of YAG and it has a 2.4 times higher spectral energy density on the NIR side.

Finally, directly NIR seeded NOPA output spectra are demonstrated for 515 nm pump pulses. It is the first time that directly generated 1600 nm pulses pumped with 515 nm are shown with YAG and GSO as continuum generation media.

In the following chapter these findings on continuum generation will be used for seeding a 515 nm pumped NOPA at 1180 nm.

8. Few cycle pulse generation in the middle infrared (MIR) based on parametric amplification

The period of a light field centered around 8 µm corresponds to 27 fs.

$$\lambda = 8\,\mu\text{m} \quad , \quad \nu = \frac{c}{\lambda} = 37.5\,\text{THz} \quad , \quad T = \frac{1}{\nu} = 27\,\text{fs} \tag{8.1}$$

For a single cycle pulse at this wavelength, this period has to be equal to its pulse duration, leading to a spectral width of 16.5 THz (assuming a Gaussian pulse shape):

$$\Delta\nu_{SCP} = \frac{0.441}{T} = \frac{0.441}{27\,\text{fs}} = 16.5\ \text{THz}\,. \tag{8.2}$$

The frequently used definition for single cycle pulse tells that the period *T* corresponds to the FWHM of the intensity distribution *Δt* in the time domain. To demonstrate how a single cycle, a half cycle and a two cycle pulse at this center frequency ν looks like in the time domain, sine and cosine electrical fields for pulses of these parameters are given in Fig. 8.0 (upper panel). As a consequence of the used definition, the field representation is broader by a factor $\sqrt{2}$. For the instantaneous intensity, the square of the cosine fields are shown in the lower panel to illustrate the ratio of the main peak to the side peaks of the field.

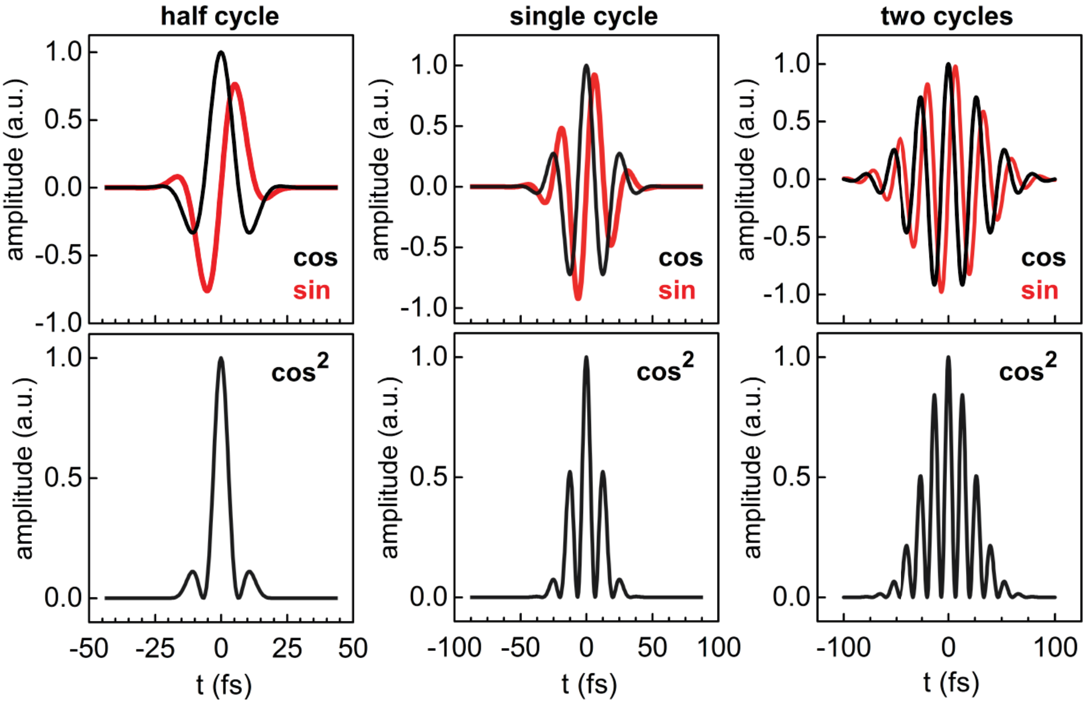

Fig. 8.0: Definition of a half cycle, single cycle and two cycle temporal field at $\nu = 37.5$ THz (upper row). Squared cosine field for instantaneous intensity (lower row).

Since a Gaussian pulse shape is hardly achieved in this spectral region with the needed spectral width, this width is compared to a more flat-top pulse, e.g. a Super-Gaussian (order 4). Assuming this pulse shape, the needed bandwidth $\Delta\nu_{\mathrm{SCP}}$ is 25 THz instead of 16.5 THz to achieve a single cycle pulse at 8 µm. This illustrates the need for precise bandwidth control. Various attempts have been realized to generate MIR pulses with these parameters, but no group was yet able to demonstrate this. A known technique for the attempt is optical-rectification or intra-pulse difference frequency mixing [Kai00, Rei03, Pup15b, Zha18]. However, the overall-efficiency is rather low here and bandwidth control is hardly feasible. Furthermore, intra-pulse frequency mixing leads to a hardly controllable phase in the MIR. With pulse synthesis, based on OPCPA chains, promising results are published [Lia17] but it comes along with high complexity of the setup. In this work the process of optical parametric amplification is used.

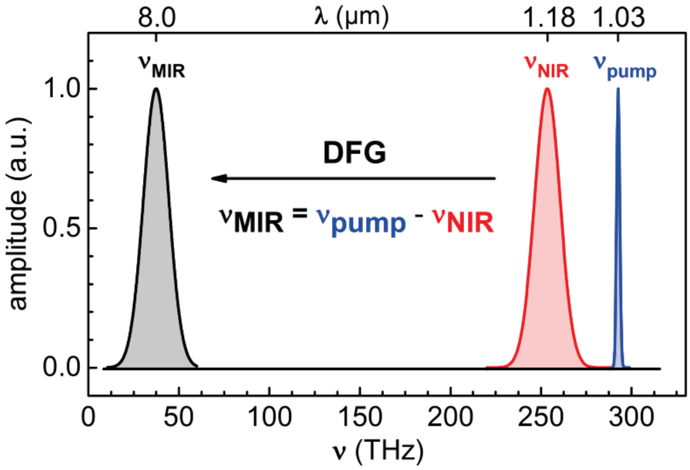

Fig. 8.1: Difference frequency mixing (DFG) scheme to generate a single cycle MIR pulse.

The concept involves an easy to use setup with great flexibility concerning the chirp management. The required spectral widths can be adjusted precisely with optical filters and selected amounts of dispersive material in the seed beam path. The pump laser offers a pulse close to 1030 nm. The major fraction of the total energy of the laser system is used to pump a second harmonic pumped, parametric amplifier [Sch08b] to generate a seed pulse at 1180 nm. With the remaining pulse energy at 1030 nm, the MIR pulses are generated as the idler of a subsequent collinear amplifier [Bra11] based on LGS [Pet15, Kno17] – see spectral schematic in Fig. 8.1. The precisely tailored NIR spectrum is transferred in a controlled fashion to the MIR.

Preliminary results

In our paper [Kno17, appendix A2] we already published preliminary results of the concept of optical parametric amplification for MIR generation. The setup is pumped by a Yb:KGW laser source (Pharos 10, LightConversion). It provides pulses centered around 1026 nm with 190 fs pulse duration at a repetition rate of 190 kHz. The total pulse energy amounts to 53 µJ.

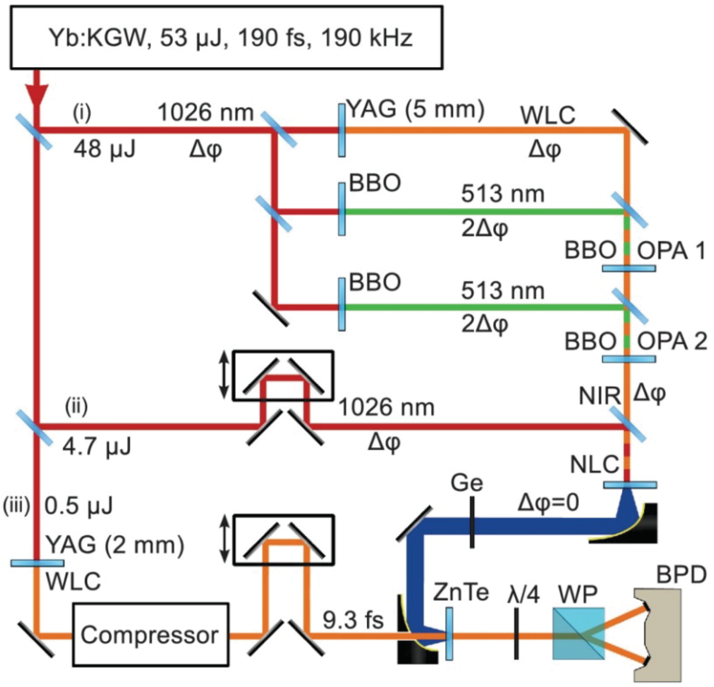

Fig. 8.2: Generation and electro-optic detection of energetic, CEP-stable multi-terahertz pulses at 190 kHz repetition rate. The pulse energies and the CEP fluctuations are given for each branch, starting with the fluctuation *Δφ* of the amplifier system. YAG: YAG crystal, BBO: 2 mm BBO crystal, WLC: white-light continuum, OPA 1,2: stage 1 and 2 of the SHG pumped OPA, NLC: nonlinear crystal for DFG, Ge: 500 µm Germanium, ZnTe: 6.5 µm ZnTe crystal, *λ/4*: quarter-wave plate, WP: Wollaston prism, BPD: balanced pair of photodiodes. Reprinted with permission from Ref. [Kno17].

A modified, commercial two stage OPA is used to generate a signal/idler pair at 900 and 1200 nm. The used OPA is white light seeded (5 mm YAG) and second harmonic pumped collinearly in two subsequent amplifier stages (OPA 1 and OPA 2) based on BBO crystals. The setup is shown in Fig. 8.2, the results are summarized in Fig. 8.3. For a more detailed explanation of the setup and CEP-stability measurements the reader is referred to the original publication [Kno17].

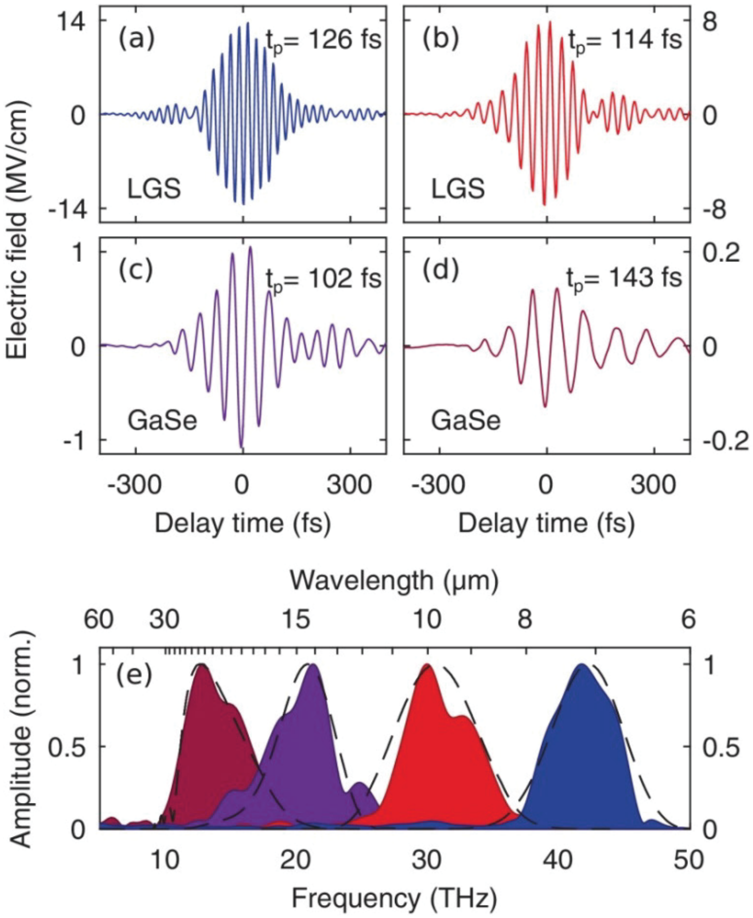

Fig. 8.3: Phase-locked multi-terahertz waveforms. (a)–(d) Waveforms generated in (a), (b) a 1 mm LGS crystal and (c), (d) a 200 µm GaSe crystal, retrieved by electro-optic detection. All field transients have been corrected for the electro-optic response function. The pulse duration t_p (intensity FWHM) is denoted next to each transient. (e) Corresponding normalized amplitude spectra obtained by Fourier transforming the corresponding waveforms in (a)–(d). (The filling colors correspond to the respective waveforms.) Dashed lines: amplitude spectra calculated by convolving the two NIR pulses and accounting for PM. Reprinted with permission from Ref. [Kno17].

The concept provides pulses with tunability from 12 to 43 THz (7 to 25 µm) using two different MIR mixing crystals – GaSe and LGS. Pulse energies of up to 0.16 µJ and peak electric fields of 13 MV/cm in the MIR are achieved. Electro-optic sampling proves the shortest pulse to be 1.8 cycles within the intensity FWHM. To obtain even shorter pulses more seed bandwidth is required. On account of this a new approach is demonstrated in the next section. An amplifier of our own design facilitates more flexibility and consequently gives the possibility for optimal chirp management and provides broader seed spectra for MIR generation.

New approach with noncollinear amplification and chirp management

This new approach was implemented in three labs during the time span of this thesis through cooperation with other institutions. At the moment the presented system is working at the group of Markus Raschke (University of Boulder, Colorado), Rupert Huber (University of Regensbug) and Peter Baum (Ludwig-Maximilians-Universität München). Due to geographic proximity all relevant results of this chapter have been taken in Peter Baum's lab.

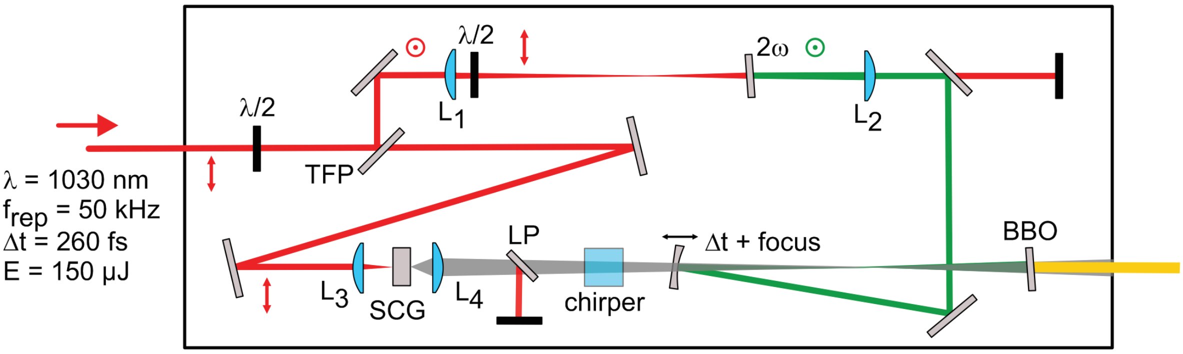

Fig. 8.4: Scheme for the noncollinear optical parametric amplifier.

- **λ/2**: zero order half wave plate for 1030 nm
- **TFP**: 1030 nm thin film polarizer for AOI = 45°
- **L_1** and **L_2**: Fused Silica, plano-convex lens with $f = 250$ mm, AR coated for 1030 and 515 nm, respectively
- **2ω**: second harmonic crystal 800 µm BBO, $\theta = 23.5°$, type I
- **L_3**: Fused Silica, plano-convex lens with $f = 50$ mm, AR coated for 1030 nm
- **L_4**: Fused Silica, plano-convex lens with $f = 30$ mm, uncoated
- **SCG**: supercontinuum generation crystal:10 mm YAG
- **LP**: High Precision Longpass Filter (Edmund Optics, 1100 nm, tilted by ~20 deg)
- **chirper**: 13.9 mm LF7 glass-block
- **Δt+focus**: spherical concave mirror HR515, $f = 250$ mm
- **BBO**: amplifier crystal, 3 mm BBO, type I, $\theta = 24.5°$

The pump laser (Pharos 20, LightConversion) offers a pulse close to 1030 nm with 260 fs pulse duration, a spectral width of approximately 6 nm (FWHM) and an available power of 10 W at a repetition rate of 50 kHz, corresponding to a pulse energy of 200 µJ. A fraction of 150 µJ is used to pump a second harmonic pumped, noncollinear parametric amplifier (NOPA) [Sch08b] to generate a seed pulse at 1180 nm. The scheme of the first noncollinear amplifier stage is shown in Fig. 8.4. The whole setup is installed on a small footprint breadboard (822 × 341 mm^2) with a housing against air turbulences. The input polarization is horizontal. Initially the pulse is split into two arms with the combination of a half wave plate and a thin film polarizer (*TFP*) under an angle of incidence of 45°. The transmission of the *TFP* (horizontal polarization), roughly 1.8 µJ, is used for continuum generation. From previous experiments it is known that the transmission of a thin film polarizer exhibits a much cleaner polarization. Therefore this arm is better suited for continuum generation. Especially with regard to long term stability for high repetition rate systems, this configuration has been proven beneficial. The vertical polarization of the reflected arm, used for pump pulse generation, cleans up anyhow after frequency conversion. With a half wave plate the polarization of the reflection is rotated back to horizontal. An anti-reflection coated, plano-convex, fused silica lens (L_1) with $f = 250$ mm is used to focus the beam towards the frequency doubling crystal (800 µm BBO, $\theta = 23.5°$, type I). The crystal is located behind the focal plane for balancing self-focusing effects. Additionally, this position allows fine-tuning the intensity on the crystal, by moving it closer or further away from the focal region, and hence allows optimizing the doubling efficiency. For the following experiments the distance from L_1 to the crystal is roughly 29 cm, corresponding to a doubling efficiency of 30 % or a pulse energy of 44.1 µJ for the second harmonic at 515 nm. After frequency doubling the light is collimated with lens L_2 ($f = 250$ mm, AR coated for 515 nm) and reflected on two high reflection mirrors with high transmission for the remaining 1030 nm light. A spherical, concave mirror (HR515, 0°) with $f = 250$ mm is fixed to a linear translation stage slightly below the beam height of incidence. This enables a small noncollinearity angle of approximately 1.5° between pump and seed, a time delay for tuning the center wavelength and focusing of the pump towards the amplifier BBO (3 mm BBO, $\theta = 32.5°$, type I). The small noncollinearity angle allows separating pump, signal and idler simply by geometry. For this reason, the NOPA is directly seeded at 1180 nm based on the findings on continuum generation of chapter 7. This is found to be the better approach than to seed the NOPA at 910 nm with use of the idler at 1180 nm for the subsequent experiment. If the idler is used, collinearity of pump and seed is essential; otherwise the resulting idler pulse gets spectrally spread. The collinear geometry requires dichroic mirrors or filters for separation of pump, signal and idler after amplification. This can potentially lead to temporal phase-distortions of the used pulse. In the used directly seeded, noncollinear arrangement the transmitted pump and idler are simply blocked with a beam dump behind the amplifier crystal. No additional optics are needed. The introduction of a small noncollinearity angle in this wavelength regime only slightly reduces the amplified bandwidth. This is an acceptable trade-off, since the bandwidth is anyway narrowed to our needs by introducing selected amounts of glass in the seed beam path. The continuum seed photons are generated by focusing the fundamental wavelength with a fused silica, plano-convex lens with $f = 50$ mm, AR coated for 1030 nm (L_3) to the front surface of a 10 mm YAG plate [Cal15, Bra09] (see also chapter 7). The generated continuum is relay-imaged towards the amplifier crystal with an uncoated fused silica, plano-convex lens with $f = 30$ mm. A longpass filter (High Precision longpass 1100 nm, Edmund Optics) is used to block the residual fundamental after continuum generation and to cut the amplified spectrum from the short wavelength side, by rotating the filter. On the one hand side, this prevents the residual fundamental to introduce distortions in the amplification process. On the other hand the limitation of the short wavelength will prevent the generation of too long MIR wavelengths in the subsequent DFG in LGS. Above 11 µm LGS starts to absorb [Che18]. Consequently, NOPA wavelengths shorter 1130 nm are cut off to prevent crystal damage. A glass block of 13.9 mm LF7 introduces a chirp of 554.6 fs^2 (for 1180 nm). As the chirp of the white light increases, the spectro-temporal overlap with the pump pulse decreases in the amplifier crystal and limits the amplified spectrum on the long wavelength side. This is advantageous because generated frequencies that do not fulfill the phase-matching conditions for the LGS of the subsequent stage, will only decrease the efficiency in MIR generation. The described chirp management inside the seed beam path allows tailoring the NOPA spectrum exactly to the required parameters of Fig. 8.1. The measured NOPA spectrum is shown in Fig. 8.5. It is measured with a fiber coupled spectrometer (Ibsen Photonics, ROCK NIR 900 – 1700) and intensity calibrated against the detector sensitivity afterwards. The center frequency corresponds to 254 THz (1180 nm) with a spectral width of 18 THz, corresponding to a Fourier limit of 24.5 fs. The output energy of 4.1 µJ equals a quantum efficiency of 21.5% of the amplification process with respect to the 515 nm pump wavelength.

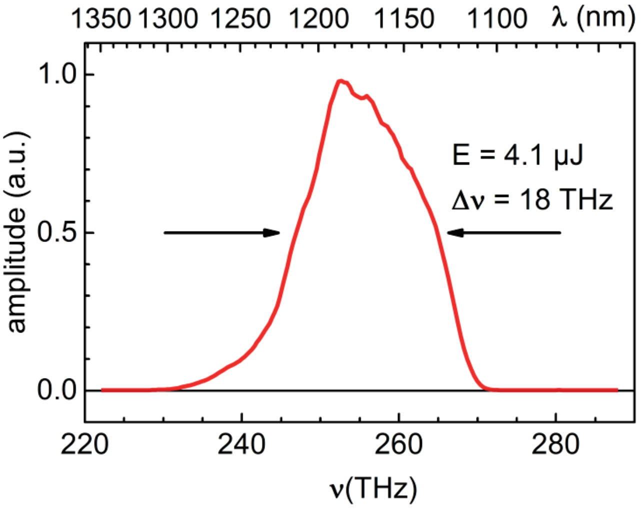

Fig. 8.5: NOPA spectrum at 254 THz with $E = 4.1$ µJ and a spectral width $\Delta\nu = 18$ THz.

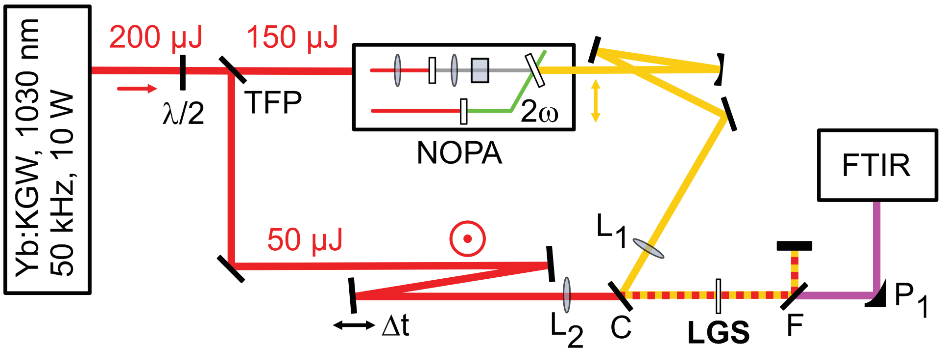

Fig. 8.6: Setup scheme for MIR generation in LGS.

- **λ/2**: zero order half-wave plate for 1030 nm
- **TFP**: thin film polarizer (AOI = 45°, for 1030 nm)
- **NOPA**: 515 nm pumped noncollinear optical parametric amplifier (for details on that part, see text and Fig. 8.4)
- **L_1, L_2**: f = 250 mm, plano-convex lens AR coated
- **C**: combiner mirror (Laser Components, HR1150/45°) reflection of the seed, transmission of pump
- **Δt**: flat mirror on mechanical translation stage for optimization of temporal overlap
- **F**: Filter to suppress DFG input pulses and transmit MIR (Edmund Optics, Germanium long pass filter, 4.5 µm)
- **P_1**: parabolic gold mirror, f = 150 mm
- **LGS**: second, collinear amplification stage for MIR generation
- **FTIR**: LASNIX, L-FTS spectrometer

To generate the broad MIR spectrum – according to Fig. 8.1 – the NOPA pulses are amplified in a subsequent collinear amplification stage based on LGS. The resulting idler pulse corresponds to the MIR field at the difference frequency of the NOPA (1180 nm) and the pump laser at 1030 nm. The collinear geometry in the LGS stage allows the use of the MIR idler without spectrally dispersing the pulse.

With a spherical silver mirror (r_{cc} = -1000 mm, LAYERTEC) the NOPA output is collimated. Afterwards, the lens L_1 (f = 250 mm, plano-convex, fused silica, AR coated) is used to image the collimated beam towards the amplifier crystal. Care is taken, that the focal plane of the beam is located in front of the crystal (roughly 1 cm). A mirror reflecting the pump beam under a small angle of incidence on a mechanical translation stage is used to adjust and optimize the temporal overlap of the two optical paths. The pump is focused with the lens L_2 (f = 250 mm, plano-convex, fused silica, AR coated) towards the amplifier crystal. The $1/e^2$ diameter of the pump on the amplifier crystal corresponds to roughly 700 µm, the focal plane is also located in front of the crystal. The peak intensity of the pump is 71 GW/cm^2 at the LGS. The spot size at the LGS of the 1180 nm beam is initially matched to the pump spot size with the help of a beam cam. Afterwards, the beam sizes of the pump and the 1180 nm beam can be optimized on the overall performance by moving the lens L_2 and the LGS crystal position along the beam path. Both arms are overlapped on the combiner mirror (*C*, in Fig. 8.6). This is a HR1150/45° mirror manufactured by LaserComponents. It has transmission of roughly 85% for 1030 nm in vertical polarization and high reflection for 1100 - 1300 nm in horizontal polarization under an angle of incidence of 30°. It is on a fused silica substrate with 1 mm thickness.

The filter *F* is an Edmund Optics long pass filter at 4.5 µm. It is a coated, 1 mm thick Germanium plate. It is used to block the two input beams. The generated MIR is transmitted.

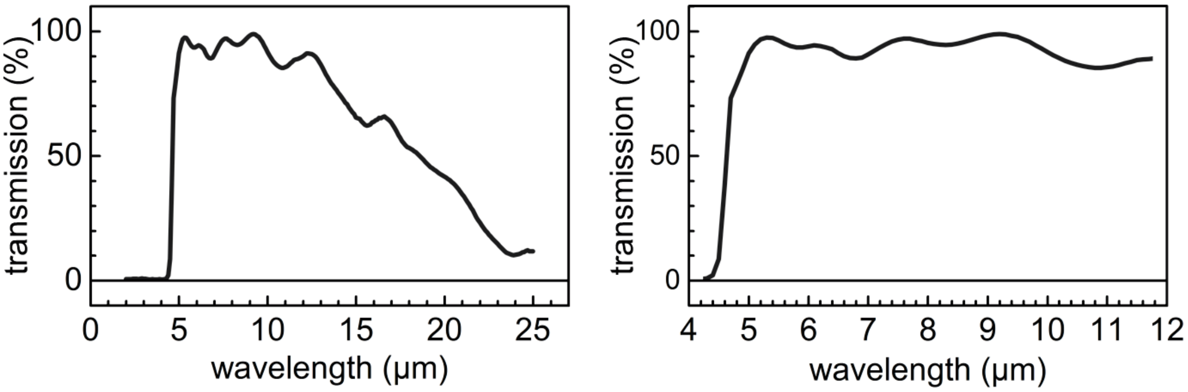

Fig. 8.7: Transmission data for AOI = 45° of the long pass filter 4.5 µm on 1 mm Germanium substrate (data supplied by Edmund Optics). Right panel: relevant range for the experiment.

The transmission curve of the filter *F* is shown in Fig. 8.7. In the experiment no transmission of the seed and the pump through the filter can be detected with a power meter and a spectrometer.

After the filter *F* the MIR gets collimated by a parabolic gold mirror (Thorlabs, f = -103.2 mm) and analyzed by a FTIR spectrometer. The spectrometer is a lamellar FTIR spectrometer (LASNIX, L-FTS) with ultra-wide coverage from 0.4 – 300 µm and a spectral resolution of 6.3 cm^{-1}. An update rate of the Fourier transformation of 2 spectra/sec allows online tweaking of the MIR field. This is really beneficial regarding the alignment of the MIR compared to a monochromator, where the spectrum update range is on the order of a few 10 sec.

The choice of the mixing crystal for MIR generation

The used LGS crystal is xz-cut with a thickness of 0.5 mm, $\theta = 48.3°$ and $\phi = 0°$. The nonlinearity of this configuration is $d_{eff} = 4.59$ pm/V. It offers large phase-matching bandwidth around 8 µm. The full width at half maximum of the acceptance bandwidth corresponds to 55cm^{-1}cm [SNLO]. For this wavelength region – compare Fig. 8.8a) – this is superior to all other known crystals and makes it possible to compensate for the comparatively lower nonlinearity with crystal thickness.

In Fig. 8.8b) the intensities and the nonlinear coefficients of the crystals are shown. The pump intensity I_p for 1030 nm correlates to the value where $G = 5$. G is the gain factor given by [Ree95]:

$$G = \frac{1}{4}\exp\left(2 \cdot L \cdot \sqrt{\frac{8 \cdot \pi^2 \cdot d_{eff}^2 \cdot I_p}{n_p \cdot n_s \cdot n_i \cdot \lambda_s \cdot \lambda_i \cdot \varepsilon_0 \cdot c}}\right), \tag{8.3}$$

n_p, n_s, n_i are the refractive indices for pump, signal and idler. L is the crystal thickness, which is set to

$$L = \frac{\text{accept b.w.(FWHM)}}{\Delta\nu_{SCP}}. \tag{8.4}$$

Here $\Delta\nu_{SCP} = 551$ cm^{-1}, corresponding to the spectral width for a single cycle pulse at 8 µm. The FWHM of the acceptance bandwidths are given in Fig. 8.8a).

Using e.g. GaSe as an amplifier medium, the needed intensity increases at least by a factor of 5 compared to the intensity for LGS in xz-cut. This is of central importance to consider, because of two-photon absorption. LGS is transparent down to 320 nm, this ensures that two photon absorption of the pump pulse (1030 nm) is not an issue, regarding damage or a change of the phase-matching condition due to a thermal gradient [Kum15]. For comparison GaSe is only transparent down to 650 nm – making it a critical choice for 1030 nm pumping. Additionally, the needed pump intensity for GaSe is close to, or almost its damage threshold [Guo15]. Moreover, in terms of surface quality LGS is superior to GaSe [Pet15], which is an important fact when working with rather large spot sizes, because surface distortions on the crystal area seen by the spots of pump and seed will directly couple to phase distortions of the resulting MIR.

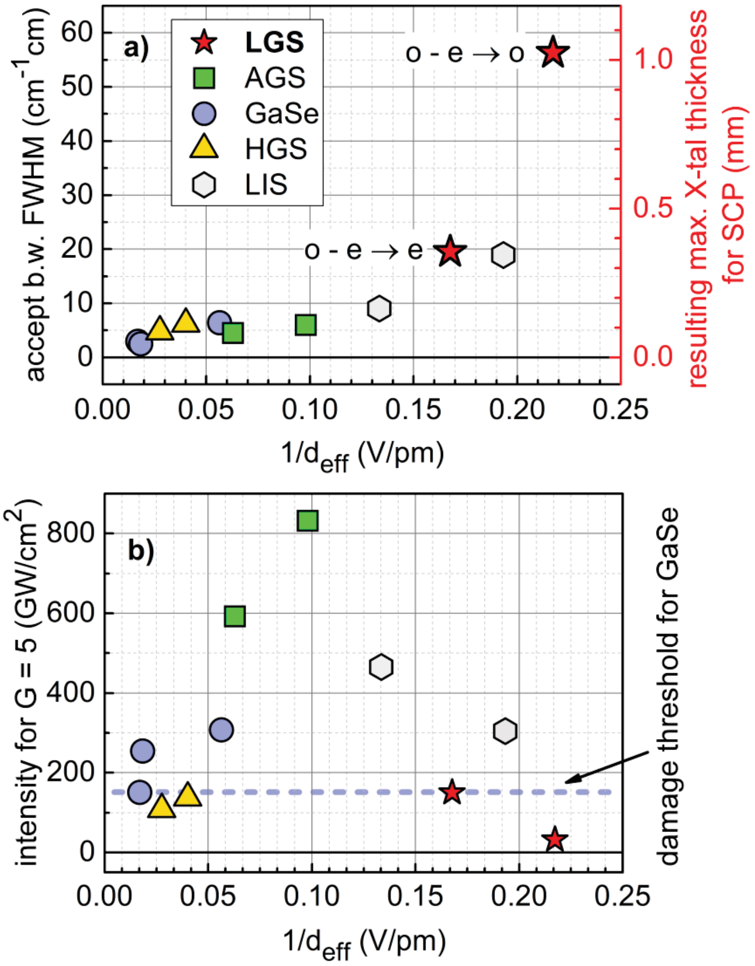

Fig. 8.8: (a) Overview of crystals offering DFG to 8 µm (with 1030 nm and 1180 nm as input wavelengths). The effective nonlinearity d_{eff} is shown reciprocal against the FWHM acceptance bandwidth of each crystal – each data point equals a certain phase matching configuration. On the right axis (in red) the maximum crystal thickness to obtain the width for a single cycle pulse (SCP) is shown. Data is taken from [SNLO].

(b) Pump intensity needed for a gain of $G = 5$ – compare Eq. (8.3) for each crystal, where the crystal thickness L is adapted to support single cycle pulses with 551 cm^{-1} bandwidth at 8 µm.

Phase-matching in xz-cut LGS

Fig. 8.9 shows the phase-matching for the xz-cut LGS crystal, which is basically obtained by, solving the equation for biaxial birefringence [Yao91, Smi18b]. For a detailed calculation see appendix A7:

$$\frac{\sin(\theta)^2 \cdot \cos(\phi)^2}{\frac{1}{n^2} - \frac{1}{n_x{}^2}} + \frac{\sin(\theta)^2 \cdot \sin(\phi)^2}{\frac{1}{n^2} - \frac{1}{n_y{}^2}} + \frac{\cos(\theta)^2}{\frac{1}{n^2} - \frac{1}{n_z{}^2}} = 0. \qquad (8.5)$$

Fig. 8.9 also compares two crystal thicknesses – 0.5 and 1.0 mm – and shows that slightly tilting the crystal from the optimum can lead to even broader phase-matching bandwidth.

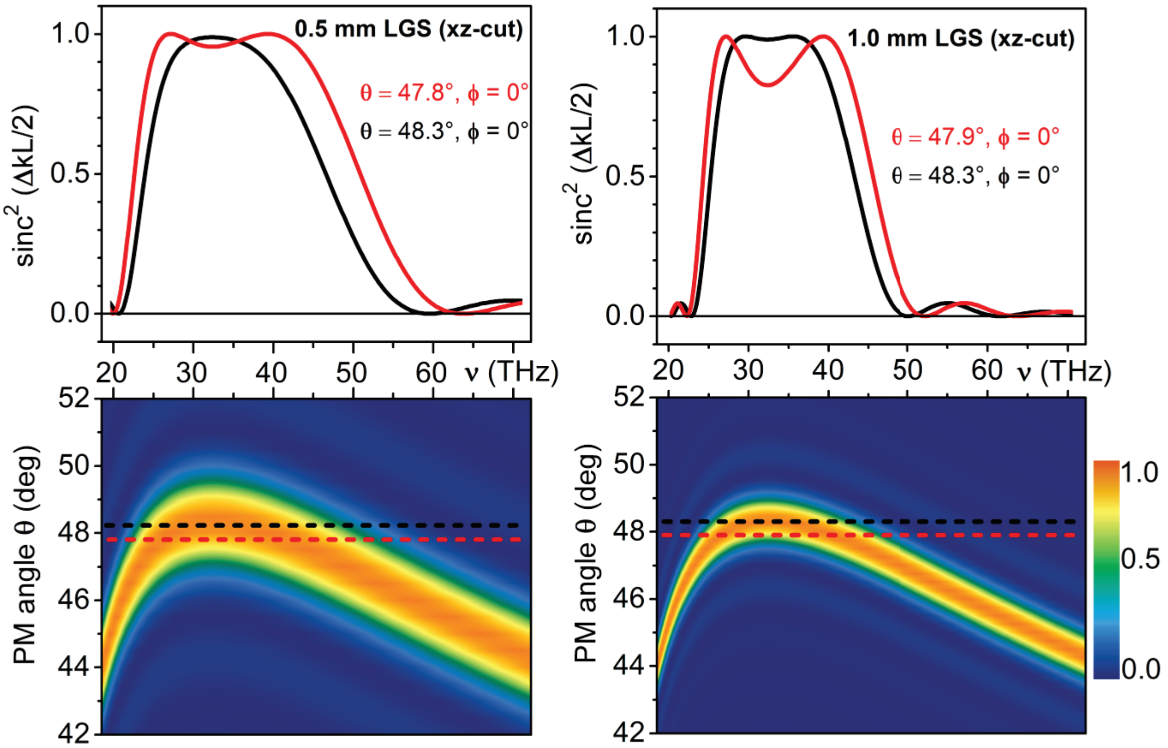

Fig. 8.9: Phase-matching of a 0.5 mm (left column) and a 1 mm xz-cut LGS (right column) as a function of the PM angle for difference frequency mixing with the pump wavelength of 1030 nm. The row above shows the *sinc²* function according to the position of the color coded slices for different tilt angles.

The possible MIR Fourier limits, obtained by Fourier transformation of the *sinc²* phase-matching functions, given in Fig. 8.9, are 29.5 fs (1.1 cycles), and 25.4 fs (0.95 cycles) for the 0.5 mm LGS at $\theta = 48.3°$ and 47.8°, respectively. For 1 mm LGS they correspond to 40.8 fs (1.5 cycles) and 35.8 fs (1.3 cycles) for $\theta = 48.3°$ and 47.9°, respectively.

The resulting, experimental amplified MIR spectrum is shown in Fig. 8.10a). It corresponds to the MIR idler of the LGS amplification of the 4.1 µJ NOPA pulses centered around 1180 nm with the 1030 nm pump pulses in 0.5 mm LGS. The obtained MIR energy corresponds to 340 nJ for maximum amplification. In order to avoid crystal damage and ensure long term stability of the MIR, the LGS was moved further away from the focal plane of the pump beam. This gives a lower but long term stable MIR energy of 200 nJ.

To prove that the MIR generation is in the **parametric amplification region**, two subsequent HR1030/0° HT1200 nm mirrors are placed behind the amplifier crystal, in a way that all pump power is reflected and all MIR power is absorbed in the mirror substrate. With a power meter the amplification of the 1180 nm pulse can be measured. With opening the pump pulse the power goes up by a factor of 1.6 – corresponding to a rise from 3.1 to 5 µJ at 1180 nm or a quantum efficiency of 8% (for 42.5 µJ pump pulse energy). This takes into account the Fresnel losses of the LGS crystal. The LGS transmission of 1180 nm is about 77%. The power in the experiment is measured with a Coherent PS19 power meter.

Scaling the gain to the MIR wavelength according to the Manley-Rowe equation this gives 250 nJ theoretically – close to the experimental value. In Fig. 8.10b) the resulting measured MIR spectrum (red) is compared to the calculated MIR spectrum (black, dotted line), where the NOPA spectrum (black) is shifted by the pump (blue). At the low frequency side of the MIR pulse the starting absorption of LGS narrows the bandwidth slightly. Reducing the chirp in the seed of the NOPA, longer NIR wavelengths will be generated. Compared to the phase-matching function for 0.5 mm LGS in Fig. 8.9, more high MIR frequencies are expected after mixing.

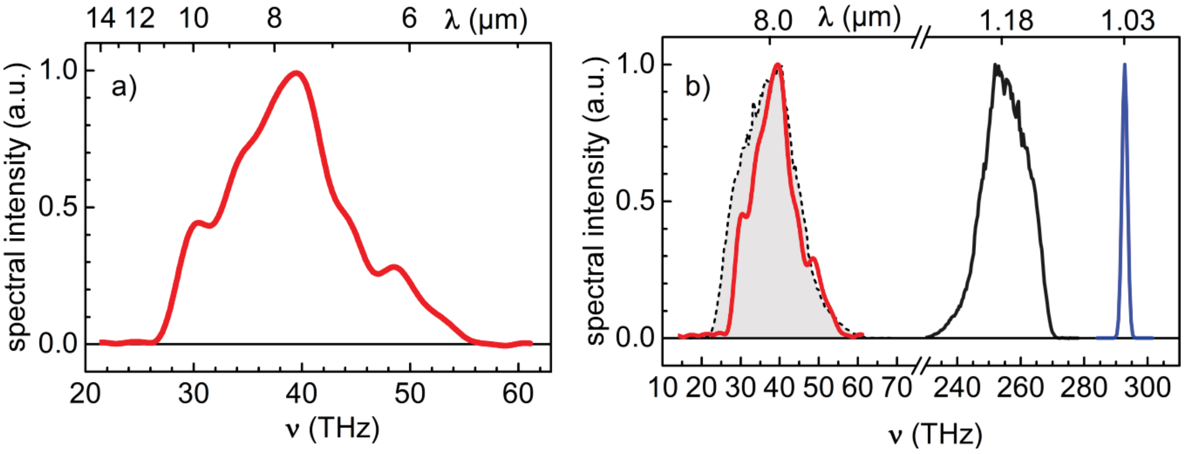

Fig. 8.10: a) MIR spectrum for 0.5 mm LGS. b) NOPA spectrum (black) and pump pulse spectrum (blue) and the calculated (shifted) DFG spectrum (black dashed line).

Chirp estimation and considerations on MIR compression

The Fourier limit of the measured spectrum corresponds to 35.5 fs – equal to 1.3 cycles. Since the NOPA output possesses an up-chirp (reddish frequencies travel faster than blueish) the difference frequency mixing inevitably leads to a down-chirp in the MIR. Hence, the MIR pulse can be compressed by transmission through proper material. In the following, an estimation for the compression by transmission through a Germanium window will be demonstrated. Therefore, the total group delay from the seed beam generated in the YAG plate to the amplified NOPA signal is calculated with respect to every dispersive material in the beam path – see Fig. 8.11 and TABLE VIII.

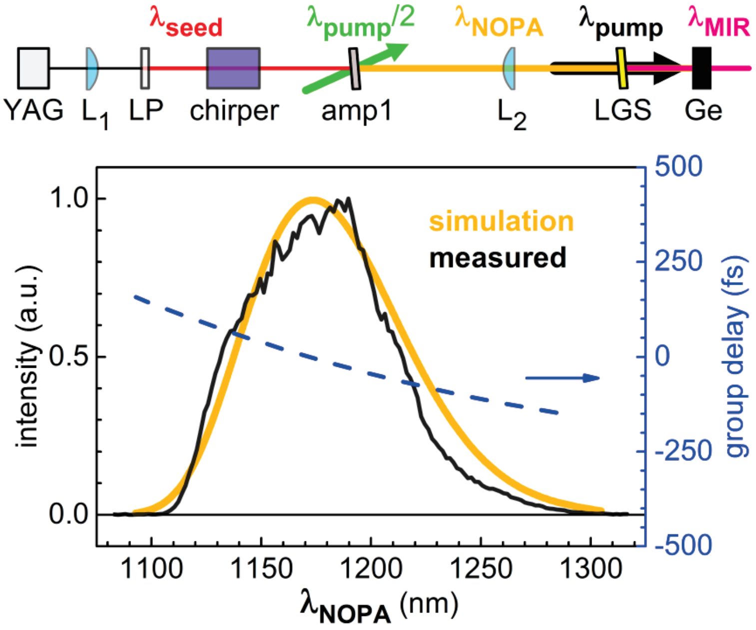

Fig. 8.11: Estimated NOPA output spectrum (orange) and group delay (blue, right axis) by adding successively all dispersion of the different materials in the beam path to the seed beam. For comparison the measured NOPA spectrum (black) is shown. For details to the materials see TABLE VIII.

With a simulated, co-propagating 515 nm pump pulse through the amplifier crystal of the NOPA, also the NOPA spectrum can be simulated, by summing up the projections of the pump intensity on the seed group delay for different, relative delays. For details to this simulation for the output spectrum and the corresponding group delay, see appendix A4. The group delay of the NOPA output is shown in blue in Fig. 8.11.

TABLE VIII: Characteristics of dispersive material in the beam path for MIR generation.

abbreviation	function	material	thickness	n(λ) reference
YAG	continuum generation	YAG	10 mm	[Zel98]
L_1	relay imaging of continuum	fused silica	3.7 mm	[Mal65]
LP	long pass filter – to block 1030 nm	fused silica	3.0 mm	[Mal65]
chirper	spectral narrowing	LF7	13.9 mm	[Pol18]
amp 1	amplification of seed	BBO	3.0 mm	[Zha00]
L_2	imaging of NOPA to LGS	fused silica	3.0 mm	[Mal65]
LGS	amplification of MIR	LGS	0.5 mm	[Kat17]
Ge	compression of MIR	Germanium	1.0 mm	[Ice76]

In Fig. 8.12 it is demonstrated how the NOPA group delay (a) is transferred to the group delay of the MIR shown as red curve in (b). Here also the group delay introduced by a 2.5 mm Germanium window is shown as grey, dashed line. The flattened group delay of the MIR pulse after transmitting through the Germanium window is shown in (c). Accordingly, the simulation shows, that it is possible to compress the MIR pulse by transmission through Germanium. The actually needed thickness of Germanium in the beam path to get close to a single cycle pulse will be shown experimentally by electro-optical sampling with an ultrashort gate pulse. The description of the used EOS setup, a simple way for generating an ultrashort pulse and the results will be discussed in the following part.

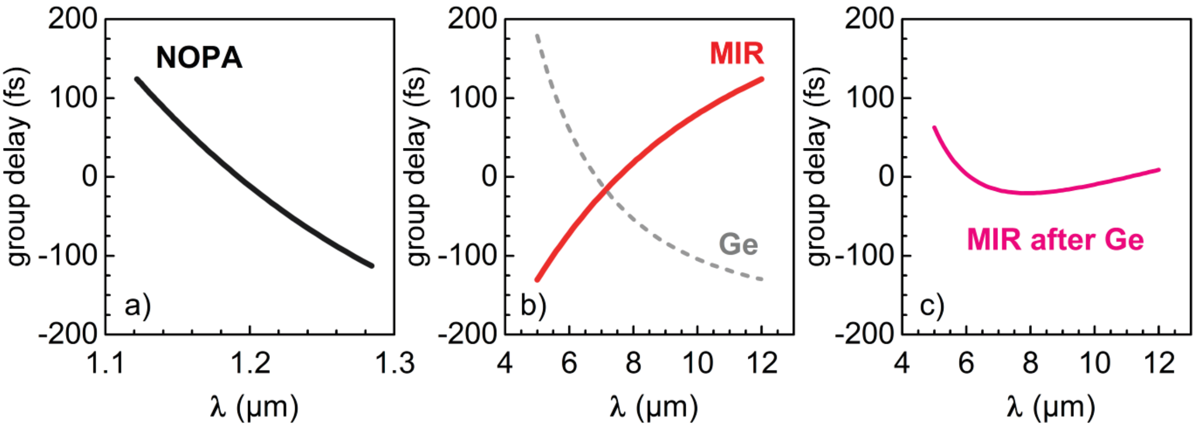

Fig. 8.12: Calculated group delay for a) the NOPA pulse, b) the resulting MIR pulse (red) and the group delay introduced by 2.5 mm Germanium (grey, dashed), c) the MIR group delay after transmission of 2.5 mm Germanium.

Sub-10 fs gate pulse generation by self-compression in 1 mm YAG

For the measurement of the electric field of a MIR pulse with electro optic sampling [Wu97, Hub00, Liu04, Kue04, Gro08, Por14, Kei16, Kno17] an ultrashort gate pulse is required. For this purpose, a very simple method to shorten a pulse is presented. Self-compression due to continuum generation of the Pharos laser in a 1 mm YAG plate is shown. The continuum is generated with an $f = 50$ mm lens. The numerical aperture corresponds to $NA \approx 0.04$, with a $1/e^2$ beam waist of 2 mm. A pulse energy of roughly 3 µJ at a repetition rate of 50 kHz with 1030 nm and 260 fs pulse duration in the YAG plate is needed. The resulting ultrashort pulse has a width of 9 fs only, without the need for an additional compression scheme. The effect was already demonstrated with a 1 kHz Ti:Sapphire laser with a 1 mm sapphire plate [appendix A1] during the time of this work. For higher average power at higher repetition rates, YAG is superior to sapphire as generation medium, due to its higher damage threshold and lower threshold for continuum generation [Bra09]. There are some attempts for self-compression based on filamentation in the literature [Cou05, Cou06, Sti06], but most of them require complex setups for filamentation in gaseous media. In contrast, the presented setup is extremely simple and relies only on a few off the shelf optics and bulk continuum generation. The arrangement for the temporal characterization of the self-compressed pulse is shown in Fig. 8.13. The energy for continuum generation is optimized with a combination of a $\lambda/2$ plate and a thin film polarizer (*TFP*) for an angle of incidence of 45°. The focal plane of the fundamental beam is placed on the front surface of the YAG plate [Bra09]. At this position the energy for continuum generation is minimized and a single filament is generated at the very end of the crystal. The newly generated frequencies close to the driving frequency remain nearly unchirped after the abrupt generation process. For the high frequency components of the continuum, the generation process stops earlier because of group velocity mismatch with the driving frequency. For these frequencies the resulting chirp increases, since they diverge out of the filament channel and hence propagate through the medium and acquire chirp. For more details on this process the reader is referred to [Bra14b] and appendix A1.

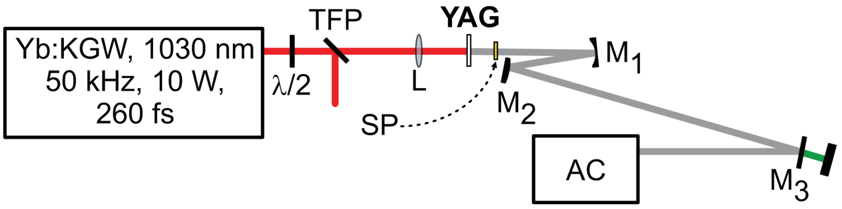

Fig. 8.13: Schematic view for measurement of self-compression in 1 mm YAG.

Downstream from the continuum generation in the 1 mm YAG plate, the fundamental is filtered by an Edmund Optics High Precision Shortpass Filter 975 nm (*SP* in Fig. 8.13). Without the short pass filter mainly the fundamental pulse is measured. This pulse is long and distorted due to highly nonlinear processes during continuum generation. The transmitted continuum is imaged with a Schiefspiegler telescope (M_1 and M_2 in Fig. 8.13) to avoid astigmatism and reflected on an Asahi XIS0780 short pass filter (M_3 in Fig. 8.13). For details concerning the Schiefspiegler telescope see chapter 3. Fig. 8.14 shows the reflection curve of the ASAHI filter under 45° for p-polarized, as well as the transmission for the used Edmund Optics High Precision Short pass filter at 975 nm.

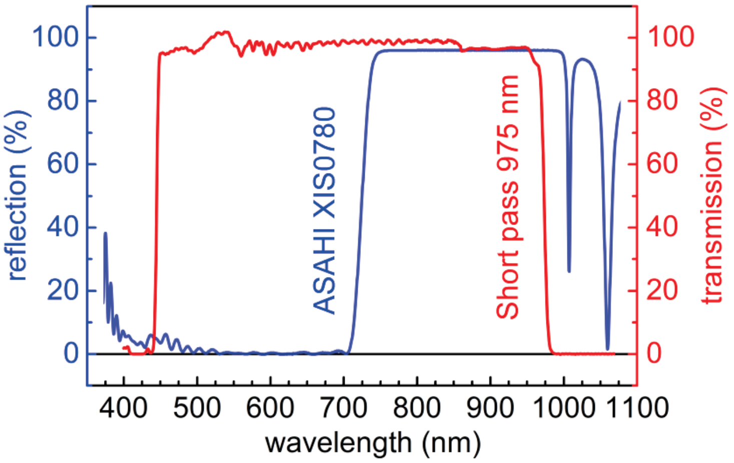

Fig. 8.14: Reflection of Asahi XIS0780 for 45° angle of incidence (p-polarization). Transmission for Edmund Optics Short Pass 975 nm.

The filter transmits the short wavelength parts of the continuum in which the temporal chirp increases as described above, while "unchirped" frequencies close to the driving fundamental are reflected towards the experiment. The experimental angle of incidence on the filter is optimized with a fiber coupled spectrometer for least spectral modulations – an angle of incidence of roughly 30° is found to give the best result.

The spectrum of the continuum is shown in Fig. 8.15 for the case of a single reflection on the ASAHI filter (red) and for comparison directly after generation (grey curve). The spectra were taken with a fiber coupled spectrometer (OceanOptics, HR4000) and intensity calibrated against the detector sensitivity afterwards.

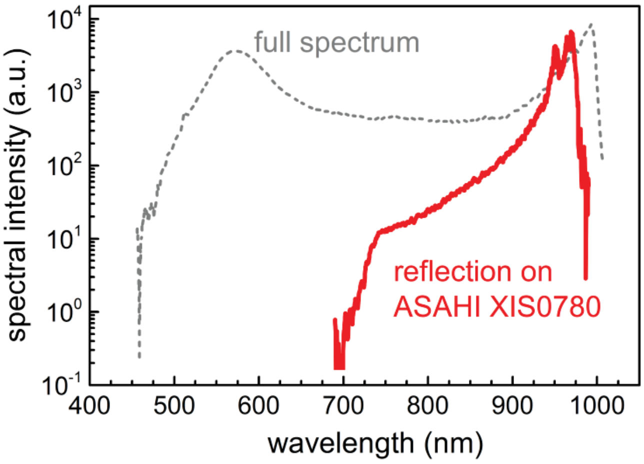

Fig. 8.15: white light spectrum generated in 1 mm YAG with an Edmund Optics High Precision Shortpass 975 nm in transmission and with ASAHI XIS0780 filter in reflection (red). For comparison the full spectrum without reflection on the ASAHI filter is shown in grey.

For temporal characterization a SHG intensity autocorrelator [Koz04] is used with a 25 µm BBO crystal, which supports frequency doubling of the full spectral width of the pulse.

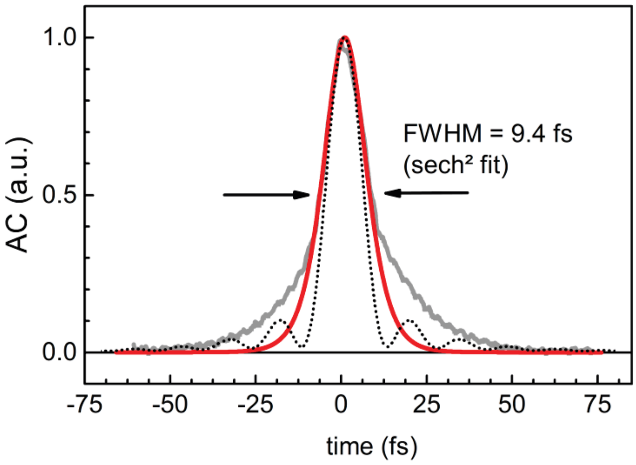

Fig. 8.16: Intensity autocorrelation measurement of the self-compressed pulse of the 1 mm YAG plate (grey). Deconvoluted pulse duration corresponds to a 9.4 fs pulse assuming a *sech*^{2} function (red). The Fourier limit of the pulse is shown as black, dotted line. A 25 µm BBO crystal was used for frequency doubling in the AC measurement.

The calculated pulse in the time domain (black, dotted line in Fig. 8.16) supports a Fourier limit of 7.8 fs. This pulse shows some wings which cannot be resolved in our measurement (grey dots). The deconvoluted pulse duration corresponds to 9.4 fs, assuming a *sech*^{2}

function. This short pulse duration is required for a reliable temporal resolution in the EOS trace. For reasonable gating of the MIR field, the gate pulse should be shorter than half a period $T = 27$ fs. With the presented strategy for gate pulse generation, this is easily achieved.

Stability of the white light generation for EOS gating

For high repetition rate laser systems the possible damage of the nonlinear crystals due to heat overload is a crucial topic. This is of particular importance for the relatively long pulse durations of 1030 nm laser systems. The stability and the "lifetime" of the 1 mm YAG continuum were monitored overnight. A power meter (Coherent, FieldMax + PS19) was used to monitor the stability, after blocking the fundamental with the short pass filter. Roughly every 5 seconds a measurement was taken. Simultaneously, the laser stability was monitored. Fig. 8.17 shows that the continuum pulse is stable for hours. After 6.5 hours the generation stopped. In the next morning a slight shift of the crystal perpendicular to the beam direction was enough to get back to stable continuum generation with the 1 mm YAG. But continuum generation was not reproducible at the same spot – a hole was burned on the YAG surface. With a photodiode the RMS of the white light pulse was measured to be 0.3% for single shot detection at 50 kHz, which is comparable to the noise of the pump laser.

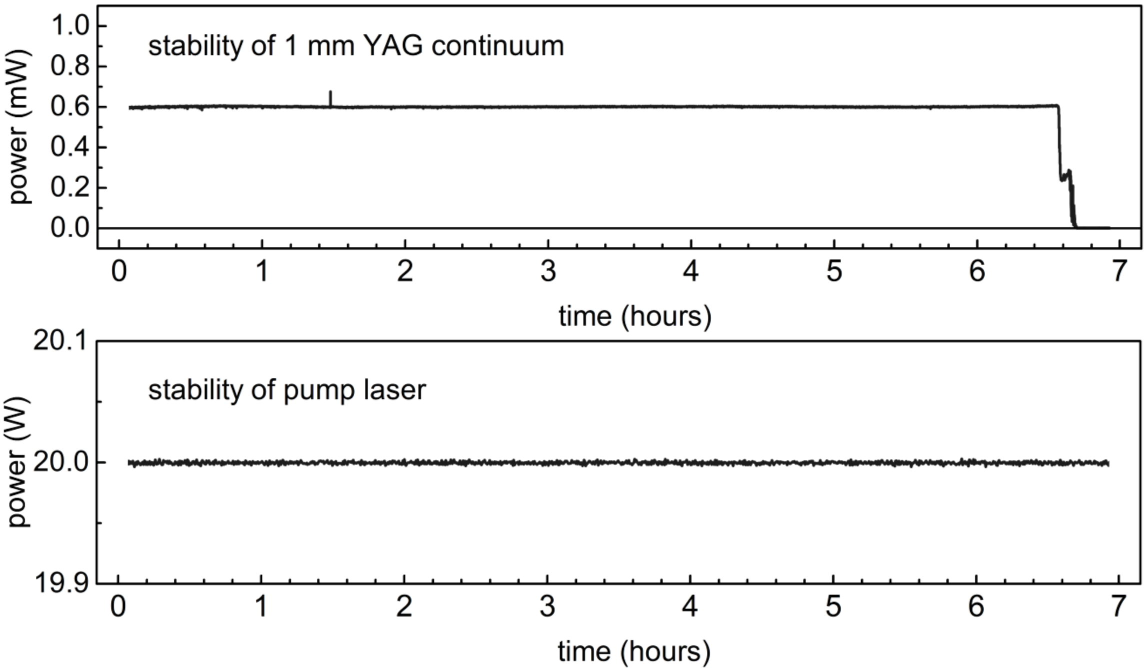

Fig. 8.17: Stability of 1 mm YAG continuum (upper panel) and of the pump laser (lower panel) both traces are measured simultaneously at a repetition rate of 50 kHz.

Pre-consideration on the phase-matching conditions in GaSe for EOS

The ultrashort gate pulse in EOS fulfills two purposes: It serves as local oscillator for detection and it is used for sum-(or differency-) frequency generation with the MIR pulse in GaSe. In the following sum-frequency generation in GaSe in a type II configuration is chosen:

$$7500\,\mathrm{nm}\,(\mathrm{e}) \; + \; 950\,\mathrm{nm}\,(\mathrm{o}) \; \rightarrow \; 840\ \mathrm{nm}\,(\mathrm{o}). \tag{8.6}$$

Sum-frequency generation is advantageous in the present case, because it offers a slightly broader phase-matching bandwidth compared to difference frequency generation. Additionally, the sum-frequency can be detected with a silicon detector whereas for difference frequency generation InGaAs detectors are needed. The phase-matching condition for sum-frequency generation reads:

$$\Delta k = k\left(\omega_{\mathrm{MIR}}\right) + k\left(\omega_{\mathrm{gate}}\right) - k\left(\omega_{\mathrm{MIR}} + \omega_{\mathrm{gate}}\right) = 0. \tag{8.7}$$

The numerical solution for this condition is found at a GaSe angle of $\theta = 19.6°$. **For optimal gating the group velocity of the gate pulse $\mathbf{v}_{gr,gate}$ and the phase velocity of the MIR $\mathbf{v}_{ph,MIR}$ should be matched** [Nah96, Ste05]. By rearranging Eq. (8.7) to

$$k\left(\omega_{\mathrm{gate}} + \omega_{\mathrm{MIR}}\right) - k\left(\omega_{\mathrm{gate}}\right) = k\left(\omega_{\mathrm{MIR}}\right), \tag{8.8}$$

and dividing by ω_{MIR} the following relation is obtained:

$$\frac{k\left(\omega_{\mathrm{gate}} + \omega_{\mathrm{MIR}}\right) - k\left(\omega_{\mathrm{gate}}\right)}{\omega_{\mathrm{MIR}}} = \frac{k\left(\omega_{\mathrm{MIR}}\right)}{\omega_{\mathrm{MIR}}}. \tag{8.9}$$

For $\boldsymbol{\omega_{MIR} << \omega_{gate}}$ this condition, from Ref. [Nah96], can be fulfilled and Eq. (8.9) can be rewritten as

$$\left(\frac{\partial k}{\partial \omega}\right)_{\mathrm{gate}} \approx \frac{k\left(\omega_{\mathrm{MIR}}\right)}{\omega_{\mathrm{MIR}}}, \tag{8.10}$$

since the left side of Eq. (8.9) is nothing but the derivative of $k(\omega_{gate})$ for small ω_{MIR} . This can also be expressed as the ratio:

$$\frac{v_{\mathrm{gr,gate}}}{v_{\mathrm{ph,MIR}}} \approx 1. \tag{8.11}$$

However, in the present case for phase-matching in GaSe this equals only

$$\frac{v_{gr,gate}\ (\lambda = 950\,\text{nm})}{v_{ph,MIR}(\lambda = 7.5\,\mu\text{m})} = 0.89\,. \tag{8.12}$$

Comparing this to values used in the original publication [Nah96], for phase-matching a far-infrared frequency of 3 THz with a gate pulse of 800 nm (375 THz) in ZnTe, gives a ratio of 1.05. So it seems an acceptable value in the present configuration, but there is still room for improvement. The two different propagation times of the MIR – phase and group velocity – were initially considered to be critical, since this could be an issue in the measurement. But the envelope and the phase of the MIR propagate nearly at the same speed. Even for a 20 µm GaSe thickness this difference is 2.3 fs, only. The group velocity mismatch (GVM) between the MIR and the gate pulse is quite large in GaSe. Taking only half the crystal thickness into account (this assumes, that in the middle of the crystal the pulses overlap in time), an acceptable GVM of 10 fs results for a 20 µm GaSe crystal. Even more decisive regarding the crystal thickness is the phase-matching bandwidth. In Fig. 8.18 the phase-matching function for sum-frequency generation of the ultrashort gate pulse and the MIR pulse is shown for various GaSe crystal thicknesses. For the calculations 20, 200 and 500 µm thickness for a GaSe crystal is used for sum-frequency generation at an angle of 20°.

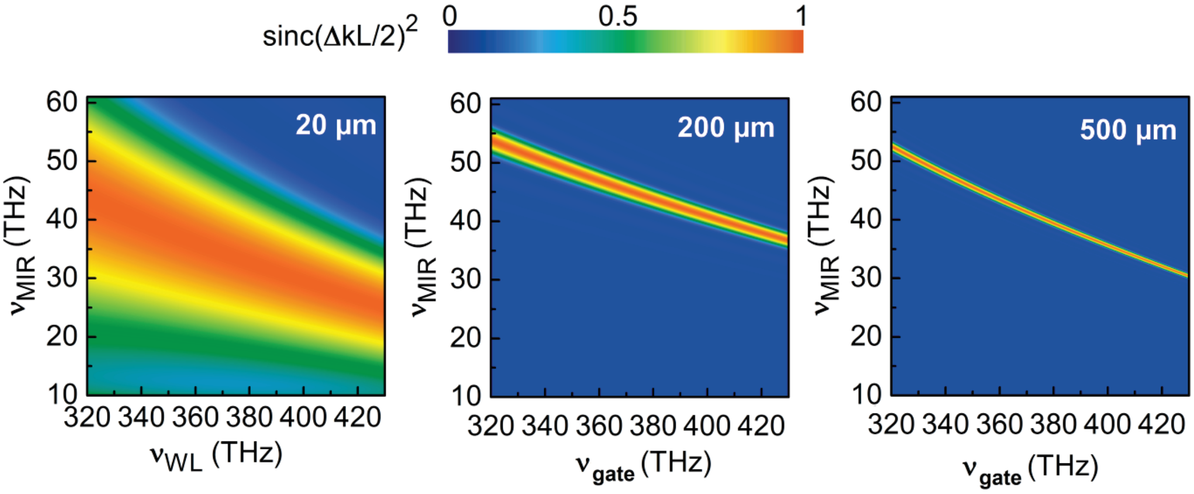

Fig. 8.18: Phase-matching function *sinc(ΔkL/2)*^{2} for $\theta = 20°$ and L = 20, 200 and 500 µm for phase-matching the MIR and the gate pulse in GaSe.

The phase-matching of a 20 µm GaSe crystal should support the used bandwidths for proper sum-frequency generation. However a thinner crystal would be beneficial. The used crystal with 22.5 µm thickness was bought as a 10 µm GaSe crystal. Even thicker GaSe crystals will only mix isolated parts of the pulses – as it is shown in Fig. 8.18 – and hence lead to hardly interpretable results for the reconstructed waveform of the MIR field.

In the experiment the resulting sum-frequency pulse can be detected with a fiber coupled spectrometer (OceanOptics, HR4000) – the spectrum is shown in Fig. 8.19. The SFG is polarized perpendicular to the gate pulse. A polarizer was used to suppress the gate pulse on the spectrometer. The possibility to monitor the SFG spectrum allows optimizing for the temporal and spatial overlap (by optimizing for highest signal) as well as for the optimal phase-matching (by optimizing for broadest spectral bandwidth). The SFG spectrum also shows some pronounced, equally spaced interference fringes. This is an interference of the main pulse with its back reflection on the detector of the spectrometer. It makes it feasible to evaluate the correct thickness of the crystal with the help of the formula for the free spectral range. With the known refractive index [Kat13] the thickness was determined to be 22.5 µm. This value deviates strongly from the given value of the supplier (10 µm). However it seems to be acceptable for the measurements.

For clarity the gate spectrum is also shown after FFT filtering out the interference fringes (red line in Fig. 8.19). It is compared with the theoretical SFG of the gate pulse (red line from Fig. 8.15) and the MIR pulse (Fig. 8.10). The theoretical curve is shown in blue. It is demonstrated that the SFG signal is clearly visible on the spectrometer and can be used for optimizing the crystal angle, focus position and temporal overlap.

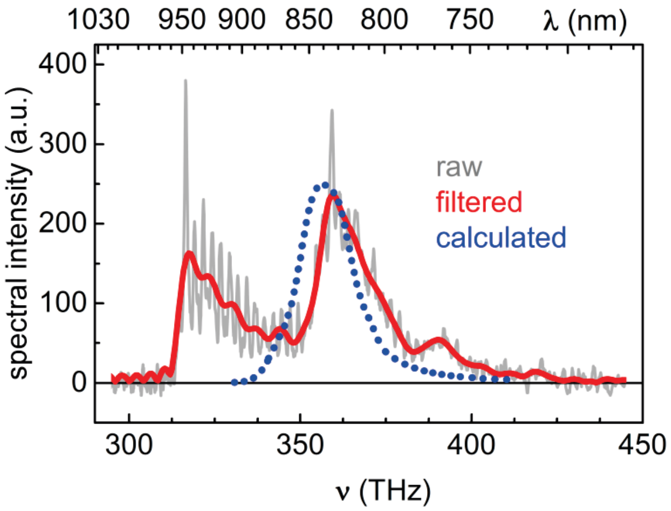

Fig. 8.19: Sum-frequency spectrum of the MIR and the gate pulse in 22.5 µm GaSe. The modulation of the gate spectrum (raw) is due to interference with its back reflection on the detector of the spectrometer (grey). Filtered gate spectrum (red) and theoretical SFG spectrum (blue).

Electro-optical sampling

The generated sum-frequency between the MIR and the gate pulse are partially overlapping in their spectrum. Depending on the instantaneous phase position of the MIR field, the generated sum frequency is shifted accordingly. In the used type II configuration, the gate and the sum frequency are cross polarized – Eq. (8.6). This leads to a detectable interference of the gate and the sum-frequency after a proper projection of the polarizations. This projection on an identical plane is introduced by a polarizer under 45° with respect to the gate pulse polarization. With the combination of a quarter-wave plate and the polarizer (here a Rochon prism is used) the overlapping region of the gate and the sum-frequency pulse are split equally between two photo detectors. The detectors integrate over the pulse duration and the spectral components of the local oscillator. The phase-difference (interference) between the gate pulse and the sum-frequency scales linearly and sign sensitively with the MIR field [Por14]. The time resolution is introduced by temporally delaying the gate pulse with respect to the MIR pulse. The resulting EOS trace corresponds to the difference of the signals of the photo detectors and is proportional to the MIR field [Gal99, Pla01].

Porer et al. showed that the signal to noise ratio of the measurement can be enhanced by selecting the spectral overlapping frequencies between sum-frequency and gate by optical filters [Por14]. In the present case, the spectral shape of the gate pulse is more or less optimal. The resulting sum-frequency spectrum falls off to the short wavelength side in the same fashion as the gate pulse – see Fig. 8.19. Consequently, on the short wavelength side no unconverted spectral parts are left. This would only increase noise on the detector.

Experimental implementation of EOS

The setup for EOS of the MIR pulses is shown in Fig. 8.20. The MIR generation setup is identical to the previously presented one shown in Fig. 8.6. Additionally, the self-compressed pulse is implemented for electro optical sampling in a 22.5 µm GaSe crystal. Therefore 3 µJ of the pump branch is split off for self-compression due to continuum generation in a 1 mm YAG plate. In order not to increase the chirp of the gate pulse, the MIR pulse is combined with the gate pulse collinearly on a gold coated off-axis parabola with a 3 mm hole inside and a focal length of $f = 152.4$ mm (P_2 in Fig. 8.20). It focuses the MIR beam and the gate pulse is imaged through the hole by the Schiefspiegler telescope. Before the gate pulse generation the fundamental beam is reflected by a mirror fixed on a piezo table (Piezosystem Jena, PX400) to introduce a relative time delay for EOS. The travel range of the piezo amounts to about 380 µm in closed loop configuration. This corresponds to a time delay of roughly 2500 fs. The angle of incidence on the mirror fixed to the piezo table is kept as small as possible, together with its small travel range the continuum generation process in the 1 mm YAG plate downstream almost free of perturbation due to the piezo movement.

The gate pulse and the MIR are overlapped in time and in space in the 22.5 µm GaSe crystal (EKSMA optics), oriented for sum-frequency generation – as described above. The quarter-wave plate (achromatic 700 – 2500 nm, B. Halle Nachfl.) and the Rochon prism split the balanced signal on two identical photo detectors of our own design [adapted from Sch08a], see. Fig. 8.21 for a circuit diagram. A USB Oscilloscope (PicoScope 5444A, pico Technology) is used to digitize the data of the photo detectors and to read in the voltage ramp applied to the piezo. For time-resolution, the piezo movement was calibrated interferometrically with a HeNe laser [Koz04] against the applied voltage.

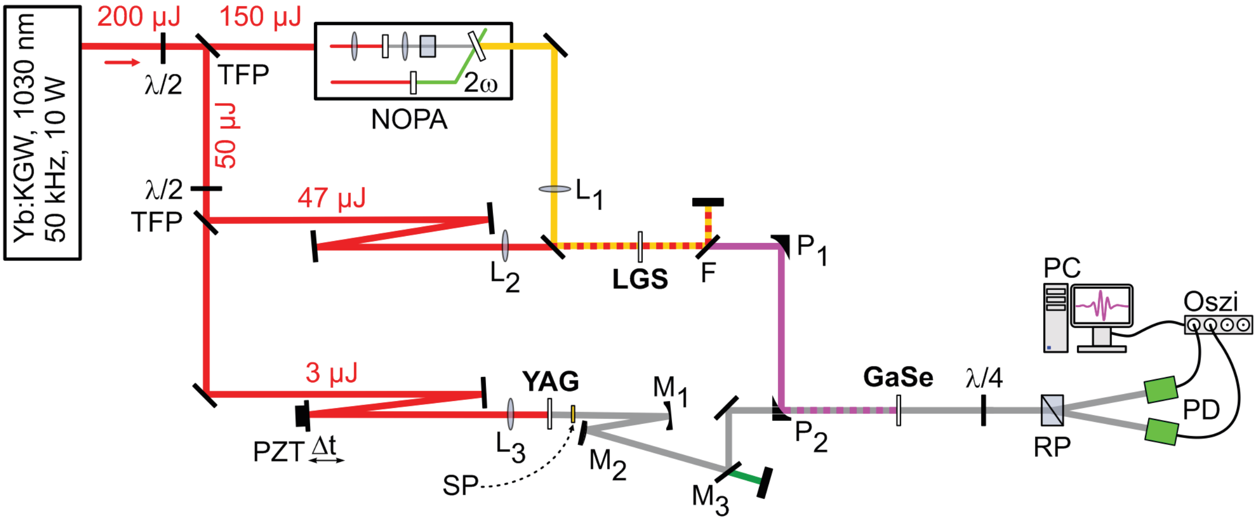

Fig. 8.20: Setup for MIR generation and electro optical sampling.

- **λ/2**: half-wave plate, zero order for 1030 nm
- **TFP**: thin film polarizer (AOI = 45°, for 1030 nm)
- **NOPA**: 515 nm pumped noncollinear optical parametric amplifier – for details see text and Fig. 8.4
- **L_1, L_2**: $f = 250$ mm, plano-convex lens AR coated
- **C**: combiner mirror (Laser Components, HR1150/45°)
- **F**: Filter to suppress DFG input pulses and transmit MIR (Edmund Optics, Germanium long pass filter, 4.5 µm)
- **P_1**: parabolic gold mirror, $f = 150$ mm
- **LGS**: DFG mixing crystal
- **PZT**: piezo table for scanning the EOS time delay
- **L_3**: $f = 50$ mm lens for SCG
- **YAG**: 1 mm YAG
- **SP**: Edmund Optics short pass filter, 950 nm, d = 1 mm
- **M_1, M_2**: Schiefspiegler telescope
- **M_3**: Asahi short pass 780 nm used in reflection
- **P_2**: off axis gold parabola with 3 mm horizontal hole, $f = 152.4$ mm
- **GaSe**: 22.5 µm GaSe mixing crystal oriented for SFG
- **λ/4**: achromatic quater-wave plate, 700 - 2500 nm (B. Halle Nachfl.)
- **RP**: Rochon prism
- **PD**: photo diodes – see subsequent circuit diagram for used parameters (Fig. 8.21)
- **Oszi**: USB-oscilloscope, *PicoScope* 5444A for reading in the data of the photo diodes and the piezo voltage with a PC.

The circuit diagram for the used photo detectors is in Fig. 8.21. To optimize the data evaluation the original version for 1 kHz from [Sch08a] is slightly modified to account for the higher repetition rate of 50 kHz, but the principle is identical. The shot-noise limit for detection is $2.6 \cdot 10^{-5}$ for a quantum efficiency of 80% of the detector, assuming 0.5 nJ gate pule energy.

In principle the short gate pulse could easily get amplified with the second harmonic of the pump laser source – a very similar setup is demonstrated in chapter 4 of this thesis. This would lead to higher gate pulse energies and consequently improve the signal to noise ratio to enable higher sensitivity in the measurement. In principle saturations occurs only when the gate pulse energy approaches roughly 8 times the MIR pulse energy.

The data evaluation will be described in the following section.

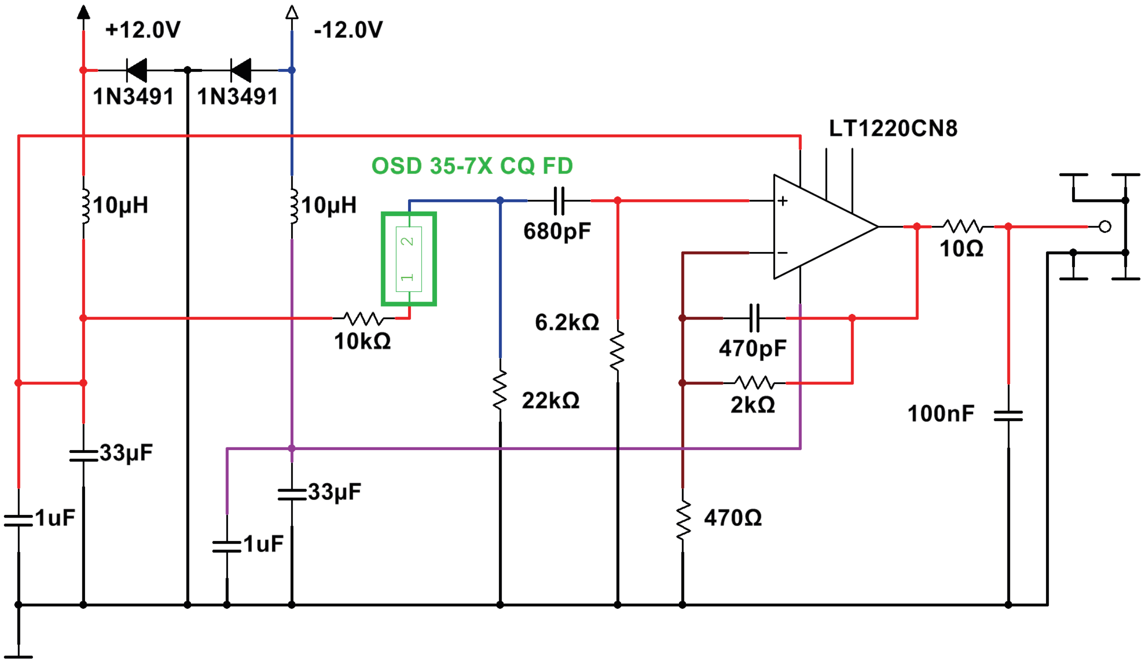

Fig. 8.21: Circuit diagram for the two detectors used in EOS. For documentation purposes of the single electronic components, only. For detailed explanation to the circuit, see Ref. [Sch08a].

Data evaluation

The data of the electro optic sampling signal is recorded with two identical photo diode detectors of our own design. The signals of the detectors are digitized continuously with a PicoScope 5000 Series oscilloscope (model 5444A, Pico Technology Ltd.) at 14 bit resolution. A sampling interval of 100 ns is chosen with full range and sample depth adjustments. Typically scan durations of 1 s are chosen. This amounts to $1 \cdot 10^7$ samples per trace. To be as fast as possible, the data is stored in Matlab 4 format and has to be read into MathCad as binary/hex code.

For each pulse a stretched signal is produced in each detector – see blue curve in Fig. 8.22. The positive going part of the signal is about one third of the full period of 20 µs and amounts to about 50 – 60 data points. An asymmetric double sigmoidal function, Eq. (8.13), is fitted to this part – red line in Fig. 8.22.

$$y = y_0 + A \cdot \frac{1}{1 + \exp\left(-\frac{x - x_c + w_1/2}{w_2}\right)} \cdot \left(1 - \frac{1}{1 + \exp\left(-\frac{x - x_c - w_1/2}{w_3}\right)}\right) \qquad (8.13)$$

Here, y_0 is the offset, x_c the center, A the amplitude, w_1 the full width at half maximum and w_2 and w_3 are variances. The shape of the detector signal allows setting w_3 to w_1, in order to eliminate one parameter.

The negative going part has a significant minimum to allow a measure of a "base line". This is evaluated by fitting a cubic polynomial to the proper part – orange in Fig. 8.22. The values of the electronic components (Fig. 8.21) differ from [Sch08a] to receive this clear minimum to optimize the evaluation by our fitting algorithm.

The full amplitude of the signal – corresponding to the pulse strength – is determined from the difference of the peak maximum of Eq. (8.8) and the extrapolated point of intersection of the rising edge and the "base line" polynomial.

The evaluation via the fitting algorithm, for both recorded channels, is done in parallel with two simultaneously running MathCad programs. For a one second scan with 50.000 peaks the evaluation is done in less than 2 mins on a PC with an Intel i7 CPU with 2.8 GHz and 8 GB RAM.

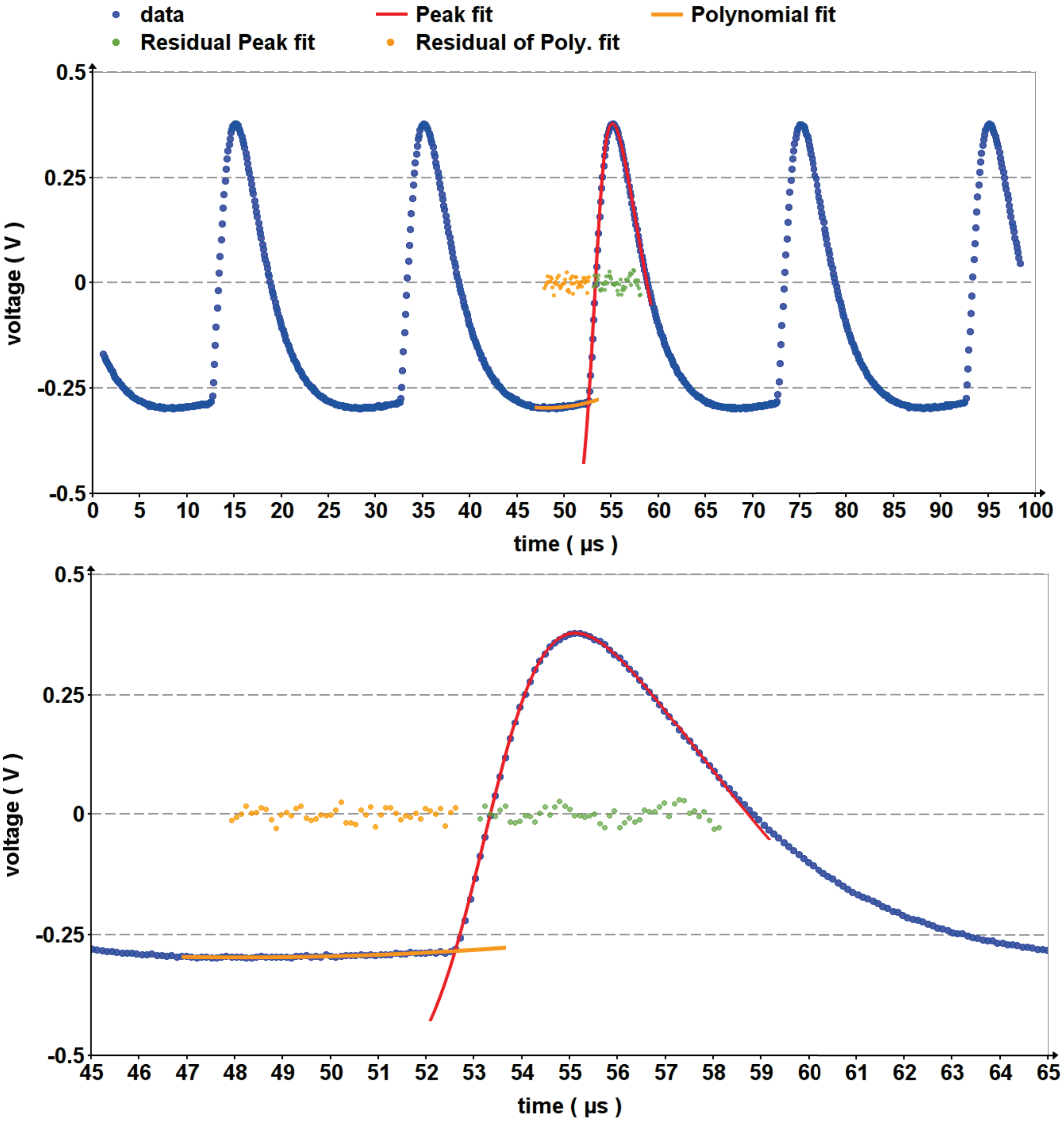

Fig. 8.22: Measured diode signal (blue), peak fit according to Eq. 8.8 (red) and residual (green dots), polynomial fit (orange line) for "base line" and residual (orange dots).

The resulting data of the fitting procedure are values, corresponding to the amplitude, for each peak of both channels. For proper smoothing of both channels a polynomial filter is used as proposed by Willson and Polo [Wil81]. With polynomial degree of $K = 5$, $S = 8$ number of smooths and $T = 217$ as range of filtering. The ratio of both processed channels corresponds to the electro optic sampling signal.

EOS Results

An EOS trace measured with the previously described setup and evaluation algorithm is shown in Fig. 8.23. The corresponding MIR spectrum, measured with the LASNIX L-FTS spectrometer, is shown above. The MIR pulse was compressed with transmission of 4 mm Germanium. 1 mm Germanium is due to the long pass filter which blocks the input wavelengths. Experimentally, additional 3 mm of AR coated Germanium is found to compress the pulse best possible. The MIR spectrum was tuned to the broadest possible bandwidth, resulting in a spectrum centered around 45 THz with a Fourier limit of 39 fs, corresponding to a 1.4 cycle pulse (red curve in Fig. 8.23, assuming a flat spectral phase) with a pulse energy of 200 nJ. The measured EOS trace (blue curve in Fig. 8.23) is close to the calculated Fourier limit.

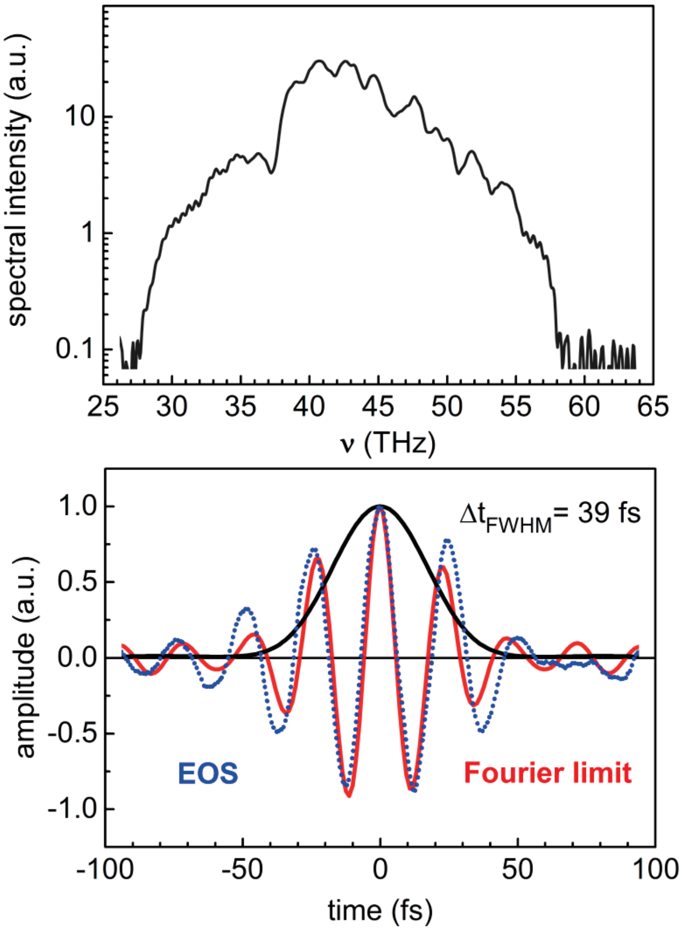

Fig. 8.23: Upper panel: MIR spectrum generated in 0.5 mm LGS with E = 200 nJ. Lower panel: calculated Fourier limit (red curve) and intensity (black line) of the measured spectrum. Measured EOS trace in 22.5 μm GaSe (blue curve).

Since the seed pulses experience the identical phase fluctuations $\Delta\phi$ as the laser fundamental in both amplification stages, the signal and the idler of both stages possess the CEP of the pump laser. Consequently, inherently phase-locked middle infrared pulses result [Kno17, Bal02b]. To verify this, the piezo (*PZT*) is fixed at a time delay T_1 of a zero crossing of the EOS trace. The change in the polarization ratio of the gate is measured with the two photodiodes, as it is done for EOS, but here with a fixed gate delay. A change in the CEP would then be directly measured as a positive or negative shift of the balanced signal of the two detectors. The results for a 1 second and a 4 second single-shot measurement are shown in Fig. 8.24 b) and c). In Fig. 8.24 a) the fixed time delay T_1 for the measurement is shown.

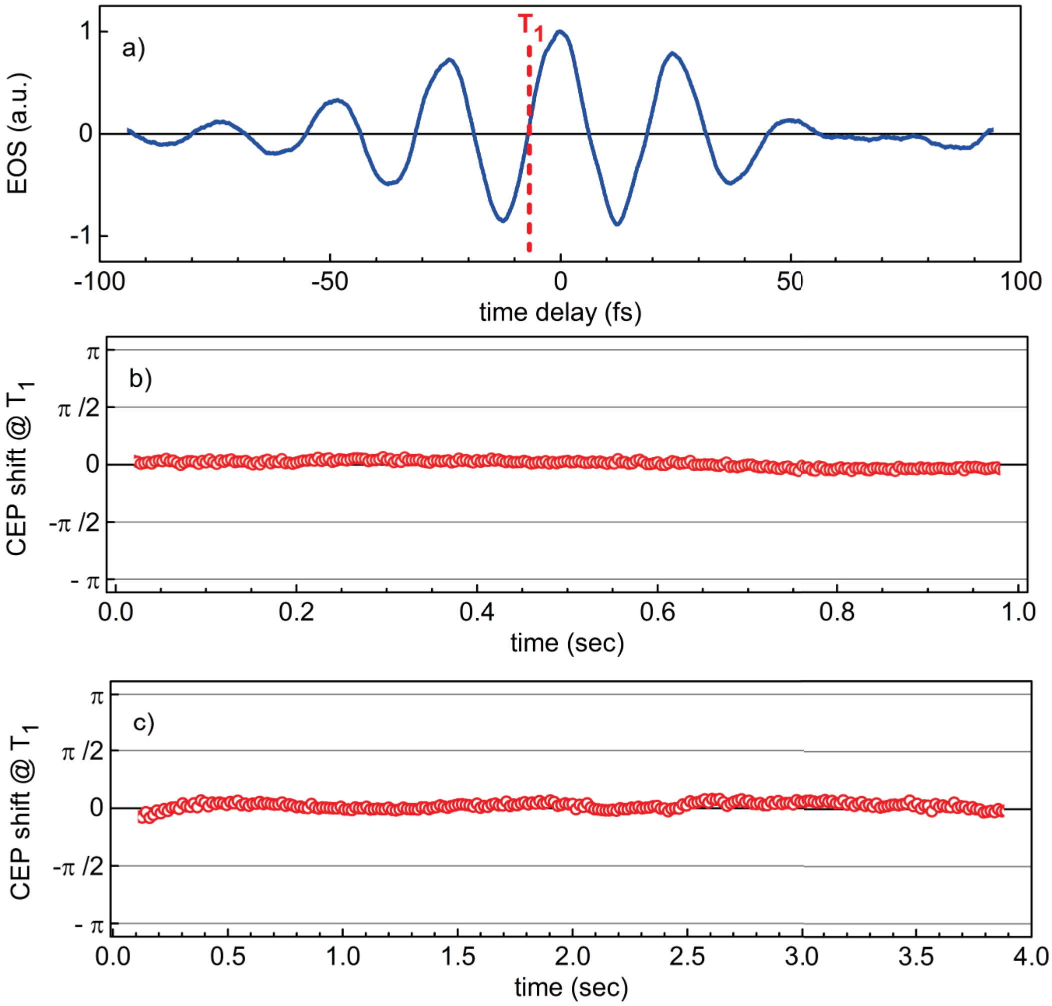

Fig. 8.24: CEP stability of the MIR field. a) EOS trace of the MIR field and position T_1 for fixed time delay. b) CEP stability over 1 sec (50.000 pulses); c) CEP stability over 4 seconds (200.000 pulses). The standard deviation of c) corresponds to 85 mrad.

It has been demonstrated, that on the time scale of a few seconds the resulting pulses are CEP stable with a standard deviation of 85 mrad. However, on longer time scales some larger phase shifts are found. This is believed to be related to some mechanical instability of the laser table due to vacuum pumps, air condition and cooling systems of the laboratory.

After re-positioning of the whole setup on the optical table and removing the aluminum breadboard of the NOPA much higher CEP stability is obtained. Also the generated MIR pulses show excellent long-term stability – see Fig. 8.25. The CEP drift is now at 94 mrad over one hour. For roughly 10 mW average MIR power at 50 kHz the deviation is only 48 µW over 13 hours.

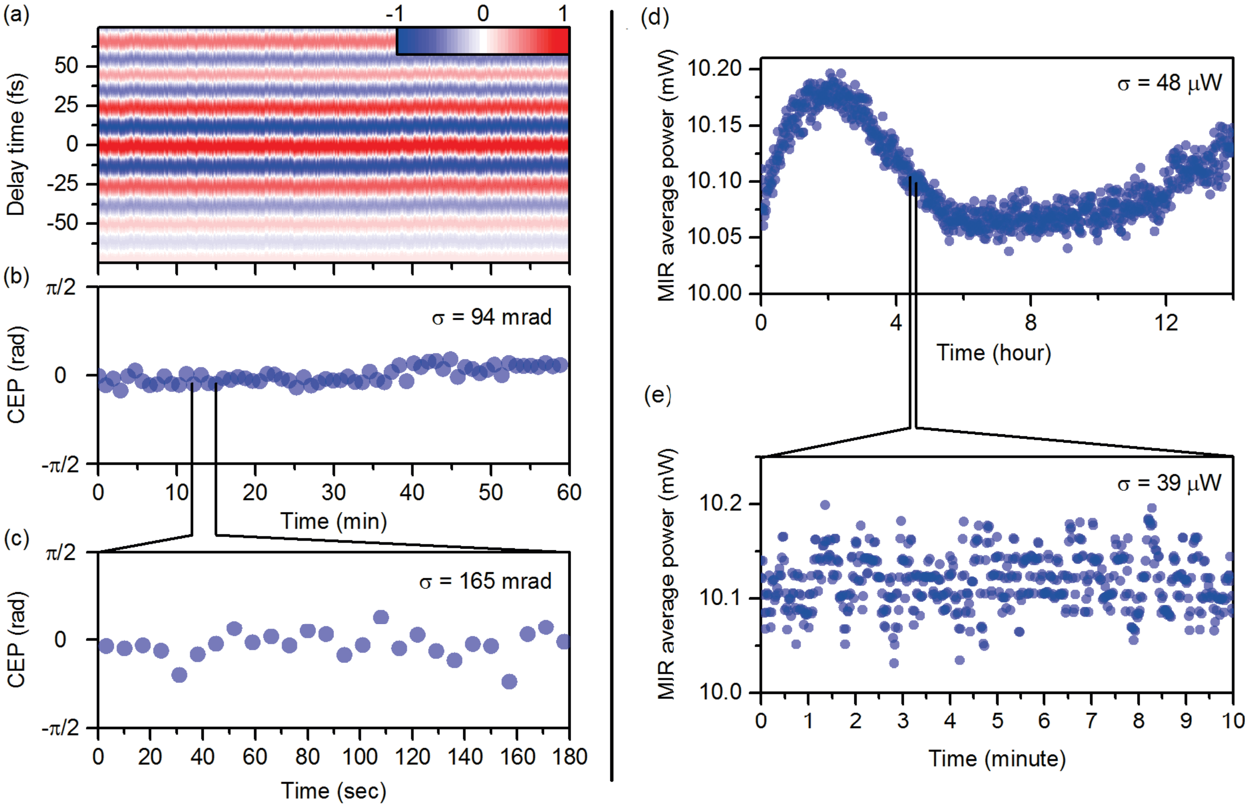

Fig. 8.25: Stability of the carrier-envelope phase (CEP). (a) Electro-optical sampling traces measured repetitively over one hour, with data points taken every 7 seconds. (b), (c) Evaluated CEP values. (d) MIR Long-term power stability. (e) Raw measurement with one data point taken every second. The quantization is digitizing noise.

In the following part signal distortions due to atmospheric absorption are discussed. They can be seen on longer time scales with oscillatory behavior – see Fig. 8.26b).

Sometimes also a contribution of the back reflection can be seen in the retrieved EOS waveform. This could be avoided with nonlinear crystals as proposed by the Huber group [Kno18].

In the present case, shown in Fig. 8.26b), the side lobe of the waveform is attributed to the third order dispersion of the pulse.

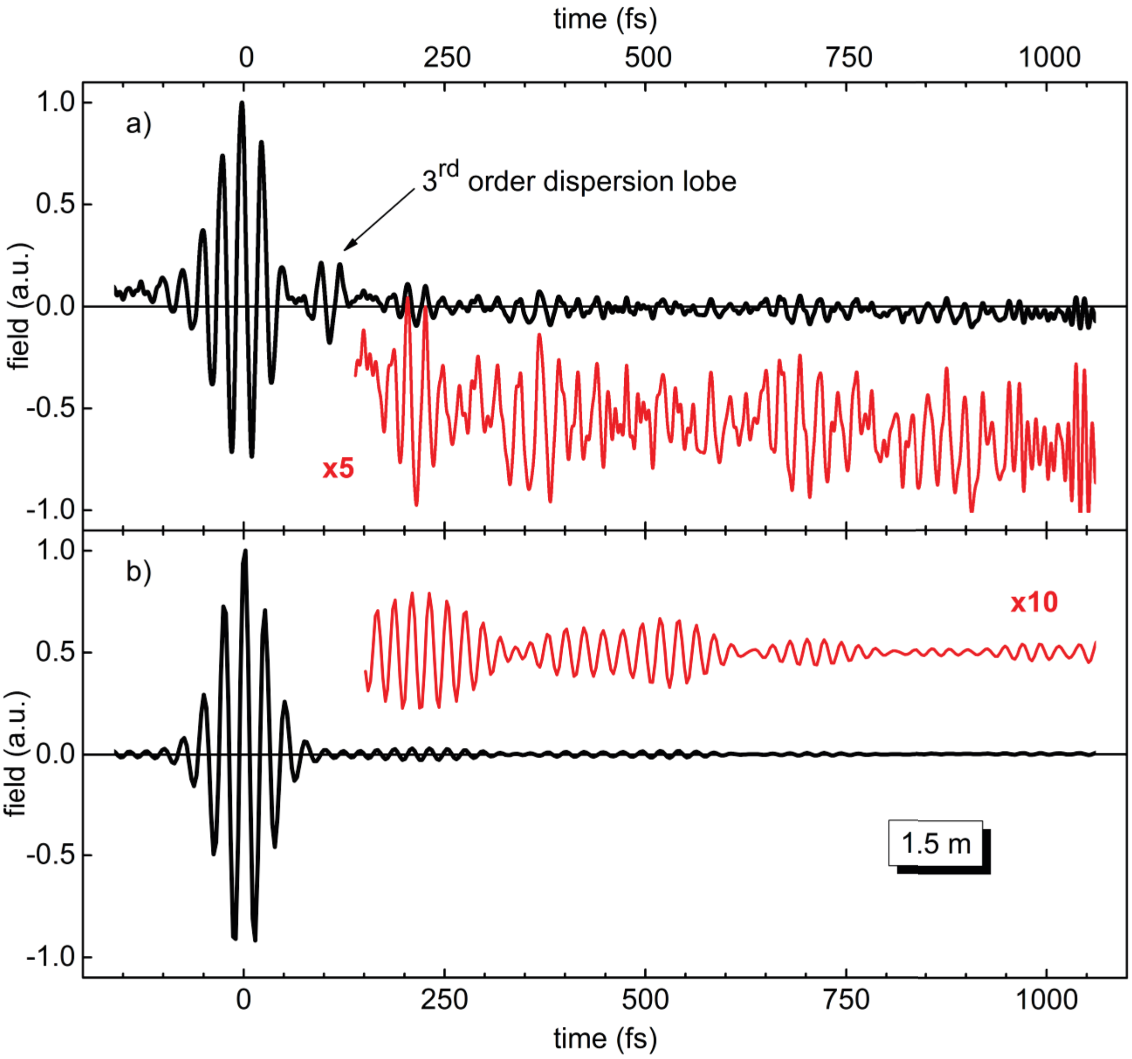

Fig. 8.26: a) Measured EOS trace up to 1000 fs delay time compared with calculated pulse for 1.5 m path way in atmosphere (b).

Influence of atmospheric absorption

Initially, the contribution of the laboratory atmosphere was expected to induce significant distortions, since atmospheric air has a number of absorption bands in the range of the MIR pulses. Interestingly, this is not a highly relevant issue in the present situation. It will be shown theoretically that the absorption bands of the atmosphere do not drastically alter the retrieved mid IR field. For slightly shorter central wavelengths, it seems relevant to remove CO_2 and in particular H_2O in the setup [Kai00].

Fig. 8.27 shows the transmission of 1.5 m atmosphere (a) and 15 m atmosphere (b). The transmission was calculated[1] using the line-by-line model ARTS [Eri10] based on molecular absorption parameters provided by the HIRTAN database [Rot08, Rot12b]. The line-by-line calculations include the water vapor continuum model MT_CKD [Clo05]. Data shown in Fig. 8.27 is for "midlatitude-summer" atmosphere [And86]. This is an average of the calculated absorption coefficients for normal atmospheric pressure of 1013 hPa, 294 K temperature and a water vapor concentration of $4.68 \cdot 10^{17}$ cm^{-3} (about 50% relative humidity) in 0 km height, and 902 hPa, 299 K and a water vapor concentration of $3.11 \cdot 10^{17}$ cm^{-3} in 1.0 km height.

The red and blue lines are the spectra as given by the pressure broadening and Doppler broadening at the stated conditions. It can be seen that there are extremely finely spaced lines that frequently lead to full absorption even for 1.5 m path length (see inset in Fig. 8.27a). The necessary spectral resolution to resolve these features is not given by the MIR spectrometer used in this work or most other work on MIR pulse generation. Rather one averages over a range of 6.3 cm^{-1} in our case, corresponding to 0.189 THz or about 25 nm. If this resolution is used for a Gaussian convolution, the spectra shown in black are obtained. It is this effective absorption spectrum that will be seen in our measurements.

---

[1] Calculated by Dr. Claudia Emde and Prof. Dr. Bernhard Mayer of the *Meteorological Institute Munich*, LMU.

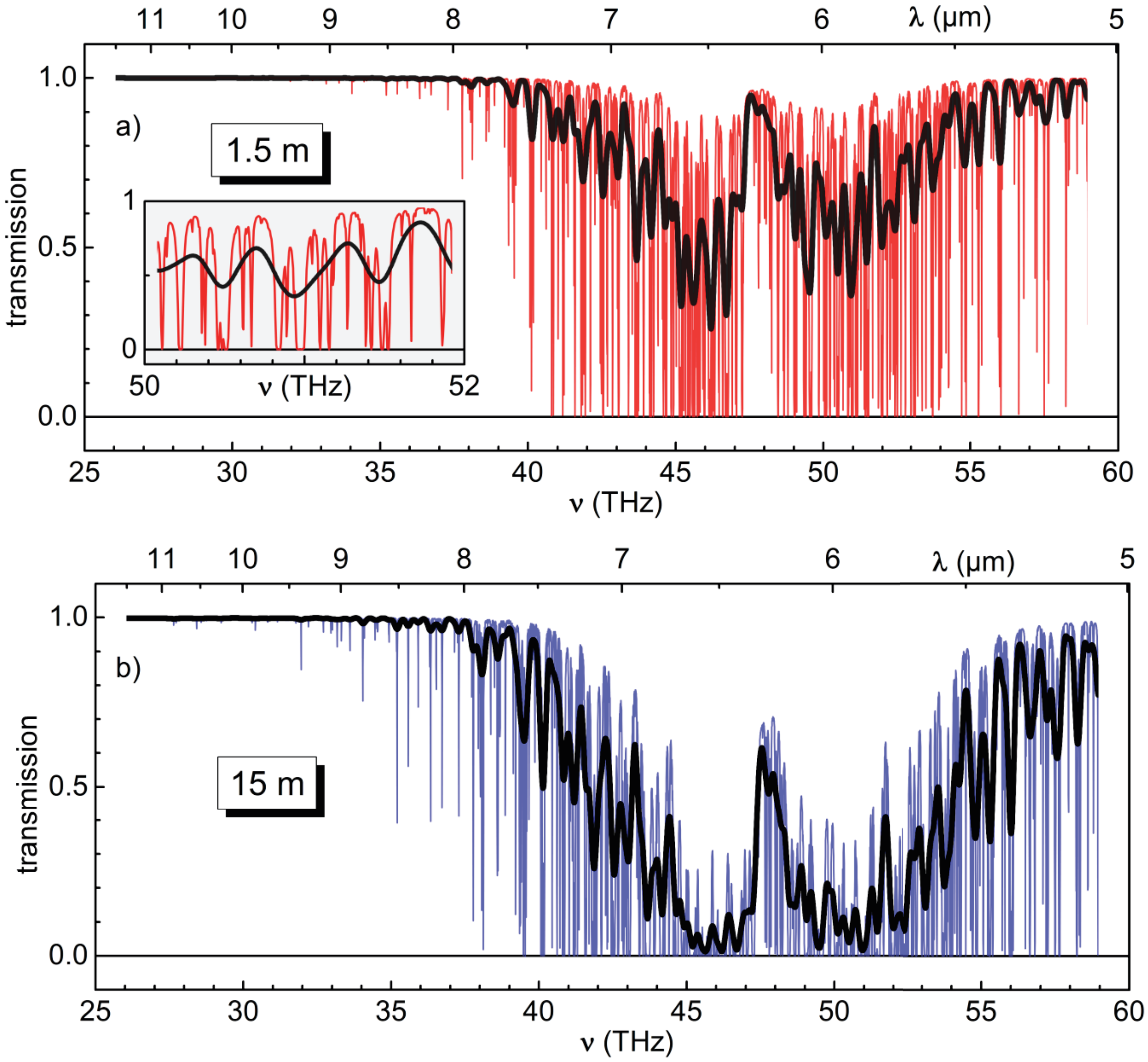

Fig. 8.27: Transmission spectrum of standard atmosphere for 1.5 m (a) and 15 m (b) path length. For 6.3 cm^{-1} optical resolution the spectra are shown in black.

The multitude of lines results from the rotational fine structure of the vibronic bands. From the formulas for the rotational energy of symmetric top molecules or only slightly asymmetric ones – as water – a series of nearly equidistant transitions (absorption lines) results. Taking out these lines from the spectrum does not significantly alter the overall shape of the electric field gradient. However, due to the regular spacing, partial rephasing will result in oscillatory signals at well-defined delay times.

An alternative way of considering the influence of the absorption is the viewpoint of absorption and later reemission of radiation. As the whole absorption process is spatially coherent over the illuminated volume, the reemission will also be coherent. As a consequence it is reemitted in the same direction and divergence as the incoming pulse. It is, however, delayed and gives rise to the later contributions to the electric field gradient, the free induction decay (FID). As the dephasing of the FID is different for different molecules, a slightly differing field gradient will result from the two viewpoints. In particular the dephasing of water is very rapid and the corresponding coherent signals will decay on the sub-ps time scale.

In Fig. 8.28 (a) and (b) a simulated pulse centered around 40 THz (λ = 7.5 μm) with a bandwidth of 16 THz is shown. This corresponds to a Fourier limit of 27.5 fs, nearly single cycle. Additionally, the pulse is shown for propagating through 1.5 (a) and 15 m atmosphere (b), by multiplying with the transmission data, shown in Fig. 8.27 (a) and (b), respectively. Although, the pulse looks heavily distorted for the cases of propagating through atmosphere, the fields in the time domain after Fourier transformation look quite similar (c). The spectral modulation shows only in some slight oscillations around the base line in the time domain. For 15 m optical pathway the pulse duration gets also slightly longer. On a longer temporal axis, there are some additional modulations, corresponding to certain absorption bands in the spectrum.

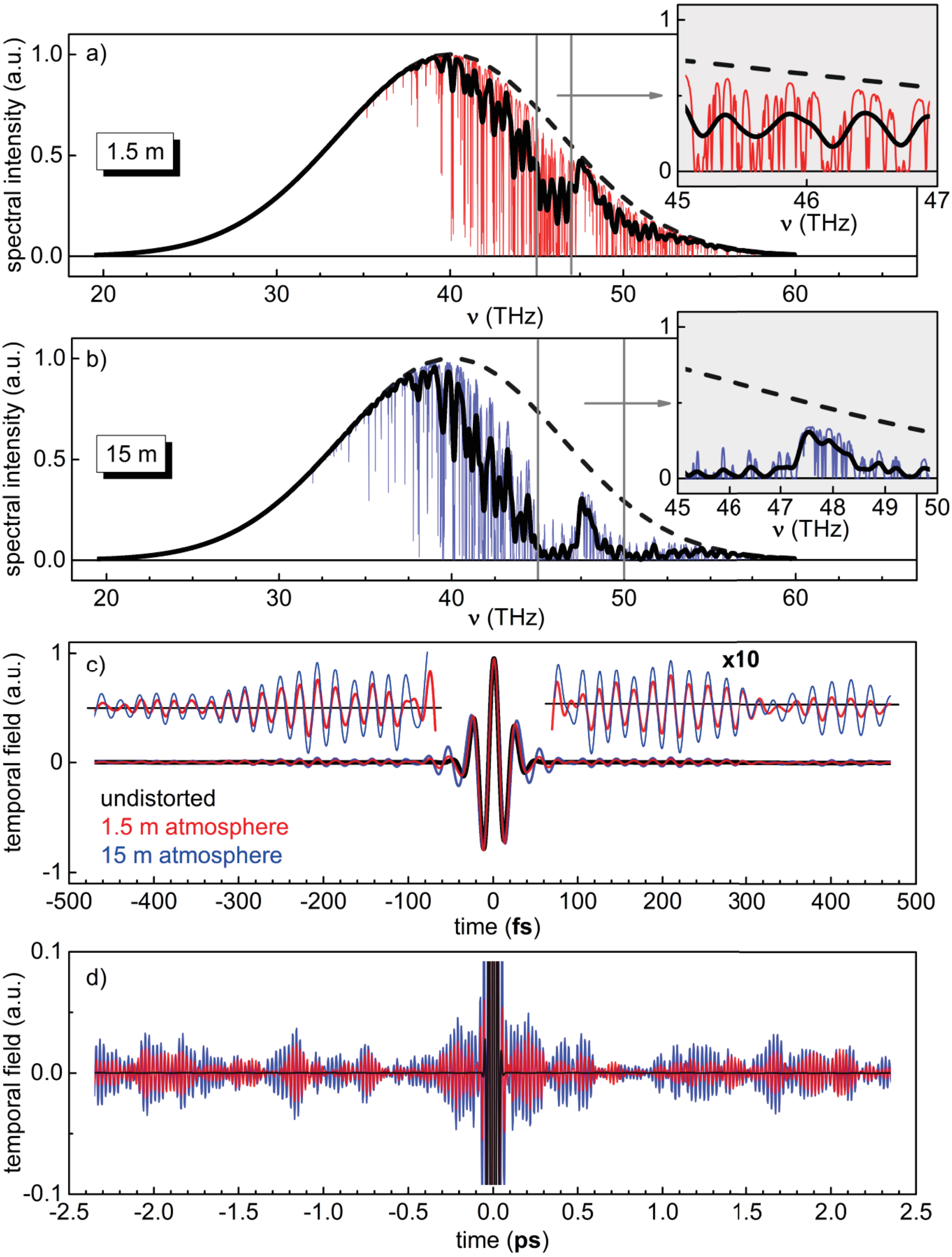

Fig. 8.28: Undistorted MIR pulse (black dashed line) and the pulse after propagating through 1.5 m (a) and 15 m atmosphere (b). Black solid lines indicate the spectra for 6.3cm^{-1} optical resolution. Pulses after Fourier transformation to the time domain (c) and (d).

The optical path length of 1.5 m is roughly the length the MIR passes through air in the present experimental setup, shown in Fig. 8.16. In the simulation the modulation is below 2% of the maximum peak. In the experiment, this will only slightly decrease the contrast.

In this chapter a new concept for field resolved optical spectroscopy in the MIR region was demonstrated. The spectral bandwidth covers more than an octave and fast EOS measurements on the 1 sec time-scale have been demonstrated. Parametric amplification of MIR pulses in LGS was shown with a quantum efficiency of 8%, resulting in 200 nJ pulses for spectra spanning from 5 – 11 µm. The over-all efficiency is at 0.1% from the 10 W average power available from the pump laser to 10 mW in the MIR region. The demonstrated pulse energies are routinely available in the lab on a day-to-day basis. Pulse energies of up to 340 nJ have been demonstrated. However, at this point the aim was to generate the shortest possible pulse and to optimize the CEP stability therefore the pump intensity was reduced. A high long-term stability over 13 hours is demonstrated. Further scaling of the amplification efficiency seems possible by scaling up the pump power.

A 1.4 cycle pulse was shown and a CEP stability of 94 mrad over one hour has been demonstrated. Even shorter pulses can be obtained by reducing the chirp in the NOPA seed beam. Still a critical part of the setup is the used filter to separate residual seed, the strong pump and the resulting MIR beam after the collinear MIR amplification in the LGS. With the use of a customized coating on a ZnSe substrate (by V. Pervak and co-workers of the MAP cluster) MIR pulse energies of up to 1 µJ in the MIR have been measured. This might have been due to a leakage of the pump. With the used Germanium filter (Fig. 8.7) definitely no pump transmission is possible. However, it might be possible that due to absorption of the 1030 nm pulse, parasitic nonlinearities are driven that might hinder optimal transmission of MIR. Therefore, it would be beneficial to use a high reflective mirror for 1030 and 1180 nm with high transmission in the MIR - but, this is still an open task.

With the compact NOPA and the compact gate pulse generation the whole setup - including the commercial pump laser system - can be implemented on an area of 1 m^2, only. Consequently, if needed the whole setup can be covered easily to remove water vapor or CO_2. This might pave the way for new, time resolved spectroscopic experiments in the fingerprint region.

In the next chapter an outlook will be given on achromatic frequency doubling of NOPA output pulses. The used NOPA is an identical setup as the one used in this chapter, pumped with an Yb-fiber pump source. Resulting spectra of these systems offer large spectral bandwidth, when they are seeded in the reddish wavelength region. Full achromatic frequency conversion of these broadband spectra to the blue or UV range is presented with resulting Fourier limits of less than 5 fs. Like the spectrally broad MIR spectra generated in this chapter, these broadband UV pulses are highly interesting for future spectroscopic experiments.

9. Achromatic second harmonic generation with a Yb:fiber laser pumped NOPA system at 200 kHz

In this section a proof of principle on the concept of achromatic second harmonic generation [Bau04] is demonstrated for a NOPA pumped by a high repetition rate Yb:fiber laser system (Coherent Monaco, 60 W output). The used laser system was a loan of Coherent and only available for a few days, so only few results are demonstrated. Since Yb-based laser systems provide rather long pulse durations, second harmonic pumped NOPA spectra show rather large bandwidths. Especially in the reddish region, the amplified signals provide bandwidths for sub-10 fs Fourier limits intrinsically – compare chapter 6. To frequency double these broad bandwidth pulses, extremely thin crystals, roughly 20 µm thickness, would have to be employed. Such thin crystals are hardly to get on the market and the doubling efficiency is low. An approach to overcome this dilemma is achromatic phase-matching [Bau04].

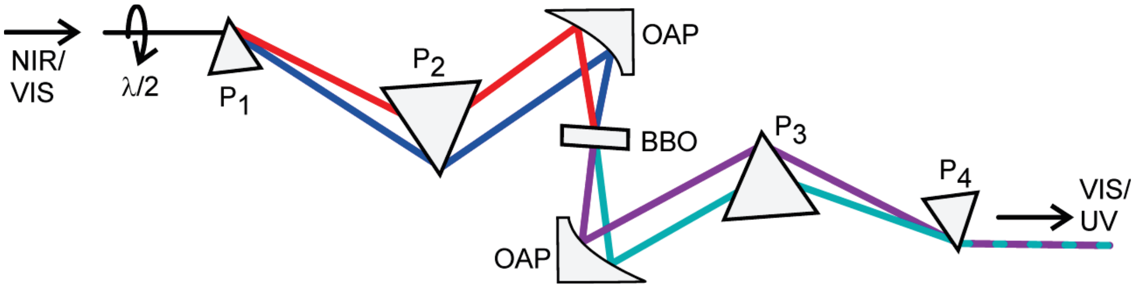

Fig. 9.1: Scheme for achromatic second harmonic generation. $\lambda/2$: half-wave plate, P_1, P_2: Fused Silica prisms (apex angle 68.7°), *OAP*: off-axis parabolic mirrors (f = 35 mm), P_3,P_4: CaF_2 prisms.

Here the pulse is transversally dispersed with a fused silica prism pair (P_1 and P_2) and focused with an off-axis parabolic mirror (*OAP*) towards the doubling crystal – see Fig. 9.1. Due to the resulting angular dispersion, a condition can be found where the doubling crystal offers optimal phase-matching to each of the dispersed frequencies. Therefore, a "thick" crystal can be used for frequency doubling which would offer a much too small acceptance bandwidth without introducing angular dispersion. This is only possible, because the effective angular dispersion of a fused silica prism and the internal phase matching angle of BBO have a nearly identical gradient – see Fig. 9.2. With the separation of the prisms P_1 and P_2 and the focal length of the *OAP* the phase-matching can be optimized. Here a focal length of f = 35 mm is used for both parabolic mirrors. A half-wave plate rotates the polarization of the incoming signal to vertical, in order to be perpendicularly polarized to the plane of the prisms angular dispersion for type I phase-matching. The losses on the fused silica prisms P_1 and P_2 are reduced by an AR coating. The second harmonic exhibits a horizontal polarization. This enables to use the prisms P_1 and P_2 in a Brewster configuration to minimize reflection losses on the prism surfaces in the UV. A full description of the concept of achromatic frequency doubling and impressive results for Ti:Sapphire pumped NOPA pulses can be found in Ref. [Bau04].

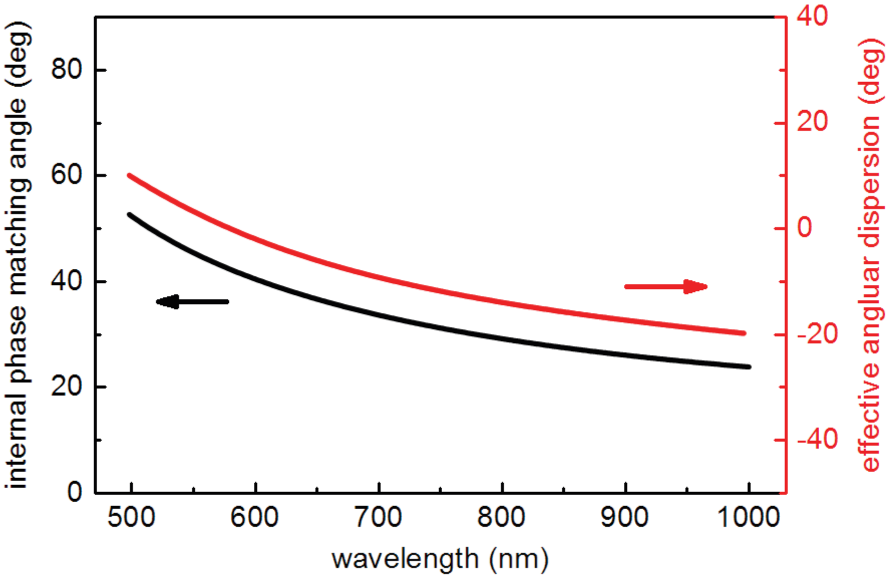

Fig. 9.2: Internal phase matching angle of BBO and effective angular dispersion of a fused silica prism with apex angle 68.7°. Figure adapted from [Bau04].

In this work a proof of principle on the concept is demonstrated briefly for NOPA pulses pumped by a Yb:fiber source. The central wavelength of the laser system is around 1035 nm with an average power of 60 W, nominally. The pulse duration is specified with 350 fs. The repetition rate is selectable by software – single shot to 1 MHz. The polarization of the laser output is vertical. For the experiment of achromatic phase matching a repetition rate of 200 kHz is chosen, corresponding to a pulse energy of 300 µJ per pulse. The beam is attenuated with the combination of a half wave plate and a thin film polarizer (*TFP*). The horizontally polarized transmission of the polarizer, roughly 20 µJ, is used to pump the NOPA system.

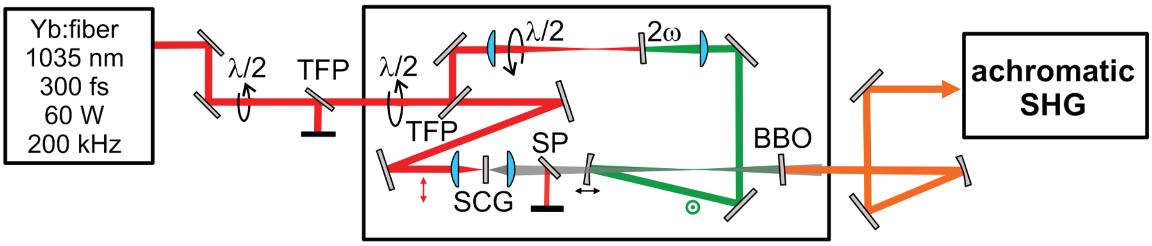

Fig. 9.3: Schematic setup for achromatic second harmonic generation.

The used NOPA setup is identical to the one described in the previous chapter 8 on MIR generation. There the system was used at 50 kHz repetition rate with 150 µJ input energy. The flexibility of the setup allows the operation with lower pulse energies at higher repetition rate. Only minor modifications are necessary. The second harmonic generation crystal is shifted slightly closer to the focal plane of the fundamental to maintain a frequency doubling efficiency of 30%. The amplifier BBO crystal is located behind the focal plane of the pump beam. Consequently a repositioning of the BBO closer to the focal plane, to increase the pump intensity, is sufficient for amplification with the lowered pulse energy.

In the previous chapter the bandwidth of the amplified output signal was spectrally narrowed to the needs of the experiment with selected amounts of dispersive material in the seed beam path. Contrary for the concept of achromatic phase-matching the broadest possible spectra are desired. Therefore no dispersive material is located in the seed beam path. The bandwidth of the NOPA output corresponds to a Fourier limit of 8 fs at 700 nm. The resulting pulse energy is 350 nJ at 200 kHz.

The spectra of both, the NOPA output and the achromatic frequency doubled second harmonic are measured with a fiber coupled Ocean Optics HR4000 spectrometer and are intensity calibrated afterwards. The achromatic frequency doubling of the NOPA signal is carried out with various thicknesses of BBO crystals. All crystals are in type I configuration and have a cutting angle close to 30°. Fig. 9.4 shows the NOPA output at 700 nm in the upper panel and the second harmonic for given crystal thicknesses in the lower panel. Also shown here is the calculated second harmonic spectrum (grey shadow). It indicates that the measured second harmonic bandwidth is almost at the theoretical limit. The measured UV spectra at 350 nm show a Fourier limit down to 4.8 fs.

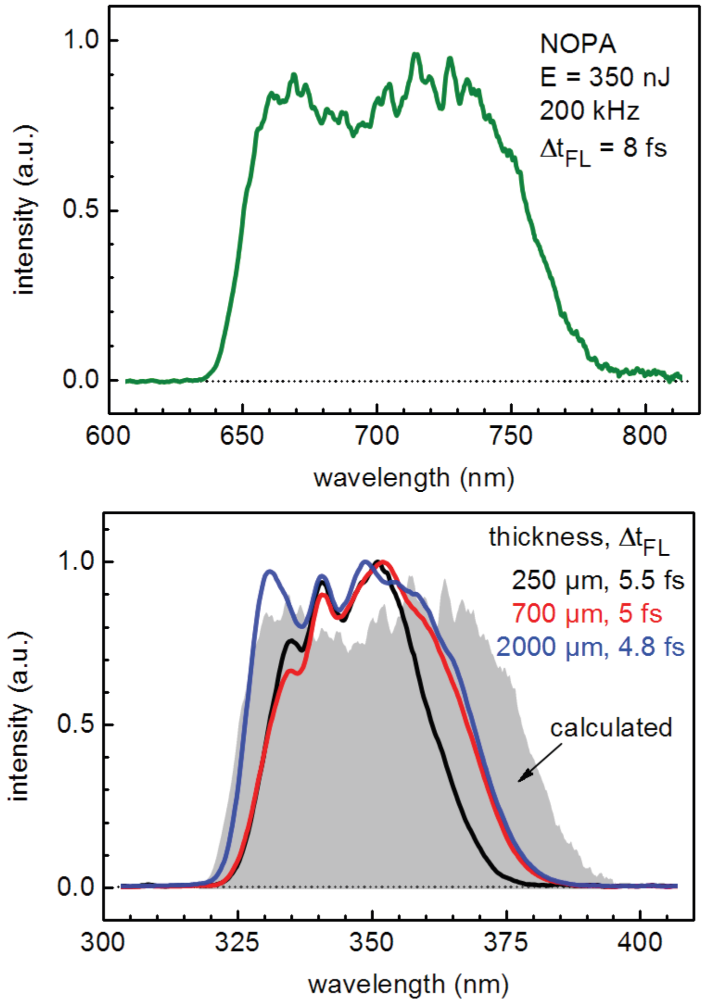

Fig. 9.4: NOPA output spectrum, centered around 700 nm (upper level), corresponding achromatic frequency doubled spectra for various BBO thicknesses (lower level)[1].

In a second experiment the central NOPA wavelength is tuned to 900 nm. The output energy is about 300 nJ per pulse, its spectral bandwidth corresponds to 7 fs. After achromatic phase-matching, spectral bandwidths corresponding to Fourier limits down to 5.8 fs are measured – see Fig. 9.5.

For comparison a non-achromatic second harmonic generated spectrum is shown (grey shadow in Fig. 9.5) for the case of frequency doubling with a 250 µm BBO. This is done by simply removing prisms P_1 and P_2. The Fourier limit here amounts to about 25 fs – a factor of 4 longer in pulse duration compared to the achromatic phase matching geometry for identical crystal thickness.

---

[1] The second harmonic spectra were measured in collaboration with Dr. Pavel Malevich (group of Prof. Dr. Jürgen Hauer, *TUM*). He is interested in broadband UV generation for 2D-UV spectroscopy.

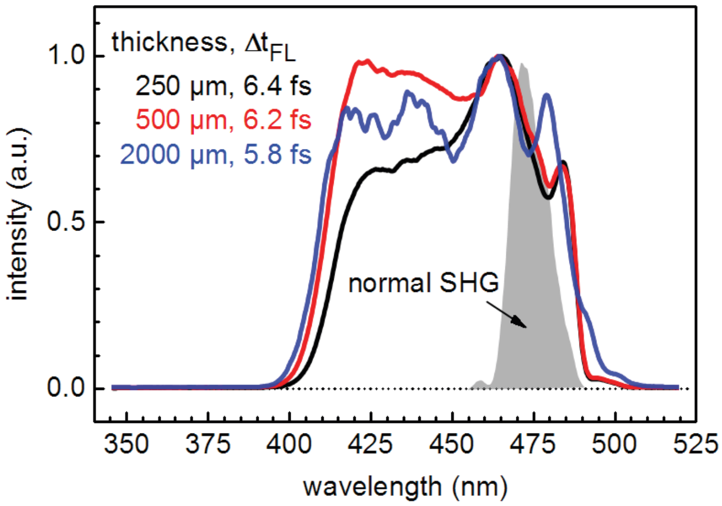

Fig. 9.5: NOPA pulses around 900 nm achromatic frequency doubled in BBO crystals of given thicknesses. For comparison the grey shaded spectrum shows the non-achromatic generation for a 250 µm crystal.

In this chapter achromatic frequency doubling for the generation of sub-10 fs UV pulses has been demonstrated. To the best of my knowledge this was done the first time starting with an Yb-based laser source at the repetition rate of 200 kHz. Nowadays Yb-based laser systems are state of the art technology. Therefore this proof of principle paves the way for future experiments with ultrashort UV pulses at high repetition rates. The shown pulses are possibly the broadest known near-UV/blue pulses leading to the potential shortest pulse duration. The spectral range that is demonstrated here is hard to obtain starting with a Ti:Sapphire pump laser system – compare Ref. [Var14]. Additionally the demonstrated pulse durations of this reference are longer compared to the Fourier limits shown here. This makes the concept of achromatic phase-matching of NOPA pulses generated with Yb-based pump laser systems highly interesting for future applications like ultrafast 2D-UV spectroscopy.

In the next chapter a compact and easy-to-use tool to measure the pulse duration of ultrashort UV pulses will be demonstrated. The autocorrelator is based on the process of two-photon absorption. Sub-10 fs pulse durations and laser repetition rates of up to 1 MHz are shown.

10. Two-photon absorption in bulk material: Convenient method to measure temporal pulse widths from the UV to the NIR

For cutting-edge spectroscopic experiments with highest temporal resolution for processes on the time scale below 50 fs the temporal characterization of the pump and the probe pulse is of major importance. For visible pulses, different approaches are available [Kan93, Iac99, Koz04, Bau04a]. For the experimentalist, the easiest tool to compress visible pulses is a second harmonic intensity autocorrelation [Koz04]. This method enables online pulse duration screening during the optimization of a prism compressor. However, many molecular systems exhibit absorption bands in the UV, requiring UV excitation and probe pulses. Therefore temporal characterization tools for pulses of this wavelength range are required. No available nonlinear crystal does support phase-matching for second harmonic generation below 400 nm. Consequently different approaches for UV characterization have to be realized, without losing the simplicity of the concept of second harmonic intensity autocorrelation.

Fig. 10.1: Newly developed, compact autocorrelator based on two-photon absorption.

In Ref. [Hom11] a method for pulse characterization for UV pulses based on two-photon absorption (TPA) is demonstrated. The benefit of this method is the absence of any phase-matching constraints – making it an ideal concept for the measurement of ultrashort UV pulses. Although it has already been demonstrated that the concept works well, the initial mobile setup was quite large, making it hard to place it in existing experimental setups. A prior integrated version inside the transient setup [Meg09] suffered from too long path lengths, making the online pulse compression more difficult due to the loss of spatio-temporal overlap while optimizing the prism compressor. In this chapter a compact version of the setup is presented. With a foot-print of only 350×200×90 mm^3 it is easy to place somewhere on the laser table.

In addition it is shown, that this concept works not only for the UV range, but also in the visible and near infrared, simply by choosing a proper two-photon absorption medium. Also a measurement of visible sub-10 fs pulses is highlighted.

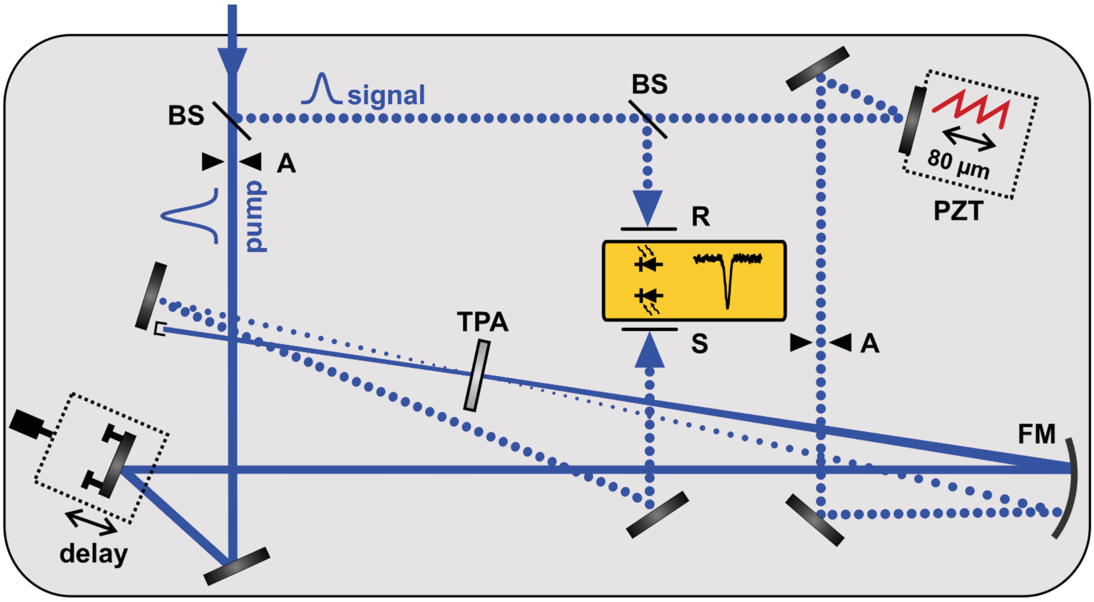

Fig. 10.2: Schematic of the beam path of the TPA based UV autocorrelator setup.

- **BS**: beam splitter, fused silica d = 200 µm, wedged (5 arc min) by LaserComponents
- **A**: aperture
- **TPA**: two-photon absorption medium at the focal planes of pump and signal (see Fig. 10.5)
- **FM**: spherical, focusing enhanced aluminum mirror (f = 200 mm) by Layertec
- **R,S**: reference and signal diode (digital integrating photodiodes with USB interface) WL-IPD4A by WieserLabs, used diodes: Hamamatsu S1336-8BQ
- **PZT**: piezo table (PZ100, Piezosystem Jena) operated at 2 Hz
- Unmarked mirrors are plane aluminum steering mirrors (enhanced aluminum by Layertec).

Using half inch sized mirrors and holders – where it is possible – as well as using a compact detector box where both a signal and a reference diode is located, made it possible to get the setup in compact shape. The setup is shown in Figs. 10.1 and 10.2. The incoming UV beam is split in two arms with a 200 µm thin beam splitter made of fused silica with a wedge angle of 5 arc minutes, to separate the reflection from the front and the back side. For vertical polarized light around 300 nm the Fresnel equations gives roughly a ratio of 10:90 for reflection to transmission for the fused silica beam splitter. With an identical second beam splitter a portion of the reflected part ("signal") of the incoming light is steered to a reference diode (R). The beam splitters are used in transmission in both the signal and the pump beam path. Hence, the setup is dispersion balanced for the dispersion of the substrates. The thickness of 200 µm of the beam splitter is chosen because the flow cell windows in the transient setup are of the same thickness. Consequently, the pulses are pre-compressed for them.

The signal is periodically shifted by a mirror mounted on a piezo table (PZT) with a frequency of 2 Hz in an open loop configuration. The piezo table is a PZ100 by Piezosystem Jena GmbH. An electronics board of our own design generates a ramp voltage signal which is amplified in a voltage amplifier ("5V10" or nanoUSB) by Piezosystem Jena GmbH before going into the piezo table. A travel range of roughly 80 µm of the piezo corresponds to a time delay of approximately 500 fs. For shorter pulses the voltage ramp can be switched to a lower amplitude, resulting in a piezo travel range of roughly 22 µm corresponding to a time delay of approximately 150 fs. With two steering mirrors the signal is sent to a spherical, concave 1" focusing mirror (FM, in Fig. 10.2) with a focal length $f = 200$ mm.

The strong pump beam is steered to the identical focusing mirror by a steering mirror on a mechanical micrometer delay stage. The stage enables the adjustment of the temporal overlap between signal and pump. Both beams are focused under a small angle towards the two-photon absorption medium which is placed in the focal plane of both beams roughly 200 mm behind the focusing mirror. The exact position of the medium is optimized by a z-scan [Bah90] measurement. By moving the medium through the focal plane while monitoring the transmission with the signal diode, the focal plane is found at the minimum transmission where the intensity is highest. At this point the effect of two-photon absorption is maximized.

Behind the two-photon absorption medium the stronger pump beam is blocked, while the signal beam is steered to the signal diode.

There is a small angle between pump and signal. Nevertheless, geometrical smearing effects can be neglected for this geometry. The spatial separation Δ of pump and signal on the focusing mirror is not greater than $\Delta = 10$ mm. With a focal length of $f = 200$ mm, this results in an external angle $\theta = arctan\left(\Delta / f \right) \approx 2.8°$. Assuming a pulse duration of Δt = 25 fs and a beam waist of w_0 = 20 µm at the focal plane for estimating the geometrical smearing effect according to Ref. [Taf96]:

$$\delta t = \frac{2 \cdot w_0}{c} \cdot \frac{\theta}{\sqrt{2}} = 4.7 \text{ fs}. \tag{10.1}$$

The measured pulse duration then amounts to

$$\Delta t' = \sqrt{\Delta t^2 + \delta t^2} = 25.4 \text{ fs}, \tag{10.2}$$

corresponding to an increase of only 1.5%. This value is an acceptable compromise regarding the complexity to build a similar setup in collinear geometry.

The used aluminum mirrors are designed by Layertech GmbH and have an enhanced reflectivity in the range of 220 – 400 nm. The data of the reflectivity provided by the company as well as test measurements at two different wavelengths with our ns OPO (EKSPLA, NT-242) are shown in Fig. 10.3. The test measurement was carried out by using two mirrors under an angle of incidence of 45° with 8 reflections. By comparing the power before and after the two mirror setup, the reflectivity can be evaluated by

$$R = \sqrt[8]{\frac{P_{out}}{P_{in}}}. \tag{10.3}$$

By engaging a half wave plate in front of the two mirrors the reflectivity could be measured for both horizontal and vertical polarized light. Since the reflectivity is >90% from 210 nm to 425 nm, these mirrors are well suited for the application in the autocorrelator setup, since it should be implemented to measure pulse durations in a broad wavelength range.

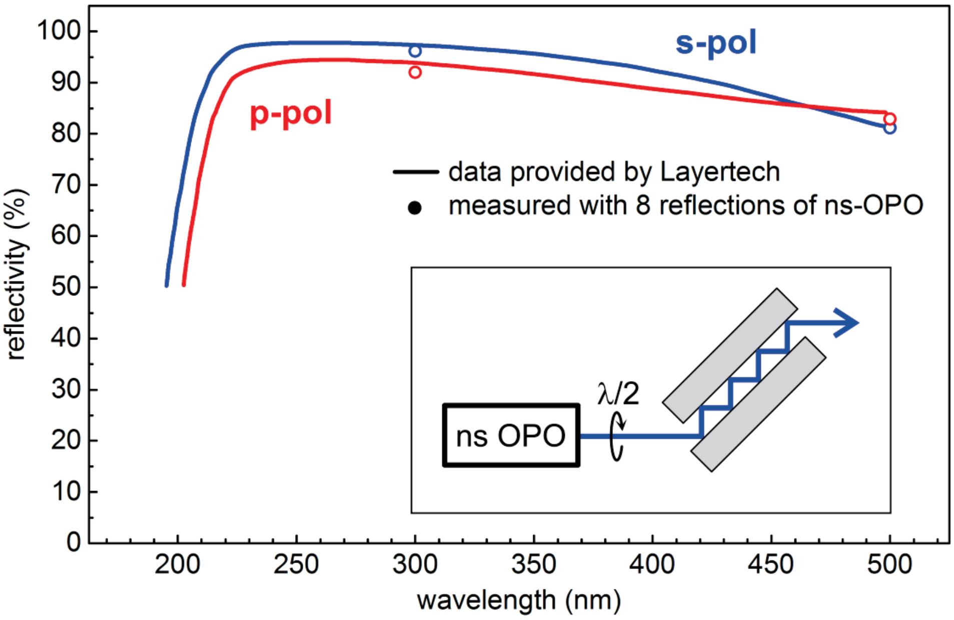

Fig. 10.3: Reflectivity of Layertech enhanced aluminum mirrors, provided by the company (lines) and test measurements with a ns OPO for 300 and 500 nm (dots).

As mentioned previously, the used beam splitters are made of UV grade fused silica, have a center thickness of 200 µm and a wedge angle of 5 arcmin. The wedge is introduced to suppress the reflection of the backside and therefore prevent it to go to the signal diode. For a plane parallel window this backside reflection would simply decrease the signal to noise ratio in the measurement. The design criteria for the wedged window is that the back and front side reflection are spatially separated by 2 mm after a distance of 40 cm from the beam splitter. The estimation can be done by applying Snell's law. Assuming a FWHM of about 1 mm of the input beam, the back reflection can then be suppressed by an aperture (A in Fig. 10.2). The angular dispersion of the fused silica wedge with $\theta = 5$ arcmin apex angle is negligible, also for deep UV pulses. Assuming a center wavelength of $\lambda = 270$ nm and a pulse duration of $\Delta t = 20$ fs the angular dispersion after propagating through the wedge reads [Dem06]

$$\frac{d\delta}{d\lambda} = \frac{2\sin(\theta/2)}{\sqrt{1 - n^2 \sin^2(\theta/2)}} \cdot \frac{dn}{d\lambda} \approx 0.6 \frac{\mu\text{rad}}{\text{nm}} . \qquad (10.4)$$

The pulse duration of 20 fs relates to a spectral band width of $\Delta\lambda = 5.4$ nm FWHM, resulting in a net angular dispersion of

$$\frac{d\delta}{d\lambda} \cdot \Delta\lambda = 3.2\,\mu\text{rad}, \qquad (10.5)$$

which is smaller by an order of magnitude than the natural divergence of the collimated UV beam with a FWHM spot size of roughly 1 mm. Consequently, the pulse duration measurement will not be falsified by angular dispersion introduced by transmission through the wedge.

The detector box accommodates the signal and the reference diode. It is a semi-commercial unit, WL-IPD4A by WieserLabs UG. After a trigger pulse the two photodiodes are integrated for a software-adjustable amount of time. Its small form factor of $60 \times 83 \times 21\ \text{mm}^3$ enables the compact size of the autocorrelator unit. An external trigger pulse can be applied directly. The supply voltage is provided via USB. Also the data can be read out directly via the same USB port – no external power supplies or data acquisition cards or boxes are required. The resolution of the analog to digital conversion is 20 bit, providing sufficient resolution for autocorrelation measurements. The photodiodes in use are a Hamamatsu S1336-BQ for both, the signal and the reference channel. The detection range of the diode is from 190 – 1100 nm.

The detector features a software selectable tunable full scale range between 50 pC and 350 pC, this offers a range of sensitivity depending on the incoming pulse energy.

To attribute this sensitivity range to experimental values, a numerical example is given. For a center wavelength of $\lambda = 300$ nm and a pulse energy $E = 100$ nJ, the loss by six reflections on mirrors, beam splitters and absorption renders an energy at the detector

$$E_{det} = E \cdot 0.08 \cdot 0.8 \cdot 0.85^6 = 2.4\,\text{nJ}\,. \tag{10.6}$$

For 300 nm this energy corresponds to $3.65 \cdot 10^9$ photons. With an average quantum efficiency of 0.5, this gives a charge value of 292 pC.

The size of the photosensitive area of the diodes is $5.8 \times 5.8\ \text{mm}^2$, so no additional imaging of the beam onto the detectors is needed. The large detector area makes the measurement sensitive to ambient stray light. Therefore the whole unit is encased. With the micrometer screw for the temporal overlap and two knobs for horizontal and vertical steering of the pump beam sticking out of the casing (see Fig. 10.1) it is possible to optimize the autocorrelation signal in an illuminated lab while the box is closed.

The two-photon absorption induced autocorrelation signal

The process of two-photon absorption (TPA) describes the phenomenon where two photons of certain energies E_1 and E_2 are absorbed simultaneously by a medium with a band gap of $E_g \leq E_1 + E_2$. Analog to linear absorption, two-photon absorption is a material property. It is proportional to the wavelength dependent TPA coefficient β. The material coefficient β can be determined with a z-scan [Bah90, Dra02, Aja18] similar to the nonlinear refractive index n_2. The decrease of a laser pulse intensity after propagating a certain distance in z-direction of a medium with the TPA coefficient β reads

$$\frac{dI}{dz} \cong -\beta \cdot I^2 . \tag{10.7}$$

In the autocorrelation measurement two replica of the input beam are spatially and temporally overlapped at the two-photon absorbing medium. Eq. (10.7) then turns into

$$\frac{dI}{dz} = -\beta \cdot \left(I_{pump} + I_{signal} \right)^2 = -\beta \cdot \left(I_{pump}^2 + I_{signal}^2 + 2 \cdot I_{pump} \cdot I_{signal} \right). \tag{10.8}$$

This term can be understood in the following way: both beams, the pump and the signal, experience two-photon absorption in the medium, independently. At the time zero a mixed contribution of both intensities is present – corresponding to the term $I_{pump} \cdot I_{probe}$ in Eq. (10.8). Hence, the variation of the relative time delay τ between pump and signal renders the autocorrelation function $S_{AC}(\tau)$.

$$S_{AC}(\tau) \propto \beta \cdot \int_{-\infty}^{\infty} I_{pump}(t) \cdot I_{signal}(t-\tau)\, dt . \tag{10.9}$$

For small transmission changes < 15% [Hom11] this can be treated like a second order intensity autocorrelation.

Under the assumption of a Gaussian pulse shape $I(t)$, $S(\tau)$ will be Gaussian, too and the FWHM pulse duration reads:

$$\Delta t_{I,FWHM} = \frac{\tau_{S,FWHM}}{\sqrt{2}}, \tag{10.10}$$

where $\tau_{S,FWHM}$ is the FWHM of the autocorrelation signal $S_{AC}(\tau)$.

Fig. 10.4 shows a typical UV TPA autocorrelation measurement in a 100 µm αBBO crystal, for frequency doubled NOPA pules around 330 nm with a deconvoluted pulse duration of 17.2 fs.

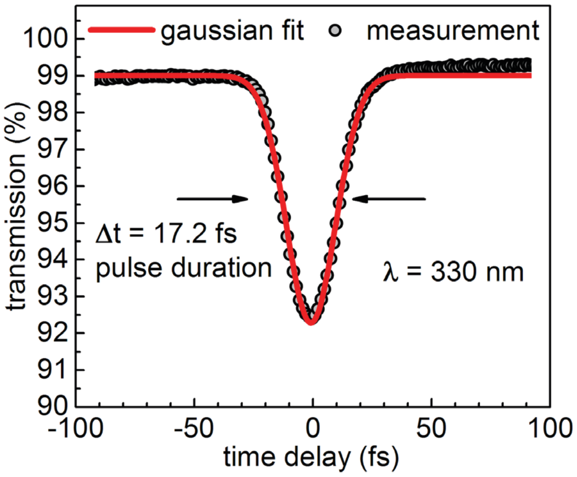

Fig. 10.4: TPA autocorrelation trace of 330 nm pulses in a 100 μm αBBO. Deconvoluted pulse duration renders 17.2 fs. Dots denote measured data points and the red line is a Gaussian fit.

The depth of the dip of the two-photon absorption autocorrelation signal is about 7% at a pulse energy from the 330 nm pulses of roughly 100 nJ.

The choice of the two-photon absorption medium for autocorrelation

In Ref. [Hom11] various materials for the UV range to be measured were characterized. In the following section this range will be extended from the UV to the visible and near infrared range. For this purpose various colored glasses are used as two-photon absorption medium.

Fig. 5 is adapted from Ref. [Hom11] and extended to the wavelength region for visible and near infrared with Schott or HOYA colored glasses. It shows the normalized two-photon absorption strength of various materials in dependence on the pulse wavelength.

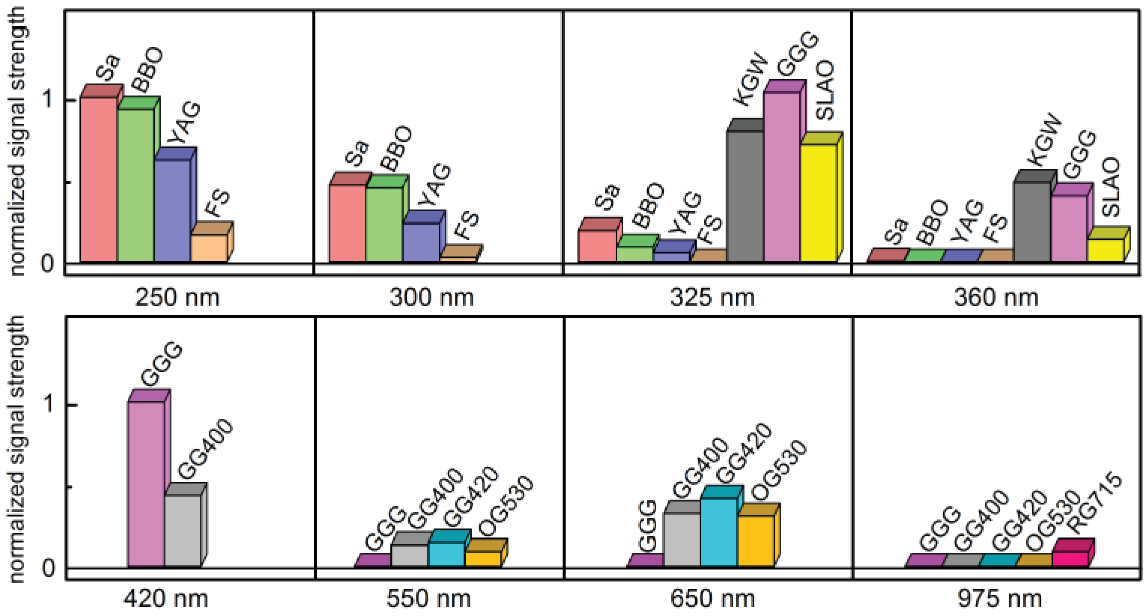

Fig. 10.5: Normalized two-photon absorption strength of various materials in dependence on the pulse wavelength. Sa: sapphire, BBO: barium borate, YAG: yttrium aluminum garnet, FS: UV grade fused silica, KGW: potassium gadolinium tungstate, GGG: gadolinium gallium garnet, SLAO: strontium lanthanum aluminate. GG400, GG420, OG530, RG715: Schott color glass. Adapted and updated from [Hom11].

The limits for each material are set on the one hand side by the condition that the wavelength of the pulse under test λ_{AC} should be larger than the one-photon absorption edge of the material $\lambda_{edge}^{(1)}$

$$\lambda_{\mathrm{AC}} > \lambda_{\mathrm{edge}}^{(1)} \ . \tag{10.11}$$

On the other hand λ_{AC} should be short enough to still allow two-photon absorption

$$\frac{1}{2} \cdot \lambda_{\mathrm{AC}} < \lambda_{\mathrm{edge}}^{(2)} \ . \tag{10.12}$$

As shown in Ref. [Hom11] the two-photon absorption edge can be different in energy from the one-photon absorption edge. Little is known about this for the crystals or glasses under discussion, but it is observed that the differences are not too large in most cases. As a rule of thumb relation (10.13) should be followed:

$$\frac{1}{2} \cdot \lambda_{\mathrm{AC}} < 0.8 \cdot \lambda_{\mathrm{edge}}^{(2)} \ . \tag{10.13}$$

Colored glasses are semiconductor-doped silica glasses. Crystalline CdS_xSe_{1-x} nanoparticles are embedded in the silica glass [Gap03, Oak93]. The variation of the absorption edge can be achieved by stoichiometric differences in the crystalline structure, given by the parameter x in the molecular formula.

The transmission curves of the materials shown in the lower panel of Fig. 10.5 are shown in Fig. 10.6. The one photon absorption edge is chosen as the wavelength where the transmission drops to a level of 50%. The data was measured with a commercial photo spectrometer (Perkin Elmer, Lambda750). The substrate thicknesses of all colored glasses are on the order of 200 µm, the thickness for the GGG crystal is 100 µm. It can be noticed that the cut-off for the very thin plates is somewhat lower than the nominal cut-off (e.g., 400 vs. 420 nm).

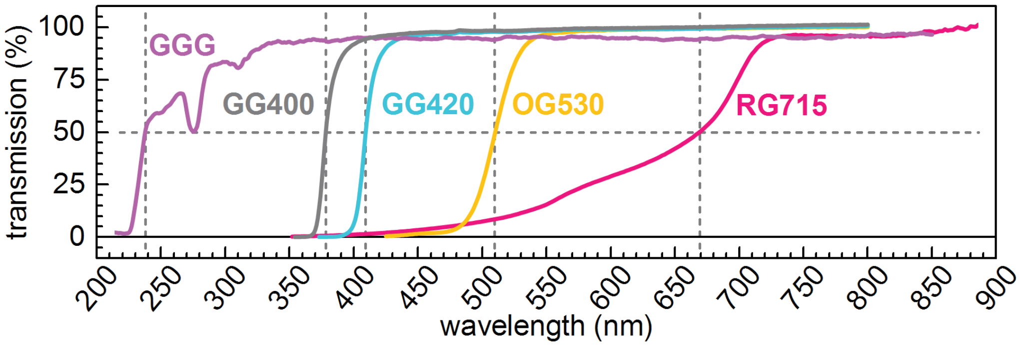

Fig. 10.6: Transmission of the colored glasses of Fig. 10.5, as well as transmission for the GGG crystal. Absorption edges are marked at 50% transmission level.

Pulse length measurement in the visible and NIR region based on TPA

The capability of measuring a two-photon absorption autocorrelation in the visible wavelength range allows a direct comparison between this method and a second-harmonic intensity autocorrelation. Up to now the validation of the pulse duration for this autocorrelation method was done indirectly via a cross correlation measurement [Hom11].

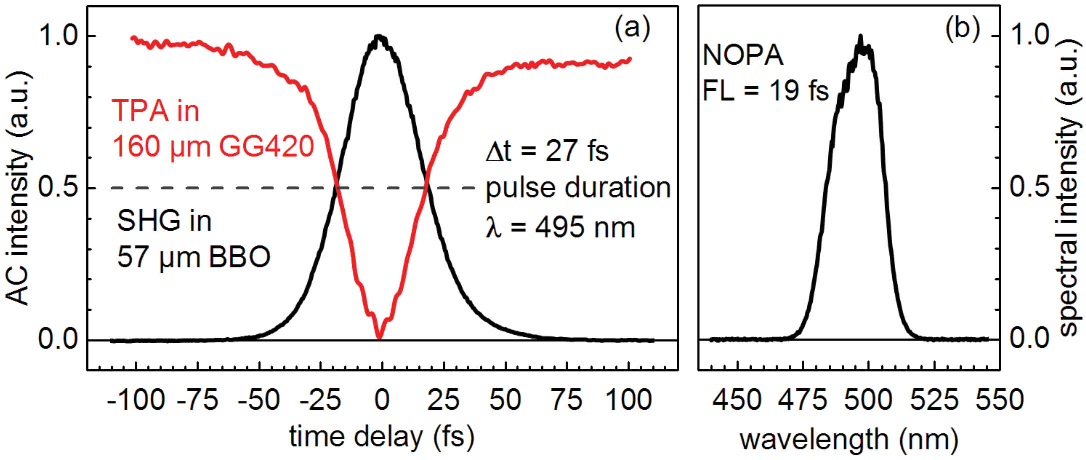

Fig. 10.7: a) comparison between SHG intensity autocorrelation (black) and TPA autocorrelation (red) of the identical pulse shown in b).

In Fig. 10.7a) a comparison of a SHG intensity autocorrelation [Koz04] is shown as a black trace. The NOPA pulse under investigation is shown in Fig. 10.7b). The pulse was compressed with a fused silica prism compressor (prisms cut for Brewster angle). For the case of SHG autocorrelation a 57 µm BBO was used for frequency doubling. For two-photon absorption autocorrelation a 160 µm GG420 was utilized. The pulse energy used for the two-photon absorption autocorrelation measurement was $E = 150$ nJ. Care was taken, that the distance of the NOPA output to each autocorrelation medium is identical. In front of the SHG autocorrelator additionally a 200 µm thick, fused silica beam splitter (as used in the TPA autocorrelator) was placed in the beam path and used in transmission, to enable identical dispersion conditions. Without readjusting of the prism compressor exactly the same pulse duration was measured by the two different approaches. For a demonstrative illustration both signals are normalized from 0 to 1 (or vice versa for the case of TPA autocorrelation) in Fig. 10.7a). The actual depth of the transmission dip in the TPA measurement was kept below 15%, to not falsify the measurement. With both methods a deconvoluted pulse duration of 27 fs was measured. This gives a direct evidence for the reliability of the pulse duration measurement via two-photon absorption.

Figures 10.8 and 10.9 show TPA pulse duration measurements with OG530 and RG715 glasses for NOPA output wavelengths of 660 nm and 975 nm, respectively. The measurement of the reddish to near infrared wavelengths requires slightly higher energy since the reflectivity of the used aluminum mirrors in the autocorrelator decreases. Metallic mirrors do not introduce phase distortions to the input pulse and since NOPA pulse energy in these wavelength regions is no problem at all, no exchange to silver mirrors was needed.

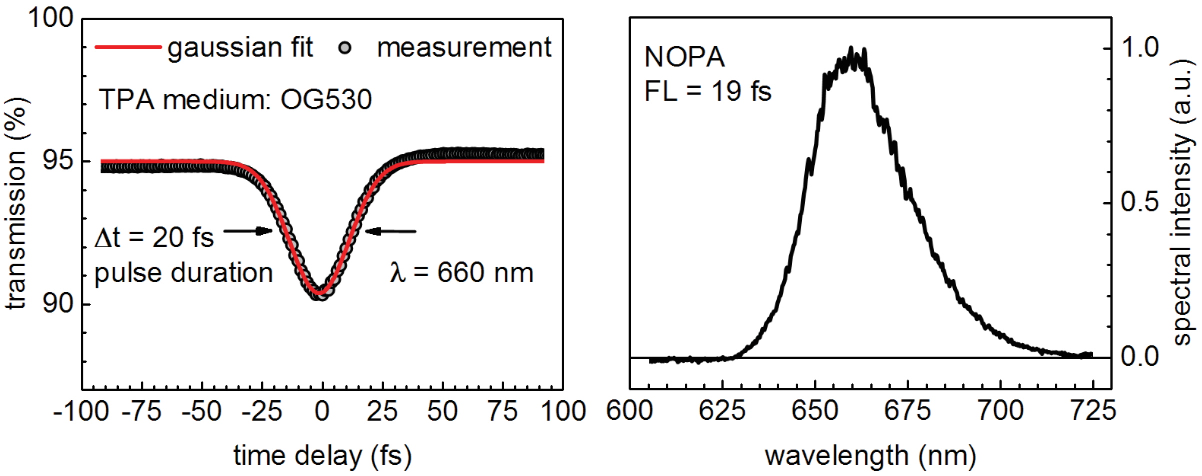

Fig. 10.8: Two-photon absorption autocorrelation (left) of 660 nm NOPA pulses (right) close to the Fourier limit in OG530 colored glass.

The 660 nm pulse with a Fourier limit of 19 fs could be compressed down to 20 fs, in an OG530 glass, as seen in Fig. 10.8. The input pulse energy was 200 nJ. For an input pulse centered around 975 nm with a Fourier limit of 27 fs, a pulse energy of 600 nJ was used. A pulse duration of 35 fs was measured in a RG715 glass – see Fig. 10.9.

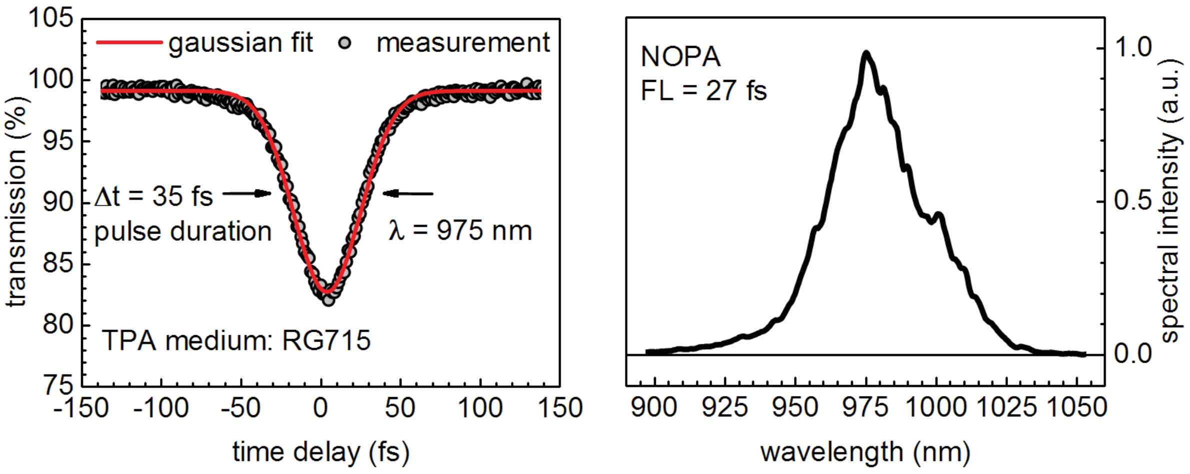

Fig. 10.9: Two-photon absorption autocorrelation (left) of 975 nm NOPA pulses (right), in RG715 colored glass.

Demonstration of a sub-10 fs pulse autocorrelation based on two-photon absorption

For ultra-broad bandwidth pulses with Fourier limits below 10 fs phase-matching in the case of second harmonic autocorrelation is a crucial topic. Very thin nonlinear crystals are needed, especially in the short wavelength region of the visible spectrum. These crystals are hardly available on the market. Most companies specify only down to 25 µm thickness with a tolerance of ± 10 µm. In most of the cases the delivered crystals have a thickness of 35 µm. For a correct SHG autocorrelation measurement of spectral bandwidths as shown in Fig. 10.10 a crystal thickness of 10 µm would have to be employed. In this section, an alternative idea for future investigation is demonstrated. Based on the fact that for two-photon absorption no phase-matching condition is required, a TPA autocorrelation measurement for an ultra-broadband NOPA source (see chapter 4) is carried out. The broadband NOPA is compressed with a combination of a fused silica prism compressor and 24 reflections on Brewster-angled chirped mirrors [Bau06].

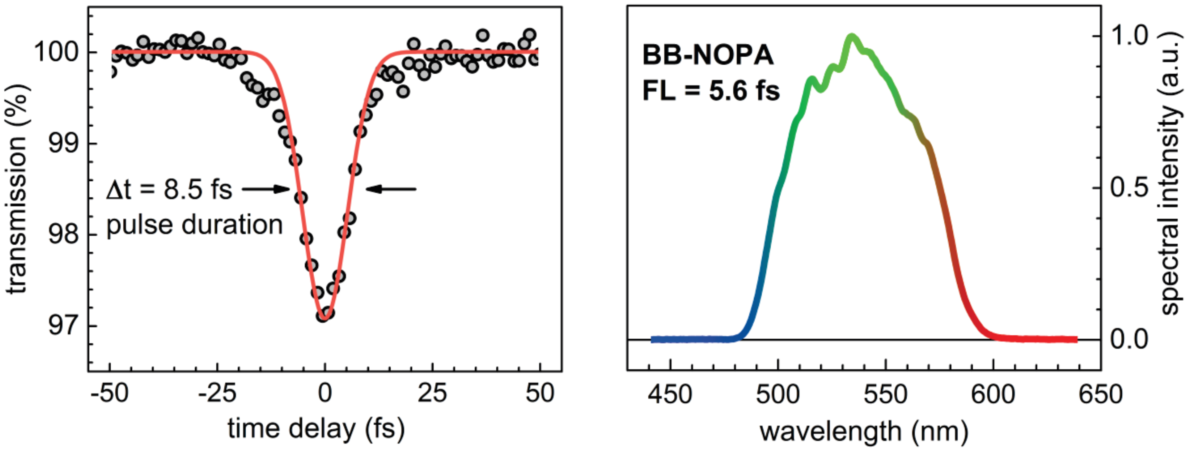

Fig. 10.10: Two-photon absorption based autocorrelation of an 8.5 fs pulse (left) of a broadband NOPA source (right). Measured in a 200 µm GG400 substrate.

Fig. 10.10 shows the autocorrelation of the broadband NOPA as short as 8.5 fs at a Fourier limit of 5.6 fs. The energy used for autocorrelation was roughly 300 nJ in a 200 µm GG400 sample. This measurement demonstrates the high potential of a two-photon absorption based measurement technique, since no limits due to phase-matching constraints are given. The nature of two-photon absorption basically only limits the spectral bandwidths of the pulses to be measured to below one octave. Thin and freestanding semiconductor films like GaN have a high two-photon absorption coefficient and should be investigated in the future for TPA autocorrelation measurements.

Using the TPA autocorrelator with repetition rates up to 1 MHz

In this section the possibility to use the presented TPA autocorrelator setup for various repetition rates is presented. Since the signal strength is dependent on intensity – compare equations (10.7) to (10.9) – the pulse energy of the input pulse has to be on the same level independent of the repetition rate. The only necessary modification to the system is to divide the laser "trigger" down to 1 kHz for the detector. For best performance a "phase locked" trigger should be chosen to ensure that the same number of shots is averaged on each scan.

An Yb:fiber laser system (Amplitude Systems, Tangerine) is used for the generation of tunable pulses with variable repetition rate. For frequency conversion a single stage, continuum seeded NOPA is used. The system is described in full detail in chapter 6 of this thesis. The NOPA output is compressed in the visible and frequency doubled to the UV. A single compressor in the visible is sufficient for compression of the UV pulses [Bau04b, Meg09].

In Fig. 10.11a) the NOPA output at 750 nm is shown. The pulse energy corresponds to 1.3 µJ at 200 kHz. With a 50 µm BBO the spectrum can be frequency doubled to 375 nm. The resulting UV pulse offers a Fourier limit of 9 fs – see Fig. 10.11b). The compressor used in the visible consists of two fused silica prisms cut for Brewster's angle. As TPA medium a 100 µm GGG crystal is chosen. A pulse duration of 15.9 fs is demonstrated for 200 kHz, 375 nm pulses in Fig. 10.11c).

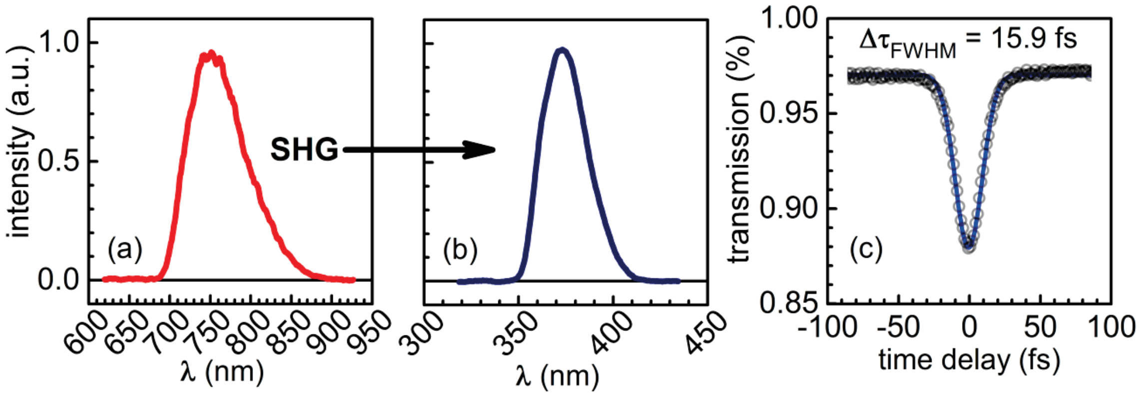

Fig. 10.11: (a) NOPA output spectrum at 750 nm with 200 kHz; (b) SHG of NOPA output at 375 nm, frequency doubled in a 50 µm BBO, E = 40 nJ; (c) two-photon absorption autocorrelation measured in 100 µm GGG crystal.

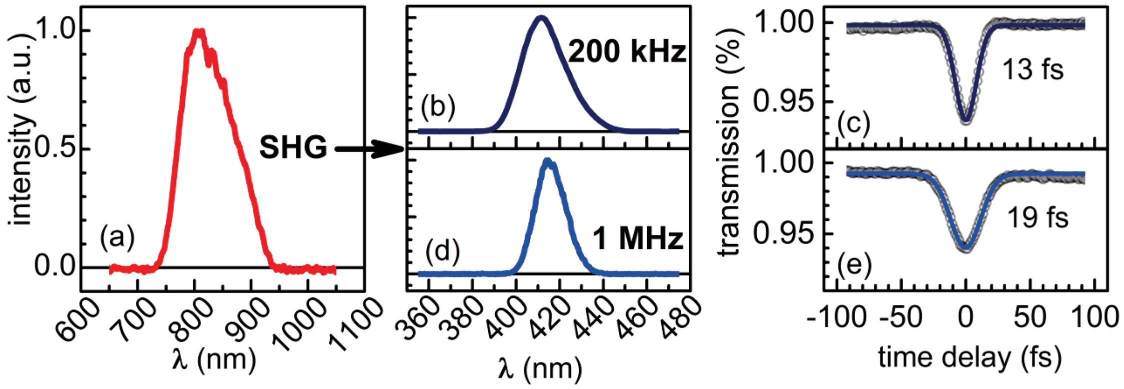

Fig. 10.12: (a) NOPA output at 820 nm, 600 nJ; (b) SHG of NOPA in 50µm BBO. E = 35 nJ for 200 kHz; (c) TPA autocorrelation with 13 fs pulse duration for 200 kHz measured in 100 µm GGG; (d) SHG of NOPA for 1 MHz; (e) TPA autocorrelation with 19 fs pulse duration for 1 MHz.

In Fig. 10.12, a 820 nm pulse is frequency doubled to 410 nm in a 50 µm BBO. At 200 kHz the Fourier limit of the blue pulse amounts to 10 fs (Fig. 10.12b). Via TPA autocorrelation a pulse duration as short as 13 fs is measured in a 100 µm GGG crystal (Fig. 10.12c). For operating the NOPA system at a repetition rate of 1 MHz slight modifications inside the NOPA are necessary. This is why the frequency doubled spectrum at a repetition rate of 1 MHz (Fig. 10.12d) is slightly narrower. The Fourier limit here amounts to 14 fs. At the repetition rate of 1 MHz a pulse duration of 19 fs can be measured by two-photon absorption in a 100 µm GGG crystal.

In this chapter a compact device with a foot-print of 360×200 mm^2 was demonstrated for characterizing pulse lengths of femtosecond pulses via the process of two-photon absorption. The possible wavelength range for the input signal is from 190 – 1100 nm without the need for changing any internal optic. Only a proper TPA medium has to be chosen according to the input wavelength. In Fig. 10.5 an overview for the TPA media is given. It has also been demonstrated that repetition rates up to 1 MHz can be used for the autocorrelation without any modifications. The setup is very robust and even bachelor students that are new to the field of laser physics find the autocorrelation signal within a few minutes. This TPA autocorrelator is a straightforward, quick and easy-to-use tool to measure pulses from sub-10 fs to a few 100 fs from the UV to the NIR range up to 1 MHz repetition rate. Additionally the absence of a phase-matching condition in TPA autocorrelation simplifies the search for proper crystal thicknesses. As demonstrated a sub-10 fs pulse can be measured with a 200 µm medium where a 10 µm crystal would be needed for a SHG autocorrelation.

11. Summary and conclusions

In this work new insights and perspectives for optical parametric amplifiers pumped by Ti:Sapphire and Yb-based laser systems have been demonstrated. In the used OPA topology it is possible to utilize repetition rates from 1 kHz to 1 MHz and input energies from 10 to 300 μJ without major changes of the design.

A new and simple method for ultra-broadband pulse generation was shown. By seeding a UV pumped NOPA with nearly un-chirped light broadband pulses with Fourier limits as low as 5 fs can be generated with severely reduced complexity from previous attempts. For single stage amplification the efficiency is low due to limited temporal overlap of pump and seed inside the gain medium. But since the seed pulses are nearly un-chirped the resulting pulses of the single amplification stage show only half of the initial laser pulse duration. This allows the implementation of a subsequent second amplification stage without losing spectral components of the pre-amplifier. Output spectra with 5 fs Fourier limits were shown with energies as high as 18 μJ.

The demonstrated setup for ultra-broadband amplification requires no pre-compression of the seed pulse. This method is known to be accompanied with huge complexity in the setup [Kob00]. Also it is not necessary anymore to temporally stretch the pump pulse to enhance the temporal overlap with a chirped seed pulse [Bau06]. The latter strategy leads to large third order chirp and therefore increases the complexity regarding pulse compression. With a combination of Brewster-angled chirped mirrors and a prism compressor the pulses were compressed easily to 6.7 fs with high satellite peak contrast. A time-bandwidth product of 0.46 was demonstrated.

For 2D-UV spectroscopy shortest UV and blue pulses are required. Such pulses are obtained by achromatic frequency doubling. Since high energy pulses are obtained with the presented method it is also expected to obtain high efficiency for frequency doubling to the UV range.

Achromatic frequency doubling of NOPA pulses pumped by Ti:sapphire lasers has already been demonstrated in 2004. This method enables the conversion of broadband visible pulses to the UV region. Consequently, shortest UV pulses can be generated with this method. During this work a proof of principle experiment was performed that this concept also works for NOPAs pumped by Yb-based laser sources at higher repetition rates, e.g., 200 kHz. Spectra at 350 nm and 450 nm have been demonstrated with Fourier limits with 4.8 fs and

5.8 fs, respectively. The shown pulses are possibly the broadest known near-UV/blue pulses leading to the potentially shortest pulse durations. The spectral range that is demonstrated here is hard to obtain starting with a Ti:Sapphire pump laser system – compare Ref. [Var14]. Additionally the demonstrated pulse durations of this reference are longer compared to the Fourier limits shown here. This makes the concept of achromatic phase-matching of NOPA pulses generated with Yb-based pump laser systems highly interesting for future applications like ultrafast 2D-UV spectroscopy. In future approaches these pulses should be optimized on efficiency and compressibility.

A compact, dispersion balanced autocorrelator for temporal pulse characterization via two-photon absorption from UV to the NIR was developed and presented in this work. It was demonstrated that the setup can be utilized for repetition rates from 1 kHz to 1 MHz. For characterization of pulses in the range from 190 – 1100 nm no optics change is needed. The capability for measuring sub-10 fs pulse durations was shown. The absence of a phase-matching condition in TPA autocorrelation simplifies the search for proper crystal thicknesses for pulse characterization. The autocorrelator has a small footprint to enable temporal pulse characterization and optimization where it is needed – for example at the sample position in transient spectroscopy setups where the pump pulse needs to be shortest. On the fly pulse characterization is possible without the need for readjusting a temporal overlap or a second pulse.

The phenomenon that after optical parametric amplification the transmitted seed light and the amplified output can propagate in significantly different directions was finally explained in detail in this work. It is explained as a consequence of Kerr lensing at the needed pump intensities in the amplifier crystal and imperfect input coupling due to a beam pointing drift.

Intensities between 150 and 200 GW/cm^2 are common to pump a NOPA crystal. For the 2 mm BBO amplifier crystal this corresponds intrinsically to a B-Integral greater than 3 for the pump wavelength of 400 nm. The intensity is needed to amplify the nJ seed light to 10 µJ. The large value of the B-Integral is fixed to the necessary pump intensity by the properties of the BBO crystal. Other crystals have very similar conditions.

In the white light crystal the needed high intensity for filamentation is mainly achieved by self-focusing. As a consequence the seed light emerges with a larger angle variation compared to the pump beam. In the amplifier crystal the pump pulse generates a Kerr lens. The pump is only displaced according to the input beam angular change. In combination, the seed light does not propagate through the middle of the Kerr lens. Therefore the amplified spectral and temporal part of the seed is refracted off the pump induced Kerr lens.

For the first time a value for the correlation of the noise of a parametric amplifier with the beam pointing stability of the pump laser was stated. For the used NOPA geometry this corresponds to $dE/d\theta = -1270$ nJ/mrad at 450 nJ pulse energy. A pointing stability of ± 20 µrad will translate to 5% energy fluctuations of the amplified NOPA signal.

This illustrates the importance regarding the beam pointing stability of the used laser source. The power stability of modern laser sources seems not to be a critical issue for OPA. Most tested systems showed the expected average power within a few minutes after starting the laser. More critical is the beam pointing drift during the warm up-phase of the system. Therefore it is recommended to monitor the beam pointing of the pump laser. If it not stabilizes after a reasonable time after starting the system, an active beam-stabilization system is necessary for stable OPA operation.

For future OPAs these findings should be considered. The Kerr lensing effect justifies that is important to place the amplifier crystal behind the focal plane of the pump beam. In this geometry it is possible to reduce the self-focusing effect by the divergence of the beam. If the needed intensity is achieved by a narrowed collimation of the pump beam, plane wavefronts are present on the front crystal surface leading to even stronger self-focusing of the beam. This will lead to higher distortions in the amplified signal and loss of phase-matching.

These new aspects regarding the Kerr-lens induced distortions are also a new motivation for the already well-established concept of Ref. [Rie00] for the use of a pre-amplifier, especially for 1 kHz, high energy NOPAs. The pre-amplifier should be operated such that only 1 – 5% of the desired final output energy is reached. In the second amplification stage this pre-amplified signal can then be amplified to the final output energy with a lower intensity and hence a lower B-Integral compared to directly amplify the lower nJ level seed photons in a single stage. A high amplification in both (or even more) stages will lead to different curvatures of the wavefronts, making the resulting pulses hard to compress. Additionally, these results should be a warning to not pump an amplifier with too high an intensity. If in an experiment for example only 100 nJ pulse energy is needed, the pump intensity can be reduced. In the used geometries this can be achieved simply by moving the crystal further away from the focal plane. It would be counterproductive to go for 10 µJ output energy or even higher and attenuate the pulses after amplification. The reduced intensity in the amplifier crystal will reduce the B-Integral and hence will lead to weaker parasitic nonlinearities and clean pulses in time, frequency and space will result.

Various crystals have been compared for supercontinuum generation with an Yb-based laser system at 1030 nm. In terms of over-all efficiency of parametric amplifiers at 1030 nm, it might be reasonable to switch from well-established YAG to YVO_4 or $GdVO_4$ for continuum generation. Roughly a factor of 3 to 4 less energy for stable continuum generation is needed, leading to higher pump energies for the amplification. The blue shift during continuum generation for to YVO_4 or $GdVO_4$ is not as pronounced as for YAG. Here the cut-off wavelength is around 600 nm, instead of 490 nm. However wavelengths below 600 nm are not fulfilling the phase-matching conditions in BBO for a pump wavelength of 515 nm, anyway. For continuum generation on the long wavelength side (> 1030 nm) of the fundamental from various crystals GSO performs best. The near infrared cut-off is above 1700 nm and it offers the largest spectral energy density of all compared crystals. It is a scintillator material, birefringent and not straightforward to purchase. However, GSO continua should be part of future investigations and characterizations. It seems to be a very promising material for seeding NIR OPAs and moreover for the use as probe pulse in transient spectroscopy in the NIR region. For generation of a near infrared plateau up to 1600 nm in YAG, a 10 mm thick plate has to be used for a fundamental wavelength of 1030 nm.

A new, simple and compact concept for few cycle, CEP-stable MIR pulse generation and detection was demonstrated. An octave spanning MIR pulse centered around 8 µm is generated starting from an Yb-based laser source. A pulse around 1180 nm is directly generated in a single stage amplification pumped by 515 nm in BBO. In a subsequent amplifier, based on 0.5 mm LGS in xz-cut, these pulses are collinearly amplified by the remaining 1030 nm pulses. The generated idler pulse results due the amplification process and corresponds to the MIR field. The resulting MIR pulses are down chirped. It was shown experimentally and theoretically that the MIR pulses can be compressed close to the Fourier limit simply by transmission through Germanium windows. The generated spectra are wider than an octave – spanning from 5 – 11 µm. A gain factor of 2 in the parametric amplification process was demonstrated, this corresponds to 600 nJ pulse energy at 50 kHz in the MIR. This equals a quantum efficiency of 10% with respect to 50 µJ pump pulses.

The MIR pulses are temporally characterized by electro-optical sampling in a 12 µm GaSe crystal oriented for sum-frequency mixing. This crystal thickness is needed to phase-match the full spectral width of the broadband MIR pulse with the ultrashort gate pulse needed for EOS. The gate pulse is directly generated in a 1 mm YAG plate by self-compression due to continuum generation of the fundamental pulse. A 9 fs pulse has been demonstrated without the need for a compression scheme. A compression down to 1.4 cycles of the MIR field is demonstrated. The used concept with a second harmonic pumped pre-amplifier and a subsequent fundamental pumped stage for MIR generation generates intrinsically phase-locked MIR pulses. A CEP measurement reveals a phase stability of better than 94 mrad over one hour. The data for the electro optic sampling signal is recorded with two identical, photo diode detectors of our own design. The signals of the detectors are digitized continuously by an USB oscilloscope at 15 bit resolution. Typically scan durations of 1 s are chosen. For each laser pulse a stretched signal is produced in each detector, which are evaluated separately by a fitting algorithm. The presented setup offers the capability for octave spanning field resolved spectroscopy in the fingerprint region with a total footprint of less than 1 m^2.

High average pump powers at high laser repetition rates lead to a number of serious issues especially with regard to the long term stability of a parametric amplifier. For UV pumped NOPAs at repetition rates between 200 kHz and 1 MHz thermal gradients in BBO crystals arise. This is introduced by two-photon absorption that occurs for wavelengths smaller than 360 nm. The thermal load cannot dissipate in the time window between two laser pulses, anymore. Consequently, the crystal heats up. It was shown that this can even be seen with a thermal camera. Temperature changes on the order of 50 °C lead to a change of the phase-matching angle by 0.2°. As a result the UV power decreases over time. For too high UV power also crystal damage might result. For third harmonic generation of an Yb-fiber laser, second harmonic generation with subsequent sum-frequency mixing to the third harmonic was demonstrated. This generates measureable heat in the THG crystal. It was demonstrated that with a time delay compensation plate (αBBO) between the SHG and THG crystal, this effect can be minimized. By temporally pre-compensation the fundamental with respect to the second harmonic, the generation locus of the main UV power is shifted to the end of the crystal. The setup of Ref. [Nil14] also uses the concept of a time-delay compensation plate between SHG and THG. Contrary to the presented concept the used plate only compensates for the GVM introduced by the SHG crystal. This surely enhances the efficiency of THG.

However, in terms of long-time stability the strategy to temporally overcompensate the pulses for the thickness of the THG crystal is more reasonable, because the temperature gradient inside the THG crystal is reduced as it has been shown. Moreover the properly oriented αBBO compensation plate corrects for the walk-off introduced by second harmonic generation. This is also beneficial for the efficiency of third harmonic generation. With this presented setup long term stable UV pulses have been presented even at repetition rates as high as 1 MHz.

For high repetition rates, the issue of non-dissipating heat due to two-photon absorption of UV pulses is also a crucial topic for the amplifier BBO of a NOPA system. Using too high pump intensity also leads to a thermal gradient inside the crystal and the amplified pulse energy decreases over time due to a change of phase-matching conditions. It was demonstrated that using a 5 mm BBO amplifier crystal with 10 GW/cm^2 pump intensity instead of 2 mm crystal thickness with 50 GW/cm^2 leads to identical output energies in combination with long term stability.

In contrast to Ref. [Lie14], the setup presented here shows better over-all efficiency, even at higher repetition rates. Additionally, the used concept to enhance the tuning range with two different pump pulses and seed continua seems to be superior to the concept of enhancing the tuning range via optical parametric amplification with subsequent continuum generation. With the presented setup smoother spectra and pulses with better peak/satellite contrast in the time domain have been obtained.

To summarize the acquired knowledge and expertise on the alignment of an OPA a guideline is given as an outlook, on how to obtain long-term stable UV pulses with 1 MHz repetition rate. In the example sub-30 fs pulses at 230 nm should be obtained starting from a 1030 nm laser system with 300 fs pulse duration and 20 W of output power

This requires a NOPA pulse centered around 460 nm with subsequent second harmonic generation. For second harmonic generation a BBO crystal with 35 µm thickness is available. At 460 nm the acceptance bandwidth for frequency doubling of the 35 µm BBO amounts to 10 nm.

The guideline is based on the NOPA topology of chapter 6. For the generation of NOPA pulses at 460 nm, the 2ω white light with the 3ω pump pulse has to be used.

Pump laser and laboratory requirements:

- Check the stability of the used laser table, no vibrations should be present. As mentioned, the beam pointing stability is crucial since angle variations of the fundamental beam will be increased in the nonlinear processes!
- Ensure a high beam pointing stability of the pump laser with $< \pm 20$ µrad.
- Ensure constant laboratory temperature with ±1°C.
- Initially the laser should be operated at 200 kHz with 4 W of power going into the NOPA. This corresponds to 20 µJ pulse energy. All alignment steps inside the NOPA are recommended to be done at the lowered repetition rate before increasing it to 1 MHz.

NOPA alignment and fine-tuning of the bandwidth for SHG:

- Optimize the 3ω pump efficiency to roughly 15%. Too high an efficiency will lead to spatio-temporal distortions in the pump beam. The NOPA pulses are hardly to compress if the pump beam is distorted. The pump energy at 343 nm should correspond to 3 µJ.
- Be sure that the amplifier crystal is located far enough behind the pump beam waist. A position of roughly 32 cm from the focusing mirror corresponds to an intensity of 10 GW/cm^2. This value should be used initially.
- Optimize the amplification at 460 nm. For optimal output energy move also the relay imaging lens of the seed beam. This is necessary due to the wavelength selective propagation of the white light – compare chapter 2. At 200 kHz the maximum output energy should be kept below 200 nJ in order to switch to 1 MHz later.
- Initially the spectral bandwidth of the NOPA output might correspond to a value of 20 nm or higher. It needs to be narrowed to the acceptance bandwidth of the BBO.
- To obtain sub-30 fs pulses at 230 nm, a spectral bandwidth of 10 nm at 460 nm has to be used for frequency doubling in the available 35 µm BBO. Larger bandwidths will only lead to elongated or distorted UV pulses and lowered doubling efficiency.
- Selected amounts of dispersive material should be introduced in the seed beam path. This leads to a narrowed output spectrum of the NOPA.
- Once a spectral bandwidth of 10 nm is obtained the repetition rate of the laser can be

increased to 1 MHz while keeping the NOPA input pulse energy constant at 20 µJ.

- Do not align the beams inside the NOPA at 1 MHz repetition rate. Only change the relay imaging of the seed and the phase-matching angle if necessary.

Second Harmonic Generation and UV autocorrelation:

- At 460 nm the acceptance angle of the 35 µm BBO amounts to 2.6° FWHM.
- Check the beam size of the NOPA output with a beam profiler. For the moment a beam size of the collimated beam of FWHM = 2.2 mm is assumed.
- To enhance the doubling efficiency, the 460 nm beam needs to be focused towards the BBO with a concave mirror. The acceptance angle of the crystal limits the focal length of the mirror to $f = 2.2\text{ mm} / \tan(2.6°) \approx 50\text{ mm}$. In the experiment a slightly longer focal length of 75 mm should be chosen to avoid too strong astigmatism. Alternatively, a Schiefspiegler – see chapter 3 – should be used.
- The 35 µm BBO should be located behind the focal plane at the position where the efficiency is highest. Behind the focus the Kerr-nonlinearity will balance the divergence of the beam and perfect phase-matching results.
- The phase-matching angle of the BBO should be optimized on the UV spectrum with a spectrometer. The broadest UV spectrum is not necessarily obtained where the doubling efficiency is highest.
- A concave mirror has to be used for collimation after SHG. For separating the wavelengths a HR mirror is beneficial. To ensure a suitable spot size of the UV beam, a focal length of $f = 250$ mm is needed. Roughly FWHM = 2 mm for the UV beam should be obtained after collimation in order to get a sharp focus inside the UV autocorrelator (chapter 10).
- A 200 µm αBBO should be used for UV autocorrelation of the 230 nm pulses.
- With the prism compressor located in the visible the resulting UV pulses can be optimized online to sub-30 fs with the presented UV autocorrelator.

This guideline summarized important details of chapters 2, 3, 4, 5, 6 and 10 of this thesis and should assist for future approaches on short UV pulse generation and characterization at 1 MHz repetition rate.

12. References

[Ada08] S. Adachi, N. Ishii, T. Kanai, A. Kosuge, J. Itatani, Y. Kobayashi, D. Yoshitomi, K. Torizuka, S. Watanabe, "*5-fs, multi-mJ, CEP-locked parametric chirped-pulse amplifier pumped by a 450-nm source at 1 kHz*," Opt. Express **16**, 14341 (2008).

[Aes11] M. Aeschlimann, T. Brixner, A. Fischer, C. Kramer, P. Melchior, W. Pfeiffer, C. Schneider, C. Strüber, P. Tuchscherer, D. V. Voronine, "*Coherent Two-Dimensional Nanoscopy*," Science **333**, 1723 (2011).

[Aja18] A. Ajami, W. Husinsky, A. Ovsianikov, R. Liska, "*Dispersive white light continuum single Z-scan for rapid determination of degenerate two-photon absorption spectra*," Appl. Phys. B **7**, 124 (2018).

[Alf70a] R. R. Alfano, S. L. Shapiro, "*Emission in the region 4000 to 7000 Å via four-photon coupling in glass*," Phys. Rev. Lett. **24**, 584 (1970).

[Alf70b] R. R. Alfano, S. L. Shapiro, "*Observation of self-phase modulation and small-scale filaments in crystals and glasses*," Phys. Rev. Lett. **24**, 592 (1970).

[And83] D. Anderson, M. Lisak, "*Nonlinear asymmetric self-phase modulation and self-steepening of pulses in long optical waveguides*," Phys. Rev. A **27**, 1393 (1983).

[And86] G. P. Anderson, , S. A. Clough, F. X. Kneizys, J. H. Chetwynd, E. P. Shettle "*AFGL atmospheric constituent profiles (0–120 km)*," Tech. Rep. AFGL-TR-86-0110, Air Force Geophys. Lab., Hanscom Air Force Base, Bedford, Mass., 1986.

[Bac13] M. Bache, H. Guo, B. Zhou, X. Zeng, "*The anisotropic Kerr nonlinear refractive index of the beta-barium borate* (β-BaB_2O_4) *nonlinear crystal*," Opt. Mater. Express **3**, 358 (2013).

[Bah90] M. Sheik-Bahae, A.A. Said, T.H. Wei, D.J. Hagan and E.W. Van Stryland, "*Sensitive Measurement of Optical Nonlinearities Using a Single Beam*," IEEE J. Quant. Electron. **26**, 760 (1990).

[Bal02a] A. Baltuška, T. Kobayashi, "*Adaptive shaping of two-cycle visible pulses using a flexible mirror*," Appl. Phys. B **75**, 427 (2002).

[Bal02b] A. Baltuška, T. Fuji, T. Kobayashi, "*Controlling the Carrier-Envelope Phase of Ultrashort Light Pulses with Optical Parametric Amplifiers*," Phys. Rev. Lett. **88**, 133901 (2002).

[Bau04] P. Baum, S. Lochbrunner, E. Riedle, "*Tunable sub-10fs ultraviolet pulses generated by achromatic frequency doubling*," Opt. Lett. **29**, 1686 (2004).

[Bau04a] P. Baum, S. Lochbrunner, E. Riedle, "*Zero-additional-phase SPIDER: full characterization of visible and sub-20-fs ultraviolet pulses*," Opt. Lett. **29**, 210 (2004).

[Bau04b] P. Baum, S. Lochbrunner, E. Riedle, "*Generation of tunable 7-fs ultraviolet pulses: achromatic phase matching and chirp management*," Appl. Phys. B **79**, 1027 (2004).

[Bau06] P. Baum, M. Breuer, E. Riedle, G. Steinmeyer, "*Brewster-angled chirped mirrors for broadband pulse compression without dispersion oscillations*," Opt. Lett. **31**, 2220 (2006).

[Bec01] A. Becker, A. Aközbek, K. Vijayalakshmi, E. Oral, C. M. Bowden, S. L. Chin, "*Intensity clamping and re-focusing of intense femtosecond laser pulses in nitrogen molecular gas*," Appl. Phys. B **73**, 287 (2001).

[Ber07] L. Bergé, S. Skupin, R. Nuter, J. Kasparian, J.-P. Wolf, "*Ultrashort filaments of light in weakly ionized, optically transparent media*," Rep. Prog. Phys. **70**, 1633 (2007).

[Bow08a] P. Bowlan, U. Fuchs, R. Trebino, U. D. Zeitner, "*Measuring the spatiotemporal electric field of tightly focused ultrashort pulses with sub-micron spatial resolution*," Opt. Express **16**, 13663 (2008).

[Bow08b] P. Bowlan, P. Gabolde, M. A. Coughlan, R. Trebino, R. J. Levis, "*Measuring the spatiotemporal electric field of ultrashort pulses with high spatial and spectral resolution*," J. Opt. Soc. Am. B **25**, A81 (2008).

[Boy03] R.W. Boyd, "*Nonlinear Optics*, Second Edition" (Academic Press, San Diego, 2003).

[Bra09] M. Bradler, P. Baum, E. Riedle, "*Femtosecond continuum generation in bulk laser host materials with sub-μJ pump pulses*," Appl. Phys. B **97**, 561 (2009).

[Bra11] M. Bradler, C. Homann, E. Riedle, "*Mid-IR femtosecond pulse generation on the microjoule level up to 5 μm at high repetition rates*," Opt. Lett. **36**, 4212 (2011).

[Bra14a] M. Bradler, E. Riedle, "*Sub-20 fs μJ-energy pulses tunable down to the near-UV from a 1 MHz Yb-fiber laser system*," Opt. Lett. **39**, 2588 (2014).

[Bra14b] "*Bulk continuum generation: The ultimate tool for laser applications and spectroscopy: From new insights to ultrafast amplifiers and spectrometers*," M. Bradler doctoral thesis at the LMU Munich (2014), http://edoc.ub.uni-muenchen.de/17456/

[Bro99] A. Brodeur, S. L. Chin, "*Ultrafast white-light continuum generation and self-focusing in transparent condensed media*," J. Opt. Soc. Am. B **16**, 637 (1999).

[Bur13] J. Burke, W. Li, A. Heimsath, C. von Kopylow, R. B. Bergmann, "*Qualifying parabolic mirrors with deflectometry*," J. Europ. Opt. Soc. Rap. Public. **8**, 13014 (2013).

[Cal15] A.-L. Calendron, H. Çankaya, G. Cirmi, and F. X. Kärtner, "*White-light generation with sub-ps pulses*," Opt. Express **23**, 13866 (2015).

[Cer00] G. Cerullo, N. Nisoli, S. Staigra, S. De Silvestri, G. Tempea, F. Krausz, and K. Ferencz, "*Mirror-dispersion-controlled OPA: a compact tool for sub-10-fs spectroscopy in the visible*," Appl. Phys. B Suppl. **70**, S253 (2000).

[Cer03] G. Cerullo, S. De Silvestri, "*Ultrafast optical parametric amplifiers*," Rev. Sci. Instrum. **74**, 1 (2003).

[Cer99] G. Cerullo, M. Nisoli, S. Stagira,S. De Silvestri, G. Tempea, F. Krausz, K. Ferencz "Mirror-dispersion-controlled sub-10-fs optical parametric amplifier in the visible," Opt. Lett. 24, 1529 (1999).

[Chi05] S.L. Chin, S.A. Hosseini, W. Liu, Q. Luo, F. Théberge, N. Aközbek, A. Becker, V.P. Kandidov, O.G. Kosareva, H. Schroeder, "*The propagation of powerful femtosecond laser pulses in optical media: physics, applications, and new challenges*," Can. J. Phys. **83**, 863 (2005).

[Chu93] Y.-H. Chuang, L. Zheng, D.D. Meyerhofer, "*Propagation of Light Pulses in a Chirped-Pulse-Amplification Laser*," IEEE J. of Quant. Electronics **29**, 270 (1993).

[Clo05] S .A. Clough, M. W. Shephard, E. J. Mlawer, J. S. Delamere, M. J. Iacono, K. Cady-Pereira, S. Boukabara, P.D. Brown, "*Atmospheric radiative transfer modeling: a summary of the AER codes*," J. Quant. Spectrosc. Radiat. Transf. **91**, 233 (2005).

[Cor86] P. B. Corkum, C. Rolland, "*Supercontinuum Generation in Gases*," Phys. Rev. Lett. **57**, 2268 (1986).

[Cou05] A. Couairon, M. Franco, A. Mysyrowicz, J. Biegert, U. Keller, "*Pulse self-compression to the single-cycle limit by filamentation in a gas with a pressure gradient*," Opt. Lett. **30**, 2657 (2005).

[Cou06] A. Couairon, J. Biegert, C. P. Hauri, W. Kornelis, F. W. Helbing, U. Keller, A. Mysyrowicz, "*Self-compression of ultra-short laser pulses down to one optical cycle by filamentation*," J. Mod. Opt. **53**, 75 (2006).

[Dem06] "*Experimentalphysik Band 2, Elektrizität und Optik*," W. Demtröder, (Springer-Verlag, Berlin, Heidelberg, New York, 2006).

[Dha14] J. A. Dharmadhikari, R. A. Deshpande, A. Nath, K. Dota, D. Mathur, A. K. Dharmadhikari, "*Effect of group velocity dispersion on supercontinuum generation and filamentation in transparent solids*," Appl. Phys. B **117**, 471 (2014).

[Dob10] A. L. Dobryakov, S. A. Kovalenko, A. Weigel, J. L. Pérez-Lustres, J. Lange, A. Müller, N. P. Ernsting, "*Femtosecond pump/supercontinuum-probe spectroscopy: Optimized setup and signal analysis for single-shot spectral referencing*," Rev. Sci. Instrum. **81**, 113106 (2010).

[Dra02] A. Dragonmir, J.G. McInerney and D.N. Nikogosyan, "*Femtosecond measurements of two-photon absorption coefficients at* $\lambda = 264\,nm$ *in glasses, crystals, and liquids*," Appl. Opt. **41**, 4365 (2002).

[Dub17] A. Dubietis, G. Tamosauskas, R. Suminas, V. Jukna, A. Couairon, "*Ultrafast supercontinuum generation in bulk condensed media*," Lith. J. Phys. **57**, 113 (2017).

[Dud06] J. M. Dudley, G. Genty, S. Coen, "*Supercontinuum generation in photonic crystal fiber*," Rev. Mod. Phys. **78**, 1135 (2006).

[Emo10] M. Emons, A. Steinmann, T. Binhammer, G. Palmer, M. Schultze, U. Morgner, "*Sub-10-fs pulses from a MHz-NOPA with pulse energies of 0.4* μJ," Opt. Express **18**, 1191 (2010).

[Eri10] P. Eriksson, S. A. Buehler, C. P. Davis, C. Emde, O. Lemke, "*ARTS, the atmospheric radiative transfer simulator, version 2*," J. Quant. Spectrosc. Radiat. Transf. **112**, 1551 (2011).

[Ern01] N. P. Ernsting, S. A. Kovalenko, T. Senyushkina, J. Saam, V. Farztdinov, "*Wave-Packet-Assisted Decomposition of Femtosecond Transient Ultraviolet-Visible Absorption Spectra: Application to Excited-State Intramolecular Proton Transfer in Solution*," J. Phys. Chem. A **105**, 3443 (2001).

[Fer13] M. R. Ferdinandus, H. Hu, M. Reichert, D.J. Hagan, E.W. Van Stryland, "*Beam deflection measurement of time and polarization resolved ultrafast nonlinear refraction*," Opt. Lett. **38**, 3518 (2013).

[Ful15] F. D. Fuller, J. P. Ogilive, "*Experimental Implementations of Two-Dimensional Fourier Transform Electronic Spectroscopy*," Annu. Rev. Phys. Chem. **66**, 667 (2015).

[Gae00] A. L. Gaeta, "*Catastrophic Collapse of Ultrashort Pulses*," Phys. Rev. Lett. **84**, 3582 (2000).

[Gal15] J. Galinis, G. Tamosauskas, I. Grazuleviciute, E. Keblyte, V. Jukna, and A. Dubietis, "*Filamentation and supercontinuum generation in solid-state dielectric media with picosecond laser pulses*," Phys. Rev. A **92**, 033857 (2015).

[Gal95] G. M. Gale, M. Cavallari, T. J. Driscoll, F. Hache, "*Sub-20-fs tunable pulses in the visible from an 82-MHz optical parametric oscillator*," Opt. Lett. **20**, 1562 (1995).

[Gal99] G. Gallot, D. Grischkowsky, "*Electro-optic detection of terahertz radiation*," J. Opt. Soc. Am. B **16**, 1204 (1999).

[Gap03] "*Optical Properties of Semiconductor Nanocrystals*," S. V. Gaponenko, (Cambridge University Press, Cambridge, 2003), chap. 3.1.1.

[Gom09] A. Gómez-Vieyra, A. Dubra, D. Malacara-Hernández, D. R. Williams, "*First-order design of off-axis reflective ophthalmic adaptive optics systems using afocal telescopes*," Opt. Express **17**, 18906 (2009).

[Gom11] A. Gomez-Vieyra, D. Malacara-Hernández, "*Methodology for third-order astigmatism compensation in off-axis spherical reflective systems*," Appl. Opt. **50**, 1057 (2011).

[Gra00] E.J. Grace, A. Ritsataki, P.M.W. French, G.H.C. New, "*New optimization criteria for slit-apertured and gain-apertured KLM all-solid-state lasers*," Opt. Commun. **183**, 249 (2000).

[Gre05] M. Greve, B. Bodermann, H. R. Telle, P. Baum, E. Riedle, "*High-contrast chemical imaging with gated heterodyne coherent anti-Stokes Raman scattering microscopy*," Appl. Phys. B **81**, 875 (2005).

[Gro08] G. I. Groma, J. Hebling, I. Z. Kozma, G. Váró, J. Hauer, J. Kuhl, E. Riedle, "*Terahertz radiation from bacteriorhodopsin reveals correlated primary electron and proton transfer processes*," Proc. Natl. Acad. Sci. **105**, 6888 (2008).

[Guo15] J. Guo, J.-J. Xie, D.-J. Li, G.-L. Yang, F. Chen, C.-R. Wang, L.-M. Zhang, Y. M. Andreev, K. A. Kokh, G. V. Lanskii, V. A. Svetlichnyi, "*Doped GaSe crystals for laser frequency conversion*," Light: Science & Applications **4**, e362 (2015).

[Har01] I. Hartl, X. D. Li, C. Chudoba, R. K. Ghanta, T. H. Ko, J. G. Fujimoto, J. K. Ranka, R. S. Windeler, "*Ultrahigh-resolution optical coherence tomography using continuum generation in an air–silica microstructure optical fiber*," Opt. Lett. **26**, 608 (2001).

[Hoe11] A. Höfer, K. Duncker, M. Kiel, S. Förster, W. Widdra, "*Laser-excited PEEM using a fully tunable fs-laser system*," IBM J. Res. & Dev **55**, 4 (2011).

[Hom08] C. Homann, C. Schriever, P. Baum, E. Riedle, "*Octace wide tunable UV-pumped NOPA: pulses down to 20 fs at 0.5 MHz repetition rate*," Opt. Express **16**, 5746 (2008).

[Hom11] C. Homann, N. Krebs, E. Riedle, "*Convenient pulse length measurement of sub-20-fs pulses down to the deep UV via two-photon absorption in bulk material*," Appl. Phys. B **104** (2011).

[Hom12] "*Optical parametric processes to the extreme: From new insights in first principles to tunability over more than 4 octaves*," C. Homann, doctoral thesis at the LMU Munich (2012), http://edoc.ub.uni-muenchen.de/16104/

[Hom13] C. Homann, M. Breuer, F. Setzpfandt, T. Pertsch, E. Riedle, "*Seeding of picosecond and femtosecond optical parametric amplifiers by weak single mode continuous lasers*," Opt. Express **21**, 730 (2013).

[Hub00] R. Huber, A. Brodschelm, F. Tauser, A. Leitenstorfer, "*Generation and field-resolved detection of femtosecond electromagnetic pulses tunable up to 41 THz*," Appl. Phys. Lett. **76**, 3191 (2000).

[Iac99] C. Iaconis, I. A. Walmsley, "*Self-Referencing Spectral Interferometry for Measuring Ultrashort Optical Pulses*," IEEE J. Quant. Elect. **35**, 501 (1999).

[Ice76] H.W. Icenogle, B.C. Platt, W.L. Wolfe, "*Refractive indexes and temperature coefficients of germanium and silicon*," Appl. Opt. **15**, 2348 (1976).

[Kai00] R. A. Kaindl, M. Wurm, K. Reimann, P. Hamm, A. M. Weiner, M. Woerner, "*Generation, shaping, and characterization of intense femtosecond pulses tunable from 3 to 20 µm*," J. Opt. Soc. Am. B **17**, 2086 (2000).

[Kan03] V. P. Kandidov, O. G. Kosareva, I. S. Golubtsov, W. Liu, A. Becker, N. Aközbek, C. M. Bowden, S. L. Chin, "*Self-transformation of a powerful femtosecond laser pulse into a white-light laser pulse in bulk optical media (or supercontinuum generation)*," Appl. Phys. B **77**, 149 (2003).

[Kan93] D. J. Kane, R. Trebino, "*Charcterization of Arbitrary Femtosecond Pulses Using Frequency Resolved Optical Gating*," IEEE J. Quant. Elect. **29**, 571 (1993).

[Kat13] K. Kato, F. Tanno, N. Umemura, "*Sellmeier and thermo-optic dispersion formulas for GaSe (Revisited)*," Appl. Opt. **52**, 2325 (2013).

[Kat17] K. Kato, K. Miyata, L. Isaenko, S. Lobanov, V. Vedenyapin, V. Petrov, "*Phase-matching properties of* $LiGaS_2$ *in the 1.025–10.5910 µm spectral range*," Opt. Lett. **42**, 4363 (2017).

[Kea16] C. Kealhofer, W. Schneider, D. Ehberger, A. Ryabov, F. Krausz, P. Baum, "*All-optical control and metrology of electron pulses*," Science **352**, 429 (2016).

[Kei16] S. Keiber, S. Sederberg, A. Schwarz, M. Trubetskov, V. Pervak, F. Krausz, N. Karpowicz, "*Electro-optic sampling of near-infrared waveforms*," Nat. Photonics **10**, 159 (2016).

[Kel65] P. L. Kelly, "*Self-focusing of optical beams*," Phys. Rev. Lett. **15**, 1005 (1965).

[Kno17] M. Knorr, J. Raab, M. Tauer, P. Merkl, D. Peller, E. Wittmann, E. Riedle, C. Lange, R. Huber, "*Phase-locked multi-terahertz electric fields exceeding 13 MV/cm at a 190 kHz repetition rate*," Opt. Lett. **42**, 4367 (2017).

[Kno18] M. Knorr, P. Steinleitner, J. Raab, I. Gronwald, P. Merkl, C. Lange, R. Huber, "*Ultrabroadband etalon-free detection of infrared transients by van-der-Waals contacted sub-10-µm GaSe detectors*," Opt. Express **26**, 19059 (2018).

[Kob00] T. Kobayashi, A. Shirakawa, "*Tunable visible and near-infrared pulse generator in a 5 fs regime*," Appl. Phys. B Suppl. **70**, S239 (2000).

[Koe06] "*Solid-State Laser Engineering*," W. Koechner (Springer, Berlin, 2006).

[Koz03] I. Z. Kozma, P. Baum, S. Lochbrunner, E. Riedle, "*Widely tunable sub-30 fs ultraviolet pulses by chirped sum frequency mixing*," Opt. Express **11**, 3110 (2003).

[Koz04] I. Z. Kozma, P. Baum, U. Schmidhammer, S. Lochbrunner, E. Riedle, "*Compact autocorrelator for the online measurement of tunable 10 femtosecond pulses*," Rev. Sci. Instrum. **75**, 2323 (2004).

[Kra16] V. Kravtsov, R. Ulbricht, J. M. Atkin, M. B. Raschke, "*Plasmonic nanofocused four-wave mixing for femtosecond near-field imaging*," Nature Nanotechnology **11**, 459 (2016).

[Kre13] N. Krebs, I. Pugliesi, E. Riedle, "*Pulse Compression of Ultrashort UV Pulses by Self-Phase Modulation in Bulk Material*," Appl. Sci. **3**, 153 (2013).

[Kue04] C. Kübler, R. Huber, S. Tübel, A. Leitenstorfer, "*Ultrabroadband detection of multi-terahertz field transients with GaSe electro-optic sensors: Approaching the near infrared*," Appl. Phys. Lett. **85**, 3360 (2004).

[Kum15] S. Chaitanya Kumar, J. Canals Casals, J. Wei, M. Ebrahim-Zadeh, "*High-power, high-repetition-rate performance characteristics of* β-BaB_2O_4 *for single-pass picosecond ultraviolet generation at 266 nm*," Opt. Express **23**, 28091 (2015).

[Kur96] N. A. Kurnit, T. Shimada, M.S. Sorem, A. J. Taylor, G. Rodriguez, T. S. Clement, D. F.V. James, P. W. Milonni, "*Measurement and Control of Optical Nonlinearities of Importance to Glass Laser Fusion Systems*," Second Annual Solid-State Lasers for Applications to ICF, International Conference, 22-25 October 1996, Paris, France.

[Kut53] "*Der Schiefspiegler: Ein Spiegelteleskop für hohe Bilddefinition*," A. Kutter, Weichardt, Biberach a.d.R 1953.

[Li01] H. P. Li, C. H. Kam, Y. L. Lam, W. Ji, "*Femtosecond Z-scan measurements of nonlinear refraction in nonlinear optical crystals*," Opt. Materials **15**, 237 (2001).

[Li14] W. Li, Z. Wang, X. Zhang, Y.E. Wu, W. Liao, L. Huang, F. Gao, W. Fan, W. Li, Q. Wu, J. Xu, "*Convenient ultra-broadband femtosecond optical gating utilizing transient beam deflection effect*," Opt. Express **22**, 31417 (2014).

[Lie14] M. Liebel, C. Schnedermann, P. Kukura, "*Sub-10-fs pulses tunable from 480 to 980 nm from a NOPA pumped by an Yb:KGW source*," Opt. Lett. **39**, 4112 (2014).

[Liu02] W. Liu, S. Petit, A. Becker, N. Aközbek, C.M. Bowden, S.L. Chin, "*Intensity clamping of a femtosecond laser pulse in condensed matter*," Opt. Commun. 202, **189** (2002).

[Liu04] K. Liu, J. Xu, X.-C. Zhanga, "*GaSe crystals for broadband terahertz wave detection*," Appl. Phys. Lett. **85**, 863 (2004).

[Lu14] C. Lu, Y. J. Tsou, H. Y. Chen, B. H Chen, Y. C. Cheng, S. D. Yang, M. C. Chen, C. C. Hsu, A. H. Kung, "*Generation of intense supercontinuum in condensed media*," Optica **1**, 400 (2014).

[Mac00] A. Maciejewski, R. Naskrecki, M. Lorenc, M. Ziolek, J. Karolczak, J. Kubicki, M. Matysiak, M. Szymanski, "*Transient absorption experimental set-up with femtosecond time resolution. Femto- and picosecond study of DCM molecule in cyclohexane and methanol solution*," J. Mol. Struc. **555**, 1 (2000).

[Mal65] I. H. Malitson, "*Interspecimen Comparison of the Refractive Index of Fused Silica*," J. Opt. Soc. Am. **55**, 1205 (1965).

[Man16] C. Manzoni, G. Cerullo, "*Design criteria for ultrafast optical parametric amplifiers*," J. Opt. **18**, 103501 (2016).

[Meg09] U. Megerle, I. Pugliesi, C. Schriever, C.F. Sailer, E. Riedle, "*Sub-50 fs broadband absorption spectroscopy with tunable excitation: putting the analysis of ultrafast molecular dynamics on solid ground*," Appl. Phys. B **96**, 215 (2009).

[Mej03] G. Méjean, J. Kasparian, E. Salomon, J. Yu, J.-P. Wolf, R. Baurayou, R. Sauerbrey, M. Rodriguez, L. Wöste, H. Lehmann, B. Stecklum, U. Laux, J. Eislöffel, A. Scholz, A.P. Hatzes, "*Towards a supercontinuum-based infrared lidar*," Appl. Phys. B **77**, 357 (2003).

[Mil08] S. Miller, F. Rotermund, G.Xu, F. Noack, V. Panyutin, V. Petrov, "*Polarization-dependent nonlinear refractive index of* BiB_3O_6," Opt. Materials **30**, 1469 (2008).

[Nah96] A. Nahata, A. S. Weling, T. F. Heinz, "*A wideband coherent terahertz spectroscopy system using optical rectification and electro-optic sampling*," Appl. Phys. Lett. **69**, 2323 (1996).

[Nik91] D. N. Nikogosyan, "*Beta Barium Borate (BBO) – A Review of Its Properties and Applications*," Appl. Phys. A **52**, 359 (1991).

[Nil14] J. Nillon, O. Crégut, C. Bressler, S. Haacke, "*Two MHz tunable non collinear optical parametric amplifiers with pulse durations down to 6 fs*," Opt. Express **22**, 14965 (2014).

[Oak93] S.M. Oak, K.S. Bindra, R. Chari and K.C. Rustagi, "*Two-photon absorption in semiconductor-doped glasses*," J. Opt. Soc. Am. B **10**, 613 (1993).

[Pen96] A. Penzkofer, M. Wittmann, M. Lorenz, E. Siegert, S. Macnamara, "*Kerr lens effects in a folded-cavity four-mirror linear resonator*," Opt. Quantum Electron. **28**, 523 (1996).

[Per94] M.D. Perry, T. Ditmire, B.C. Stuart, "*Self-phase modulation in chirped-pulse amplification*," Opt. Lett. **19**, 2149 (1994).

[Pet15] V. Petrov, "*Frequency down-conversion of solid-state laser sources to the mid-infrared spectral range using non-oxide nonlinear crystals*," Prog. Quantum Electron. **42**, 1 (2015).

[Pie00] J. Piel, M. Beutter, E. Riedle, "*20 – 50-fs pulses tunable across the near infrared from a blue-pumped noncollinear parametric amplifier*," Opt. Lett. **25**, 180 (2000).

[Pie06] J. Piel, E. Riedle, L. Gundlach, R. Ernstorfer, R. Eichberger, "*Sub-20 fs visible pulses with 750 nJ energy from a 100 kHz noncollinear parametric amplifier*," Opt. Lett. **31**, 1289 (2006).

[Pla01] P. C. M. Planken, H.-K. Nienhuys, H. J. Bakker, T. Wenckebach, "*Measurement and calculation of the orientation dependence of terahertz pulse detection in ZnTe*," J. Opt. Soc. Am. B **18**, 313 (2001).

[Pol18] M. N. Polyanskiy, "*Refractive index database*," https://refractiveindex.info. Accessed on 2018-07-26.

[Por14] M. Porer, J.-M. Ménard, R. Huber, "*Shot noise reduced terahertz detection via spectrally post filtered electro-optic sampling*," Opt. Lett. **39**, 2435 (2014).

[Pup15a] M. Puppin, Y. Deng, O. Prochnow, J. Ahrens, T. Binhammer, U. Morgner, M. Krenz, M. Wolf, R. Ernstorfer, "*500 kHz OPCPA delivering tunable sub-20 fs pulses with 15 W average power based on an all-ytterbium laser*," Opt. Express **23**, 1491 (2015).

[Pup15b] I. Pupeza, D. Sánchez, J. Zhang, N. Lilienfein, M. Seidel, N. Karpowicz, T. Paasch-Colberg, I. Znakovskaya, M. Pescher, W. Schweinberger, V. Pervak, E. Fill, O. Pronin, Z. Wei, F. Krausz, A. Apolonski, J. Biegert, "*High-power sub-two-cycle mid-infrared pulses at 100 MHz repetition rate*," Nat. Photonics **9**, 721 (2015).

[Ran00] J. K. Ranka, R. S. Windeler, A. J. Stentz, "*Visible continuum generation in air–silica microstructure optical fibers with anomalous dispersion at 800 nm*," Opt. Lett. **25**, 25 (2000).

[Ran96] J. K. Ranka, R. W. Schirmer, A. L. Gaeta, "*Observation of Pulse Splitting in Nonlinear Dispersive Media*," Phys. Rev. Lett. **77**, 3783 (1996).

[Ras13] M.R. Rashidian Vaziri, F. Hajiesmaeilbaigi, M. H. Maleki, "*New ducting model for analyzing the Gaussian beam propagation in nonlinear Kerr media and its application to spatial self-phase modulations*," J. Opt. **15**, 035202 (2013).

[Raz66] Y. P. Razer, "*Breakdown and heating of gases under the influence of a laser beam*," Sov. Phys. Usp. **8**, 650 (1966).

[Ree94] M.K. Reed, M.K. Steiner-Shepard, D.K. Negus, "*Widely tunable femtosecond optical parametric amplifier at 250 kHz with a Ti:sapphire regenerative amplifier*," Opt. Lett. **19**, 1855 (1994).

[Ree95] M. K. Reed, M. K. Steiner-Shepard, M. S. Armas, D. K. Negus, "*Microjoule-energy ultrafast optical parametric amplifiers*," J. Opt. Soc. Am. B **12**, 2229 (1995).

[Rei03] K. Reimann, R. P. Smith, A. M. Weiner, T. Elsaesser, M. Woerner, "*Direct field-resolved detection of terahertz transients with amplitudes of megavolts per centimeter*," Opt. Lett. **28**, 471 (2003).

[Rei14] M. Reichert, H. Hu, M. R. Ferdinandus, M. Seidel, P. Zhao, T.R. Ensley, D. Peceli, J.M. Reed, D.A. Fishman, S. Webster, D.J. Hagan, E.W. Van Stryland, "*Temporal, spectral, and polarization dependence of the nonlinear optical response of carbon disulphide*," Optica **1**, 436 (2014).

[Rie00] E. Riedle, M. Beutter, S. Lochbrunner, J. Piel, S. Schenkl, S. Spörlein, W. Zinth, "*Generation of 10 to 50 fs pulses tunable through all of the visible and the NIR*," Appl. Phys. B **71**, 457 (2000).

[Rie13] E. Riedle, M. Bradler, M. Wenninger, C. F. Sailer, I. Pugliesi, "*Electronic transient spectroscopy from the deep UV to the NIR: unambiguous disentanglement of complex processes*," Faraday Discuss. **163**, 139 (2013).

[Rot08] L. S. Rothman, I. E. Gordon, A. Barbe, D. Chris Benner, P. F. Bernath, M. Birk, V. Boudon, L. R. Brown, A. Campargue, J.-P. Champion, K. Chance, L. H. Coudert, V. Dana, V. M. Devi, S. Fally, J.-M. Flaud, R.R. Gamache, A. Goldman, D. Jacquemart, I. Kleiner, N. Lacome, W.J. Lafferty, J.-Y. Mandin, S. T. Massie, S. N. Mikhailenko, C. E. Miller, N. Moazzen-Ahmadi, O. V. Naumenko, A.V. Nikitin, J. Orphal, V.I. Perevalov, A. Perrin, A. Predoi-Cross, C. P. Rinsland, M. Rotger, M.Simeckova, M. A. H. Smith, K. Sung, S. A. Tashkun, J. Tennyson, R. A. Toth, A. C. Vandaele, J. Vander Auwera, "*The HITRAN 2008 molecular spectroscopic database*," J. Quant. Spectrosc. Radiat. Transf. **110**, 533 (2008).

[Rot12a] J. Rothhardt, S. Demmler, S. Hädrich, J. Limpert, and A. Tünnermann "*Octave-spanning OPCPA system delivering CEP-stable few-cycle pulses and 22 W of average power at 1 MHz repetition rate*," Opt. Express **20**, 10870 (2012).

[Rot12b] C. Richard, I. E. Gordon, L. S. Rothman, M. Abel, L. Frommhold, M. Gustafsson, J.-M. Hartmann, C. Hermans, W. J. Lafferty, G. S. Orton, K. M. Smith, H. Tran, "*New section of the HITRAN database: Collision-induced absorption (CIA)*," J. Quant. Spectrosc. Radiat. Transf. **113**, 1276 (2012).

[Rot14] C. Rothhardt, J. Rothhardt, A. Klenke, T. Peschel, R. Eberhardt, J. Limpert, A. Tünnermann, "*BBO-sapphire sandwich structure for frequency conversion of high power lasers*," Opt. Mat. Express **4**, 1092 (2014).

[Ryb14] W. Ryba-Romanowski, B. Macalik, A. Strzep, R. Lisiecki, P. Solarz, R. M. Kowalski, "*Spectral transformation of infrared ultrashort pulses in laser crystals*," Optical Materials **36**, 1745 (2014).

[Sch08a] C. Schriever, S. Lochbrunner, E. Riedle, D. J. Nesbitt, "*Ultrasensitive ultraviolet-visible 20 fs absorption spectroscopy of low vapor pressure molecules in the gas phase*," Rev. Sci. Instrum. **79**, 013107 (2008).

[Sch08b] C. Schriever, S. Lochbrunner, P. Krok, E. Riedle, "*Tunable pulses from below 300 to 970 nm with durations down to 14 fs based on a 2 MHz ytterbium-doped fiber system*," Opt. Lett. **33**, 192 (2008).

[Sie86] "*Lasers*," A. E. Siegmann, (University Science Books, Mill Valley, USA, 1986), pp. 584

[Skr12] C. Skrobol, I. Ahmad, S. Klingebiel, C. Wandt, S. Trushin, Z. Major, F. Krausz, and S. Karsch, "*Broadband amplification by picosecond OPCPA in DKDP pumped at 515 nm*," Opt. Express **20**, 4619 (2012).

[Smi15] "*Crystal Nonlinear Optics*, First Edition," A. V. Smith, (AS-Photonics, LLC, Albuquerque, 2015).

[Smi18] personal message from Arlee Smith to Eberhard Riedle.

[SNLO] *SNLO nonlinear optics code*, available from A.V. Smith, AS Photonics, Albuquerque, NM, (2017), "http://www.as photonics.com" and references given therein to the crystal properties.

[Sta14] T. Stanislauskas, R. Budriunas, R. Antipenkov, A. Zaukevicius, J. Adamonis, A. Michailovas, L. Giniunas, R. Danielius, A. Piskarskas, and A. Varanavicius, "*Table top TW-class OPCPA system driven by tandem femtosecond Yb:KGW and picosecond Nd:YAG lase*rs," Opt. Express **22**, 1865 (2014).

[Ste05] A. G. Stepanov, J. Kuhl, I. Z. Kozma, E. Riedle, G. Almási, J. Hebling, "*Scaling up the energy of THz pulses created by optical rectification*," Opt. Express **13**, 5762 (2005).

[Ste06] A. Steinmann, A. Killi, G. Palmer, T. Binhammer, U. Morgner, "*Generation of few-cycle pulses directly from a MHz-NOPA*," Opt. Express **14**, 10627 (2006).

[Ste09] "Spektrale Einengung abstimmbarer Femtosekundenimpulse mit dispersiven Materialien," P. Sterflinger, bachelor thesis at the LMU Munich (2009).

[Sti06] G. Stibenz, N. Zhavoronkov, G. Steinmeyer, "*Self-compression of millijoule pulses to 7.8 fs duration in a white-light filament*," Opt. Lett. **31**, 274 (2006).

[Sto78] R. H. Stolen, C. Lin, "*Self-phase-modulation in silica optical fibers*," Phys. Rev. Lett. **17**, 1448 (1978).

[Str85] D. Strickland and G. Mourou, "*Compression of amplified chirped optical pulses*," Opt. Commun. **56**, 219 (1985).

[Taf96] G. Taft, A. Rundquist, M. M. Murnane, I. P. Christov, H. C. Kapteyn, K. W. DeLong, D. N. Fittinghoff, M. A. Krumbügel, J. N. Sweetser, R. Trebino, "*Measurement of 10-fs Laser Pulses*," IEEE Select. Topics Quantum. Electron. **2**, 575 (1996).

[Var14] R. B. Varillas, A. Candeo, D. Viola, M. Garavelli, S. De Silvestri, G. Cerullo, C. Manzoni, "*Microjoule-level, tunable sub-10 fs UV pulses by broadband sum-frequency generation*," Opt. Lett. **39**, 3849 (2014).

[Wei08] X. Wei, L. Qian, P. Yuan, H. Zhu, D. Fan, "*Optical parametric amplification pumped by a phase-aberrated beam*," Opt. Express **16**, 8904 (2008).

[Wei09] "*Ultrafast Optics*", A. M. Weiner, (John Wiley & Sons , Hoboken, NJ, USA, 2009).

[Wil81] P. D. Willson, S. R. Polo, "*Polynomial filters of any degree*," J. Opt. Soc. Am. **71**, 599 (1981).

[Wil97] T. Wilhelm, J. Piel, E. Riedle, "*Sub-20-fs pulses tunable across the visible from a blue pumped single pass noncollinear parametric converter*," Opt. Lett. **22**, 1494 (1997).

[Wit13] "Der Schiefspiegler in der Laserphysik: vollständig achromatische und anastigmatische Abbildung und Verstärkung von 10 fs-Superkontinua," E. Wittmann, master thesis at the LMU Munich (2013).

[Wit96] M. Wittmann, A. Penzkofer, "*Spectral superbroadending of femtosecond laser pulses*," Opt. Commun. **126**, 308 (1996).

[Wol18] J.P. Wolf, "*Short-pulse lasers for weather control*," Reports on Progress in Physics **81**, 026001 (2018).

[Wu97] Q. Wu, X.-C. Zhanga, "*Free-space electro-optics sampling of mid-infrared pulses*," Appl. Phys. Lett. **71**, 1285 (1997).

[Yab72] E. Yablonovitch, N. Bloembergen, "*Avalanche ionization and the limiting diameter of filaments induced by light pulses in transparent media*," Phys. Rev. Lett. **29**, 907 (1972).

[Yao91] J. Yao, W. Sheng, W. Shi, "*Accurate calculation of the optimum phase-matching parameters in three-wave interactions with biaxial nonlinear-optical crystals*," J. Opt. Soc. Am. B **9**, 891 (1991).

[Yar88] "*Quantum Electronics*, Third Edition," A. Yariv, (John Wiley & Sons, New York, USA, 1988).

[Yar95] "*Optical Electronics*," A. Yariv, (Oxford University Press, USA, 1995), 4th edition, pp. 290

[Zel98] D.E. Zelmon, D.L. Small, R. Page, "*Refractive-index measurements of undoped yttrium aluminum garnet from 0.4 to 5.0 µm*," Appl. Opt. **37**, 4933 (1998).

[Zha00] D. Zhang, Y. Kong, J. Zhang, "*Optical parametric properties of 532-nm-pumped beta-bariumborate near the infrared absorption edge*," Opt. Commun. 184, **485** (2000).

[Zha18] J. Zhang, K. F. Mak, N. Nagl, M. Seidel, D. Bauer, D. Sutter, V. Pervak, F. Krausz ,O. Pronin, "*Multi-mW, few-cycle mid-infrared continuum spanning from 500 to 2250cm*$^{-1}$," Light: Science & Applications **7**, 17180 (2018).

[Zio04] M. Ziolek, R. Naskrecki, and J. Karolczak, "*Some temporal and spectral properties of femtosecond supercontinuum important in pump–probe spectroscopy*," Opt. Commun. **241**, 221 (2004).

Appendix A1

Direct Generation of 7 fs Whitelight Pulses from Bulk Sapphire

E. Wittmann, M. Bradler, and E. Riedle

Ultrafast Phenomena XIX pp 725-728

Reprinted with permission from Springer Publishing

Direct Generation of 7 fs Whitelight Pulses from Bulk Sapphire

Emanuel Wittmann, Maximilian Bradler, and Eberhard Riedle

LS für BioMolekulare Optik, Ludwig-Maximilians-Universität München, Oettingenstr. 67 80538 München, Germany

E-Mail: e.wittmann@physik.uni-muenchen.de

Abstract: Generation of sub-10 fs continuum pulses without external compression is demonstrated. We investigate the propagation of the newly generated wavelengths and find that a short crystal in combination with an achromatic telescope leads to nearly chirp free continua

New insights into bulk Filamentation

Supercontinuum generation (SCG) in bulk material is a generally applicable method to broaden the spectrum of femtosecond laser pulses at various wavelengths. The Fourier limit for a possible compression of, e.g., an 800 nm pumped continuum from sapphire, amounts to about 4 fs. Yet, no results have been published which show that bulk continua have intrinsically such short pulse durations. This is in striking contrast to the situation in continua generated in gas-filled hollow core fibers or in gas filamentation. There compression to below 4 fs has been shown. In precise investigations of the continuum generation and propagation we now find that the inability to compress the continuum stems from the highly wavelength dependent effective generation locus and propagation. This knowledge gives us the chance for ideal control of the process and therefore the ability to generate sub 10 fs pulses without the use of any external compression scheme. This validates that the new frequencies generated during filamentation develop highly coherently.

Propagation properties of new frequencies and generation of sub-10-fs pulses during SCG

Two processes should be differentiated when the over-all appearance of continuum generation in a bulk material is considered. First, the spatial area or depth into the material where the new colors are developing has to be considered. Second, the propagation in the remaining material before exiting into free space has to be understood. That these issues are far from trivial is proven by the fact that a full collimation of a bulk continuum has not been reported and consequently the full temporal compression has not yet been achieved. In preliminary experiments we imaged the continuum from a 3 mm sapphire with a singlet lens and found that the blue part of the spectrum focuses earlier than the red part. In a semi-quantitative interpretation this could be attributed to the chromatic error. To circumvent this issue, we used a Schiefspiegler [1] that images all spectral components without chromatic error. We still found the blue spectral components focused earlier. An explanation would be that during filamentation all colors are generated at once, but short wavelengths fall behind the filament channel because of their lower group velocity. Without guiding by the filament, they start to diverge. The wavelengths close to the pump follow the channel longer and diverge later, leading to the observed color dependent propagation.

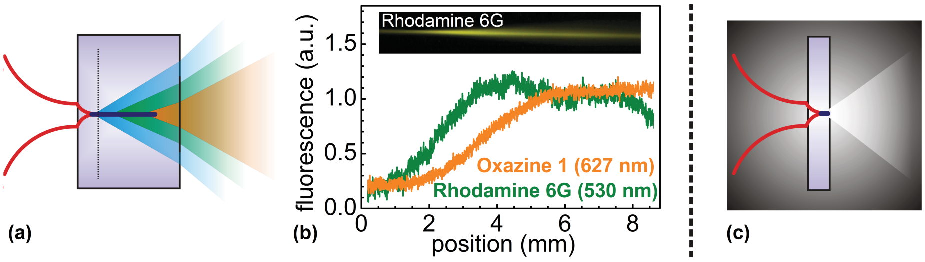

Fig 1 a) Scheme of bulk continuum generation and wavelength dependent beam propagation. b) Fluorescence of Rhodamine 6G (green) and Oxazine 1 (orange) to monitor the beam propagation during filamentation in ethanol. c) All colors diverge equally in a short crystal.

To verify this concept, a continuum is generated in ethanol and monitored from the side with a high resolution camera. To visualize the propagation of selected wavelength ranges we use a solvent (instead of sapphire) and Rhodamine 6G (absorbing around 530 nm) or Oxazine 1 (627 nm) were added separately. These laser dyes partly absorb the newly generated light and fluoresce so that the beam propagation can be monitored from the side. Fig 1 (b) shows the corresponding fluorescence signal and the side view from filamentation in ethanol with Rhodamine 6G (top). A strong signal is only found when the light has already broadened from the 8 μm filament and the dye absorption is not saturated as inside the channel. We find that different colors start to diverge at different positions in the solvent. Our proposed model is confirmed and we can explain the difficulty of properly imaging a continuum. To avoid the wavelength selective propagation, the continuum has to be generated at the very end of the crystal. The crystal should be terminated at the dashed line in Fig 1 (a) so that no spectral and local separation occurs and all colors start to diverge simultaneously as shown in Fig 1 (c). We find a short crystal length on the order of 1 mm suitable. This should lead to a chirp free continuum as the newly generated colors pass through no extra material, and all colors having the same spatial properties. With a 1 mm sapphire plate, we optimize the continuum generation onto the output face. A careful alignment still renders a continuum with little fluctuations. The pump source is a small fraction of the output of a Ti:sapphire amplifier (CPA 2001; Clark MXR) with a pulse duration of 170 fs and a central wavelength of 778 nm, focused with a f = 50 mm plano-convex lens. We obtain a continuum spanning down to 430 nm. For an anastigmatic and achromatic collimation or imaging of the generated continuum we use a reflective Schiefspiegler telescope [1], consisting of a suitable combination of a convex and a concave mirror. This allows us to measure the pulse duration of the newly generated frequencies with a SHG intensity autocorrelator without the loss of any frequencies due to aberrations. The main peak of the autocorrelation signal corresponds to a 7 fs continuum pulse.

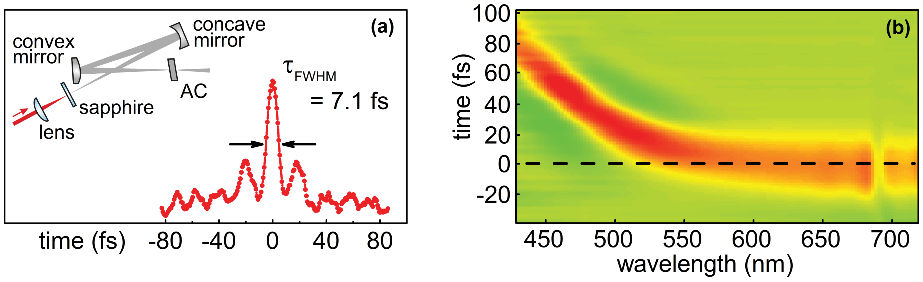

Fig 2 a) Schiefspiegler geometry for imaging the newly generated colors of a 1 mm sapphire continuum and autocorrelation trace demonstrating a 7 fs pulse. b) Transient absorption measurement in 200 µm GG400 to determine the chirp of the continuum generated in a 1 mm sapphire plate.

For a better insight into the spectrotemporal distribution of the continuum and to show that the autocorrelation signal does not correspond to a coherence spike [2] due to the complexity of the continuum pulse, the chirp of the sapphire continuum is determined with our transient spectrometer [3]. Fig 2 (b) shows the transient signal of the continuum generated in the 1 mm sapphire plate. With a 200 nJ, 25 fs pump pulse at 470 nm and the sapphire continuum as probe we measured the cross correlation via two-photon absorption in a 200 µm GG400 (Schott AG) substrate. Two-photon absorption of pump and probe only occurs for temporal overlap and allows determining the group delay for every wavelength. Since only reflective optics are used in the probe beam path, the signal represents the intrinsic spectral chirp of the continuum after propagation through just a short length of air. Fig 2 (b) shows that all spectral components from 500 to 700 nm coincide in time. The chirp for the short wavelength range mainly originates from the propagation in air. These chirped components of the pulse appear as broad and structured wings in the autocorrelation trace.

Conclusion & Outlook

It is possible to obtain sub-10 fs white light pulses directly from bulk filamentation. In the literature only a few examples for white light compression can be found, but until now the appropriate setup always is accompanied by huge complexity. By studying the propagation properties of the continuum we found a straightforward way to simplify the effort for generation of short continuum pulses. An elaborate apparatus can be replaced by a lens, a 1 mm sapphire plate and the adequate adjustment for the incident pulse energy. With the imaging by a Schiefspiegler also any chromatic aberrations as well as astigmatism can be avoided. Such pulses are highly interesting for broadband amplification, ultrafast 2D spectroscopy, or spectroscopic experiments.

[1] A. Kutter, Der Schiefspiegler: Ein Spiegelteleskop für hohe Bilddefinition (Weichhardt, 1953)
[2] Rick Trebino, Frequency-Resolved Optical Gating: The measurement of Ultrashort Laser Pulses, (Kluwer Academic Publishers, Boston / Dordrecht / London, 2000), Chap. 4
[3] U. Megerle, I. Pugliesi, C. Schriever, C.F. Sailer, E. Riedle, "Sub-50 fs broadband absorption spectroscopy with tunable excitation: putting the analysis of ultrafast molecular dynamics on solid ground", Appl. Phys. B 96, 215-231 (2009).

Appendix A2

Phase-locked multi-terahertz electric fields exceeding 13 MV/cm at a 190 kHz repetition rate

M. Knorr, J. Raab, M. Tauer, P. Merkl, D. Peller, E. Wittmann, E. Riedle, C. Lange, R. Huber

Opt. Lett. **42**, 4367 (2017)

Reprinted with permission from the Optical Society of America (OSA)

Optics Letters

Phase-locked multi-terahertz electric fields exceeding 13 MV/cm at a 190 kHz repetition rate

MATTHIAS KNORR,[1] JÜRGEN RAAB,[1] MAXIMILIAN TAUER,[1] PHILIPP MERKL,[1] DOMINIK PELLER,[1] EMANUEL WITTMANN,[2] EBERHARD RIEDLE,[2] CHRISTOPH LANGE,[1] AND RUPERT HUBER[1,*]

[1] *Department of Physics, University of Regensburg, 93040 Regensburg, Germany*
[2] *LS für BioMolekulare Optik, Ludwig-Maximilians-Universität München, Oettingenstrasse 67, 80538 München, Germany*
**Corresponding author: rupert.huber@ur.de*

Received 6 July 2017; accepted 12 September 2017; posted 18 September 2017 (Doc. ID 301260); published 20 October 2017

We demonstrate a compact source of energetic and phase-locked multi-terahertz pulses at a repetition rate of 190 kHz. Difference frequency mixing of the fundamental output of an Yb:KGW amplifier with the idler of an optical parametric amplifier in GaSe and $LiGaS_2$ crystals yields a passively phase-locked train of waveforms tunable between 12 and 42 THz. The shortest multi-terahertz pulses contain 1.8 oscillation cycles within the intensity full width at half-maximum. Pulse energies of up to 0.16 μJ and peak electric fields of 13 MV/cm are achieved. Electro-optic sampling reveals a phase stability better than 0.1 π over multiple hours, combined with free carrier-envelope phase tunability. The scalable scheme opens the door to strong-field terahertz optics at unprecedented repetition rates.

OCIS codes: (140.3070) Infrared and far-infrared lasers; (190.4970) Parametric oscillators and amplifiers; (320.7100) Ultrafast measurements; (320.7110) Ultrafast nonlinear optics; (120.5050) Phase measurement.

https://doi.org/10.1364/OL.42.004367

Ultrashort pulses in the terahertz and mid-infrared region of the electromagnetic spectrum have attracted tremendous interest in the past few years as resonant probes of low-energy elementary excitations in condensed matter [1,2]. The combination of carrier-envelope phase (CEP)-stable pulses with ultrabroadband electro-optic sampling [3–8] has allowed for studies of electronic and structural dynamics of molecules and solids, on timescales faster than a single cycle of the carrier wave [1,2]. The recent advent of high-power sources [9–13] has prompted an ongoing revolution of ultrabroadband terahertz nonlinear optics and resonant terahertz quantum control of condensed matter [14–20]. In particular, when the ponderomotive energy exceeds the fundamental bandgap of semiconductors or dielectrics, the carrier wave acts like an alternating bias field that can accelerate and recollide quasiparticles [15,16]. It can drive dynamical Bloch oscillations and high-harmonic generation [17], or induce the tunneling of electrons out of sharp metal tips [18] or through the tunneling junction of a scanning tunneling microscope (STM) [19,20]. In the multi-terahertz range, non-perturbative dynamics of this nature, often dubbed "lightwave electronics," have occurred for field amplitudes typically above 10 MV/cm.

Optical rectification, i.e., difference frequency generation (DFG) within the broad spectrum of a single femtosecond near-infrared (NIR) pulse, gives rise to passively phase-locked terahertz pulses [3–8,21]. While this concept warrants a particularly stable CEP, its observed low quantum efficiency has made it a popular choice for the generation of probe pulses [1,2]. Difference frequency mixing between the signal waves of two optical parametric amplifiers (OPAs) driven by the same pump laser, in contrast, has generated CEP-stable few- and single-cycle multi-terahertz pulses with field amplitudes in excess of 10 MV/cm or even above 100 MV/cm [9–11,22]. An innovative in-line scheme of two-color parametric amplification in a single OPA has further improved long-term CEP stability of the transients [13]. Owing to the large required pulse energies, amplifier-based terahertz sources have been limited to repetition rates in the few-kilohertz regime. Yet, a broad variety of future applications, such as frequency comb metrology and molecular fingerprinting with solid-based high-harmonic sources, lightwave-STM, and strong-field light-matter interaction with massively improved signal-to-noise ratios, call for substantially increased repetition rates while keeping the field amplitudes above 10 MV/cm. Such sources have been limited to wavelengths shorter than 5 μm [23].

Here, we introduce a table-top light source generating multi-terahertz few-cycle transients with field strengths exceeding 13 MV/cm at a repetition rate as high as 190 kHz. Our approach exploits DFG of femtosecond NIR pulses from a laser amplifier and the idler output of an OPA pumped by the second harmonic of the laser. The source is tunable between 12 and 42 THz. Its design ensures inherent phase locking, while its compact layout using only one OPA provides excellent phase stability.

The schematic of the source is sketched in Fig. 1. We start with 190 fs pulses centered at a wavelength of 1026 nm from a commercial regenerative Yb:KGW laser amplifier system (PHAROS 10; Light Conversion) with a repetition rate set

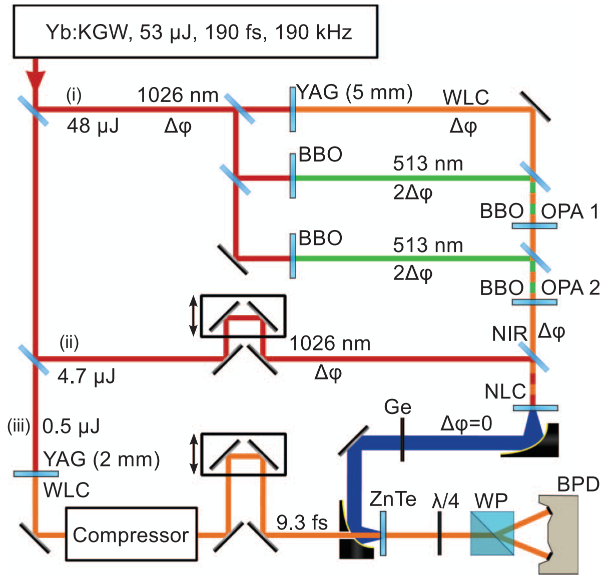

Fig. 1. Generation and electro-optic detection of energetic, CEP-stable multi-terahertz pulses at a 190 kHz repetition rate. The pulse energies and the CEP fluctuations are given for each branch, starting with the fluctuation $\Delta\varphi$ of the amplifier system. YAG, YAG crystal; BBO, 2 mm BBO crystal; WLC, white-light continuum; OPA 1/2, stages 1 and 2 of the SHG pumped OPA; NLC, nonlinear crystal for DFG; Ge, 500 μm germanium; ZnTe, 6.5 μm ZnTe crystal; $\lambda/4$, quarter-wave plate; WP, Wollaston prism; BPD, balanced pair of photodiodes.

to 190 kHz. The pulse energy of 53 μJ is split into three branches serving as (i) the pump of a NIR OPA, (ii) the pump of a multi-terahertz DFG stage, and (iii) the generation pulse of a gate for electro-optic detection. The compact OPA encompasses two amplification stages, both of which are driven by the second harmonic of the laser. A white-light continuum from a 5 mm YAG crystal [24] seeds the first OPA process in a 1 mm thick type-II beta barium borate (BBO) crystal. Subsequently, the idler wave of the first OPA stage is seeded into a second identical BBO crystal to boost the energy of the signal and idler pulses. Typical energies of 4.2 and 3.2 μJ are reached for a signal/idler pair at 900 and 1200 nm.

Since the seed pulses are subject to the same phase fluctuation $\Delta\varphi$ as the laser fundamental, and the frequency-doubled pulses feature a CEP fluctuation of $2\Delta\varphi$, the signal and idler waves in both OPA stages share the CEP of the pump laser [22]. Thus, difference frequency mixing of any pair of waves including the signal, idler, and laser fundamental, is expected to give rise to inherently phase-locked multi-terahertz pulses. We mix the laser fundamental with the idler output of the OPA because this process only depletes the more scalable laser fundamental, whereas the OPA output is amplified. We branch off pulses with an energy of 4.7 μJ from the laser output [branch (ii)]. Since the laser frequency is centered at 292 THz, while the OPA idler frequency (wavelength) is tunable between 280 (1070 nm) and 250 THz (1200 nm), the difference frequency can be set between 12 and 42 THz. Phase-matched DFG is possible throughout this spectral range using GaSe [3–7,9–11,21] or $\mathrm{LiGaS_2}$ (LGS) [12,13,25] as a nonlinear medium. Both crystals are excellent materials for broadband terahertz generation due to their large nonlinear coefficients, broadband infrared transparency, and strong birefringence that allows for widely tunable phase matching (PM). We choose a 1 mm thick LGS crystal (cut for DFG with type-II PM in the XY-plane) for the generation of pulses centered above 28 THz, while a 200 μm thick GaSe crystal allows for DFG at lower frequencies, due to its relatively low phonon frequencies.

Figures 2(a) and 2(b) depict the phase-matching function $|\mathrm{sinc}(\Delta kL/2)|$ as a function of the phase-matching angle and the difference frequency for the two crystals. Here, the phase-matching angle corresponds to the internal propagation angle relative to the Z-axis in GaSe, and relative to the X-axis in LGS. The stationary points located at a frequency of 15 THz in GaSe and 31 THz in LGS represent perfect group-velocity matching between the seed and terahertz pulses. Under the respective angles [Figs. 2(c) and 2(d)], the phase-matching bandwidth is determined by the group velocity dispersion [11]. For the relatively low NIR driving frequencies used here, the group velocity dispersion is low, and the maximal phase-matching bandwidth [Figs. 2(c) and 2(d), blue curves] of our mixing crystals substantially exceeds the maximal multi-terahertz bandwidth set by the present NIR spectra [Figs. 2(c) and 2(d), red curves].

The two generating NIR pulses (beam diameter: 2.5 mm) are focused into the mixing crystal with a focal diameter of 130 μm [intensity full width at half-maximum (FWHM)] to reach an estimated combined peak intensity of $200\ \mathrm{GW/cm^2}$. The emitted terahertz radiation is isolated from the NIR pulses by transmission through a germanium filter placed under the Brewster angle. We trace the electric field of these pulses directly by electro-optic sampling with a few-femtosecond gate pulse. For this purpose, part of the laser fundamental [branch (iii), 0.5 μJ] generates a white-light continuum in a 2 mm YAG crystal [24]. A smooth spectrum ranging from 770 to 890 nm is selected from the supercontinuum and compressed by a double pass through a pair of fused silica prisms separated by 52 cm.

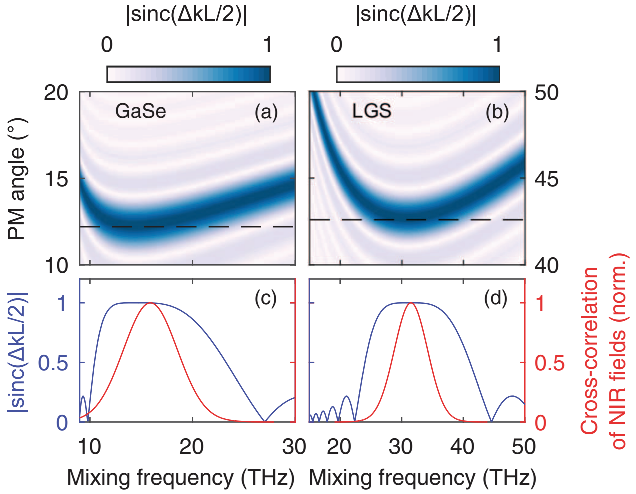

Fig. 2. PM in GaSe and LGS. (a), (b) PM function $|\mathrm{sinc}(\Delta kL/2)|$ (color coded) as a function of the PM angle and the mixing frequency for type-II DFG in (a) a 200 μm thick GaSe crystal and (b) a 1 mm thick LGS crystal for a pump wavelength of 1026 nm. The black dashed lines indicate the cross sections shown in (c) and (d). (c), (d) PM curves for perfect group velocity matching (blue curves) and the cross-correlation between the driving NIR pulses (red curves).

The resulting 9.3 fs pulse (intensity FWHM retrieved by frequency-resolved optical gating) is used as the electro-optic gating pulse. It is focused collinearly with the multi-terahertz radiation into a ⟨110⟩-cut ZnTe sensor of a thickness of 6.5 μm contacted to a 300 μm thick ⟨100⟩-cut ZnTe substrate to sample the waveforms of the multi-terahertz pulses.

Figure 3 depicts typical field transients generated in various mixing crystals under different phase-matching angles, as detected by ultrabroadband electro-optic sampling. In all cases, the existence of well-defined waveforms clearly proves CEP stability of the terahertz pulse trains emerging from the LGS [Figs. 3(a) and 3(b)] and GaSe [Figs. 3(c) and 3(d)] crystals. The corresponding Fourier spectra [Fig. 3(e)] cover the frequency range from 10 to 46 THz, corresponding to a wavelength range between 30 and 6.5 μm. A numerical simulation [Fig. 3(e), broken curves] faithfully reproducing the experimental spectra [Fig. 3(e), solid curves] confirms that the bandwidths are mainly set by the spectra of the NIR driving pulses. The terahertz pulse duration (intensity FWHM) assumes values between 102 [Fig. 3(c)] and 143 fs [Fig. 3(d)]. While the pulse width is typically close to the Fourier transform limit (factor 1.2–1.3), the phonon absorption edge of GaSe leads to a slight dispersion of the lowest frequency components in the transient depicted in Fig. 3(d). Nonetheless, this waveform contains only 1.8 optical cycles within its intensity FWHM.

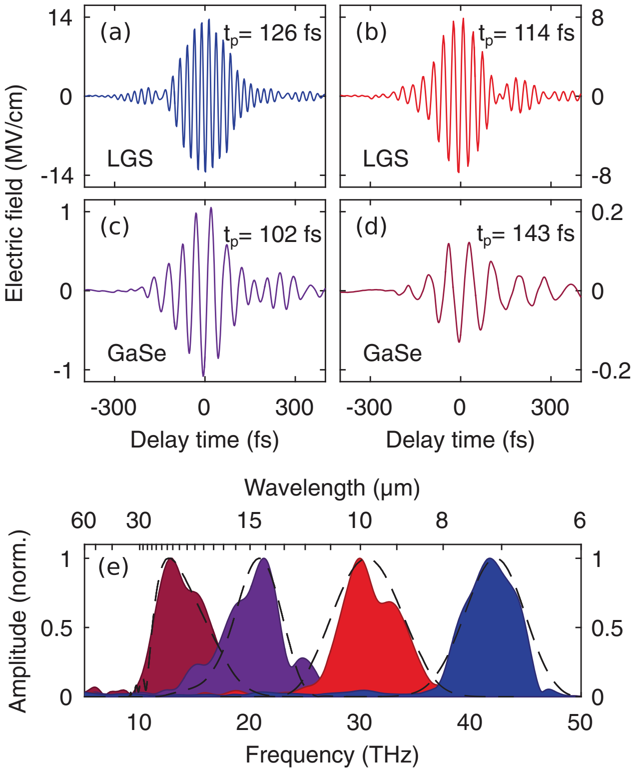

Fig. 3. Phase-locked multi-terahertz waveforms. (a)–(d) Waveforms generated in (a), (b) a 1 mm LGS crystal and (c), (d) a 200 μm GaSe crystal, retrieved by electro-optic detection. All field transients have been corrected for the electro-optic response function. The pulse duration t_p (intensity FWHM) is denoted next to each transient. (e) Corresponding normalized amplitude spectra obtained by Fourier transforming the corresponding waveforms in (a)–(d). (The filling colors correspond to the respective waveforms.) Dashed lines: amplitude spectra calculated by convolving the two NIR pulses and accounting for PM.

The average power of the terahertz pulse train of Fig. 3(a) is measured with a power meter to be as high as 31 mW, corresponding to a pulse energy of 0.16 μJ at 42 THz. Here, an excellent quantum efficiency of 24% with respect to the DFG pump pulses is found. The efficiency with respect to the 1200 nm seed pulses is even 30%. By measuring both the absolute form of the electromagnetic carrier wave and the Gaussian focal diameter of the terahertz intensity of 21 μm (FWHM determined with the help of a knife edge and pinholes), we determine a peak electric field of 13 MV/cm—a value comparable to benchmarks that were so far reserved to high-field sources operating at kilohertz rates.

By carefully adjusting the time delay between the two NIR pulses that drive the DFG process, we can readily control the absolute CEP ϕ_{THz} of the field transients. Figure 4 shows a measured waveform with a frequency centered at 12 THz for three representative values of ϕ_{THz}. Such precise CEP control is important for non-perturbative nonlinearities, such as high-harmonic generation, occurring on sub-cycle timescales [17].

In order to utilize the possibility of CEP control in practical experiments, however, the pulse train needs to keep a constant phase over multiple hours. The extremely compact one-box architecture of the new source—the two-stage OPA and the MIR generation are hosted in a single box with a footprint of 35 cm × 70 cm—promises excellent long-term stability. A corresponding test is presented in Fig. 5, where the same terahertz waveform is repeatedly measured over the course of 6 h. In total, 60 traces are taken. We extract ϕ_{THz} of each transient by subtracting the delay times of the zero-crossings of the carrier wave from the temporal position of the maximum of the envelope function, calculated via a Hilbert transformation. The resulting evolution of ϕ_{THz} is plotted in Fig. 5(b). From these data, we derive a standard deviation of ϕ_{THz} of less than 0.1 π from its mean value. To the best of our knowledge, this result sets a new record in the class of passively CEP-stable OPA-based terahertz sources [13].

Our system opens exciting new possibilities for lightwave electronics at high repetition rates. High-harmonic [17] and high-order sideband generation [15,16] driven at repetition rates of 190 kHz and beyond should facilitate multi-octave spanning terahertz-to-ultraviolet frequency combs with average powers exceeding the currently achievable level by orders of magnitude. Intense few-cycle pulses centered at several tens of terahertz may also extend lightwave-STM [19,20] to

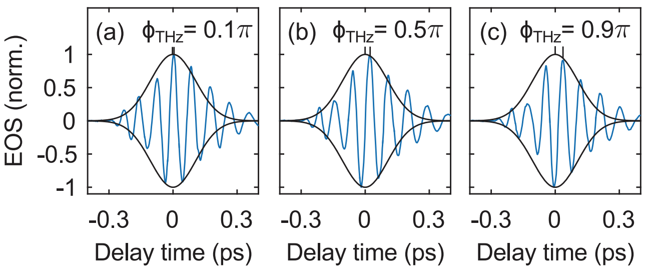

Fig. 4. Carrier envelope tunability. Electro-optic trace of multi-terahertz field transients centered at a frequency of 12 THz for three different values of the CEP ϕ_{THz} set via the femtosecond delay between the generating NIR pulses.

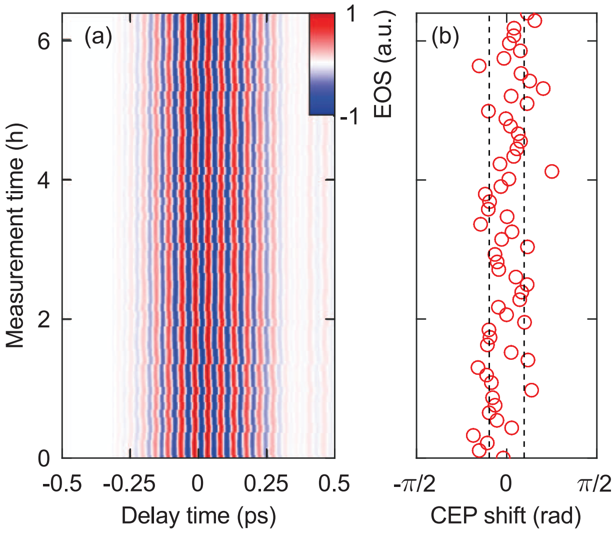

Fig. 5. Long-term CEP stability of the multi-terahertz transients. (a) Electro-optic traces of 60 consecutive measurements of the same field transient generated in a 500 μm thick GaSe emitter over the course of 6 h. (b) CEP shift of the transients with respect to their common mean. The black dashed lines indicate the standard deviation of less than 0.1 π.

attosecond timescales. Furthermore, the identical CEP of all NIR pulses provides additional flexibility for frequency mixing: for instance, DFG between the signal and idler waves should enable mid-infrared center frequencies of up to 84 THz, whereas multiple DFG branches obtained by separately mixing signal and idler pulses with the laser fundamental may be exploited for two-dimensional multi-terahertz spectroscopy [26]. By shifting the power splitting of the pump laser in favor of the DFG pump in the present setup, we should also be able to go from the DFG regime into the OPA regime [22,27,28]. This may lead to a further increase of the terahertz output, while staying safely below the damage threshold of the crystals. Finally, our parametric approach should lend itself naturally to the latest power-scaled pump sources. Using a high-power Yb:YAG femtosecond amplifier [29] with a comparable pulse energy of 55 μJ, multi-terahertz radiation with peak electric fields in excess of 10 MV/cm may be expected at the full repetition rate of up to 20 MHz.

In conclusion, we employed a second-harmonic pumped OPA concept for the generation of multi-terahertz pulses tunable from 12 to 42 THz. We reach a very competitive average power with peak fields exceeding 13 MV/cm and pulse durations down to 1.8 cycles at a repetition rate of 190 kHz. Electro-optic sampling with sub-10 fs gate pulses was used for the characterization of the waveforms. Excellent long-term stability was shown, resulting from the compact architecture. The high field amplitudes, combined with the free tunability and excellent long-term stability of the CEP, open the door to the observation of non-perturbative terahertz nonlinearities at vastly increased repetition rates.

Funding. H2020 Future and Emerging Technologies (FET) (665158); Munich-Centre for Advanced Photonics (MAP); Deutsche Forschungsgemeinschaft (DFG) (SFB 689).

Acknowledgment. The authors thank M. Furthmeier for his technical assistance.

REFERENCES

1. R. Ulbricht, E. Hendry, J. Shan, T. F. Heinz, and M. Bonn, Rev. Mod. Phys. **83**, 543 (2011).
2. P. U. Jepsen, D. G. Cooke, and M. Koch, Laser Photon. Rev. **5**, 124 (2011).
3. Q. Wu and X.-C. Zhang, Appl. Phys. Lett. **71**, 1285 (1997).
4. R. Huber, A. Brodschelm, F. Tauser, and A. Leitenstorfer, Appl. Phys. Lett. **76**, 3191 (2000).
5. K. Liu, J. Xu, and X.-C. Zhang, Appl. Phys. Lett. **85**, 863 (2004).
6. C. Kübler, R. Huber, S. Tübel, and A. Leitenstorfer, Appl. Phys. Lett. **85**, 3360 (2004).
7. M. Porer, J.-M. Ménard, and R. Huber, Opt. Lett. **39**, 2435 (2014).
8. S. Keiber, S. Sederberg, A. Schwarz, M. Trubetskov, V. Pervak, F. Krausz, and N. Karpowicz, Nat. Photonics **10**, 159 (2016).
9. A. Sell, A. Leitenstorfer, and R. Huber, Opt. Lett. **33**, 2767 (2008).
10. C. Manzoni, M. Först, H. Ehrke, and A. Cavalleri, Opt. Lett. **35**, 757 (2010).
11. F. Junginger, A. Sell, O. Schubert, B. Mayer, D. Brida, M. Marangoni, G. Cerullo, A. Leitenstorfer, and R. Huber, Opt. Lett. **35**, 2645 (2010).
12. I. Pupeza, D. Sánchez, J. Zhang, N. Lilienfein, M. Seidel, N. Karpowicz, T. Paasch-Colberg, I. Znakovskaya, M. Pescher, W. Schweinberger, V. Pervak, E. Fill, O. Pronin, Z. Wei, F. Krausz, A. Apolonski, and J. Biegert, Nat. Photonics **9**, 721 (2015).
13. K. Kaneshima, N. Ishii, K. Takeuchi, and J. Itatani, Opt. Express **24**, 8660 (2016).
14. T. Kampfrath, K. Tanaka, and K. A. Nelson, Nat. Photonics **7**, 680 (2013).
15. B. Zaks, R. B. Liu, and M. S. Sherwin, Nature **483**, 580 (2012).
16. F. Langer, M. Hohenleutner, C. P. Schmid, C. Poellmann, P. Nagler, T. Korn, C. Schuller, M. S. Sherwin, U. Huttner, J. T. Steiner, S. W. Koch, M. Kira, and R. Huber, Nature **533**, 225 (2016).
17. M. Hohenleutner, F. Langer, O. Schubert, M. Knorr, U. Huttner, S. W. Koch, M. Kira, and R. Huber, Nature **523**, 572 (2015).
18. G. Herink, D. R. Solli, M. Gulde, and C. Ropers, Nature **483**, 190 (2012).
19. T. L. Cocker, V. Jelic, M. Gupta, S. J. Molesky, J. A. J. Burgess, G. D. L. Reyes, L. V. Titova, Y. Y. Tsui, M. R. Freeman, and F. A. Hegmann, Nat. Photonics **7**, 620 (2013).
20. T. L. Cocker, D. Peller, P. Yu, J. Repp, and R. Huber, Nature **539**, 263 (2016).
21. R. A. Kaindl, F. Eickemeyer, M. Woerner, and T. Elsaesser, Appl. Phys. Lett. **75**, 1060 (1999).
22. A. Baltuška, T. Fuji, and T. Kobayashi, Phys. Rev. Lett. **88**, 133901 (2002).
23. M. Bradler, C. Homann, and E. Riedle, Opt. Lett. **36**, 4212 (2011).
24. M. Bradler, P. Baum, and E. Riedle, Appl. Phys. B **97**, 561 (2009).
25. V. Petrov, A. Yelisseyev, L. Isaenko, S. Lobanov, A. Titov, and J.-J. Zondy, Appl. Phys. B **78**, 543 (2004).
26. C. Somma, G. Folpini, K. Reimann, M. Woerner, and T. Elsaesser, Phys. Rev. Lett. **116**, 177401 (2016).
27. C. Homann, M. Bradler, M. Förster, P. Hommelhoff, and E. Riedle, Opt. Lett. **37**, 1673 (2012).
28. M. Bradler, J. C. Werhahn, D. Hutzler, S. Fuhrmann, R. Heider, E. Riedle, H. Iglev, and R. Kienberger, Opt. Express **21**, 20145 (2013).
29. P. Russbueldt, T. Mans, J. Weitenberg, H. D. Hoffmann, and R. Poprawe, Opt. Lett. **35**, 4169 (2010).

Appendix A3

MathCad program for Schiefspiegler geometry

For calculating the focus distance from the telescope and the angles for astigmatism compensation

"Schiefspiegler" - Calculator

data beam:

center wavelength $\lambda := 500 \cdot nm$

initial wavefront $R_0 := 1000\ mm$

initial beam waist $w_0 := 8\ \mu m$

data Schiefspiegler:

curvature mirror 1 $R_{m1} := -150\ mm$

curvature mirror 2 $R_{m2} := 200\ mm$

distance d1 $d_1 := 127\ mm$

distance d12 $d_{12} := 103\ mm$

angle θ1 $\theta_1 := 3.4\ ^\circ$

$$M_{R\_s}(R_m, \gamma) := \begin{bmatrix} 1 & 0 \cdot m \\ \frac{2}{R_m} \cos(\gamma) & 1 \end{bmatrix} \qquad M_{R\_t}(R_m, \gamma) := \begin{bmatrix} 1 & 0 \cdot m \\ \frac{2}{R_m \cdot \cos(\gamma)} & 1 \end{bmatrix} \qquad M_d(d) := \begin{bmatrix} 1 & d \\ 0 \cdot \frac{1}{m} & 1 \end{bmatrix}$$

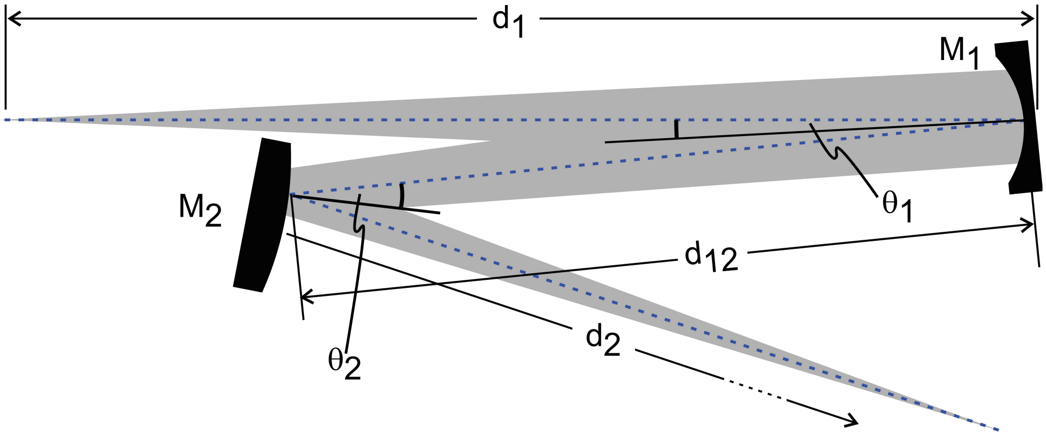

inital Gaussian factor q $q_0 := \left(\frac{1}{R_0} - \frac{1i \cdot \lambda}{\pi \cdot {w_0}^2} \right)^{-1}$

estimated focus distance $z_t := 500\ mm$ $\qquad z_s := z_t$

estimated angle θ2 $\theta_2 := 10^\circ$

total matrix system sagittal $M_{tot\_s} := M_d(z_s) \cdot M_{R\_s}(R_{m2}, \theta_2) \cdot M_d(d_{12}) \cdot M_{R\_s}(R_{m1}, \theta_1) \cdot M_d(d_1)$

total matrix system tangential $M_{tot\_t} := M_d(z_t) \cdot M_{R\_t}(R_{m2}, \theta_2) \cdot M_d(d_{12}) \cdot M_{R\_t}(R_{m1}, \theta_1) \cdot M_d(d_1)$

solver block:

$$q_t := \left(\frac{1}{R_0} - \frac{1\mathrm{i} \cdot \lambda}{\pi \cdot (40\ \mu m)^2}\right)^{-1} \qquad q_s := \left(\frac{1}{R_0} - \frac{1\mathrm{i} \cdot \lambda}{\pi \cdot (40\ \mu m)^2}\right)^{-1}$$

$$M_{tot\_s} = M_d(z_s) \cdot M_{R\_s}(R_{m2}, \theta_2) \cdot M_d(d_{12}) \cdot M_{R\_s}(R_{m1}, \theta_1) \cdot M_d(d_1)$$

$$M_{tot\_t} = M_d(z_t) \cdot M_{R\_t}(R_{m2}, \theta_2) \cdot M_d(d_{12}) \cdot M_{R\_t}(R_{m1}, \theta_1) \cdot M_d(d_1)$$

$$q_t = \frac{M_{tot\_t_{0,0}} \cdot q_0 + M_{tot\_t_{0,1}}}{M_{tot\_t_{1,0}} \cdot q_0 + M_{tot\_t_{1,1}}} \qquad q_s = \frac{M_{tot\_s_{0,0}} \cdot q_0 + M_{tot\_s_{0,1}}}{M_{tot\_s_{1,0}} \cdot q_0 + M_{tot\_s_{1,1}}}$$

$$Re\left(\frac{1}{q_t}\right) = 0 \cdot \frac{1}{m} \qquad Re\left(\frac{1}{q_s}\right) = 0 \cdot \frac{1}{m}$$

$$Im(z_t) = 0 \qquad Im(z_s) = 0$$

$$Im(\theta_2) = 0 \qquad z_t - z_s = 0$$

$$\begin{bmatrix} M_{tot\_t} \\ \vdots \end{bmatrix} := \mathrm{find}(M_{tot\_t}, M_{tot\_s}, z_s, z_t, q_s, q_t, \theta_2)$$

distantce to focal planes $z_t = (403.3 + 1.3\mathrm{i} \cdot 10^{-29})\ mm$ $z_s = (403.3 + 4\mathrm{i} \cdot 10^{-30})\ mm$

calculated angle θ2 $\mathrm{Re}(\theta_2) = 8.959\ ^\circ$

Appendix A4

MathCad program for the chirp estimation and compensation for MIR generation in DFG

For calculating the resulting chirp of a 515 nm pumped NOPA signal, the signal for DFG with 1030 nm. The resulting chirp for MIR is also estimated and a chirped mirror design is calculated to get a flat MIR GD.

Chirp Estimation and compensation for MIR Generation in DFG

Einschließen << R:\Berechnungen\Sellmeier\Sellmeier.mcdx

$\lambda_{pump} := 1026\ nm$

SCG

$d_{YAG} := 9\ mm$

relay imaging lens

$d_{FS1} := 3.7\ mm$

filter

$d_{FS2} := 3\ mm$

chirper

$d_{LF7} := 13.9\ mm$

amplifier

$d_{BBO} := 3\ mm$

air

$d_{air} := 1.5\ m$

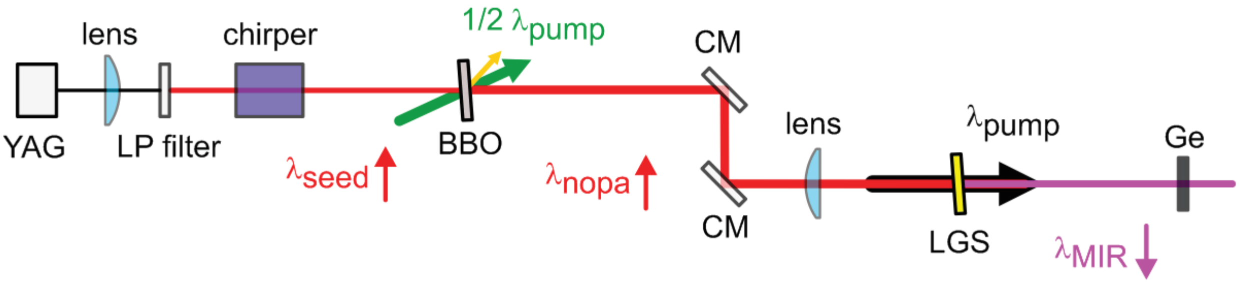

$$\Delta t_{NOPA}\left(\lambda_{NOPA}, \delta\right) := \left\| \begin{array}{l} \Delta t \leftarrow \dfrac{d_{YAG}}{c} \cdot \left(n_{YAG}\left(\lambda_{NOPA}\right) - \lambda_{NOPA} \cdot \dfrac{\mathrm{d}}{\mathrm{d}\lambda_{NOPA}} n_{YAG}\left(\lambda_{NOPA}\right) \right) \\ \Delta t \leftarrow \Delta t + \dfrac{d_{FS1}}{c} \cdot \left(n_{FS}\left(\lambda_{NOPA}\right) - \lambda_{NOPA} \cdot \dfrac{\mathrm{d}}{\mathrm{d}\lambda_{NOPA}} n_{FS}\left(\lambda_{NOPA}\right) \right) \\ \Delta t \leftarrow \Delta t + \dfrac{d_{FS2}}{c} \cdot \left(n_{FS}\left(\lambda_{NOPA}\right) - \lambda_{NOPA} \cdot \dfrac{\mathrm{d}}{\mathrm{d}\lambda_{NOPA}} n_{FS}\left(\lambda_{NOPA}\right) \right) \\ \Delta t \leftarrow \Delta t + \dfrac{d_{LF7}}{c} \cdot \left(n_{LF7}\left(\lambda_{NOPA}\right) - \lambda_{NOPA} \cdot \dfrac{\mathrm{d}}{\mathrm{d}\lambda_{NOPA}} n_{LF7}\left(\lambda_{NOPA}\right) \right) \\ \Delta t \leftarrow \Delta t + \dfrac{\delta \cdot d_{BBO}}{6\ c} \cdot \left(n_{oBBO}\left(\lambda_{NOPA}\right) - \lambda_{NOPA} \cdot \dfrac{\mathrm{d}}{\mathrm{d}\lambda_{NOPA}} n_{oBBO}\left(\lambda_{NOPA}\right) \right) \\ \Delta t \leftarrow \Delta t + \dfrac{d_{air}}{c} \cdot \left(n_{air}\left(\lambda_{NOPA}\right) - \lambda_{NOPA} \cdot \dfrac{\mathrm{d}}{\mathrm{d}\lambda_{NOPA}} n_{air}\left(\lambda_{NOPA}\right) \right) \end{array} \right.$$

$$\lambda_{MIR} := 5\ \mu m, 5.1\ \mu m \,..\, 12\ \mu m = \begin{bmatrix} 5 \cdot 10^{-6} \\ \vdots \end{bmatrix} m$$

$$\lambda_{NOPA} := \frac{1}{\dfrac{1}{\lambda_{pump}} - \dfrac{1}{\lambda_{MIR}}} = \begin{bmatrix} 1.291 \cdot 10^{3} \\ \vdots \end{bmatrix} nm \qquad shift := 5.16549\ ns$$

$$step_{1200} := \left\| \begin{array}{l} \text{for } i \in 1, 2 \,..\, 6 \\ \quad \left\| \ matrix^{\langle i \rangle} \leftarrow \overrightarrow{\Delta t_{NOPA}\left(\lambda_{NOPA}, i\right) - shift} \right. \\ matrix \end{array} \right.$$

Pump pulse "settings":

$$\Delta bbo := \left\| \begin{array}{l} \text{for } i \in 1, 2 \,..\, 6 \\ \quad \left\| \ \Delta bbo_{i} \leftarrow \dfrac{i \cdot d_{BBO}}{6} \right. \\ \Delta bbo \end{array} \right. = \begin{bmatrix} 0.5 \\ 1 \\ 1.5 \\ 2 \\ 2.5 \\ 3 \end{bmatrix} mm \qquad v_{g\_515} := \frac{c}{1.703} = \left(1.76 \cdot 10^{8}\right) \frac{m}{s}$$

duration: $\Delta t_{515} := 200\ fs$

$$I_{515}\left(t, t_0\right) := \exp\left(-4 \cdot \ln(2) \cdot \frac{\left(t - t_0\right)^2}{{\Delta t_{515}}^2}\right)$$

delay: $shift_{515} := -290\ fs$

$$step_{515} := \frac{\Delta bbo}{v_{g\_515}} + shift_{515} = \begin{bmatrix} 2550.298 \\ 5390.597 \\ 8230.895 \\ 11071.193 \\ 13911.491 \\ 16751.79 \end{bmatrix} fs$$

Group delays of seed in steps through the crystal:

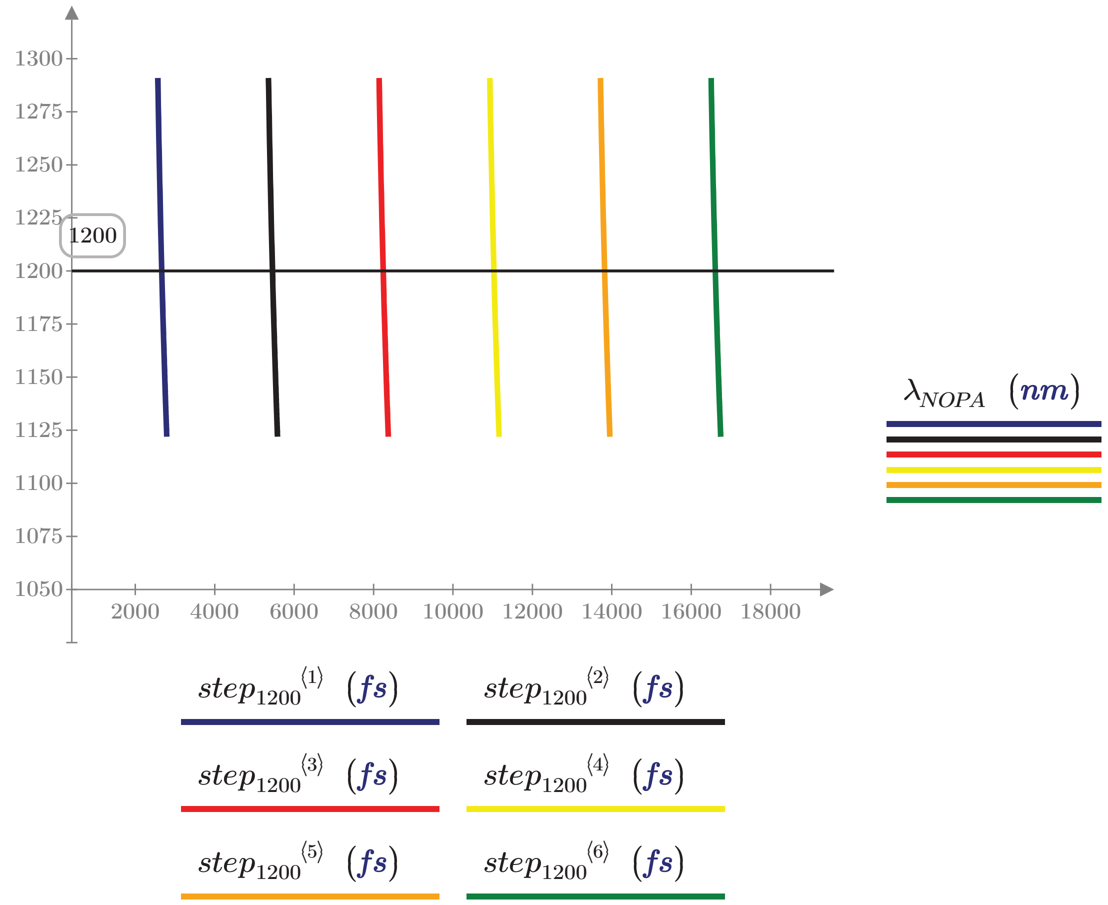

Group delay steps of pump pulse through the crystal:

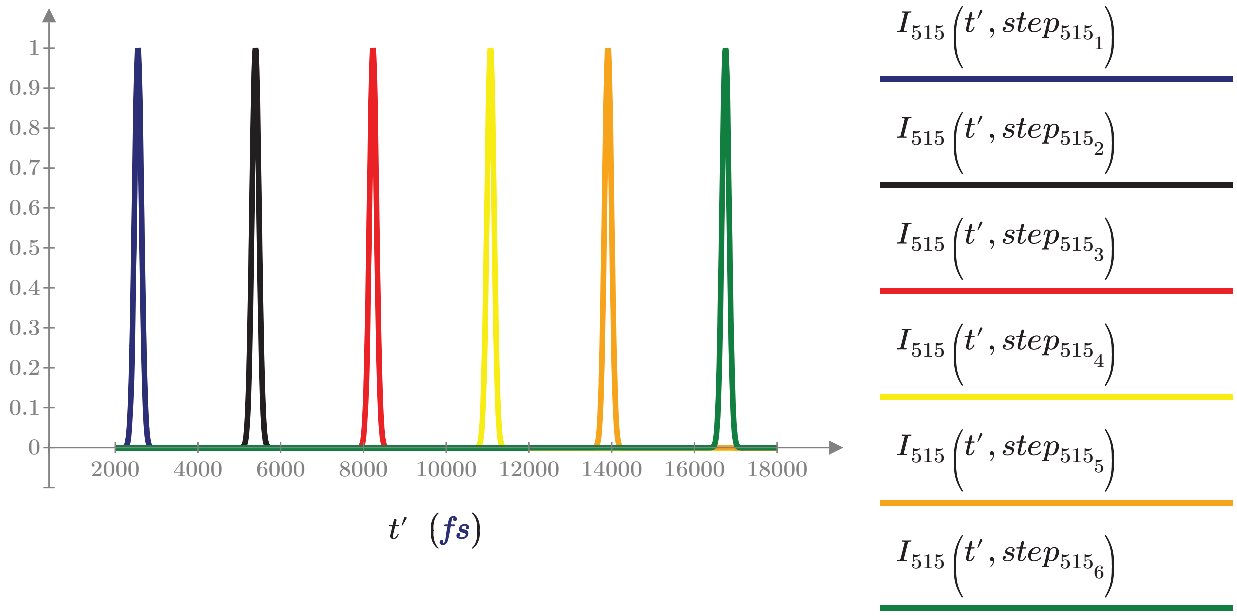

projection on wavelength axis:

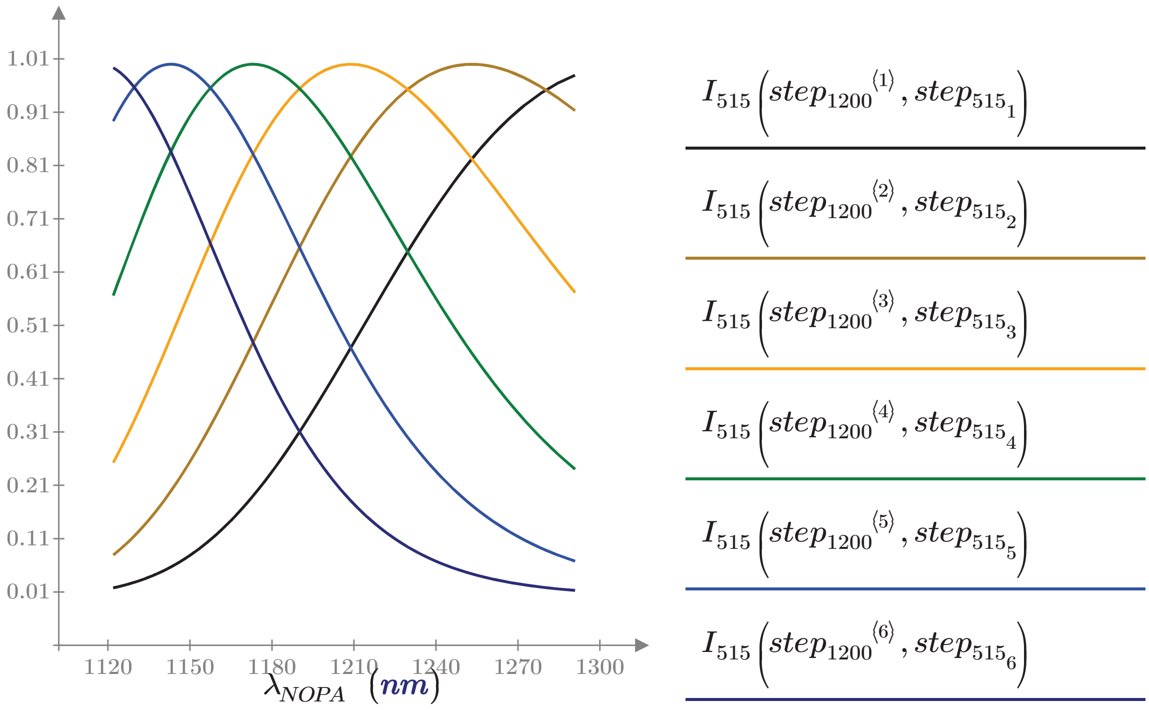

sum of projections:

$$\begin{aligned} NOPA := {} & I_{515}\left(step_{1200}^{\langle 1\rangle}, step_{515_1}\right) + I_{515}\left(step_{1200}^{\langle 2\rangle}, step_{515_2}\right) + I_{515}\left(step_{1200}^{\langle 3\rangle}, step_{515_3}\right) \hookleftarrow \\ & + I_{515}\left(step_{1200}^{\langle 4\rangle}, step_{515_4}\right) + I_{515}\left(step_{1200}^{\langle 5\rangle}, step_{515_5}\right) + I_{515}\left(step_{1200}^{\langle 6\rangle}, step_{515_6}\right) \end{aligned}$$

power for gain-narrowing:

$n := 8$ $\qquad$ $NOPA := NOPA^{n}$

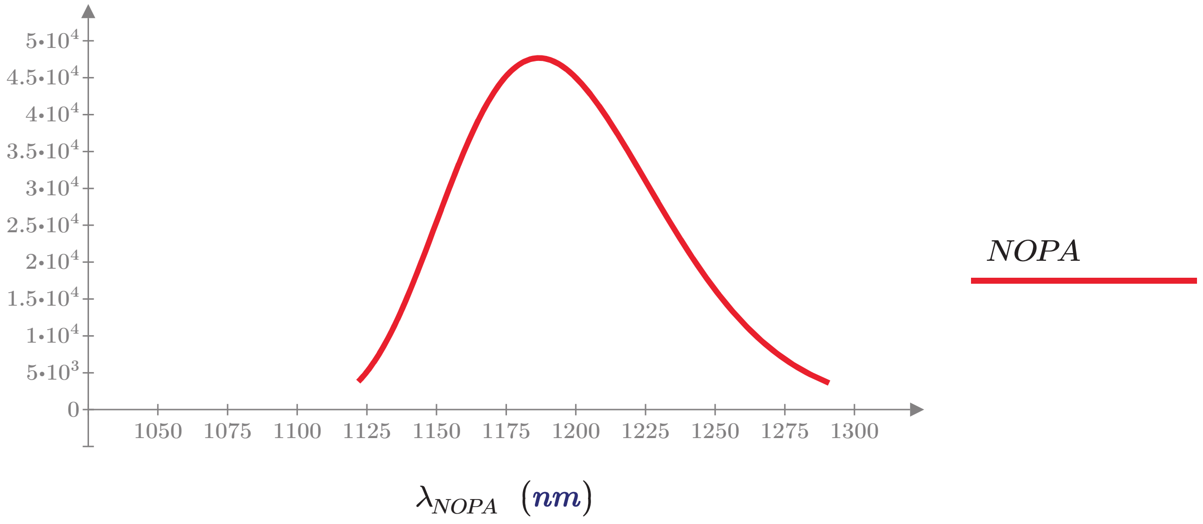

Phase due to material in beam path:

$$\phi\left(\lambda_{NOPA}\right) := \left\| \begin{array}{l} \phi \leftarrow d_{YAG} \cdot n_{YAG}\left(\lambda_{NOPA}\right) \\ \phi \leftarrow \phi + d_{FS1} \cdot n_{FS}\left(\lambda_{NOPA}\right) \\ \phi \leftarrow \phi + d_{FS2} \cdot n_{FS}\left(\lambda_{NOPA}\right) \\ \phi \leftarrow \phi + d_{LF7} \cdot n_{LF7}\left(\lambda_{NOPA}\right) \\ \phi \leftarrow \phi + d_{BBO} \cdot n_{oBBO}\left(\lambda_{NOPA}\right) \\ \phi \leftarrow \phi + d_{air} \cdot n_{air}\left(\lambda_{NOPA}\right) \\ \phi \leftarrow \overrightarrow{\frac{2\,\pi}{\lambda_{NOPA}} \cdot \phi} \\ \phi \end{array} \right.$$

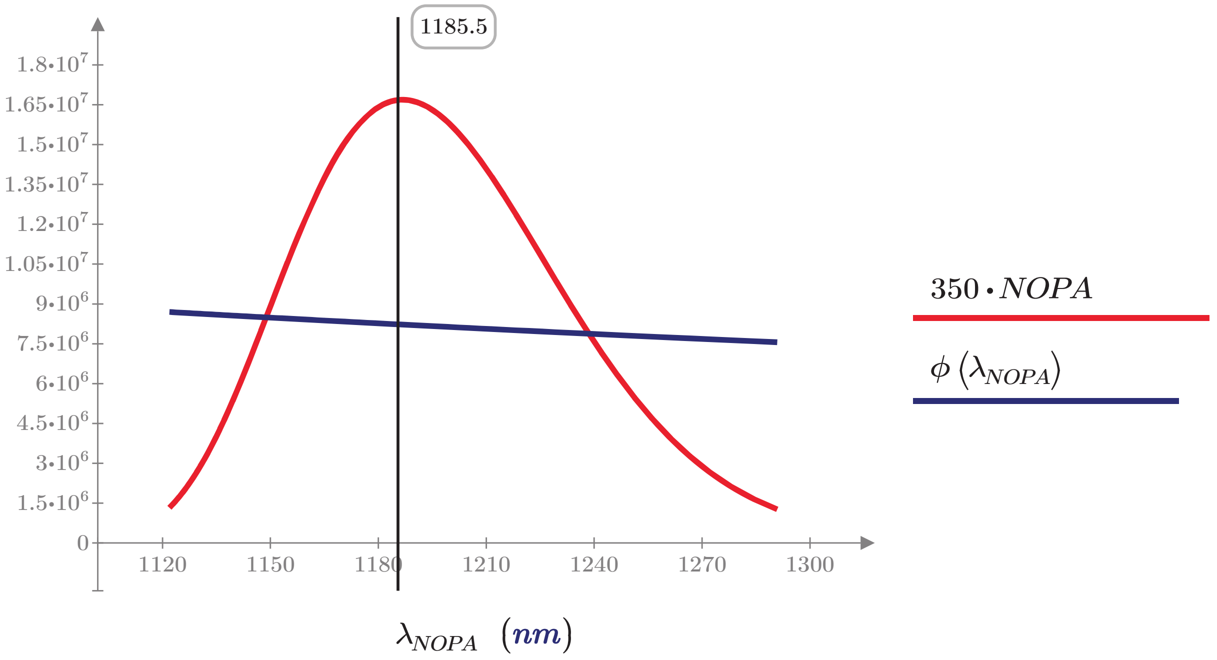

$$\nu := \frac{c}{\lambda_{NOPA}} = \begin{bmatrix} 232.237 \\ \vdots \end{bmatrix} THz \qquad \omega := 2\,\pi \cdot \nu = \begin{bmatrix} 1.459 \cdot 10^{3} \\ \vdots \end{bmatrix} THz$$

Spectrum in frequency domain:

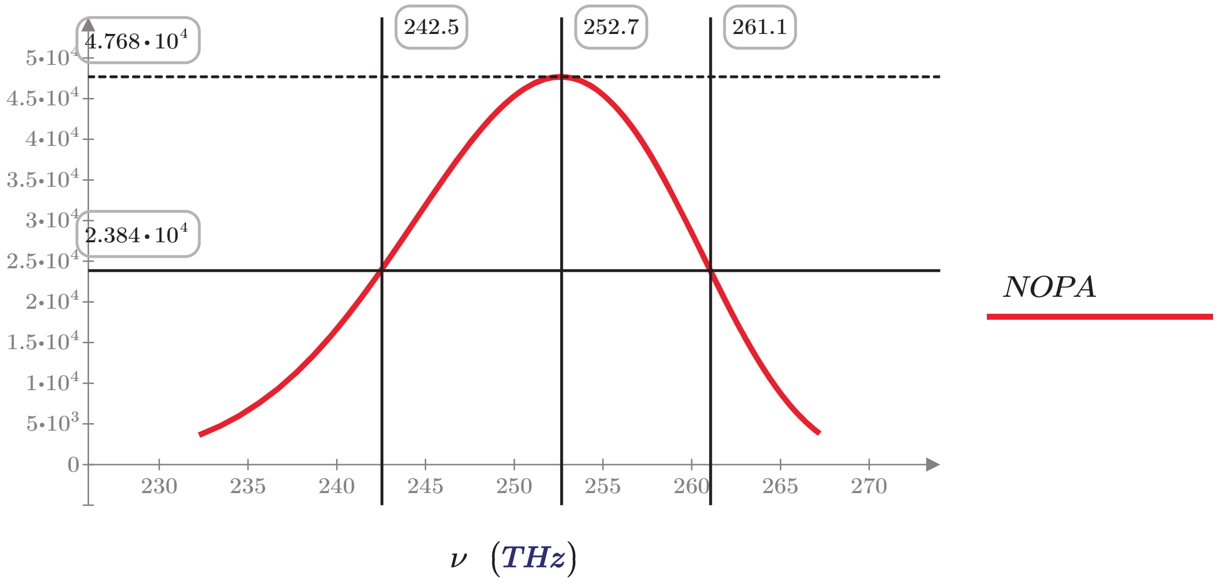

Group Delay (D1) and Group Delay-Dispersion (D2):

```
D1 :=
    $\phi \leftarrow \phi(\lambda_{NOPA})$
    $end \leftarrow \text{rows}(\omega)$
    for $i \in 1,2..end-1$
        $D1_i \leftarrow \dfrac{\phi_{i+1} - \phi_i}{\omega_{i+1} - \omega_i}$
    $D1$
```

$$= \begin{bmatrix} 5.182 \cdot 10^6 \\ \vdots \end{bmatrix} fs$$

```
D2 :=
    for $i \in 1,2..\text{rows}(D1)-1$
        $D2_i \leftarrow \dfrac{D1_{i+1} - D1_i}{\omega_{i+1} - \omega_i}$
    $D2$
```

$$= \begin{bmatrix} 814.306 \\ \vdots \end{bmatrix} fs^2$$

Determination of spectral width:

```
$left :=$
    $a \leftarrow \frac{\max(NOPA)}{2}$
    for $i \in 1, 2 .. \mathrm{rows}(NOPA)$
        if $NOPA_i > a$
            return $i$
```

```
$right :=$
    $a \leftarrow \frac{\max(NOPA)}{2}$
    for $i \in left, left+1 .. \mathrm{rows}(NOPA)$
        if $NOPA_i < a$
            return $i$
```

$$\Delta\nu := \nu_{right} - \nu_{left}$$

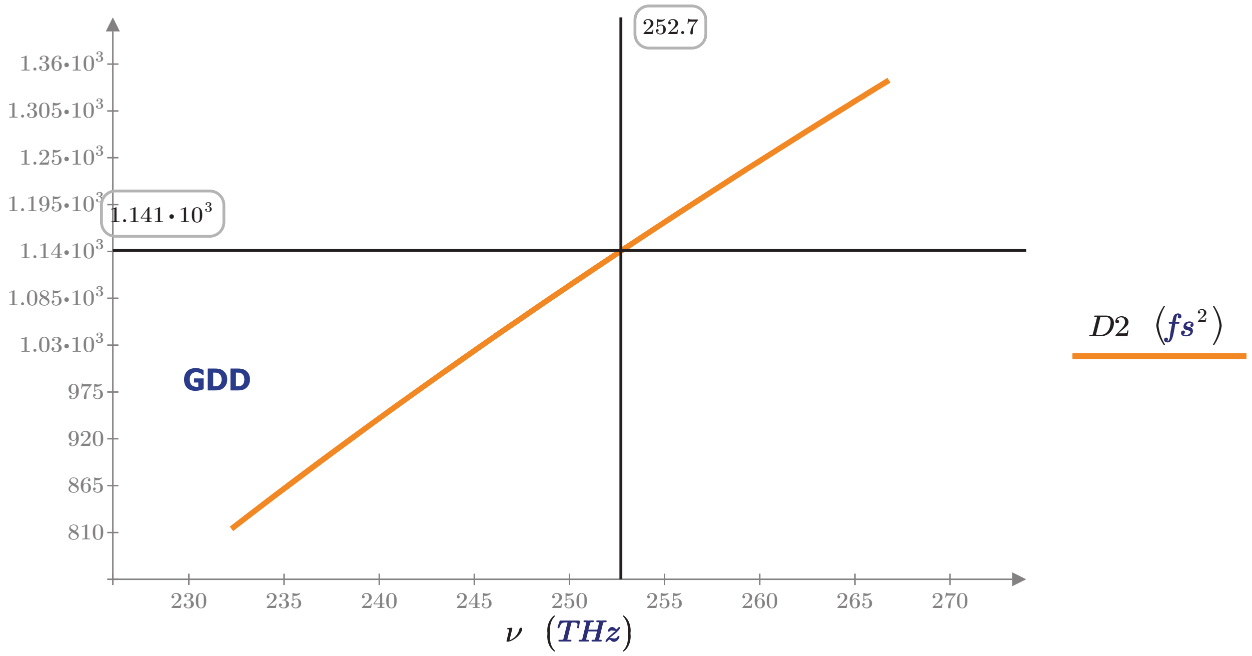

width: $\Delta\nu := 18.6\ THz$

GDD @ central ν $D2_0 := 1.141 \cdot 10^3\ fs^2$

Fourier limit: $\Delta\tau_0 := \frac{0.441}{\Delta\nu} = 23.7\ fs$

Pulse duration: $\Delta\tau := \Delta\tau_0 \cdot \sqrt{1 + \left(\frac{4 \cdot \ln(2)}{{\Delta\tau_0}^2} \cdot D2_0\right)^2} = 135.5\ fs$

Calculation for the GD of a chirped mirror to get a flat phase in the MIR after transmission of a Germanium plate:

$$GD_{CM}(\lambda, c0, c1, c2, c3, c4) := c0 + c1\cdot\lambda + c2\cdot\lambda^2 + c3\cdot\lambda^3 + c4\cdot\lambda^4$$

$d_{Ge} := 4\ mm$ $d_{air\_MIR} := 1\ m$ $d_{FS3} := 4\ mm$ $d_{LGS} := 0.5\ mm$

$$\Delta t_{MIR}(\lambda_{MIR}, c0, c1, c2, c3, c4) :=$$

$$\lambda_{NOPA} \leftarrow \frac{1}{\frac{1}{\lambda_{pump}} - \frac{1}{\lambda_{MIR}}}$$

$$\Delta t \leftarrow \frac{d_{YAG}}{c}\cdot\left(n_{YAG}(\lambda_{NOPA}) - \lambda_{NOPA}\cdot\frac{d}{d\lambda_{NOPA}}n_{YAG}(\lambda_{NOPA})\right)$$

$$\Delta t \leftarrow \Delta t + \frac{d_{FS1}}{c}\cdot\left(n_{FS}(\lambda_{NOPA}) - \lambda_{NOPA}\cdot\frac{d}{d\lambda_{NOPA}}n_{FS}(\lambda_{NOPA})\right)$$

$$\Delta t \leftarrow \Delta t + \frac{d_{FS2}}{c}\cdot\left(n_{FS}(\lambda_{NOPA}) - \lambda_{NOPA}\cdot\frac{d}{d\lambda_{NOPA}}n_{FS}(\lambda_{NOPA})\right)$$

$$\Delta t \leftarrow \Delta t + \frac{d_{LF7}}{c}\cdot\left(n_{LF7}(\lambda_{NOPA}) - \lambda_{NOPA}\cdot\frac{d}{d\lambda_{NOPA}}n_{LF7}(\lambda_{NOPA})\right)$$

$$\Delta t \leftarrow \Delta t + \frac{d_{BBO}}{c}\cdot\left(n_{oBBO}(\lambda_{NOPA}) - \lambda_{NOPA}\cdot\frac{d}{d\lambda_{NOPA}}n_{oBBO}(\lambda_{NOPA})\right)$$

$$\Delta t \leftarrow \Delta t + GD_{CM}(\lambda_{NOPA}, c0, c1, c2, c3, c4)$$

$$\Delta t \leftarrow \Delta t + \frac{d_{FS3}}{c}\cdot\left(n_{FS}(\lambda_{NOPA}) - \lambda_{NOPA}\cdot\frac{d}{d\lambda_{NOPA}}n_{FS}(\lambda_{NOPA})\right)$$

$$\Delta t \leftarrow \Delta t + \frac{d_{LGS}}{2\cdot c}\cdot\left(n_{zLGS}(\lambda_{NOPA}) - \lambda_{NOPA}\cdot\frac{d}{d\lambda_{NOPA}}n_{zLGS}(\lambda_{NOPA})\right)$$

$$\Delta t \leftarrow \Delta t + \frac{d_{air}}{c}\cdot\left(n_{air}(\lambda_{NOPA}) - \lambda_{NOPA}\cdot\frac{d}{d\lambda_{NOPA}}n_{air}(\lambda_{NOPA})\right)$$

$$\Delta t \leftarrow \Delta t + \frac{d_{Ge}}{c}\cdot\left(n_{Ge}(\lambda_{MIR}) - \lambda_{MIR}\cdot\frac{d}{d\lambda_{MIR}}n_{Ge}(\lambda_{MIR})\right)$$

$$\Delta t \leftarrow \Delta t + \frac{d_{air\_MIR}}{c}\cdot\left(n_{air}(\lambda_{MIR}) - \lambda_{MIR}\cdot\frac{d}{d\lambda_{MIR}}n_{air}(\lambda_{MIR})\right)$$

$c0 := 0\ fs$ $\quad c1 := 100\ \frac{fs}{\mu m}$ $\quad c2 := -100\ \frac{fs}{\mu m^2}$

$c3 := 10\ \frac{fs}{\mu m^3}$ $\quad c4 := -10\ \frac{fs}{\mu m^4}$

$$0 = \overrightarrow{\Delta t_{MIR}\left(\lambda_{MIR}, c0, c1, c2, c3, c4\right)}$$

sets the Group Delay of the MIR after a Germanium plate to 0

with the help of a chirped mirror in the NIR (non-collinear, directly seeded)

$$\begin{bmatrix} c0 \\ c1 \\ c2 \\ c3 \\ c4 \end{bmatrix} := \mathbf{minerr}\left(c0, c1, c2, c3, c4\right)$$

$len := \mathrm{length}\left(\lambda_{MIR}\right) = 71$ $\quad len2 := \mathrm{trunc}\left(\frac{len}{2}\right)$

$$off := \Delta t_{MIR}\left(\lambda_{MIR_{len2}}, c0, c1, c2, c3, c4\right)$$

$$GD_{MIR} := \overrightarrow{\Delta t_{MIR}\left(\lambda_{MIR}, c0, c1, c2, c3, c4\right)} - off$$

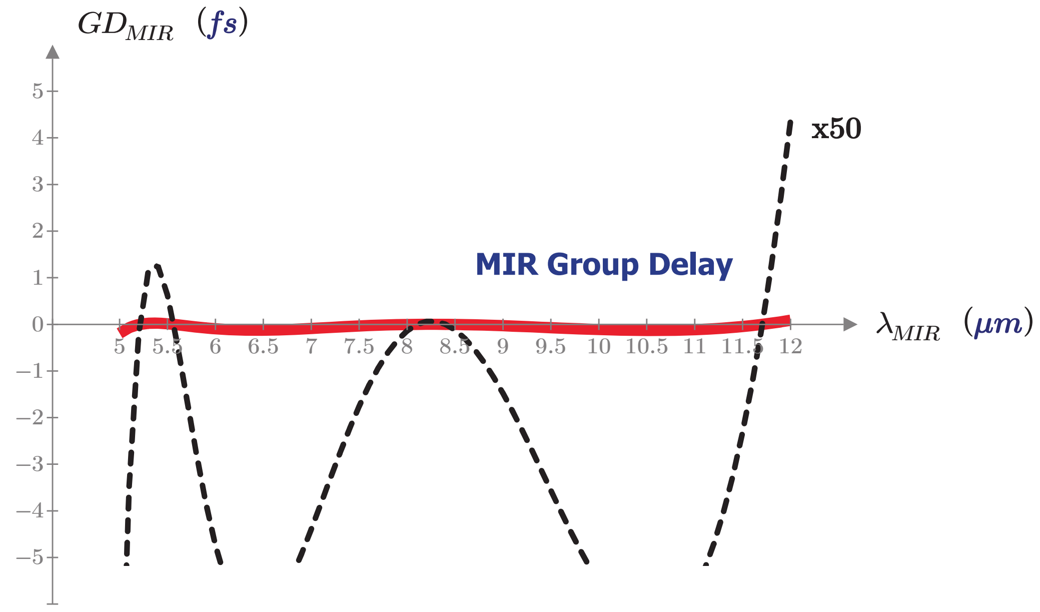

$$offset_{CM} := GD_{CM}\left(\lambda_{NOPA_{len2}}, c0, c1, c2, c3, c4\right)$$

$$\Delta t_{CM} := GD_{CM}\left(\lambda_{NOPA}, c0, c1, c2, c3, c4\right) - offset_{CM}$$

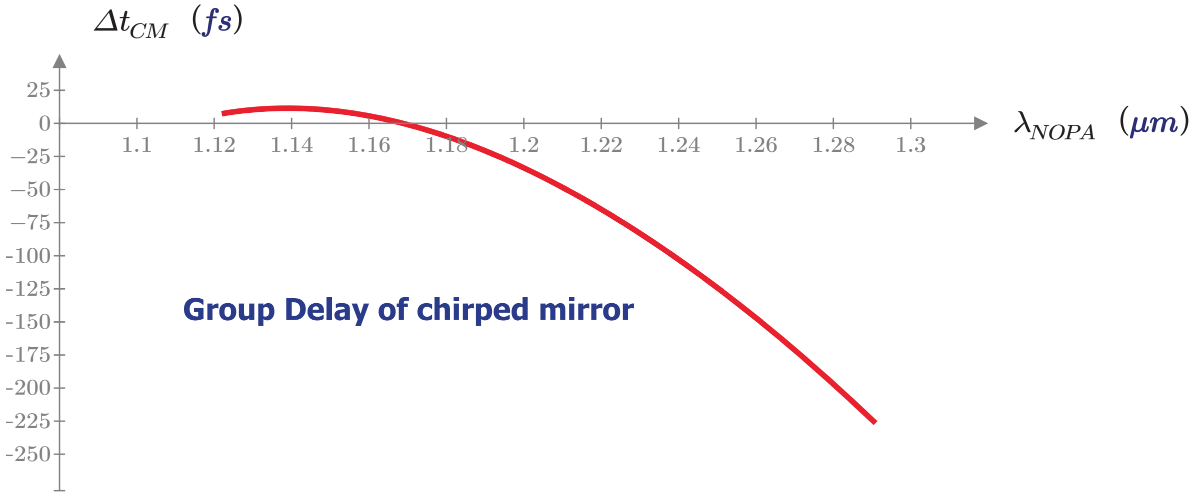

$offset_{NOPA} := 1.66 \cdot 10^4 \ fs$ $\Delta t_{NOPA} := step_{1200}^{\langle 6 \rangle} - offset_{NOPA}$

$\Delta t_{NOPA\_CM} := \Delta t_{NOPA} + \Delta t_{CM}$

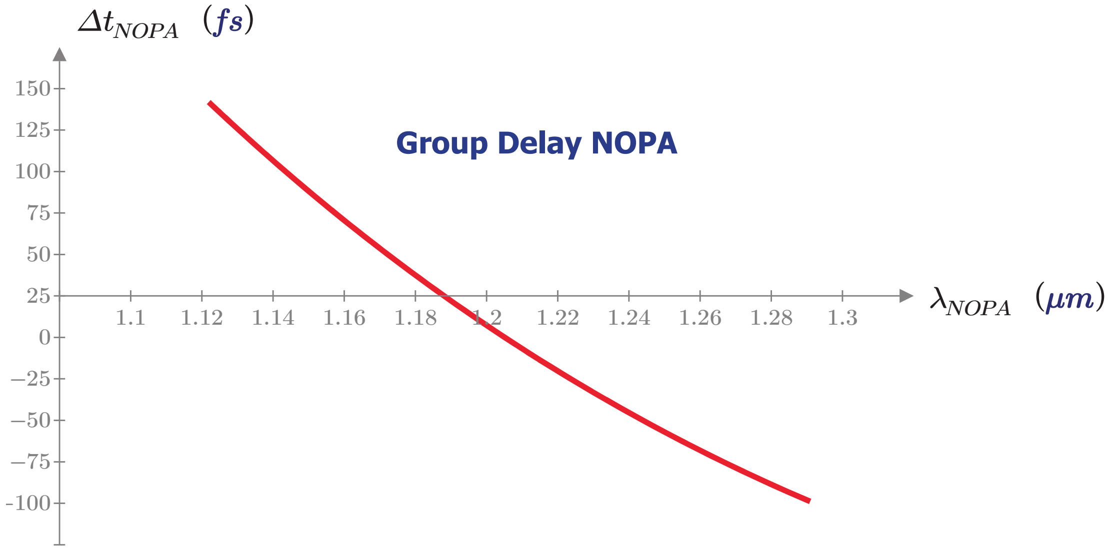

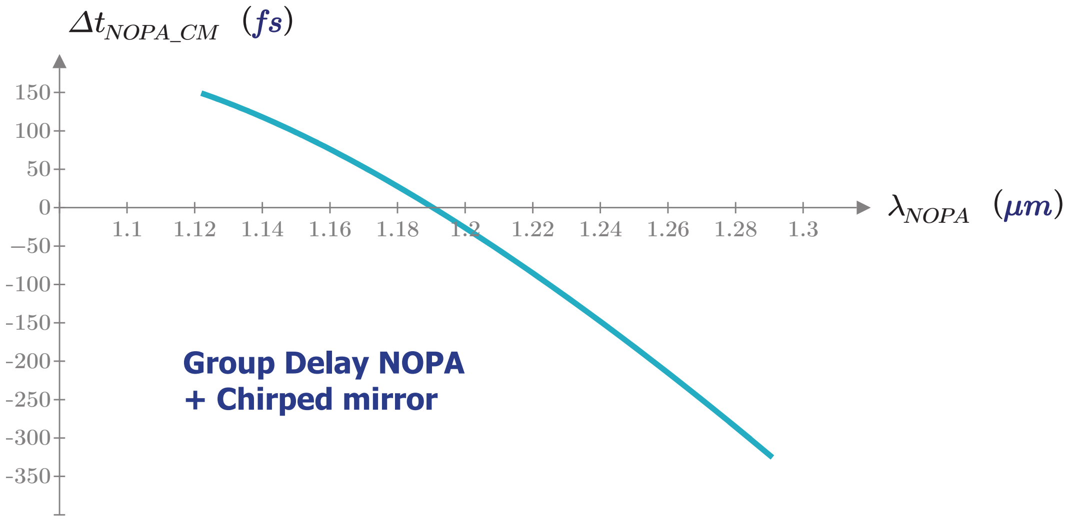

GDD NOPA with Chirped mirror

```
$D2_{NOPA\_CM} :=$ for $i \in 1, 2 .. \mathrm{rows}(\Delta t_{NOPA\_CM}) - 1$
    $D2_{NOPA\_CM_i} \leftarrow \dfrac{\Delta t_{NOPA\_CM_{i+1}} - \Delta t_{NOPA\_CM_i}}{\omega_{i+1} - \omega_i}$
  $D2_{NOPA\_CM}$
```

$$= \begin{bmatrix} 3.237 \cdot 10^3 \\ \vdots \end{bmatrix} fs^2$$

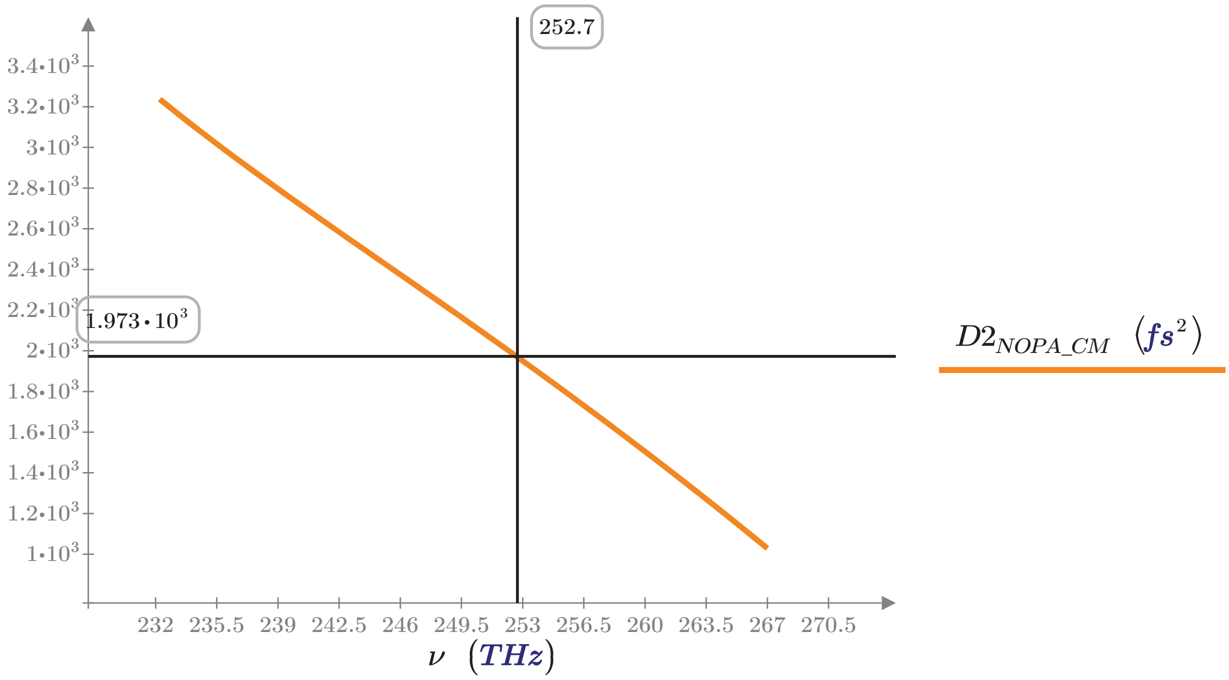

GDD @ central ν $D2_0 := 1973\ fs^2$

Fourier limit: $\Delta\tau_0 := \dfrac{0.441}{\Delta\nu} = 23.7\ fs$

Pulse duration with Chirped mirror:

$$\Delta\tau := \Delta\tau_0 \cdot \sqrt{1 + \left(\frac{4 \cdot \ln(2)}{\Delta\tau_0^{\,2}} \cdot D2_0\right)^2} = 231.9\ fs$$

Appendix A5

MathCad program for OPA amplification with depleted pump and signal bandwidth

For calculating the NOPA output energy in dependence of pump depletion and signal bandwith by summing over the three coupled differential equations in infinitesimal small steps.

OPA Amplification with depleted pump and signal bandwidth

Einschließen << R:\Berechnungen\Sellmeier\Sellmeier.mcdx

E.Wittmann, 16.4.18

crystal parameters $d := 2\ mm$ $d_{eff} := 2.05\ \frac{pm}{V}$

$n_p(\lambda, \theta) := n_{BBO}(\lambda, \theta)$ $n_s(\lambda) := n_{oBBO}(\lambda)$ $n_i(\lambda) := n_{oBBO}(\lambda)$

pump
-p

signal
-s

idler
-i

$\lambda_p := 387\ nm$ $\lambda_s := 550\ nm$ $\lambda_i := \left| \left(\frac{1}{\lambda_p} - \frac{1}{\lambda_s} \right)^{-1} \right|$

$\Delta\lambda_s := 40\ nm$

$\Delta\nu := \frac{c}{\lambda_s^{\ 2}} \cdot \Delta\lambda_s = 39.6\ THz$ $\tau_{FL} := \frac{0.441}{\Delta\nu} = 11.1\ fs$

$I_p := 180\ \frac{GW}{cm^2}$ $I_s := 0.03\ \frac{MW}{cm^2}$ $I_i := 0\ \frac{MW}{cm^2}$ *starting values*

$\omega_p := \frac{2\ \pi\ c}{\lambda_p}$ $\omega_s := \frac{2\ \pi\ c}{\lambda_s}$ $\omega_i := \frac{2\ \pi\ c}{\lambda_i}$

$$\Delta k'(\theta') := \frac{\omega_p \cdot n_{BBO}(\lambda_p, \theta')}{c} - \frac{\omega_s \cdot n_{oBBO}(\lambda_s)}{c} - \frac{\omega_i \cdot n_{oBBO}(\lambda_i)}{c}$$

solver blockphase matching angle:

$\Theta' := 27\ deg$

$\Delta k'(\Theta') = 0\ \frac{1}{m}$

$\theta := \mathrm{find}(\Theta')$

phase matching angle: $\theta = 27.826\ deg$

crystal "slices" / steps $d = 2\ mm$ $\Delta d := 5\ \mu m$ $ii := \frac{d}{\Delta d} = 400$

$n_p := n_p\left(\lambda_p, \theta\right)$ $n_s := n_s\left(\lambda_s\right)$ $n_i := n_i\left(\lambda_i\right)$

building the spectral bandwidth for signal and idler + phase-mismatch:

```
$\lambda_{s\_bw} :=$ for $i \in 1, 2 .. \frac{\Delta\lambda_s}{nm}$
    $\lambda_{short} \leftarrow \lambda_s - \frac{\Delta\lambda_s}{2}$
    $\lambda_{bw_i} \leftarrow \lambda_{short} + i \cdot nm$
    $\lambda_{bw}$
```

$= \begin{bmatrix} 531 \\ \vdots \end{bmatrix} nm$

$$\lambda_{i\_bw} := \left(\frac{1}{\lambda_p} - \frac{1}{\lambda_{s\_bw}}\right)^{-1}$$

$$\Delta k_{bw}\left(\theta', \lambda'_s, \lambda'_i\right) := \frac{\omega_p \cdot n_{BBO}\left(\lambda_p, \theta'\right)}{c} - \frac{\omega_s \cdot n_{oBBO}\left(\lambda'_s\right)}{c} - \frac{\omega_i \cdot n_{oBBO}\left(\lambda'_i\right)}{c}$$

$iii := \text{length}\left(\Delta k_{bw}\right)$

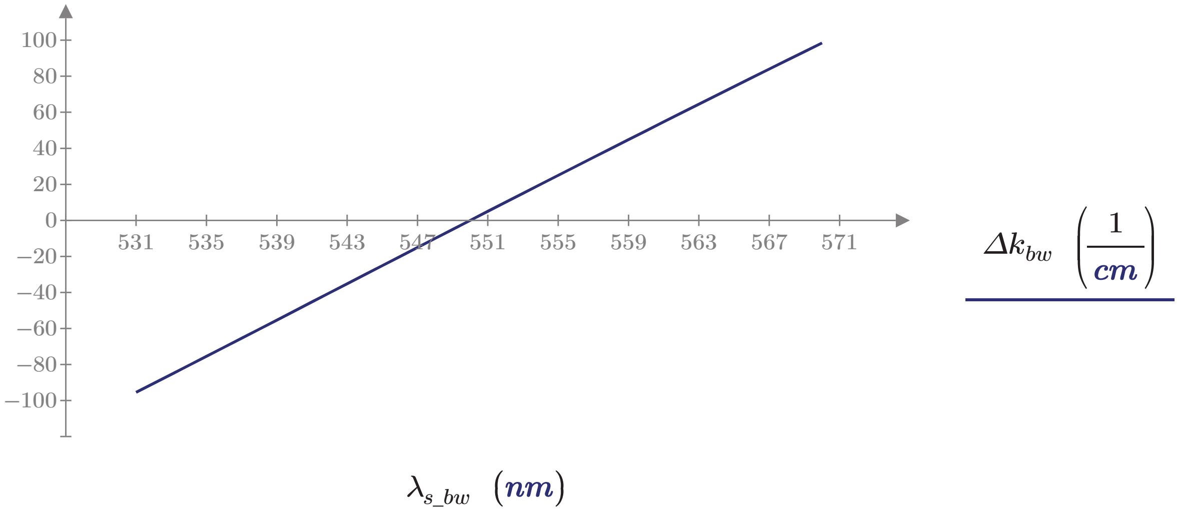

Formulas from Yariv, Optical Electronics **4th edition pp.290**

new field variable "A" (for convinience...)

field E

$$A_p := \sqrt{\frac{2 \cdot I_p}{\sqrt{\frac{\varepsilon_0}{\mu_0}} \cdot \omega_p}} = 16.693\ s^{\frac{1}{2}} \cdot \frac{V}{m}$$

$$E_p := \sqrt{\frac{\omega_p}{n_p}} \cdot A_p = \left(9.023 \cdot 10^{8}\right) \frac{V}{m}$$

$$A_s := \sqrt{\frac{2 \cdot I_s}{\sqrt{\frac{\varepsilon_0}{\mu_0}} \cdot \omega_s}} = 0.008\ s^{\frac{1}{2}} \cdot \frac{V}{m}$$

$$E_s := \sqrt{\frac{\omega_s}{n_s}} \cdot A_s = \left(3.676 \cdot 10^{5}\right) \frac{V}{m}$$

$$A_i := \sqrt{\frac{2 \cdot I_i}{\sqrt{\frac{\varepsilon_0}{\mu_0}} \cdot \omega_s}} = 0\ s^{\frac{1}{2}} \cdot \frac{V}{m}$$

$$E_s := \sqrt{\frac{\omega_i}{n_i}} \cdot A_i = 0\ \frac{V}{m}$$

$$\kappa := d_{eff} \cdot \varepsilon_0 \cdot \sqrt{\frac{\mu_0}{\varepsilon_0} \cdot \frac{\omega_p \cdot \omega_s \cdot \omega_i}{n_p \cdot n_s \cdot n_i}} \qquad (8.6\text{-}19)$$

here the "d" in Yariv referrs to the deff SNLO value times ε0

```
$loop :=$ for $j \in 2..ii$
    for $m \in 1,2..iii$
        $\Delta A_{i_{1,m}} \leftarrow A_i$
        $\Delta A_{s_{1,m}} \leftarrow A_s$
        $\Delta A_{p_{1,m}} \leftarrow A_p$
    for $m \in 1,2..iii$
        $\Delta A_{i_{j,m}} \leftarrow \Delta A_{i_{j-1,m}} + \frac{1i}{2} \kappa \cdot \overline{\Delta A_{p_{j-1,m}}} \cdot \Delta A_{s_{j-1,m}} \cdot \Delta d \cdot \exp\left(1i \cdot \Delta k_{bw_m} \cdot d\right)$
        $\Delta A_{s_{j,m}} \leftarrow \Delta A_{s_{j-1,m}} + \frac{1i}{2} \kappa \cdot \Delta A_{p_{j-1,m}} \cdot \overline{\Delta A_{i_{j-1,m}}} \cdot \Delta d \cdot \exp\left(-1i \cdot \Delta k_{bw_m} \cdot d\right)$
        $\Delta A_{p_{j,m}} \leftarrow \Delta A_{p_{j-1,m}} + \frac{1i}{2} \kappa \cdot \Delta A_{s_{j,m}} \cdot \Delta A_{i_{j,m}} \cdot \Delta d \cdot \exp\left(1i \cdot \Delta k_{bw_m} \cdot d\right)$
    $\begin{bmatrix} \Delta A_p \\ \Delta A_s \\ \Delta A_i \end{bmatrix}$
```

coupled differential equations (8.6-18)
α ≈ σ ≈ 0

Yariv indices: **1 signal; 2 idler; 3 pump**

line above parameter means complex conjugated

$$pump := \frac{1}{2} \cdot \frac{\omega_p}{n_p} \cdot \sqrt{\frac{\varepsilon_0}{\mu_0}} \cdot \left(\overrightarrow{loop_1 \cdot \overline{loop_1}}\right) \cdot n_p \qquad (8.6\text{-}16)$$

```
pump :=  out ← 0
         for m ∈ 1,2..iii
             out ← pump^⟨m⟩ + out
         out ← out / iii
         out
```

$$signal := \frac{1}{2} \cdot \frac{\omega_s}{n_s} \cdot \sqrt{\frac{\varepsilon_0}{\mu_0}} \cdot \left(\overrightarrow{loop_2 \cdot \overline{loop_2}}\right) \cdot n_s \qquad (8.6\text{-}16)$$

```
signal :=  out ← 0
           for m ∈ 1,2..iii
               out ← signal^⟨m⟩ + out
           out ← out / iii
           out
```

$$idler := \frac{1}{2} \cdot \frac{\omega_i}{n_i} \cdot \sqrt{\frac{\varepsilon_0}{\mu_0}} \cdot \left(\overrightarrow{loop_3 \cdot \overline{loop_3}}\right) \cdot n_i \qquad (8.6\text{-}16)$$

```
idler :=  out ← 0
          for m ∈ 1,2..iii
              out ← idler^⟨m⟩ + out
          out ← out / iii
          out
```

$d := 1..ii = \begin{bmatrix} 1 \\ \vdots \end{bmatrix}$ $\qquad$ $d := d \cdot \Delta d = \begin{bmatrix} 0.005 \\ \vdots \end{bmatrix} mm$

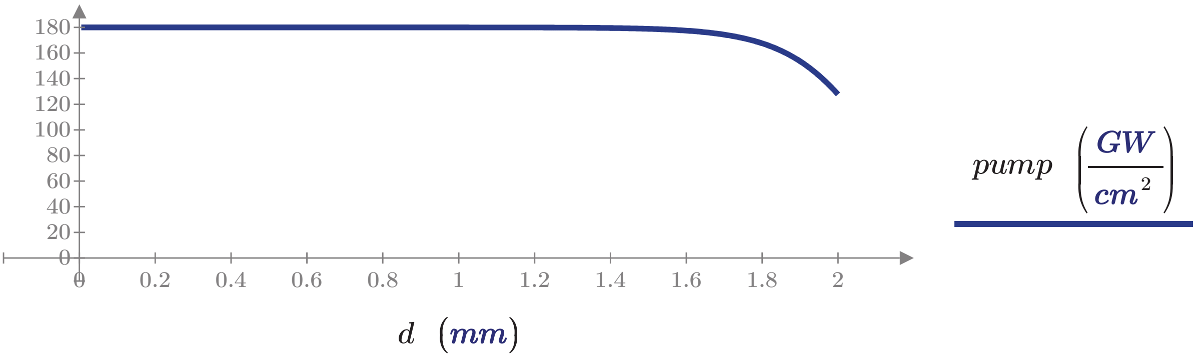

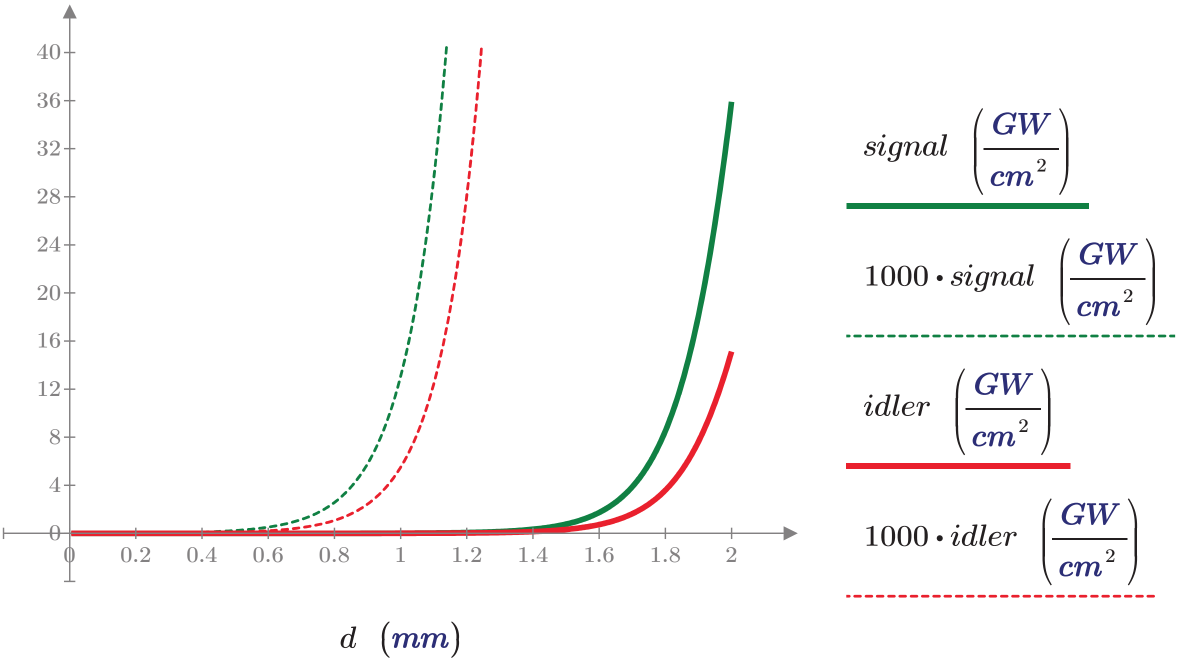

$I_{NOPA} := signal_{ii} = 36\ \frac{GW}{cm^2}$

$I_p = 180\ \frac{GW}{cm^2}$

$\Delta t := 130\ fs$

$w := 280\ \mu m$

$E_{NOPA} := I_{NOPA} \cdot \Delta t \cdot \pi \cdot w^2 = 11.5\ \mu J$

$E_{pump} := I_p \cdot \Delta t \cdot \pi \cdot w^2 = 57.6\ \mu J$

$$\eta_{OPA} := \frac{E_{NOPA}}{E_{pump}} \cdot \frac{\lambda_s}{\lambda_p} = 0.28$$

Appendix A6

MathCad program for estimation of the nonlinear refractive index n_2

For estimating the nonlinear refractive index by the Abbé number and the d-line refractive index of a material

n2 Abschätzung / Berechnung
nach *IEEE J. Quant. Elec. 14, 601 (1978)*

E. Wittmann, 11.01.17

n_d Brechungsindex der Fraunhofer d-Linie (587 nm) und ν_d ist die Abbé Zahl von refractiveindex.info

$$n_2\left(10^{-13}\mathrm{ESU}\right) = \frac{68\cdot\left(n_d-1\right)\cdot\left(n_d^2+2\right)^2}{\nu_d\cdot\left(1.517+\frac{\left(n_d^2+2\right)\cdot\left(n_d+1\right)}{6\cdot n_d}\cdot\nu_d\right)^{1/2}}$$

$$n_2\left(m^2/W\right) = \frac{40\pi}{c}\cdot\frac{n_2\left(\mathrm{ESU}\right)}{n} \approx 4.19\cdot10^{-7}\,\frac{n_2\left(\mathrm{ESU}\right)}{n}$$

BK7: $n_d := 1.5168$ $\nu_d := 64.17$

$$n_2 := \frac{68\,\left(n_d-1\right)\,\left(n_d^{\,2}+2\right)^2}{\nu_d\cdot\left(1.517+\frac{\left(n_d^{\,2}+2\right)\,\left(n_d+1\right)}{6\,n_d}\,\nu_d\right)^{\frac{1}{2}}} = 1.148$$

$$n2 := \frac{n_2\cdot10^{-13}}{n_d}\cdot4.19\cdot10^{-7}\,\frac{m^2}{W}$$

$$n2 = \left(3.172\cdot10^{-16}\right)\,\frac{cm^2}{W}$$

Appendix A7

MathCad program to estimate needed parameters to generate a single cycle pulse in the MIR

For calculating the needed phase-matching properties of biaxial crystals (LGS) and needed beam parameters for optical parametric amplification

Calculation Phase-matching for single-cycle-puls (SCP) in MIR

Einschließen << R:\Berechnungen\Sellmeier\Sellmeier.mcdx

$\lambda_{MIR0} := 8\ \mu m$ $\qquad \nu_{MIR0} := \dfrac{c}{\lambda_{MIR0}} = 37.5\ THz$ $\qquad T_{MIR} := \dfrac{1}{\nu_{MIR0}} = 26.7\ fs$

$\Delta\nu_{MIR} := \dfrac{0.441}{T_{MIR}} = 16.5\ THz$ $\qquad \Delta\nu_{MIR} = 551.25\ cm\_1$

$$Gauß\left(\nu, \nu_0, \Delta\nu\right) := e^{-4 \cdot \ln(2) \cdot \frac{\left(\nu - \nu_0\right)^2}{\Delta\nu^2}}$$

$\nu := 10\ THz, 10.1\ THz .. 60\ THz = \begin{bmatrix} 10 \\ \vdots \end{bmatrix} THz$ $\qquad \lambda := \dfrac{c}{\nu} = \begin{bmatrix} 30 \\ \vdots \end{bmatrix} \mu m$

$Gauß_{MIR} := Gauß\left(\nu, \nu_{MIR0}, \Delta\nu_{MIR}\right)$

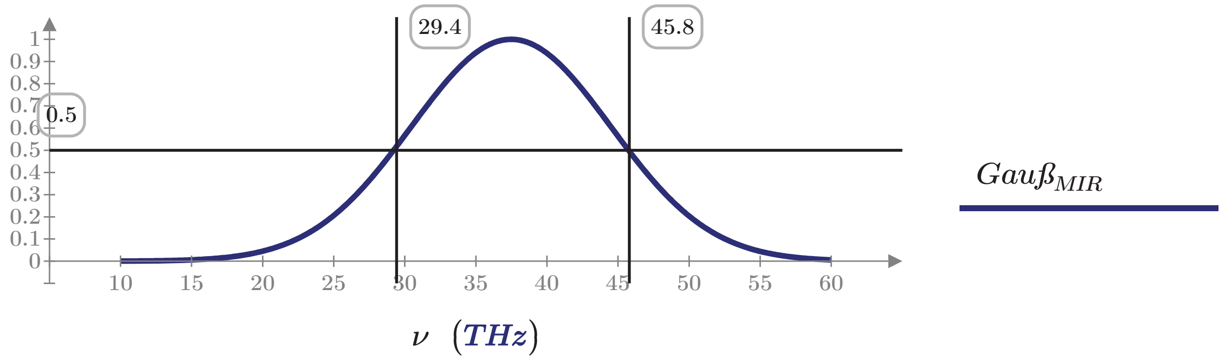

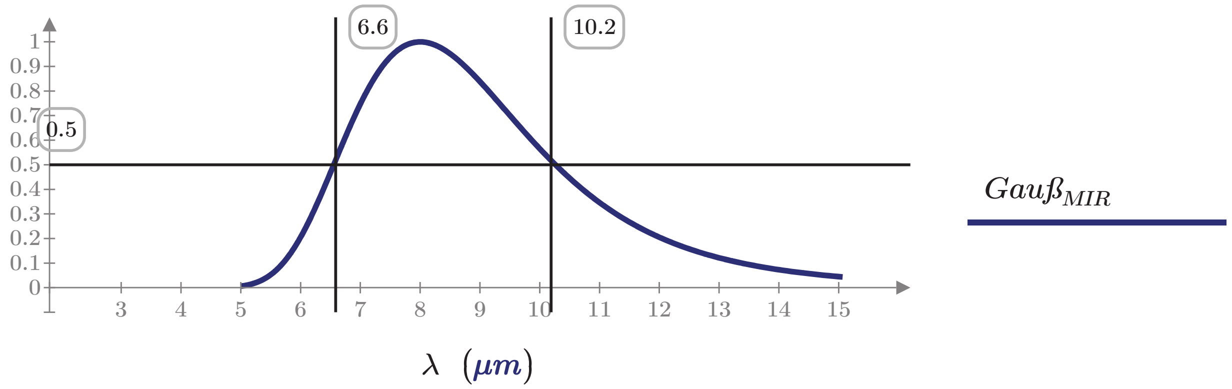

Abschätzung spektrale Breiten aller Pulse:

$\lambda_{pump} := 1030\ nm$

$\nu_{pump} := \frac{c}{\lambda_{pump}}$

$\Delta\lambda_{pump} := \frac{{\lambda_{pump}}^2}{c} \cdot \frac{0.441}{300\ fs} = 5.2\ nm$

$\lambda_{pump\_low} := \lambda_{pump} - \frac{\Delta\lambda_{pump}}{2}$

$\lambda_{pump\_high} := \lambda_{pump} + \frac{\Delta\lambda_{pump}}{2}$

$\nu_{NIR0} := \nu_{pump} - \nu_{MIR0} = 253.6\ THz$

$\lambda_{NIR0} := \frac{c}{\nu_{NIR0}} = 1182.2\ nm$

$\Delta\lambda_{NIR} := \frac{{\lambda_{NIR0}}^2}{c} \cdot \Delta\nu_{MIR} = 77\ nm$

$\nu_{red0} := 2 \cdot \nu_{pump} - \nu_{NIR0} = 328.5\ THz$

$\lambda_{red0} := \frac{c}{\nu_{red0}} = 912.5\ nm$

$\Delta\lambda_{red} := \frac{{\lambda_{red0}}^2}{c} \cdot \Delta\nu_{MIR} = 45.9\ nm$

$\nu1 := 220\ THz, 220.5\ THz \,..\, 400\ THz = \begin{bmatrix} 220 \\ \vdots \end{bmatrix} THz$

$\lambda1 := \frac{c}{\nu1} = \begin{bmatrix} 1.363 \\ \vdots \end{bmatrix} \mu m$

$Gauß_{NIR} := Gauß\left(\nu1\ ,\ \nu_{NIR0}\ ,\ 1.5 \cdot \Delta\nu_{MIR}\right)$

$Gauß_{red} := Gauß\left(\nu1\ ,\ \nu_{red0}\ ,\ 1.5 \cdot \Delta\nu_{MIR}\right)$

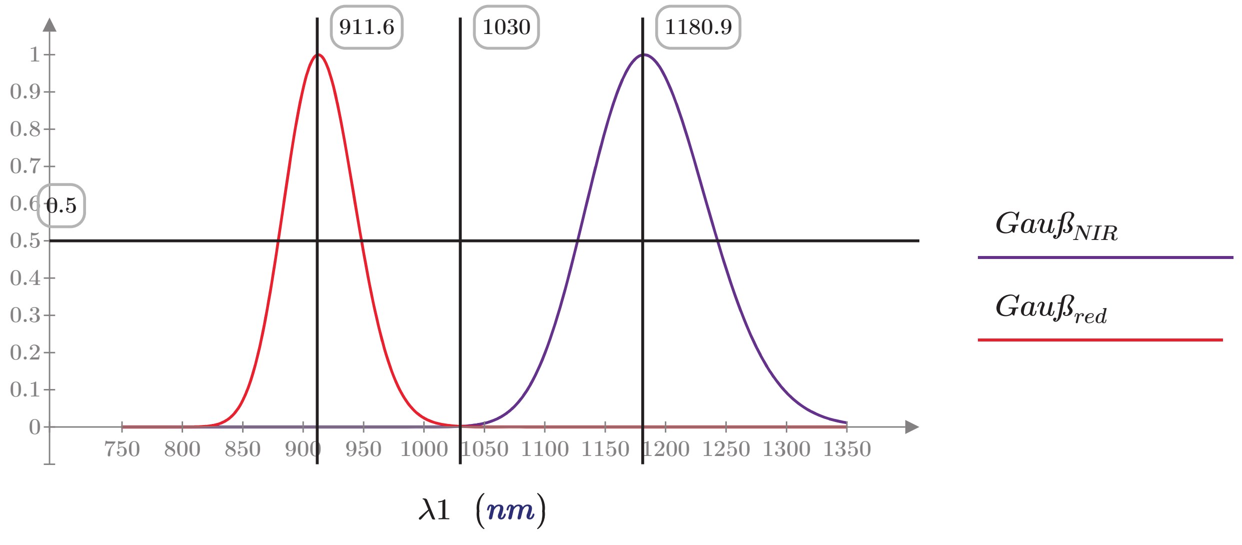

Abschätzung Energie bei 8 µm:

$f := 50\ kHz$

$P := 10\ W$

$E_{toth} := \frac{P}{f} = 200\ \mu J$

$E_{WL} := 1.3\ \mu J$

$E_{pump2h} := 80\ \mu J$

$E_{rest} := E_{toth} - E_{WL} - E_{pump2h} = 118.7\ \mu J$

$\eta_{SHG} := 30\%$

$E_{pump1} := E_{rest} \cdot \eta_{SHG} = 35.61\ \mu J$

$E_{pump1} \cdot f = 1.781\ W$

$\eta_{OPA} := 25\%$

$E_{red} := E_{pump1} \cdot \eta_{OPA} \cdot \frac{\lambda_{pump}}{2 \cdot \lambda_{red0}} = 5\ \mu J$

$E_{NIR} := E_{pump1} \cdot \eta_{OPA} \cdot \frac{\lambda_{pump}}{2 \cdot \lambda_{NIR0}} = 3.9\ \mu J$

$\eta_{DFG} := 20\%$

$E_{NIR2} := E_{pump2h} \cdot \eta_{DFG} \cdot \frac{\lambda_{pump}}{\lambda_{NIR0}} + E_{NIR} = 17.8\ \mu J$

$E_{MIR} := E_{pump2h} \cdot \eta_{DFG} \cdot \frac{\lambda_{pump}}{\lambda_{MIR0}} = 2060\ nJ$

$Verh := \frac{E_{NIR2}}{E_{NIR}} = 4.59$

LGS xz o,o-e:

$d_{LGS} := 0.5\ mm$

$\theta := 47.7°$

$\phi := 0.0°$

$d_{LGS\_2} := \frac{d_{LGS}}{2} \cdot 2 \cdot \pi$

$$\frac{\sin(\theta)^2\ \cos(\phi)^2}{\frac{1}{n^2}-\frac{1}{n_{xLGS}(\lambda)^2}}+\frac{\sin(\theta)^2\ \sin(\phi)^2}{\frac{1}{n^2}-\frac{1}{n_{yLGS}(\lambda)^2}}+\frac{\cos(\theta)^2}{\frac{1}{n^2}-\frac{1}{n_{zLGS}(\lambda)^2}}=0$$

$n_{eff}(\lambda, n) := \mathbf{minerr}(n)$

$n_{pump} := n_{eff}\left(\lambda_{pump}, 0.5\left(n_{xLGS}\left(\lambda_{pump}\right)+n_{zLGS}\left(\lambda_{pump}\right)\right)\right) = 2.126$

```
$\Delta kL2 :=$
    $i \leftarrow 1$
    for $\lambda_{NIR} \in 1103\ nm, 1104\ nm .. 1370\ nm$
        $\lambda_{MIR_i} \leftarrow \frac{1}{\frac{1}{\lambda_{pump}}-\frac{1}{\lambda_{NIR}}}$
        $\Delta k_i \leftarrow \left(\frac{n_{pump}}{\lambda_{pump}}-\frac{n_{yLGS}(\lambda_{NIR})}{\lambda_{NIR}}-\frac{n_{yLGS}(\lambda_{MIR_i})}{\lambda_{MIR_i}}\right) \cdot d_{LGS\_2}$
        $i \leftarrow i+1$
    $\begin{bmatrix} \lambda_{MIR} & \Delta k \end{bmatrix}$
```

$\lambda_{MIR} := \Delta kL2_{1,1} = \begin{bmatrix} \vdots \\ 10.5 \\ \vdots \end{bmatrix} \mu m$

$\Delta k := \Delta kL2_{1,2} = \begin{bmatrix} \vdots \\ -0.289 \\ \vdots \end{bmatrix}$

$FWHM := 0.800\ mm$

$\tau_{FWHM} := 260\ fs$

$$I_{pump} := \frac{E_{pump2h}}{\tau_{FWHM} \cdot FWHM^2} \cdot \frac{8 \cdot \ln(2)^{\frac{3}{2}}}{\sqrt{\pi}} = 125.2\ \frac{GW}{cm^2}$$

$$gain := \frac{1}{4} \cdot \exp\left(2 \cdot d_{LGS} \cdot \sqrt{\frac{8\ \pi^2 \cdot {d_{eff}}^2 \cdot I_{pump}}{n_{pump} \cdot n_{NIR} \cdot n_{MIR} \cdot \lambda_{NIR0} \cdot \lambda_{MIR0} \cdot \varepsilon_0 \cdot c}}\right) = 4.9$$

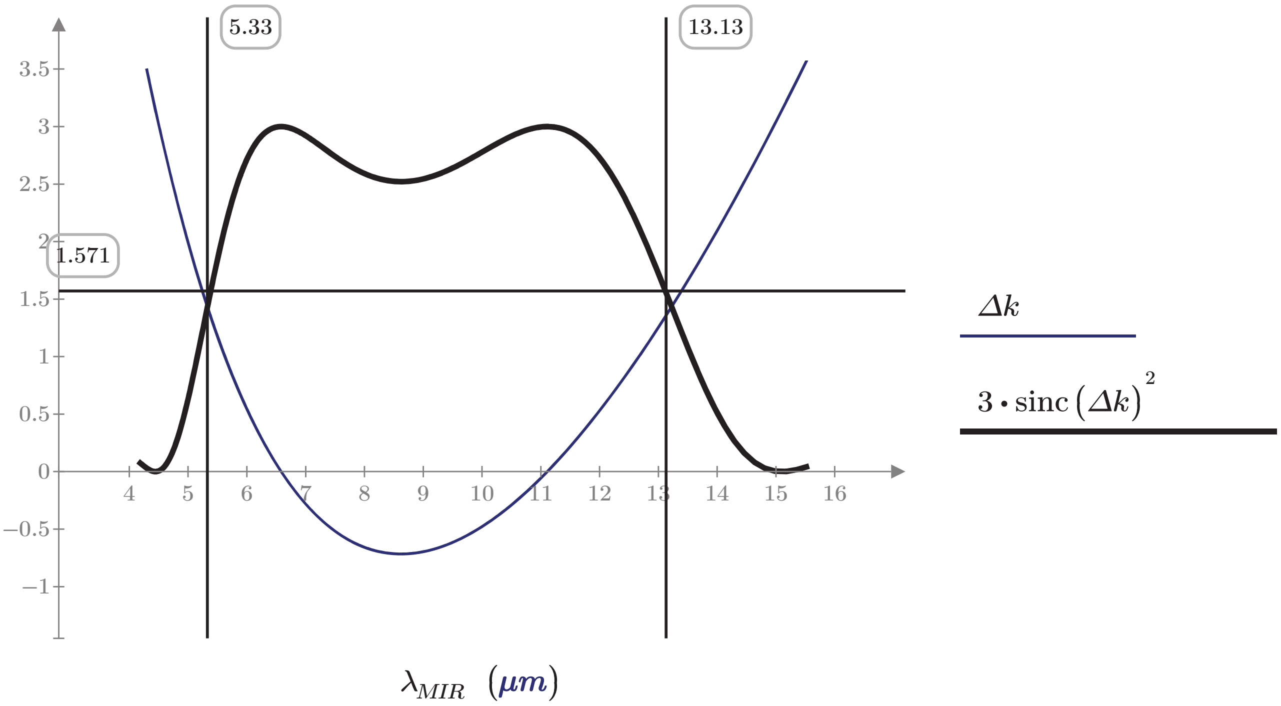

Danksagung

An dieser Stelle möchte ich mich bei allen Personen bedanken die direkten oder indirekten, sicher aber positiven, Einfluss auf die Entstehung der vorliegenden Arbeit ausgeübt haben.

An erster Stelle möchte ich mich bei meinem Doktorvater **Prof. Dr. Eberhard Riedle** bedanken - für das Bereitstellen der Forschungsthematik, den Zugang zu Labor und das Bereitstellen von Equipment sowie für das Herstellen von interessanten Kontakten und Kooperationen. Darüber hinaus vielen Dank für ihre investierte Zeit in kurzen, langen, stressigen oder entspannten Diskussionen, direkte Unterstützung im Labor und für die Hilfestellung beim Vollführen der verschiedenen Drahtseilakte. Der Leitsatz "einfach machen" und die Mentalität, hier und da nochmal ziemlich genau hinzusehen und kritisch zu hinterfragen, werden mich über die Promotion hinaus begleiten.

Ein richtig großes Dankeschön möchte ich auch meinen Kollegen am BMO aussprechen – **Roland Wilcken**, **Matthias Block**, **Qi Hu**, **Henrietta Volfova**, **Bastian Baudisch** und **Max Bradler**. Danke euch für die schöne Zeit, den Austausch und eure Hilfe! **Roland, Qi** und **Matthias** möchte ich ganz besonders danken; für Unterstützung im Labor, am PC und für die wissenschaftlichen Diskurse beim **Kiosk** oder am **China Turm** (nach Feierabend)!

Für die gelungene und gute Zusammenarbeit zur Erzeugung von extrem breiten Mittelinfrarotpulsen durch parametrische Verstärkung sei **Prof. Dr. Peter Baum**, **Prof. Dr. Rupert Huber** und deren Mitarbeitern **Dr. Yuya Morimoto**, **Matthias Knorr**, **Philip Merkl** und ganz besonders **Bo-Han Chen** herzlich gedankt.

Dr. Pavel Malevich sei auch herzlichst für die Unterstützung bei den Testmessungen für die achromatische Phasenanpassung gedankt.

Prof. Dr. Tobias Brixner danke ich für das Initiieren unseres gemeinsamen Projekts und den hieraus resultierenden, schönen und stabilen Messungen mit dem zwei Farben NOPA System bei MHz Wiederholrate. Der Dank gilt gewiss gleichermaßen seinem Team in Würzburg. Speziell seien hier **Dr. Victor Lisinetskii, Dr. Matthias Hensen, Sebastian Pres** und **Bernhard Huber** genannt.

Einen wahnsinnig großen Dank auch an **Rudolf Schwarz**, **Christian Hausmann** und **Alfons Stork**, von unserer Mechanikwerkstatt, für eure präzise Arbeit und spontane Einsatzbereitschaft wenn es pressierte (und das war oft)!

Abschließend möchte ich mich bei **meiner Familie** und **all meinen Freunden** für den mentalen Beistand während dieser Schaffensperiode bedanken. Ohne diesen hätte ich oft verzagen können, aber ihr wart ja da – Danke: *May your songs always be sung and may you stay forever young*.

Hiermit erkläre ich, die vorliegende Arbeit selbstständig verfasst und keine anderen als die angegebenen Quellen und Hilfsmittel verwendet zu haben.

München, den 17. Dezember 2018

Emanuel Wittmann